BINDING SERVICES
Tel +44 (0)29 2087 4949
Fax +44 (0)29 20371921
e-mail bindery@cardiff.ac.uk

The Laser Ablation ICP-MS Analysis of Olivine-Hosted Melt Inclusions from the Mull Plateau Group Lavas, Mull, Scotland

Kevin Jones

Submitted in partial fulfilment of the requirements for the degree of Ph.D.

Cardiff University

ProQuest LLC
789 East Eisenhower Parkway
P.O. Box 1346
Ann Arbor, MI 48106-1346

DECLARATION

This work has not previously been accepted in substance for any degree and is not being concurrently submitted in candidature for any degree.

Signed.....(Candidature)

Data.....

STATEMENT 1

This thesis is the result of my own investigations, except where otherwise stated.

Other sources are acknowledged by footnotes giving explicit references. A bibliography is appended.

Signed.....(Candidature)

Data.....

STATEMENT 2

I hereby give consent for my thesis, if accepted, to be available for photocopying and for inter-library loan, and for the title and summary to be available to outside organisations.

Signed.....(Candidature)

Data.....

Abstract

The Laser Ablation ICP-MS Analysis of Olivine-Hosted Melt Inclusions from the Mull Plateau Group Lavas, Mull, Scotland

Kevin Jones, Cardiff University 2005

The 840 km^2 lava field of the Isle of Mull, Scotland, represents only a small part of the North Atlantic Tertiary Igneous Province. The cause of this igneous activity at approximately 60 Ma, was the arrival and decompression melting of a hot plume. Previous work on the Mull lavas has focused on the whole rock geochemistry. The aim of this study is the analysis of olivine-hosted melt inclusions by Laser-Ablation Inductively-Coupled-Plasma Mass-Spectrometry (LA-ICP-MS). Melt inclusions are small aliquots of melt trapped by growing crystals (i.e. olivine, plagioclase) during magma evolution prior to and during eruptions. Therefore, melt inclusions analysis can provide valuable information on crystallisation temperatures, the sequence of phase changes in the host magma during cooling, cooling rates, the composition and volatile content of the host magma and liquid lines of decent. In the context of Continental Flood Basalts, melt inclusions also have the potential to provide information on the timing, extent and geochemical effects of crustal contamination.

Whole rock data indicated that the parental magmas of Mull Plateau Group lavas represent 4 to 13% melting of a depleted mantle source, located in the spinel-garnet transition zone. Whereas, melt inclusion data show that these parental magmas are mixtures of partial melts of between 2 and 20%, and that the whole rock values only reflect the mean extent of melting. These parental magmas rose through the lithosphere, with little interaction, before ponding near the lithospheric-crust boundary. Fractionation of spinel, olivine and clinopyroxene occurred concurrently with contamination of up to 8% Lewisian granulite by both Assimilation during Turbulent Assent and Assimilation during Fractional Crystallisation processes, with the hottest, most voluminous mantle melts suffering the greatest contamination. Many of the MPG lavas contain olivine phenocrysts enclosing decrepitated melt inclusions, which decrepitate in response to a drop in pressure, but without a corresponding drop in temperature. Therefore, the parental magmas of the MPG lavas rose rapidly from the lower crust, before being emplaced on Mull.

Acknowledgements

I would like to thank my supervisors Dr Andrew Kerr and Prof. Julian Pearce for being bold enough to take me on as their student (despite me being a sceptical mature student), and for their interest and help during the course of this thesis. I would also like to thank Cardiff University, School of Earth, Ocean and Planetary Science, for their financial support during the past three years. Thanks must also go to Dr Iain McDonald for his invaluable support in the development of the laser-ablation system, and without whom the whole project may have failed. Also deserving of mention are Peter Fisher for this help in using the Scanning Electron Microscope, Lawrence for producing over 40 thin sections, and not least all the secretarial and administration staff who do all the hard work behind the scenes.

Special thanks must go to my parents Malcolm and Florence Jones, my siblings Gillian Jones, Debra Jones and Allison Terrell and to my daughters Georgia and Abigail Jones for their unwavering support not only during the course of this thesis, but also during the preceding six years of undergrad study with the Open University and Cardiff University. When thing got bad and I was down, you always found a way of showing me the light, thus failure was never an option.

I would also like to thank all my fellow PhD students, both past and present for putting up with my rants and ravings. Alan for his friendship and company on numerous Friday nights out, for an Englishman he has a very Welsh outlook on life. The curry club Shaun, Graham, Dave, Richard, Sara and of course Andrew who now knows the Heinrich manoeuvre, for chickpea curries and stimulating conversations. Then there is Julia. What can I say about someone who shared exam stress, armed guards in the Western Ghats, curry breakfasts in Mumbai, fish suppers in Spain and so much more. You have maturity beyond your years, and have always accepted me for what I am. For that, I am eternally grateful.

Finally, to Paul and Diane, many thanks, just for listening and being there, when I needed humans, rather than Microsoft as company.

The Laser Ablation ICP-MS Analysis of Olivine-Hosted Melt Inclusions from the Mull Plateau Group Lavas, Mull, Scotland.

Chapter 1 – Introduction

Chapter 2 – Mull as part of the North Atlantic Igneous Province

Chapter 3 – Field Locations and Petrography of Samples

Chapter 4 – Melt Inclusions and Methods of Analysis

Chapter 5 Melt Inclusion Analysis by LA-ICP-MS

Chapter 6 - Whole Rock and Melt Inclusion Data Interpretation

Chapter 7 Concluding discussion

References

Appendices

List of Figures

Chapter 1
Introduction

1.1 Aims

The aims of this study are: 1) to carry out a comprehensive analysis of olivine-hosted melt inclusions in basaltic lava flows from Mull: 2) in-depth examination and modelling of geochemical data: 3) interpretation of results, with respect to the evolutionary history of the volcanism that affected Mull and the North Atlantic region during the Tertiary. The Isle of Mull, which is part of the Inner Hebrides is located off the west coast of Scotland, and chosen as the field area for this study due to the excellent outcrop and freshness of the basaltic flows. These mafic lava flows are part of the plume-related Tertiary North Atlantic Igneous Province continental basalt sequence, and as such gives us an excellent window into the early processes that shaped and contributed to the opening of the North Atlantic Ocean.

1.2 Large Igneous Provinces

Large Igneous Provinces (LIPs) are enormous crustal emplacements of primarily mafic intrusive and extrusive igneous rocks, which have their origins in processes other than those associated with sea floor spreading, or subduction zones. LIPs manifest themselves in a number of forms including continental flood basalts (e.g. North Atlantic Igneous Province, Deccan Traps, Siberian Traps), submarine ridges (e.g. Ninety East Ridge), oceanic plateaus (e.g. Kerguelen Plateau, Ontong Java Plateau), ocean basin flood basalts (e.g. East Mariana Basin), volcanic rifted margins (e.g. Hatton Bank, Seychelles Bank, Brazilian Margin) and sea mount groups (e.g. Hawaiian-Emperor Seamounts) (Fig. 1.1). Research into the processes of LIP formation has intensified over the past two decades as new data have become available from seismic tomography, geochemistry, marine geophysics and petrology (e.g. Campbell and Griffiths, 1990; Coffin and Eldholm, 1994; Saunders, 1997; Kerr *et al.*, 1999; Kempton *et al.*, 2000).

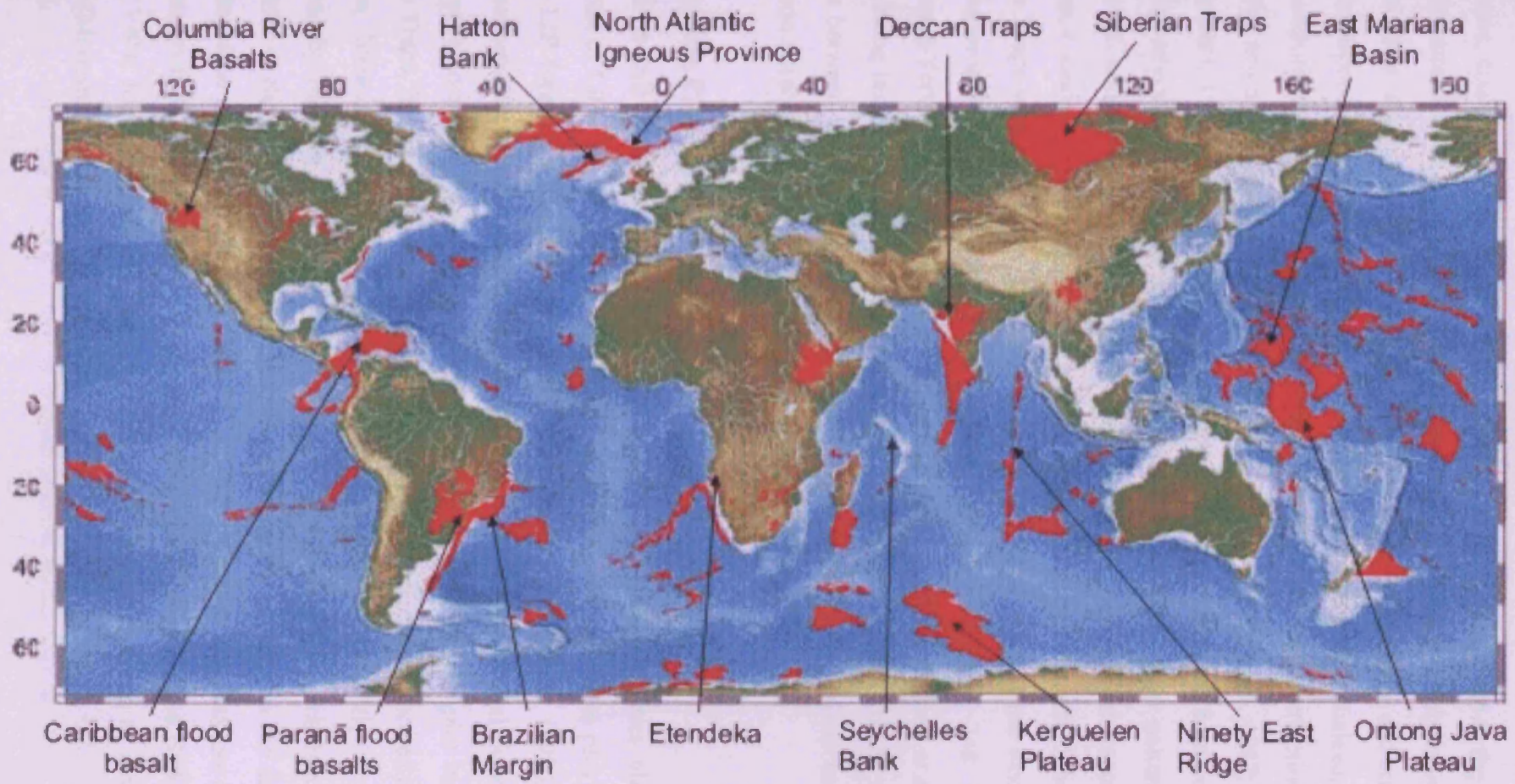

Fig. 1.1. Worldwide distribution of continental and oceanic Large Igneous province. (After Saunders, 1997)

The increase in magmatic activity associated with LIPs, whether subaerial or submarine, could possibly have had a global effect on past climate due to the release of vast amounts of ash and volatiles. Such activity would almost certainly have changed the chemistry, and possibly the circulation patterns of the hydrosphere and atmosphere, with corresponding severe adverse affects on the Earth's biosphere. Indeed, there are good temporal correlations between LIP formation and major biotic extinctions of both terrestrial and marine flora and fauna (Rich *et al.*, 1986; Officer *et al.*, 1987; Rampino and Stothers, 1988; White, 1989). Even though most correlations are based on limited and relatively uncertain age determinations, there seems to be a clear pattern of LIPs and mass extinctions occurring simultaneously in the geological record. Most significant among these relationships are the correlations between the Siberian and Deccan Traps with the two largest mass extinctions to have affected the world during the Phanerozoic Eon, namely the Permian-Triassic extinction (~248 Ma) and Cretaceous-Tertiary (~65 Ma) respectively (Officer *et al.*, 1987; Campbell *et al.*, 1992). Even among lesser extinction events, there seems to be correlation with LIP formation such as between the North Atlantic Igneous Province (NAIP) and Palaeocene-Eocene extinction event (56.5 Ma) (Rea *et al.*, 1990; Thomas, 1990).

1.3 Mantle Plumes

It is still a matter of great discussion what part mantle plumes play in the formation of LIPs. The consensus amongst most workers is that plumes play a pivotal role in LIP formation (e.g. Saunders, 1997). Campbell and Griffiths, (1990) showed that plate tectonic reconstructions place a number of major continental flood basaltic (CFB) provinces over known hotspots at the time of volcanism. Examples include the Deccan Traps, NAIP, Parana and Karoo, which are believed to have formed above the Reunion, Iceland, Tristan de Cunha and Crozet hotspots respectively. It has also suggested by Morgan (1972, 1981) that there is no evidence for volcanism in these areas prior to the formation and impingement of the mantle plumes on the underlying crust. Based on the MgO content of CFBs it has been proposed that hotspots are zones of anomalously hot material rising from the deep mantle (McKenzie and Bickle, 1988; Coffin, 1994; Kerr, 1995a), and that CFBs are the first manifestation of new mantle plumes (Morgan, 1972, 1981; Richards *et al.*, 1989).

1.3.1 Origins of Mantle Plumes

Mantle plumes must originate from deep within the mantle, possibly the core-mantle boundary or the 670 km discontinuity. Plumes cannot form from localised anomalous concentrations of radioactive heating being carried through the mantle, since these will not generate temperatures high enough to provide the buoyancy needed to bring a plume to the top of the mantle (Griffiths, 1986). Laboratory work carried out by Whitehead and Luther (1975) suggests that a newly formed plume originating from the core-mantle boundary layer would consist of two parts: a large bulbous head and a relatively narrow tail (Fig. 1.2).

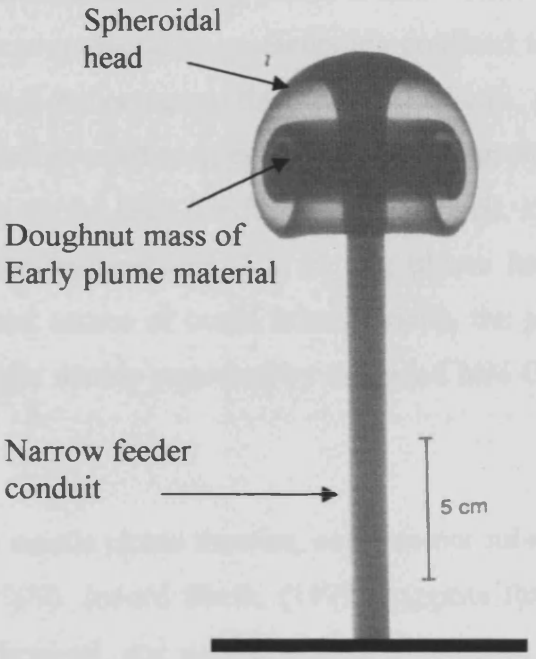

Fig. 1.2. Diagram showing the plume created in laboratory experiments by Whitehead and Luther, (1975)

In laboratory experiments with plumes driven by buoyancy resulting from thermal expansion, the convection of heat leads to striking effects (Griffiths, 1986). As long as there is an uninterrupted supply of hot fluid from a source region, a starting plume consists of a large spheroidal head and narrow feeder conduit. As the plume head rises, a thin boundary layer of bordering mantle is heated by conduction until its temperature and density become comparable to that of the plume, at which point it becomes incorporated into the plume head by convection processes. Thus, a plume head would be a mixture of material from the hot source region and the cooler mantle through which it is rising (Campbell and Griffiths, 1990). Flow in the tail, before it is

tilted by large scale shearing in the mantle, does not entrain a significant amount of the surrounding mantle, nor does it cool dramatically as it ascends (Loper and Stacey, 1983). However, the temperature in the tail remains significantly higher than the average temperature in the plume head, and its composition the same as the source region of the plume. The source material rises up the conduit until it reaches the head, where it spreads out radially over the cap, and wrapped into the spherical eddy. Therefore, the source material becomes a thin sheet with a large surface area, losing heat to the entrained material as the two are wrapped together, leading to a compositionally and thermally zoned head (Campbell and Griffiths, 1990). Apart from the plume axis, the hottest part of the plume is the thin layer of source material covering the top of the head. The doughnut shaped mass (Fig. 1.2), containing the source mantle material, which forms the head of the starting plume is also warmer than the average head temperature, but the large temperature gradients are confined to the axial conduit and the perimeter of the head. In contrast to the thermal gradients, if the plume source region and overlying mantle have differing compositions, compositional zoning will persist in the order of ~10 km in the head (Griffiths and Campbell, 1990). Therefore, Campbell and Griffiths, (1990) suggest that if a starting plume has the composition of OIB-type mantle (enriched source of ocean island basalt), the plume head will be zoned with layers of OIB-type mantle separated by entrained Mid Ocean Ridge Basalt (MORB) type mantle.

Even though most scientists accept mantle plume theories, some do not subscribe to this view (Anderson, 1985; Sheth, 1999). Indeed Sheth, (1999) suggests that the geodynamic, thermal, petrological, geochemical, and geochronological evidence from the Deccan Traps do not require or support a mantle plume origin. He also argues that the Reunion plume played no part in the formation of the Deccan Traps, or indeed that the Reunion plume even exists at all. As alternatives Sheth, (1999) quotes the work of Anderson, (1994) and Anderson *et al.* (1992), where they invoke hotcells and/or melting of the perisphere (enriched high level mantle that is distributed all around the globe). However, these ideas are contrary to the prevailing views on LIPs, and are not supported by the evidence from the NAIP, where the most convincing theory is still one that evokes a deep-seated mantle plume.

1.3.2 Plume-Lithosphere Interactions

A mantle plume will ascend until it impinges on the base of the lithosphere causing dynamic uplift or doming, at the same time the plume will spread out laterally to form a zone of high ambient temperature mantle, with a diameter of ~1000 km (Courtney and White, 1986) or possibly as great as 2000 km beneath a plate (White and McKenzie, 1989). Voluminous magmatism results because of decompression melting of plume material, resulting from extension within the overlying plate, where the plume has a passive role responding to structural changes in the overlying lithosphere (White *et al.*, 1987; McKenzie and Bickle, 1988; White and McKenzie, 1989; Fig. 1.3), or possibly due to the plume playing a more active role in driving plate separation. Material within the ascending plume head may already be above its solidus temperature prior to impingement onto the base of the lithosphere, resulting in extensive melting without the need for any substantial lithospheric extension (Richards *et al.*, 1989; Griffiths and Campbell, 1990; Fig. 1.4). It is also suggested that the active role of mantle plumes in LIP production may even lead to continental break up (Morgan, 1981; Coffin 1994).

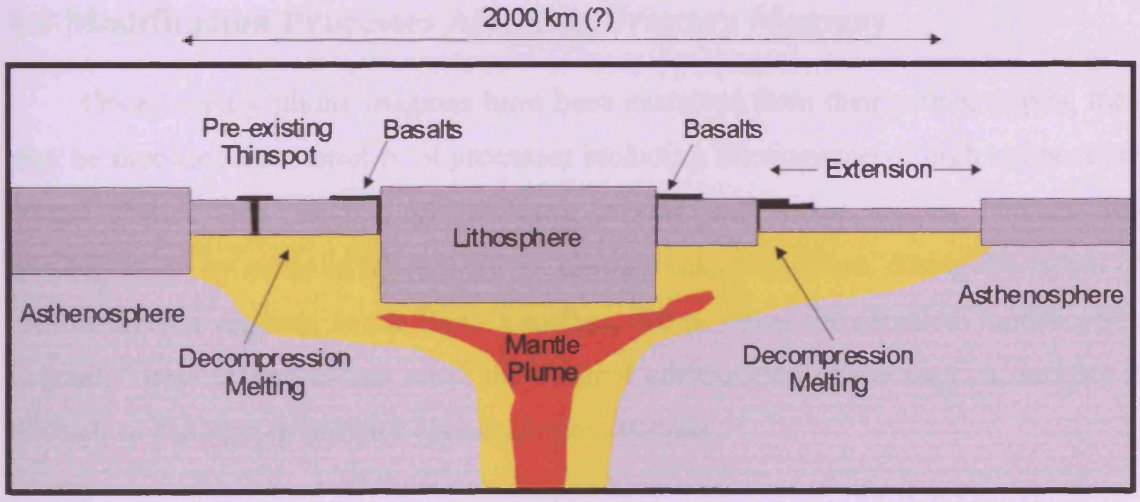

Fig. 1.3. Passive plume model, where melting is restricted to pre-existing topography at the base of the lithosphere, or contemporaneous extension (White and McKenzie, 1989). (Modified from Saunders *et al.*, 1992)

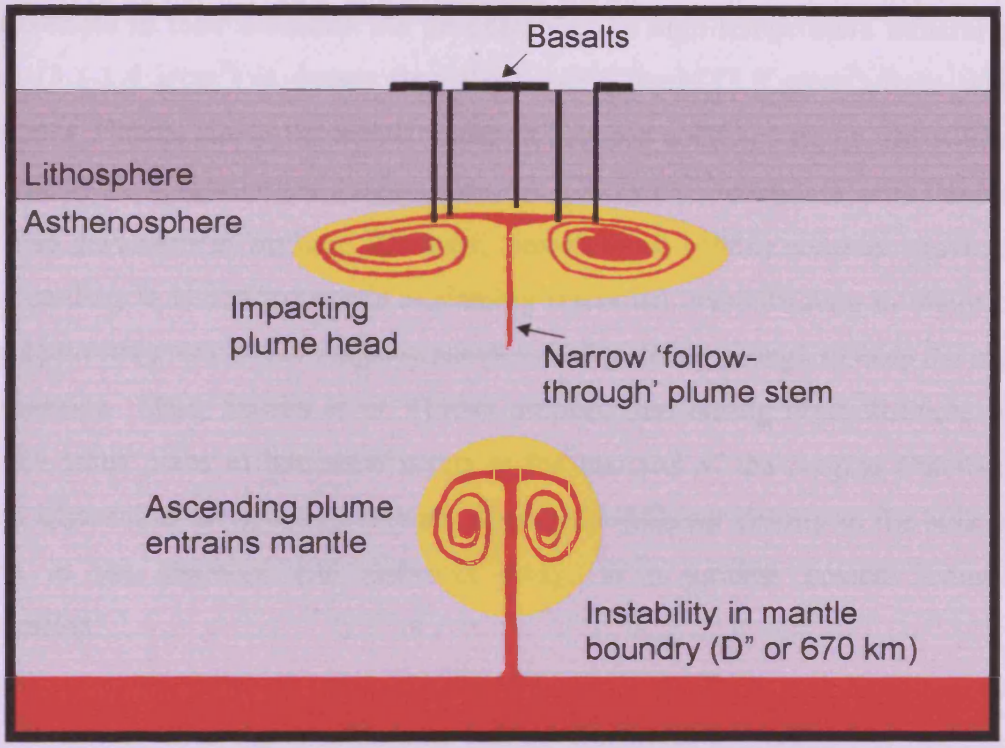

Fig. 1.4. Active plume model where the ascending plume undergoes melting prior to lithosphere interactions (Griffiths and Campbell, 1990). (Modified from Saunders *et al.*, 1992)

1.4 Modification Processes Affecting Primary Magmas

Once primary plume magmas have been extracted from their source region, they may be modified by a number of processes including fractionation of high temperature crystal phases (e.g. olivine, plagioclase), mixing with other magma batches and contamination by melts of lithospheric or crustal rocks. Therefore, during the ascent of mantle-derived magmas to the Earth's surface, the potential for chemical modification is great. These processes can mask the original composition of the magma, making it difficult to distinguish primary chemical compositions.

1.4.1 Fractional Crystallisation

The crystallisation history of most magmas can be complex, mainly due to fractional crystallisation processes (Bowen, 1928). Fractional crystallisation consists of separating minerals from a residual magma, and can be accomplished in a number of ways. Firstly, it can occur by separating whole crystals from the residual liquid because

of differences in their densities. As an example, the high temperature mineral phase olivine (3.3-3.4 g/cm^3) is denser than the basaltic liquid (3.0 g/cm^3) from which it crystallises. Hence, due to the density contrast between solid and liquid, the solids sink and settle to the bottom of the magma chamber, producing a cumulate, with the process known as gravitational settling. However, Sparks *et al.* (1984) consider gravitational crystal settling to be inadequate in explaining fractional crystallisation in many cases, due to convective motions in magma chambers being strong enough to keep the crystals in suspension. Thus, Sparks *et al.* (1984) propose that during crystallisation, which generally takes place in boundary layers at the margins of the magma chamber, the magma adjacent to the growing crystals develops a different density to the bulk of the magma in the chamber and convects away, in a process coined "convective fractionation".

No matter how the mechanisms behind fractional crystallisation operate, the outcome is the same, that is the chemical composition of the magma is altered, due to the crystallising phase having a different composition to the melt. Therefore, if the liquid was erupted post the onset of fractionation; the composition would be different from the starting or primary composition of the melt.

1.4.2 Magma Mixing

If a fresh magma batch is injected into a pre-existing magma chamber, a hybrid liquid between the two compositions may be produced. The parental magmas can be derived from differing sources, such as silicic melt from the deep continental crust, and basaltic magma from the upper mantle. Alternatively, magmas may be derived from a common parental magma, but follow differing evolutionary tracks, such as found in compositionally zoned magma chambers. There are several methods by which magma mixing can occur:

1. Hot plume material replenishing magma into an evolving magma chamber. This is the most likely scenario in CFBs systems as episodically replenished primitive magma mingles and mixes with cooler magma that has evolved through crystal fractionation processes (Fig. 1.5a).

2. During the rise and flow of magmas through narrow conduits, erupted magmas can form mixed lavas and pyroclasts (Snyder *et al.*, 1997) (Fig. 1.5b).

3. Magma mixing can occur through the convective overturn and stirring in magma chambers, when underlying, initially denser mafic magma cools and exsolves volatile fluids, making it less dense than the overlying silicic magma. The underlying vesiculating magma develops metre-scale Rayleigh-Taylor instabilities (Lister and Kerr, 1989), causing detachment of buoyant blobs, some of which may become mingled mafic inclusions within the felsic host if solidification is rapid, or totally mixed if longer residence in hot magma allows (Fig. 1.5c).

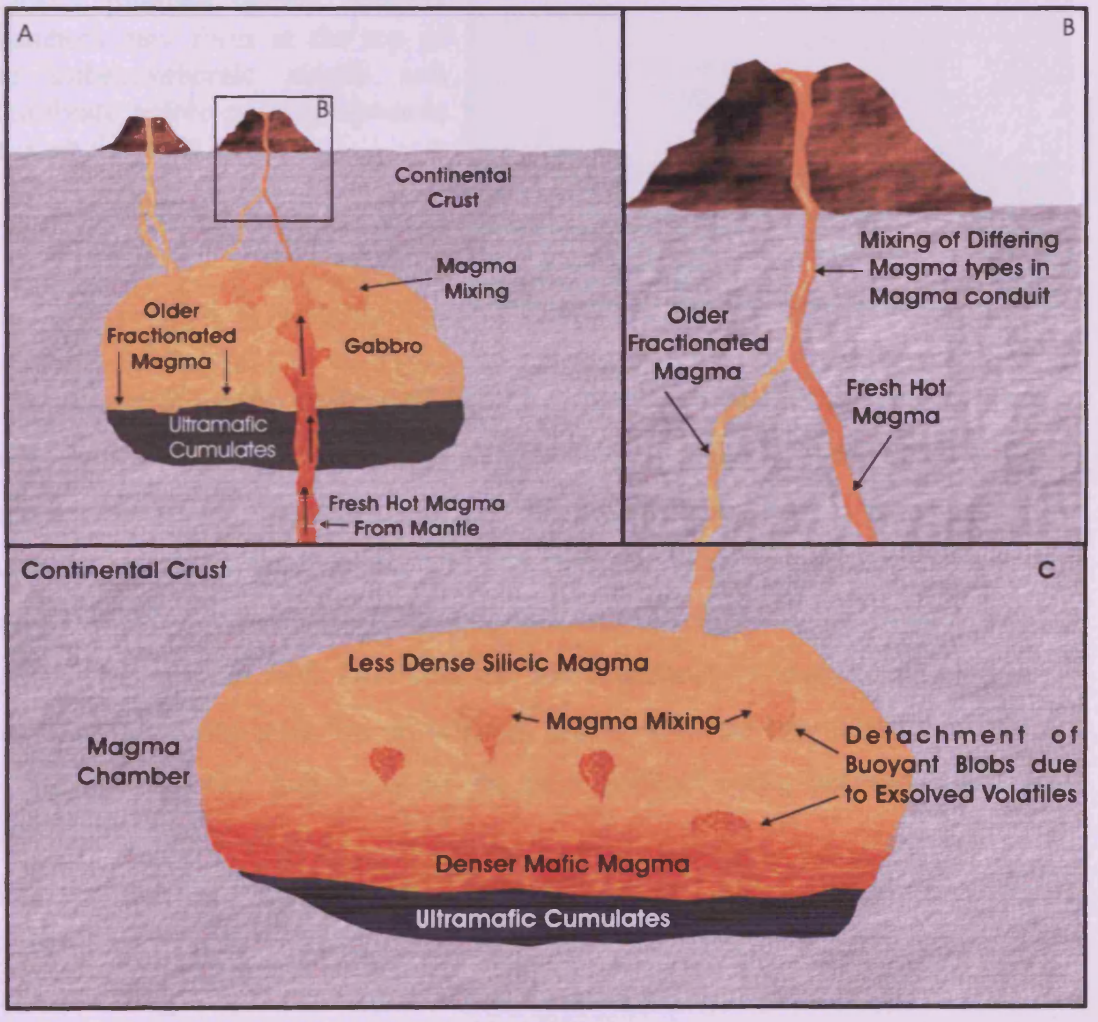

Fig. 1.5a-c. Schematic diagram of the differing processes of magma mixing. (A) Replenishment of evolved magma by hot primitive magma for mantle. (B) Mixing of magmas in chamber evacuation conduits. (C) Mixing in layered magma chamber by convective overturn.

1.4.3 Crustal Contamination

As primary magmas progress upward from their depth of segregation, which underneath continents may be more than 100 km, they encounter low-density crustal rocks. At this point, the rising basaltic magmas may reach a state of zero or negative buoyancy and pond, forming a magma chamber within the crust or at the crustal-lithospheric mantle boundary (MOHO) (Fig. 1.6). The magma may then equilibrate with the confining rock, before pushing upwards towards the surface, whilst undergoing contamination by crustal derived contaminants (Kerr *et al.*, 1995).

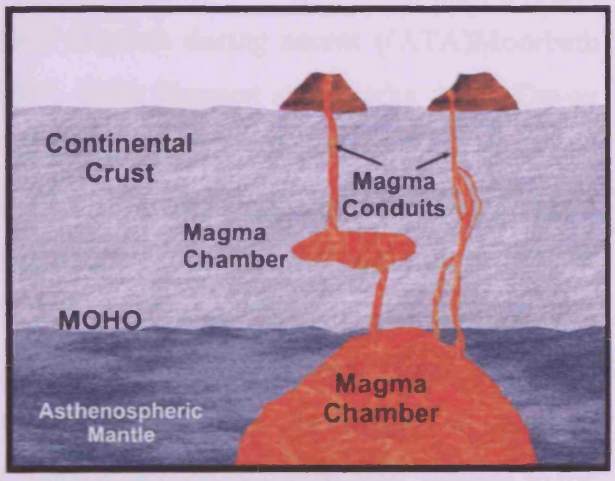

Fig. 1.6. Schematic cross section of volcanic pluming system. Magma chambers may form at the top of the asthenosphereic mantle and equilibrate before pushing upwards through the crust.

Work carried out on continental basaltic provinces have revealed the occurrence of two contrasting styles of crustal contamination (Huppert and Sparks, 1980; Thompson *et al.*, 1986; Kerr *et al.*, 1995). In the first, contamination is accompanied by concurrent fractional crystallisation, and occurs primarily in magma chambers, where the latent heat released by fractionation allows fusion of the wall rocks. DePaolo (1981) has termed this process AFC (Assimilation and Fractional Crystallisation) (Fig. 1.7). The AFC model depends on the existence of a near spherical (low surface-to-volume ratio) magma chamber, and leads to the most evolved rocks becoming the most contaminated.

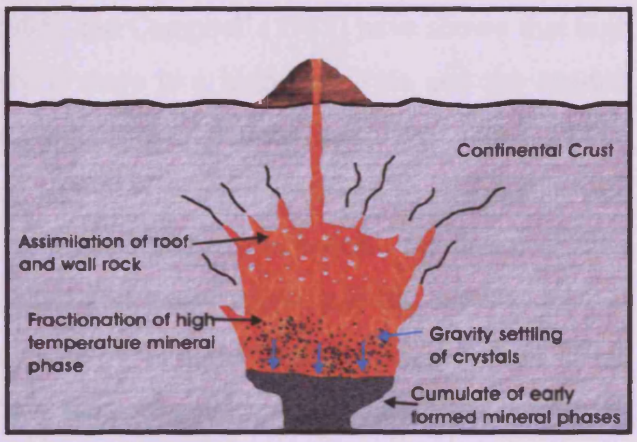

Fig. 1.7. Schematic cross section through magma chamber undergoing assimilation and fractional crystallisation (AFC) (DePaolo, 1981).

The second mode of crustal contamination is assimilation of a fusible acidic fraction of crust by the most basic (hottest) magmas during ascent ((ATA)Moorbath and Thompson, 1980; Thompson *et al.*, 1982, 1986; Huppert and Sparks, 1985; Devey and Cox, 1987; Kerr *et al.*, 1995). The ATA process requires that the magma chambers have high surface-to-volume ratios (Fig. 1.8), thus allowing a large surface area of magma to be in contact with the surrounding country rock, permitting partial melting of the more volatile and large ion lithophile rich fraction of the surrounding crust in a comparatively short time frame (Patchett, 1980; Huppert and Sparks, 1985). The ATA process is also dependent on the flow regime operating in the magma conduits. If laminar flow conditions prevail, most heat transfer will be by conduction, leading to the formation of a chilled margin on the magma chamber and/or conduit walls, therefore shielding later magmas from contamination.

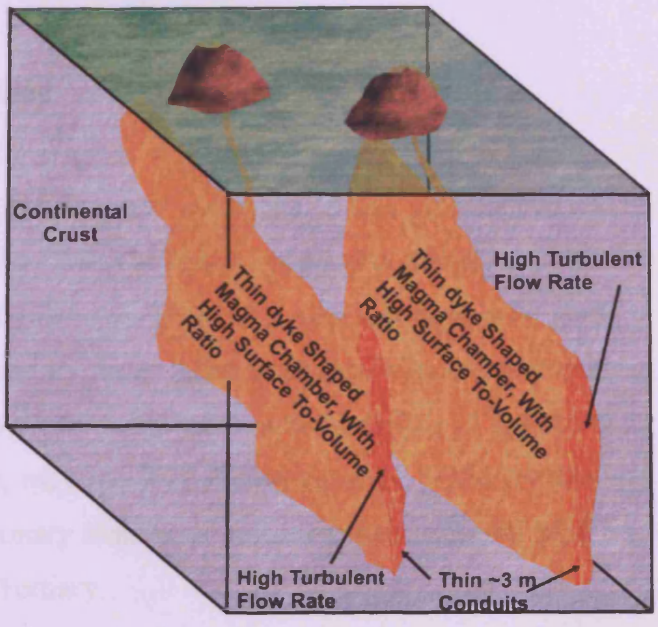

Fig. 1.8. Schematic diagram of sill like magma chambers with high surface to volume ratios, needed for the partial fusion of the country rock in the ATA process.

However, Huppert and Sparks (1985) and Campbell (1985) have shown that high Mg basaltic magmas ascend turbulently if there is a high flow rate and the conduit width is greater than ~3 m. Under such conditions, it is far less likely that a chilled margin would form, therefore bringing turbulently ascending hot basic magma into constant contact with the surrounding wall rock. As a result, the more fusible components of the wall rock can be melted and incorporated into the magma. Kerr *et al.* (1995) have shown that the most contaminated lavas from the Mull plateau group lavas are the most primitive or Mg rich, thus suggesting that these lavas have been contaminated by crustal derivatives by the ATA process.

1.5 Olivine Fractionation and Melt Inclusions

Olivine is normally the first mineral phase to fractionate out of subalkalic basaltic magmas, except possibly for Cr-spinel, which is often found as solid inclusions within olivine, and may act as nucleation points for olivine growth (Kerr, 1998). As well as containing solid inclusions, olivine often contains fluid and melt inclusions. Melt inclusions are small portions of melt trapped by the imperfect growth of crystals during magma evolution prior to and during eruption. Therefore, studies of these melt inclusions can provide valuable information on crystallisation temperature, the sequence of phase changes in the host magma during cooling, constraints on cooling rates, volatile content of the host magma, liquid line of decent, and contamination of magmas by mixing and crustal contamination processes.

1.6 Broad objectives of this study

Despite extensive work on the NAIP, many questions remain unanswered on the nature of the magmas that supplied the CFB, the history of magma mixing and amount of crustal contamination that affected the lavas. Therefore, attempts have been made to analyse olivine-hosted melt inclusions by laser ablation inductively coupled plasma mass spectrometry (LA-ICP-MS). In-depth examination and modelling of geochemical data, and the interpretation of results, may result in answering some of the outstanding questions with respect to the evolutionary history of volcanism that affected Mull and the North Atlantic region during the Tertiary.

Chapter 2

Mull as part of the North Atlantic Igneous Province

2.1 Introduction

The Island of Mull comprises one of several Tertiary igneous centres that collectively are known as the British Tertiary Igneous Province (BTIP), which is the easternmost manifestation of igneous activity within the wider North Atlantic Igneous Province. In Britain the igneous activity, which spanned 11 my (63-52 Ma), resulted in the accumulation of thick sequences of basaltic lavas, and the establishment of major volcanic centres. The remains of which, can now be seen on Skye, St Kilda, Rum, Ardnamurchan, Arran and Mull (Emeleus, 1991).

The Tertiary age of these rocks was not recognised until the work of Geikie (1871), and Judd (1874), (see summary in Geikie, 1897). In the early twentieth century a succession of detailed maps and memoirs were published by the Geological Survey of Great Britain, covering Skye (Harker, 1904; Anderson and Dunham, 1966), Rum (Harker, 1908), Mull (Bailey *et al.*, 1924), Arran (Tyrrell, 1928) and Ardnamurchan (Richey and Thomas, 1930). Since 1945 work has continued, but with the emphasis on geochemical investigation, most notably by (Carter *et al.*, 1978; Thompson, 1982; Dickins *et al.*, 1987; Thompson and Morrison, 1988; Kerr, 1993, 1997, 1998), and has led to a much better understanding of mantle melting processes, fractionation processes and contamination of the magmas by crustal rock.

2.2 The North Atlantic Igneous Province

During the Palaeogene (65-23.3 Ma), widespread magmatism occurred throughout the proto-North Atlantic region, and this was one of the first LIPs to be recognised. As early as 1880 Giekie was struck by the similarity of the basaltic successions in the northwest British Isles, Faeroes and Iceland This idea being further developed by Holmes and Harwood (1918), who suggested a broadly related, originally

contiguous province, which also incorporated East and West Greenland. More recently igneous rocks found in Canada and the North Atlantic Basin have also been shown to be part of this province, which is collectively known as the North Atlantic Igneous Province (NAIP) (Saunders *et al.*, 1997). The onshore basaltic sequences of the NAIP taken together cover an area much smaller that other LIPs. However, when the offshore sequences, such as the Voring and Rockall Plateaus are included, the total area for the NAIP increases to ~1.3 x 10^6 km^2 (Eldholm and Grue, 1994), comparable to the Parana or Deccan Traps (Mahoney, 1988).

2.2.1 Tomographic evidence for the North Atlantic Plume

Recent tomographic work by Bijwaard and Spakman (1998) provides solid evidence in support of a mantle plume beneath Iceland. From the data set of Engdahl *et al.* (1998), Bijwaard and Spakman constructed a relatively high-resolution global mantle tomography model. In Fig. 2.1, the low velocity anomalies are compared to the ak135 model developed by Kennett *et al.* (1995) for the mantle below Iceland, stretching from the core-mantle boundary (CMB) to the surface. Bijwarrd and Spakman (1998) have interpreted the low velocity anomaly as a non-cylindrical tilted column that is a little broader in a north-south direction than in an east-west direction. From the CMB to the transition zone, the width of the anomaly is rather constant being ~400-700 km in an east-west direction. Once above the transition zone the anomaly increases its width to about 1500 km, almost as wide as the North Atlantic Ocean. In the upper mantle the anomaly lies beneath Iceland, but shifts towards the Faeroes Islands at ~1000 km depth, before returning to below Iceland at ~2000 km, from which point it tends to migrate in the direction of Greenland.

Bijwaard and Spakman (1998), concluded that the origins of the Iceland plume is at or near the CMB, where it has an approximate width of >1000 km. It then rises as a relatively narrow <500 km column to within 400 km of the surface, at which point it spreads out laterally to 1200 km in width. Overall, the shape of the anomaly is deflected towards the east, perhaps indicating that the hotspot is not stationary (Steinberger, 2000).

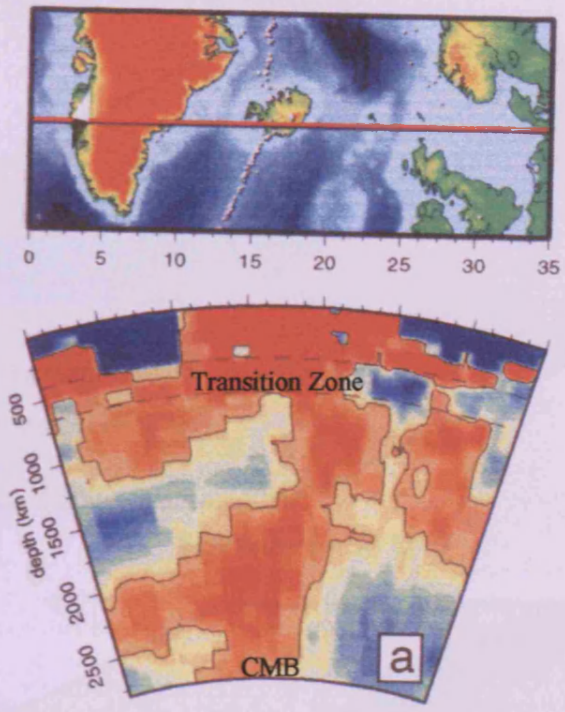

Fig. 2.1. Cross section through the model of Bijwaard and Spakman (1998), showing a large plume shaped anomaly beneath Iceland.

2.2.2 Seismic evidence for the North Atlantic Plume

The hotspot origin for the NAIP is further supported by the work of Holbrook *et al.* (2001) on the volcanic rifted margins (VRM) of the North Atlantic. Using data from the Seismic Investigation of the Greenland Margin (SIGMA), they drew the following conclusions: The thermal anomaly linked with the break-up of Greenland from Europe was modest ~ 100± 50°C, comparatively uniform along the margins and short lived. From the thick crust >30 km, and low P-wave velocities ~7.1 km s^{-1} along the North Atlantic plume track, Holbrook *et al.* (2001) suggest that active up welling occurs below present day Iceland, and that this has been the case for ~60 Ma. They suggest that a plume of ~300 km radius and ΔT of ~125°C affected the margin around 61 Ma (Fig. 2.2a) and laterally delivered warm material from its upper portions to more distal portions of the margin. As the crust broke-up 56 Ma (Fig. 2.2b), the lower part of the plume head continued to supply material by active up-welling into the proximal areas of the margin. By ~45 Ma (Fig 2.2c) the plume head was exhausted, and excess magmatism was mostly confined to a narrow <200 km zone.

Fig. 2.2a. Prior to break-up, a rising plume head ($\Delta T=125^{\circ}C$) impacts the continental lithosphere and spreads laterally to emplace warm material beneath the continent. (Modified from Holbrook *et al.*, 2001)

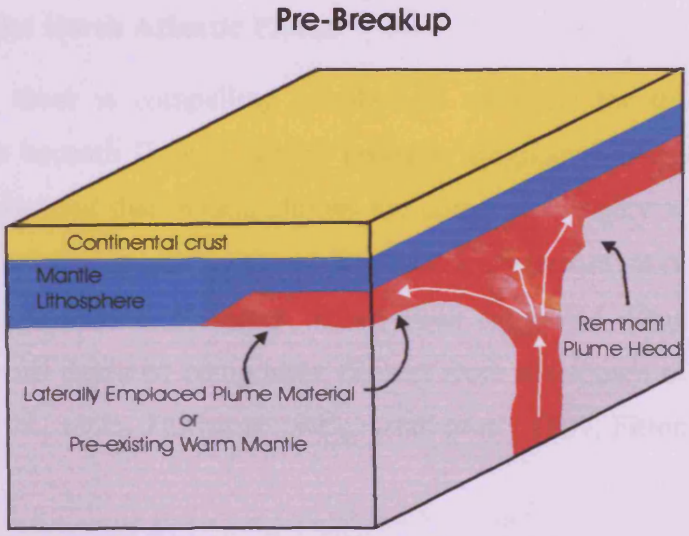

Fig. 2.2b. At break-up ~55 Ma, strongly active up-welling (white arrows) occurs above remnant plume head and plume stem, building 30 km thick igneous crust in the hotspot-proximal region. (Modified from Holbrook *et al.*, 2001)

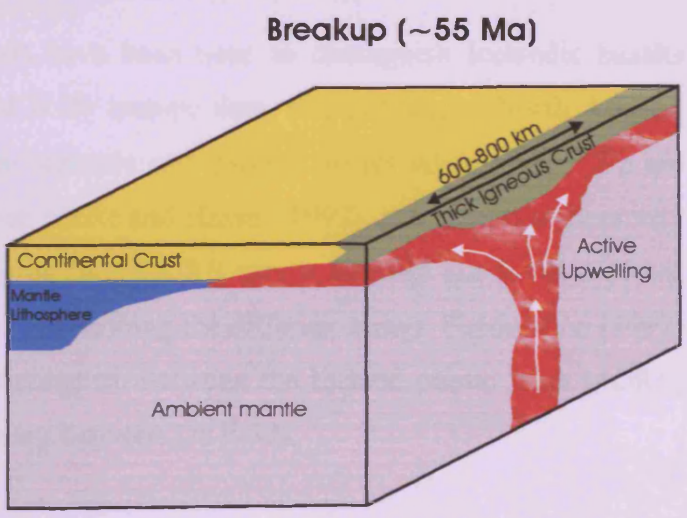

Fig. 2.2c. At ~45 Ma, the warm mantle reservoir has been exhausted, and excess magmatism is strongly focused above the plume stem. (Modified from Holbrook *et al.*, 2001)

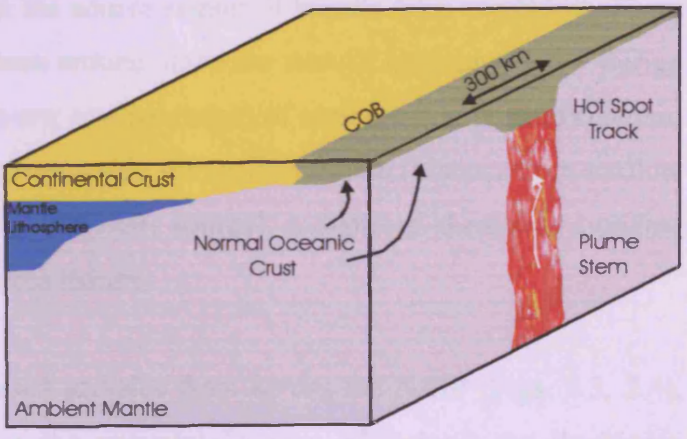

2.2.3 Geochemical evidence for the North Atlantic Plume

As we have already seen, there is compelling geophysical evidence for the existence of a hot, narrow plume beneath Iceland, which probably originated at the CMB. Until recently, it as been assumed that mantle plumes are composed largely of material enriched in incompatible trace elements (with resultant isotopic enrichment or depletion) relative to MORB-source mantle. However, it has been suggested some plumes possibly contain a substantial depleted component distinct from the source of MORB (Hart *et al.*, 1992; Kerr *et al.*, 1995; Thirlwall, 1995; Arndt *et al.*, 1997; Fitton *et al.*, 1997).

Several geochemical methods have been used to distinguish Icelandic basalts from N-MORB. One method used is Pb isotope data, this is because North Atlantic MORB and Icelandic basalts form separate and parallel arrays when $^{208}Pb/^{204}Pb$ are plotted against $^{207}Pb/^{204}Pb$. However, Mertz and Haase, (1997), point out that there may be considerable overlap in these fields, thus MORB cannot be ruled out as the depleted end member if Pb isotopes are used for defining the different arrays. Fitton *et al.* (1997) used Nb/Y versus Zr/Y plots to distinguish between the Iceland plume from MORB, but again there is considerable overlap between the fields.

Kempton *et al.* (2000) has published Sr-Nd-Pb-Hf data, which suggest there are at least four mantle components in the source region of basalts from the NAIP. These four components appear to have been around since the start of igneous activity during the Palaeogene. These components are; one (or range) of enriched component(s) within Icelandic plume; a depleted component within the Iceland Plume (distinct from shallow Normal Mid Ocean Ridge Basalt (N-MORB) source); a depleted sheath surrounding the plume; a shallow N-MORB source mantle.

Kempton *et al.* (2000) analysed samples from across the NAIP (Figs. 2.3, 2.4), with zero-aged rocks coming from the neovolcanic zone of Iceland, the Reykjanes Ridge and Kolbeinsy Ridge. Samples aged ~2-35 Ma were recovered from Deep Sea Drilling Program (DSDP) leg 49, with samples aged 52-57 Ma coming from the Ocean Drilling Program (ODP) legs 152 and 162. Samples from the Godan Spur (DSDP, leg 80) were also analysed, as they are Cretaceous (~95 Ma) in age, and as such should

represent the composition of MORB prior to the arrival of the plume under the North Atlantic.

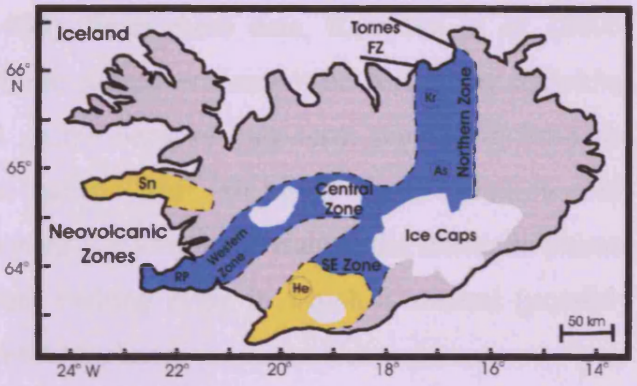

Fig. 2.3. Map of the neovolcanic zones on Iceland (western, central, northern and southern). Grey shading (Tertiary aged lavas), yellow shading (alkalic volcanism), Sn (Snaefellsnes), RP (Reykjanes Peninsula), He (Hekla), Kr (Krafla). (Modified from Kempton *et al.*, 2000)

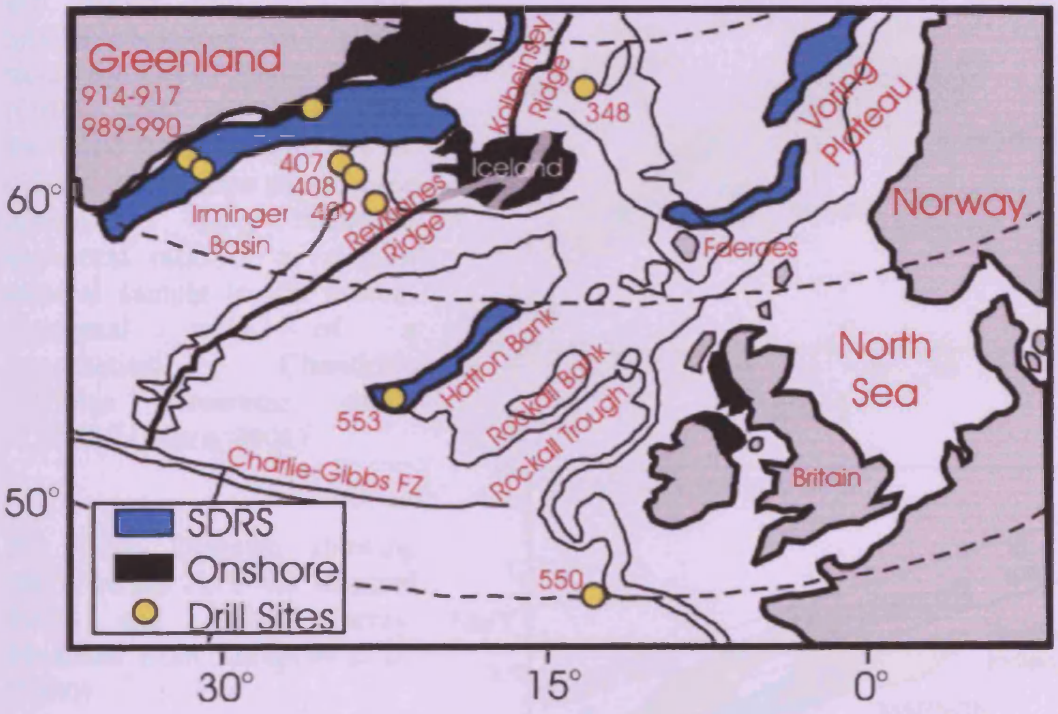

Fig. 2.4. Map of the North Atlantic, showing the sample locations (green dots) for the analysis carried out be Kempton *et al.* (2000). Numbers indicate ODP and DSDP drill sites. (Modified from Kempton *et al.*, 2000)

Kempton *et al.* (2000) used Hf-Nd systematics to identify the various mantle components of the Icelandic plume. Fig. 2.5a, shows the Hf-Nd isotope data from the NAIP basalts, compared to global fields for MORB and OIBs, also shown is the mantle regression line of Vervoort *et al.* (1999). From these data, Kempton *et al.* (2000) conclude that the depleted Icelandic plume component cannot be derived by remelting or residual mantle from the enriched plume because long-term separation from the upper mantle is necessary to attain the higher $^{176}Hf/^{177}Hf$ ratios. Thus, Kempton *et al.* (2000) suggest that the depleted component is a long-lived trait of the Icelandic plume, and represents the residue of an ancient melting event in which a mineral (possibly garnet) with a high Lu/Hf ratio was a residual phase.

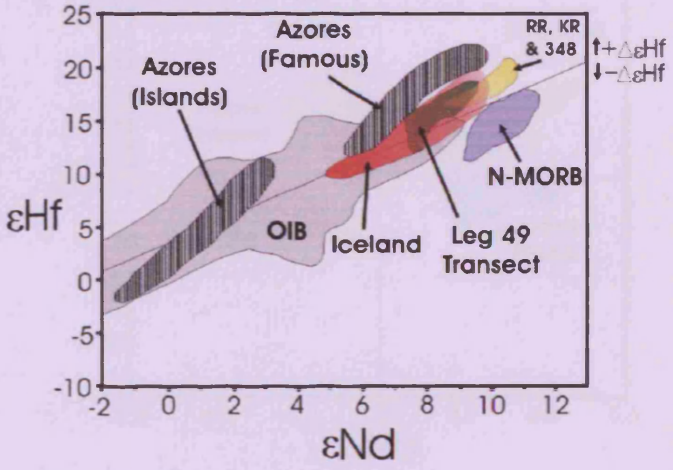

Fig. 2.5a. Diagram showing εHf versus εNd for NAIP basalts compared with global fields for Ocean Island Basalts (OIB) and Normal-MORB. Modified from Kempton *et al.* (2000). The epsilon parameter ε compares the measured elemental ratio of a rock or mineral sample to the present elemental ratio of a hypothetical Chondritic Uniform Reservoir called "CHUR" (Faure, 2001)

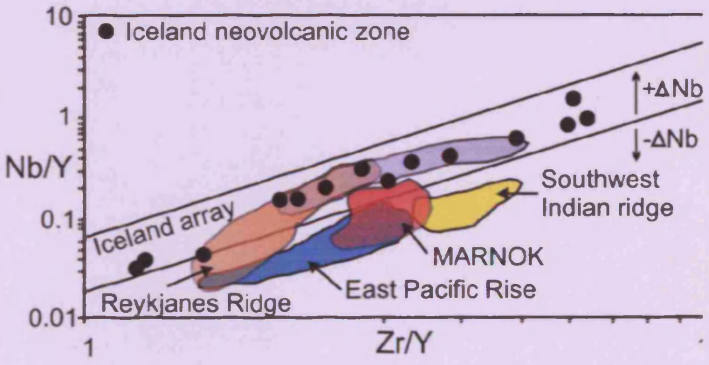

Fig. 2.5b. Diagram showing Nb/Y versus Zr/Y for selected fields and Iceland array. Modified from Kempton *et al.* (2000)

This view is further supported by Fig. 2.6, which is a plot of ΔεHf (vertical deviation of sample values from the mantle array regression line in Hf-Nb space, (Fig. 2.5a)), against ΔNb (vertical deviation of a sample from the lower boundary of the Iceland array when Nb/Y is plotted against Zr/Y, (Fig. 2.5b)). The high positive values of ΔNb are consistent with the presence of a plume below Iceland, but are unable to distinguish

whether it is the depleted or enriched component. However, ΔεHf values can distinguish isotopically depleted from enriched plume components as well as Iceland plume from normal MORB. Thus, the depleted composition could not be generated by re-melting of the enriched Iceland component, because this would not affect the Hf isotope ratios. In addition, the depleted isotope signatures are found in samples that are depleted in incompatible trace elements. Thus, the evidence points to the Iceland plume being heterogeneous, consisting of incompatible trace element enriched blobs in a depleted, more voluminous and less fusible matrix, both of which seem to be distinct from N-MORB.

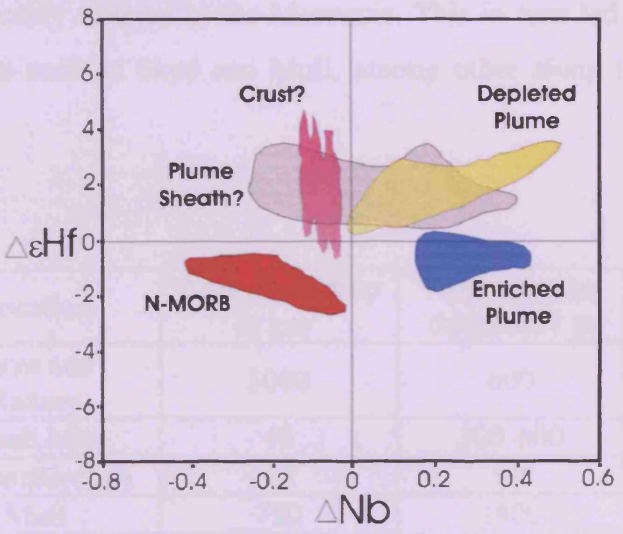

Fig. 2.6. Diagram of ΔεHf versus ΔεNb for basalts from the NAIP. Showing the fields for the differing components that make up the Icelandic Plume. (See Kempton *et al.* (2000) for field locations of analysed samples.

2.3 British Tertiary Igneous Province

The British Tertiary Igneous Province (BTIP) preserves an excellent record of Palaeogene igneous activity. The classic areas in are in Scotland (Skye, Mull, Rum, Eigg, Muck, Canna and Arran), Ireland (Antrim and the Mourne Mountains) and the Bristol Channel (Lundy). Some of the present day sub-aerial areas covered by Palaeogene basalts and their locations are given in Fig. 2.7. It is now generally believed that the Tertiary magmatism of Western Britain was caused by the arrival of the Icelandic plume below the North Atlantic region ~63 Ma (White, 1988). Thompson and Gibson, (1991) suggest that this early volcanism occurred in Western Britain, because the region had already been considerably thinned in the Mesozoic. This in turn led to the formation of the igneous centres such as Skye and Mull, among other along the west coast of Britain.

Fig. 2.7. Distribution of basaltic lavas for selected areas in the BTIP. After (Craig, 1991)

Location	Area of outcrop in km^2	Approximate thickness / m
Skye and Raasey	1090	600
Small Isles	46	300-600
Ardnamurchan	15	90
Mull	720	1800
Morven	116	460
Eigg	630	?
N. E. Ireland	3900	800

2.3.1 Mull

The volcanic rocks on Mull (Fig. 2.8) represent the remains of one of these igneous centres. Presently these lava flows cover an area greater than 700 km^2, and have a thickness greater than 1800 m (Emeleus, 1991), although the greatest thickness for a complete section is ~1000 m on Ben More. Most of the succession is composed of transitional (tholeiitic-alkali) basalts, which vary from picritic basalts (>14 wt% MgO) near the base of the succession, to basaltic-hawaiites near the top of the succession. However, there are more evolved lavas (hawaiites, mugearites and trachytes), found

mainly near the top of Ben More (Kerr, 1995). Intruded into this lava succession is an intrusive complex composed of numerous cone sheets, ring dykes and larger intrusive bodies, with a wide range of compositions from ultramafic to rhyolitic (Skelhorn *et al.*, 1969). This central complex was formed during the later stages of the evolution of the Mull igneous centre, at the same time migrating from the south (centre 1) though centre 2, to the north (centre 3) (Fig. 2.8). The emplacement of this central complex led to the circulation of hot hydrothermal fluids within the lava succession, with the resultant affect of altering the lavas closest to its location. However, to the western and northern fringes of the island the lavas remain reasonably unaltered and fresh (Bailey *et al.*, 1924; Walker, 1970).

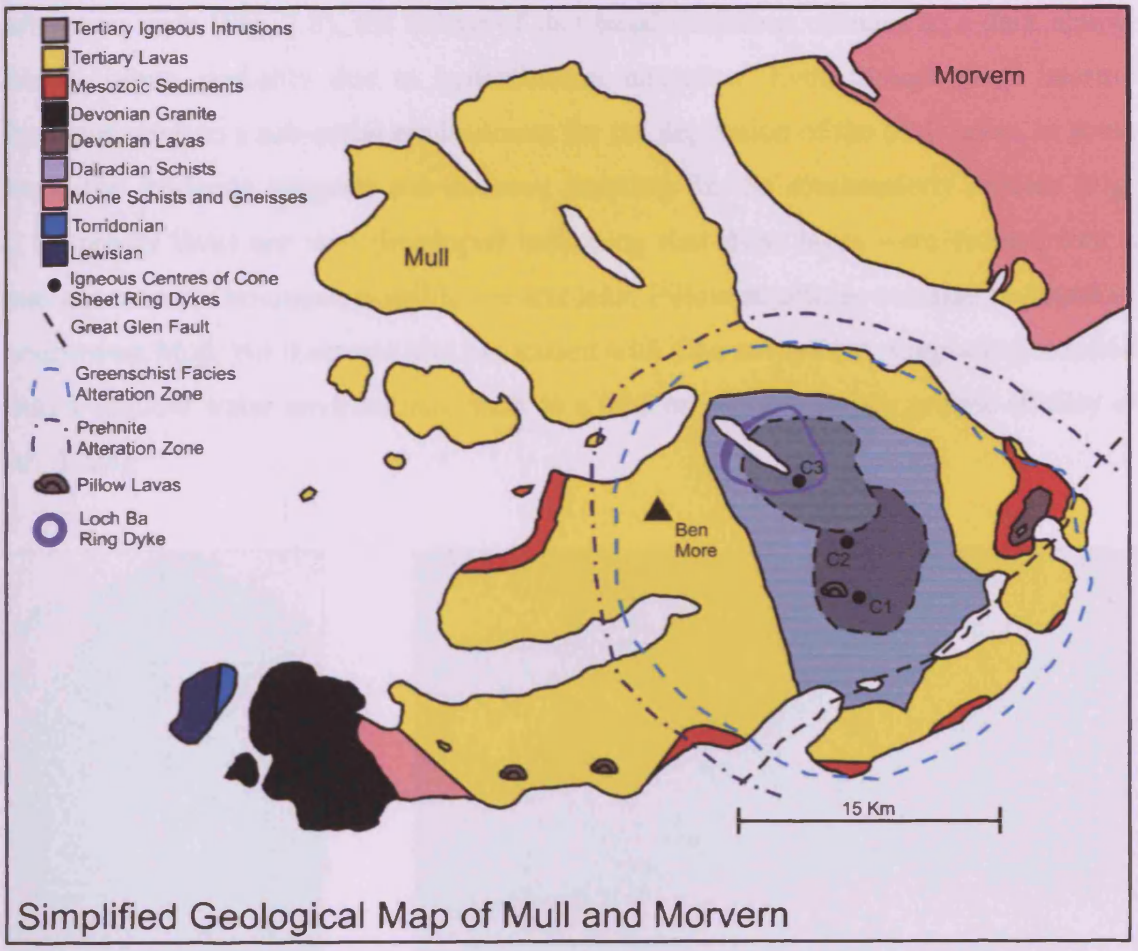

Fig 2.8. A simplified geological map of Isle of Mull showing the extent of the lavas, and the positions of the three centres of igneous activity.

Evidence points to the fact that most of the lavas on Mull were erupted sub-aerially; this can be inferred from the red oxidised and lateritised flow tops of the Mull main lava sequence. Also present are thin leaf beds (Fig. 2.9a), and occasionally plant remains still in situ (Fig. 2.9b). Bailey *et al.* (1924), on seeing this fossilised tree give it the status of being the "most arresting single geological phenomenon on the island". Over most of mull the lavas overlay a basal mudstone, which is often massive, with a fine grained texture, generally the thickness of this layer never exceeds 3 m, and was interpreted by Bailey *et al.* (1924) as being mainly weathered latertic basaltic ash, but they also suggest that there may have been some input of other (non volcanic) sediments. The usual colour of this deposit is purplish-brown to deep red (Fig. 2.10), indicating the presence of ferric oxide. Inside the area covering the greenschist facies alteration zone (Fig. 2.8), the colour of this basal mudstone changes to a dark almost black colour, probably due to hydrothermal alteration. Even though these lateritic horizons point to a sub-aerial environment for the deposition of the Mull lavas, in some areas the evidence suggests sub-aqueous eruption. In the southeasterly caldera (Fig. 2.8), pillow lavas are well developed indicating that these lavas were erupted into a sub-aqueous environment, possible a crater lake. Pillow structures can also be found in south-west Mull, but these are also associated with pipe amygdales, suggesting eruption into a shallow water environment, such as a lake or possibly boggy ground (Bailey *et al.*, 1924).

Fig. 2.9a
Showing leaf (*Phyllites ardtunensis sp*) (Bailey *et al.*, 1924)

Fig. 2.9b
Showing Macculloch's tree submerged in lava. (Bailey *et al.*, 1924)

Fig. 2.10. Showing the basal mudstone that underlies the Tertiary lavas across most of Mull. [NM440852]

2.3.2 Age and duration of activity

Using the $^{40}Ar/^{39}Ar$ criteria of Pringle (1993) and Singer and Pringle (1996), Chambers and Pringle (2001) analysed whole rock (250-500 μm) and felsic concentrate (106-250 μm) sieved fractions of samples from Mull.

Of all the samples analysed, eight met with all the reliability criteria including sample B1, which was located at the base of the plateau lava succession in the west of Mull. Experiments showed that sample B1 reached an incremental heating crystallisation age of 60.6 ± 0.3 Ma, thus giving a maximum age for the onset of magmatism on Mull. From the top of the Mull main lava sequence, samples BM64 and BM67 were analysed (previously sampled by Kerr, 1993), they are located at an elevation of 700 m in the Ben More sequence. The best age estimate for these BM samples is a weighted mean age of both analyses, giving an age of 58.38 ± 0.19 Ma.

These plateau lava eruptions were eventually superseded by the development of a central volcano. Chambers and Pringle (2001) analysed a number of samples (SO17, SO33) from the first (oldest) of the three volcanic centres (C1), also known as the central group lavas (CG). Sample SO33 reached an apparent age plateau at 58.94 ± 0.3 Ma, whereas sample SO17, which contained a slight excess in argon give an age of

59.66 ± 0.3 Ma. The combined weighted mean age of 59.05 ± 0.27 Ma is accepted as the age of the SO or C1 samples.

The youngest samples analysed are from the Loch Ba ring dyke (LB1), and some cross cutting dykes (MD1-MD3). Sample LB1 gives an age for the Loch Ba ring dyke of 58.48 ± 0.18 Ma, whereas the age obtained from samples MD1-MD3 for the cross cutting dykes is ~ 58.0 Ma. A weighted mean of all three dykes gives an approximate age of 58.12 ± 0.13 Ma, for the youngest volcanic activity on Mull.

2.4 Geochemistry of the Igneous Rocks: Mull

The compositional variations of igneous rocks at rifted continental margins have the potential to provide information on the nature of high-level volcanic plumbing systems, magma mixing processes, and source regions for magma. Generally, such igneous rocks are unavailable to geologists, due to subsidence, burial, or uplift and erosion. Mull is almost unique, in that it affords geologists the opportunity to examine the chemical evolution of a magmatic centre from its inception to the end of volcanic activity. The Mull igneous complex is situated just to the north of the Great Glen fault, which Bailey *et al.* (1924) believed to be a major controlling factor in its evolution. This fault marks a major boundary between Archaean (>2500 Ma) Lewisian basement gneiss and Late Proterozoic (1000-600 Ma) Moine schists to the north, and Early Proterozoic (<2500 Ma) basement overlain by Dalradian (~ 600 Ma) metasediments to the south (Kerr *et al.*, 1999).

Bailey *et al.* (1924) carried out the first geochemical (15 samples) and petrological study of Mull. Even though he only had limited geochemical capabilities, using these and the observed petrographical characteristics of analysed lavas, he recognised two main lava types. The early formed "plateau type" (renamed the Mull Plateau Group by Morrison *et al.* (1980)), and the younger "Non-porphyritic central" type (renamed the Central Mull Tholeiite type by Kerr (1994)). Subsequently these lava types were recognised worldwide, and are now known respectively as the alkaline and tholeiitic types. It was not until the 1970's onwards, that further geochemical work was

carried out on Mull, most notably Morrison (1979); Thomson (1986); Kerr (1993); Seedhouse (1994); Preston (1996).

The first and thus oldest expression of igneous activity on Mull was the formation of the predominantly basaltic lava succession, which was estimated to be ~1800 m by Bailey *et al.* (1924). Walker (1970) proposed on the evidence of secondary amygdale mineral assemblages, that the original thickness of the lava pile was in excess of 2200 m, but has over the last 60 Ma been weathered and eroded to its present day thickness. This view is further supported by the work of Kerr (1997) on the plugs of Mull and Morvern, where he shows that the plugs have extensive aureoles indicating considerable magma throughput . In Fig. 2.11, the yellow triangles represent the Mull Main Lava Sequence, whereas the red squares represent plugs, even from a simple Harker diagram it is clear that some of the plugs have chemical compositions not represented in the lava succession. Thus supporting the view that the top of the lava pile has been eroded away.

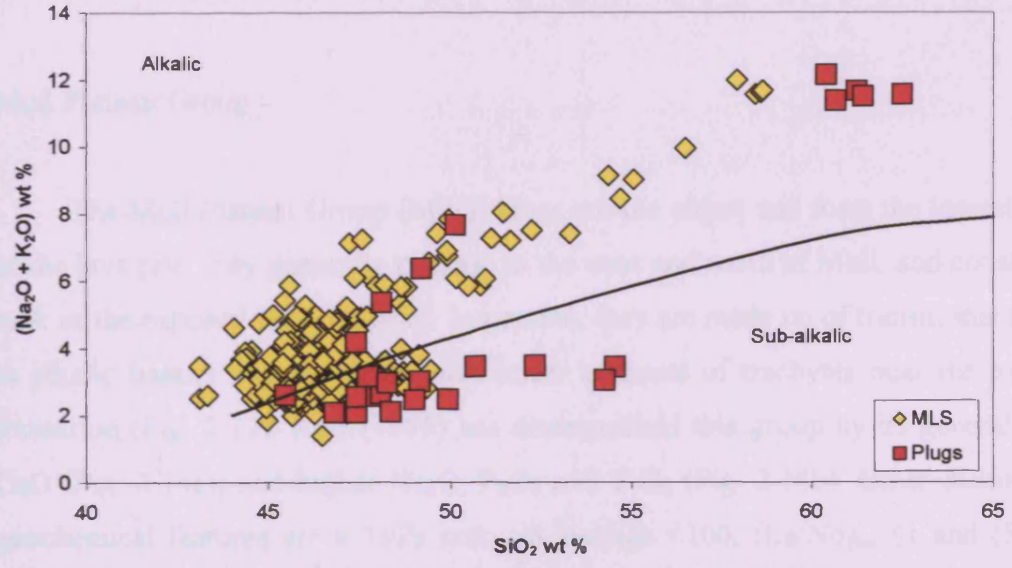

Fig. 2.11. Harker discrimination diagram of the Mull Main lava Sequence, and volcanic plugs from Mull and Morvern. Some of the plugs have chemical compositions not represented in the MLS, thus suggesting that there has been erosion of the lavas on Mull. Data Kerr (1997)

2.4.1 Mull-Morvern Tertiary Lava Succession

Even though most of the lavas have to a lesser or greater extent been contaminated by Lewisian crust. Kerr (1995) has, after modelling post-melt generation processes divided the Mull lavas into three groups on their geochemical characteristics (Fig. 2.12).

Type	Silica Saturation	Ti/Zr	$(La/Nd)_n$	$(Sm/Yb)_n$	TiO_2^{10}
Plateau group	Transitional	<100	≤1	>1	1.7
Coire Gorm	Transitional	>100	≤1	~1	1.5
Central Mull	Tholeiitic	>100	<1	~1	1.0

Superscript 10 after TiO_2 indicates that these are average TiO_2 values at 10 wt% MgO

Fig. 2.12. Table showing the chemical characteristics of the three Mull magma types (Kerr, 1995)

Mull Plateau Group

The Mull Plateau Group (MPG) lavas are the oldest and form the lowest ~750 m of the lava pile, they generally outcrop in the west and north of Mull, and constitute the bulk of the exposed lavas on Mull. In general, they are made up of transitional tholeiitic to alkalic basalts and hawaiites with lesser amounts of trachytes near the top of the formation (Fig. 2.13). Kerr (1995) has distinguished this group by its generally lower CaO (Fig. 2.14a), and higher Na_2O, P_2O_5 and TiO_2 (Fig. 2.14b). Other distinguishing geochemical features are a Ti/Zr ratio on average <100, $(La/Nd)_{cn}$ ≤1 and $(Sm/Yb)_{cn}$ >1, (Figs 2.14e and 2.14f).

Coire Gorm magma type

The Coire Gorm (CG) magma type lavas lie stratigraphically above the MPG and have a thickness of ~250 m. Generally, they have similar major element concentrations to the MPG, but unlike the MPG, the CG lavas are all basaltic. However, Kerr (1995)

has shown that the CG lavas differ in that they generally have lower levels of incompatible trace elements, Ti/Zr ratios >100 and $(Sm/Yb)_{cn}$, $(La/Nd)_{cn}$ ratios of ~1 (Figs 2.14e and 2.14b).

Central Mull Tholeiites

The Central Mull Tholeiites (CMT) are the youngest preserved lavas on Mull, they are at least 900 m thick and outcrop in the southeast of Mull and Beinn Chaisgidle caldera (centre 2, Fig.2.8). The CMT differ from the MPG and CG lavas, in that they are more silica saturated (Fig. 2.12), with lower amounts of K_2O and Na_2O, making them distinctly tholeiitic. The CMT lavas also have higher levels of CaO, Sc and V, and lower incompatible trace element concentrations, with $(Sm/Yb)_{cn}$ and $(La/Nd)_{cn}$ ratios of ~1 and ~1.5 respectively (Figs 2.14e and 2.14f).

Thus, the Mull Plateau Group and Coire Gorm lavas have similar transitional major element concentrations, but differ from the Central Mull lavas which are tholeiites. Whereas, the Central Mull Tholeiites and Coire Gorm lavas share similar trace element concentrations, but differ from the Mull Plateau Group. Kerr *et al.* (1999) suggests that these differing trace element ratios reflect changes in the depth of partial melting over time, from deep melting in the presence of garnet (MPG) to shallower melting with only small amounts of residual garnet in the source (CG + CMT).

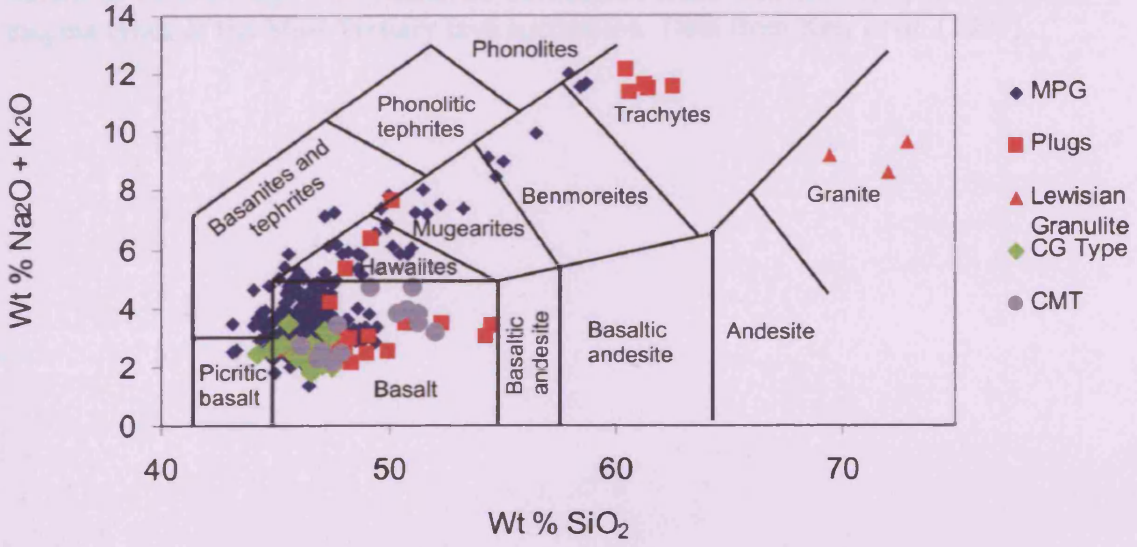

Fig. 2.13. Harker diagram of the differing Mull lava types and Lewisian Granulite. Data Kerr *et al.* (1999)

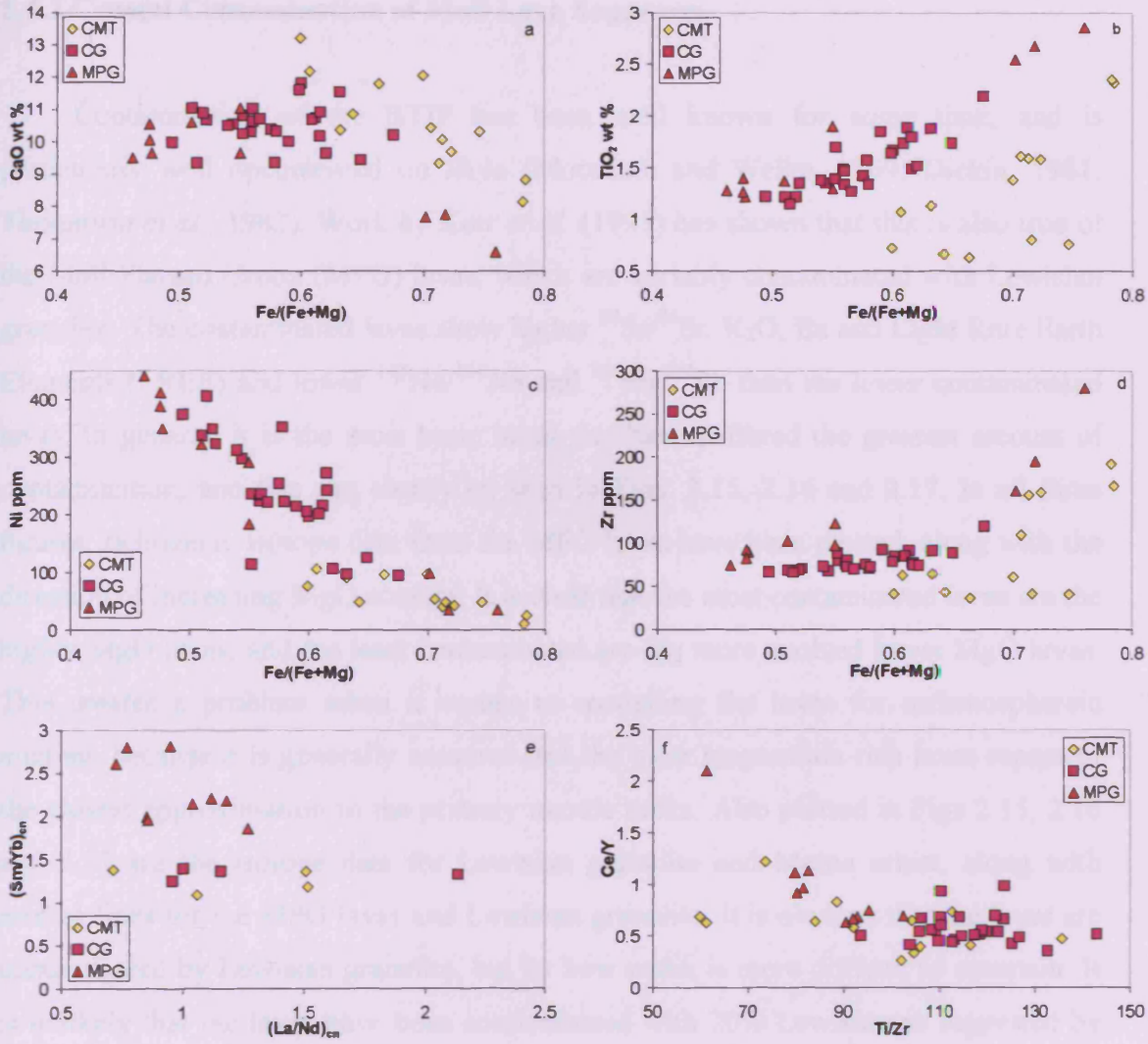

Fig. 2.14. Selected plots of major and trace elements versus $Fe_2O_3/(Fe_2O_3+MgO)$ shown as Fe/(Fe+Mg), and chondrite normalised trace element plots, for the three magma types of the Mull Tertiary lava succession. Data from Kerr *et al.* (1999)

2.4.2 Crustal Contamination of Mull Lava Sequence

Contamination of the BTIP has been well known for some time, and is particularly well documented on Skye (Moorbath and Welke, 1969; Dickin, 1981; Thompson *et al.*, 1982). Work by Kerr *et al.* (1995) has shown that this is also true of the Mull Plateau Group (MPG) lavas, which are variably contaminated with Lewisian granulite. The contaminated lavas show higher $^{87}Sr/^{86}Sr$, K_2O, Ba and Light Rare Earth Elements (LREE) and lower $^{143}Nd/^{144}Nd$ and $^{206}Pb/^{204}Pb$ than the lesser contaminated lavas. In general, it is the most basic lavas that have suffered the greatest amount of contamination, and this can clearly be seen in Figs. 2.15, 2.16 and 2.17. In all three figures, radiogenic isotope data from the MPG lavas have been plotted, along with the direction of increasing MgO content. It is clear that the most contaminated lavas are the higher MgO lavas, and the least contaminated are the more evolved lower MgO lavas. This creates a problem when it comes to modelling the lavas for asthenosphereic melting, because it is generally assumed that the most magnesium rich lavas represent the closest approximation to the primary mantle melts. Also plotted in Figs 2.15, 2.16 and 2.17 are the isotope data for Lewisian granulite and Moine schist, along with mixing lines for the MPG lavas and Lewisian granulite. It is obvious that the lavas are contaminated by Lewisian granulite, but by how much is more difficult to ascertain. It is unlikely that the lavas have been contaminated with 20% Lewisian as suggested by the mixing line between $^{208}Pb/^{204}Pb$ and $^{206}Pb/^{204}Pb$, as this would have led to the overall composition become more intermediate, which is not the case. Therefore, it is more likely that the upper limits of contamination of the MPG lavas by Lewisian crust are in the order of 5-10%.

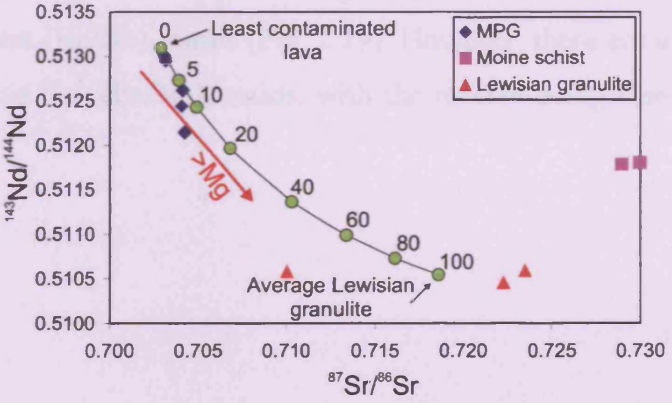

Fig. 2.15. Plot of $^{143}Nd/^{144}Nd$ versus $^{87}Sr/^{86}Sr$ radiogenic isotope ratios for the MPG lavas, Lewisian granulite and Moine schist. Also plotted is the mixing line between the least contaminated MPG lava and average Lewisian granulite. Data Kerr *et al.* (1999)

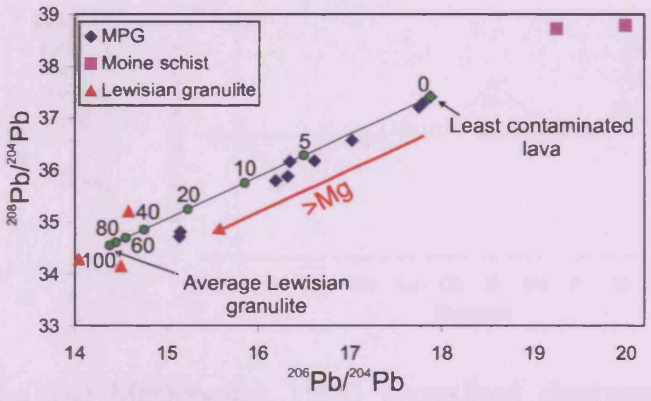

Fig. 2.16. Plot of $^{208}Pb/^{204}Pb$ versus $^{206}Pb/^{204}Pb$ radiogenic isotope ratios for the MPG lavas, Lewisian granulite and Moine schist. Also plotted is the mixing line between the least contaminated MPG lava and average Lewisian granulite. Data Kerr *et al.* (1999)

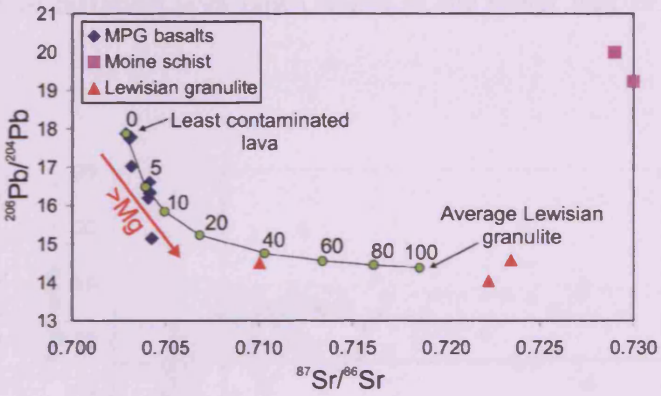

Fig. 2.17. Plot of $^{206}Pb/^{204}Pb$ versus $^{87}Sr/^{86}Sr$ radiogenic isotope ratios for the MPG lavas, Lewisian granulite and Moine schist. Also plotted is the mixing line between the least contaminated MPG lava and average Lewisian granulite. Data Kerr *et al.* (1999)

Kerr *et al.* (1995) have shown that the lower half of the MPG lavas can be separated into distinct units based on their chemistry. Generally, the units are of two types: (1) a high MgO basalt (>8% MgO), relatively enriched in Ba and K (Fig. 2.18a): and (2) a low MgO basalt hawaiites type, with lower Ba and K values (Fig. 2.18b). It is also clear from Fig. 2.18, that the high MgO lavas have a distinctive Nb trough, which is not present in the low MgO lavas. When mantle normalised $(Ba/Nb)_n$ are plotted against MgO for the lower MPG lavas, there seems to be a correlation, albeit imperfect between the two. In general the higher MgO lavas have the highest $(Ba/Nb)_n$ ratios, and the lowest MgO lavas have the lowest $(Ba/Nb)_n$ ratios (Fig. 2.19). However, there are a number of high MgO lavas that have low $(Ba/Nb)_n$ ratios, with the reverse being true for some of the lower MgO lavas.

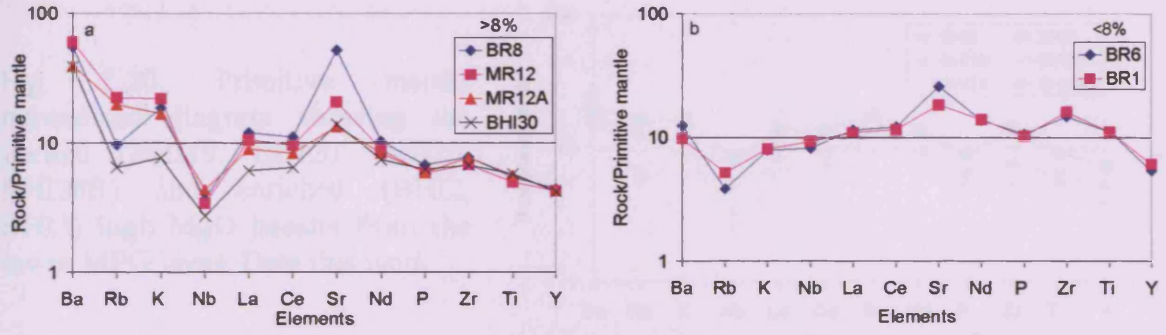

Fig. 2.18. Primitive mantle (Sun and McDonough 1989) normalised diagrams showing typical analysis of the two differing lava types found in the lower half of the MPG (Data from this work).

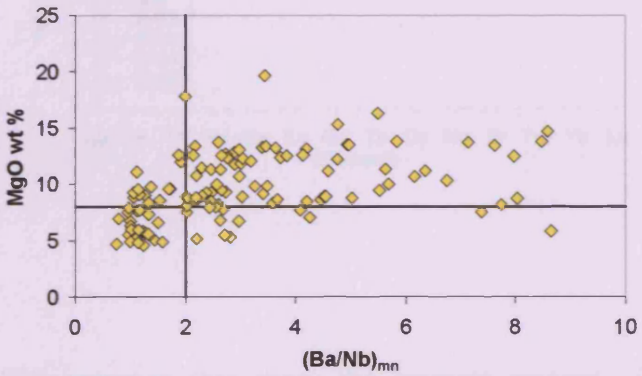

Fig. 2.19. Plot of MgO versus $(Ba/Nb)_{mn}$ for lavas from the lower half of the MPG. The horizontal and vertical lines mark 8% MgO and $(Ba/Nb)_{mn} = 2$, and it can be seen that most basalts plot in the *lower left* and *upper right* quadrants. Data Kerr *et al.* (1999)

Kerr *et al.* (1995) point out that the enrichment in Ba and K and Nb trough in the high MgO basalts could be produced by contamination of magma from an asthenosphereic mantle source by a lithospheric mantle source. Indeed, some of the early MPG lavas do show enrichment in incompatible elements (Fig. 2.20 and 2.21), which Kerr (1993) has interpreted as a small fraction melt from the lithosphere. However, it is only a few of the very earliest lavas that display this enrichment, and Kerr (1993) has show that the contaminant is relatively enriched in both high field strength elements HFSE, (including Nb) and the large ion lithophile (LIL) elements. Thus, this contamination could not be responsible for the characteristic trace element signatures seen in most of the more basic MPG lavas.

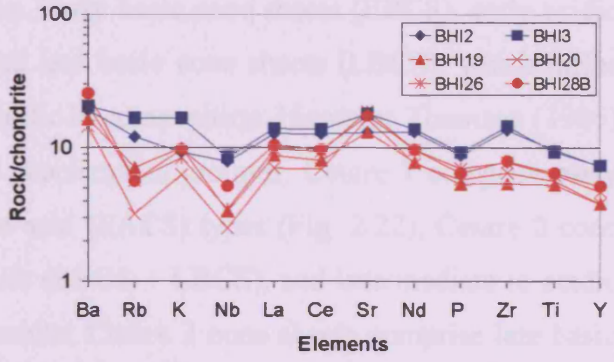

Fig. 2.20. Primitive mantle normalised diagram showing the normal (BHI19, BHI20, BHI26, BHI28B) and enriched (BHI2, BHI3) high MgO basalts from the lower MPG lavas. Data this work.

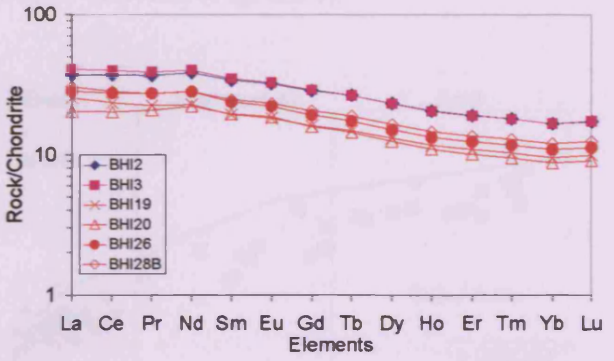

Fig. 2.21. Chondrite normalised REE plot showing the normal (BHI19, BHI20, BHI26, BHI28B) and enriched (BHI2, BHI3) high MgO basalts from the lower MPG lavas. Data this work

2.4.3 Mode of contamination

Since it is the most basic MPG magmas that show the greatest amount of contamination with Lewisian granulite (Figs 2.15, 2.16 and 2.17), Kerr *et al.* (1995) suggests that they have been contaminated by Assimilation during Turbulent Assent (ATA) (Section 1.4.3) process, probably in thin dyke and/or sill like magma chambers. Whereas the lack of contamination affecting the more basaltic-hawaiitic lavas, is probably because of fractionation within the refractory upper lithosphere (Fig 1.7). Therefore, when these magmas past through the crust, they would have already cooled considerably, and as a result been less likely to fuse and incorporate acidic Lewisian crust.

2.5 Mull Cone Sheets

The three igneous centres on Mull are all associated with separate cone sheet suites, which range in composition from basic to acidic. Bailey *et al.* (1924) divided

these cone sheet suites into three groups. Early basic cone sheets (EBCS), early acidic to intermediate cone sheets (EACS) and late basic cone sheets (LBCS), which differ from the EBCS in that they are ferrodioritic in composition. However Thomson (1986) has further divided the cone sheets on geochemical grounds. Centre 1 comprise early basic (EBCS) and early intermediate to acid (EACS) types (Fig. 2.22), Centre 2 cone sheets comprise both early and late basic (EBCS + LBCS), and intermediate to acidic (EACS +LACS) varieties (Fig. 2.23), whilst Centre 3 cone sheets comprise late basic (LBCS) and late intermediate to acid (LACS) varieties (Fig. 2.24).

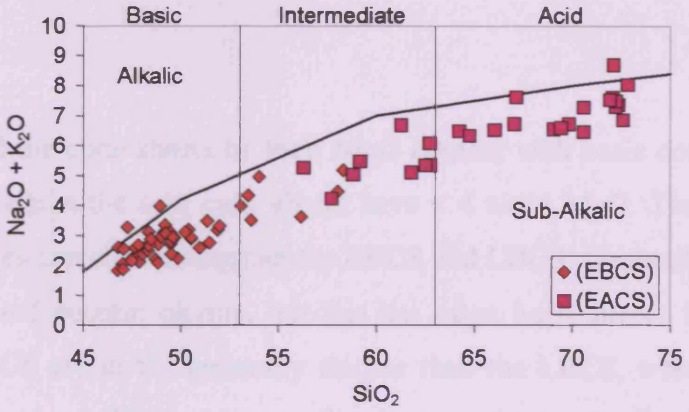

Fig. 2.22. Alkali-silica diagram of the (EBCS) and (EACS) centre 1, Mull. Data from Thompson (1986)

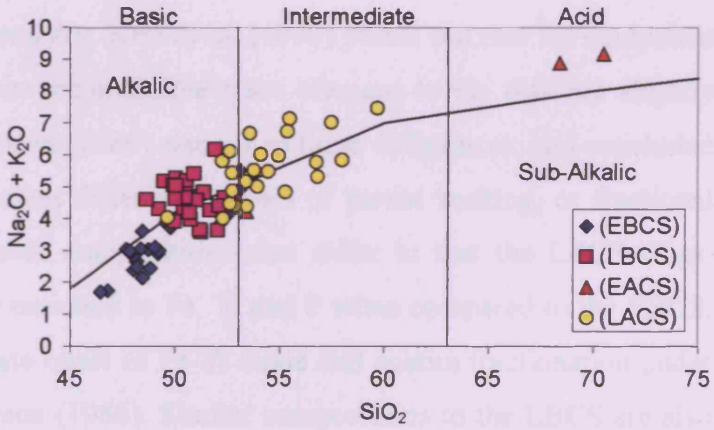

Fig. 2.23. Alkali-silica diagram of the (EBCS), (LBCS), (EACS) and (LACS) centre 2, Mull. Data from Thompson (1986)

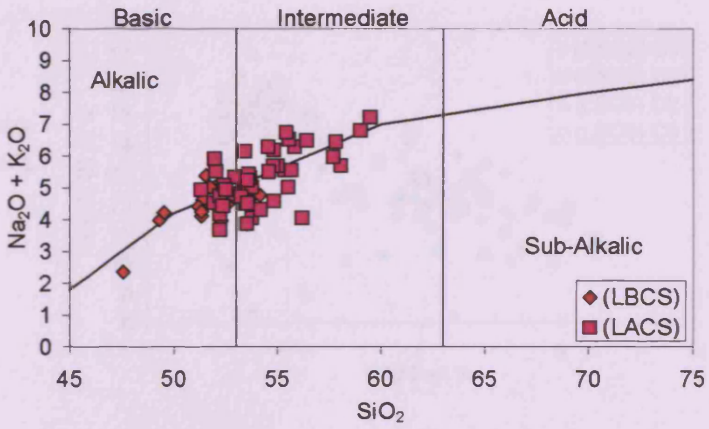

Fig. 2.24. Alkali-silica diagram of the (LBCS) and (LACS) centre 3, Mull. Data from Thompson (1986)

Kerr *et al.* (1999) divided the cone sheets by their MgO content with basic cone sheets having > 4 wt % MgO, whilst the acid cone sheets have < 4 wt % MgO. Their field and petrographic differences can also distinguish the EBCS and LBCS. Generally, the EBCS are course grained and contain olivine, but this has often been altered by hydrothermal activity. The EBCS are in the generally thicker than the LBCS, which also lack olivine and are finer grained. The two types of basic cone sheets can also be divided on the basis of their chemistry. Kerr *et al.* (1999) points out that for equivalent MgO content the LBCS contain incompatible trace element levels that are slightly higher than for the EBCS. Thomson (1986) also noted these differences, and concluded that the EBCS and LBCS represent differing degrees of partial melting, or fractional crystallization. The major element compositions also differ in that the LBCS (Figs. 2.25, 2.26 and 2.27) as they are enriched in Fe, Ti and P when compared to the EBCS, this has been attributed to the late onset of Fe-Ti oxide and apatite fractionation under low oxygen fugacity by Thompson (1986). Similar compositions to the LBCS are also found in some of the plugs located in northern Mull and Morvern, as well as some of the youngest basic dykes (Kerr *et al.* 1999).

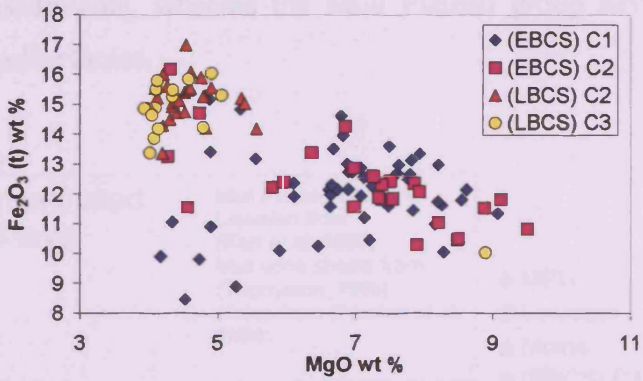

Fig. 2.25. Plot of Fe_2O_3 (t) versus MgO for basic cone sheets. Data from Thompson (1986)

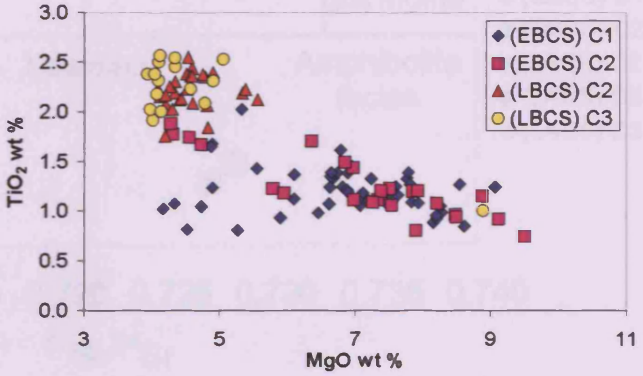

Fig. 2.26. Plot of TiO_2 versus MgO for basic cone sheets. Data from Thompson (1986)

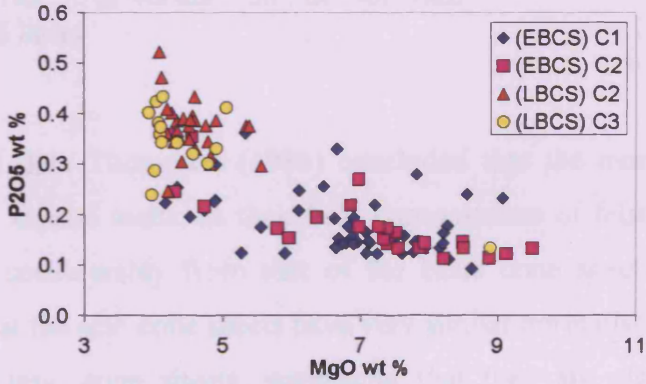

Fig. 2.27. Plot of P_2O_5 versus MgO for basic cone sheets. Data from Thompson (1986)

The basic cone sheets also show strong negative Nb anomalies, which are inferred to reflect crustal contamination especially when coupled to low $^{206}Pb/^{204}Pb$ and high $^{87}Sr/^{86}Sr$ ratios (Kerr *et al.*, 1995). Generally the Nb levels have been reduced by the assimilation of crustal rocks, but the increased levels of the large-ion lithophile elements (Rb, Ba, K, Sr) has resulted in a greatly exaggerated Nb anomalies. Fig. 2.28, shows that the Mull cone sheets all possess high $^{87}Sr/^{86}Sr$ and low $^{143}Nd/^{144}Nd$ when compared to the least contaminated MPG lava, and this is also true of most of the MPG lavas plotted. The trend for the Sr-Nd isotopes suggests that the Mull cone sheets have

been contaminated by Moine metasediments, whereas the Mull Plateau group have been contaminated by Lewisian granulite facies.

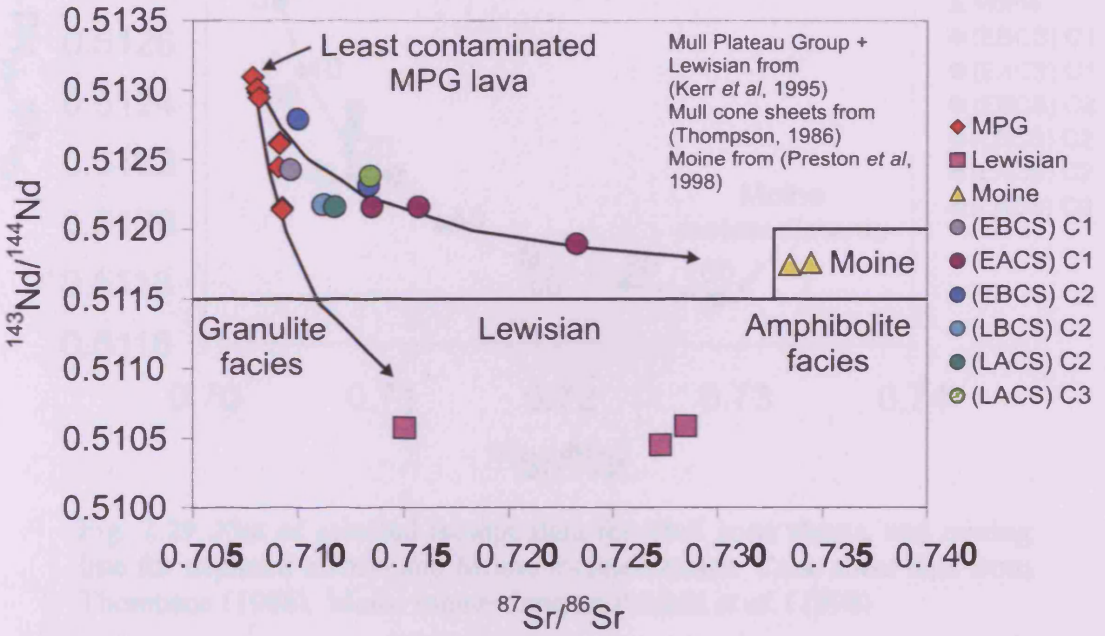

Fig. 2.28. plot of $^{143}Nd/^{144}Nd$ versus $^{87}Sr/^{86}Sr$ for Mull cone sheets and MPG lavas

Using isotopic and elemental data Thompson (1986) concluded that the more acidic cone sheets do not represent crustal melts, as their bulk compositions of felsic Moine and Lewisian rocks differ considerably from that of the basic cone sheets. Thompson (1986) also points out that the acid cone sheets have very similar normalised multi-element plots to the more basic cone sheets, suggesting that they are also contaminated by a crustal component. On a plot of $^{143}Nd/^{144}Nd$ v $^{87}Sr/^{86}Sr$, (Fig. 2.29), it is clear that the cone sheets associated with the differing igneous centres all show a negative correlation, that is within each centre, the most evolved rocks are the most contaminated. Therefore, the evidence points to crustal contamination occurring concomitantly with fractional crystallization (section 1.4.3).

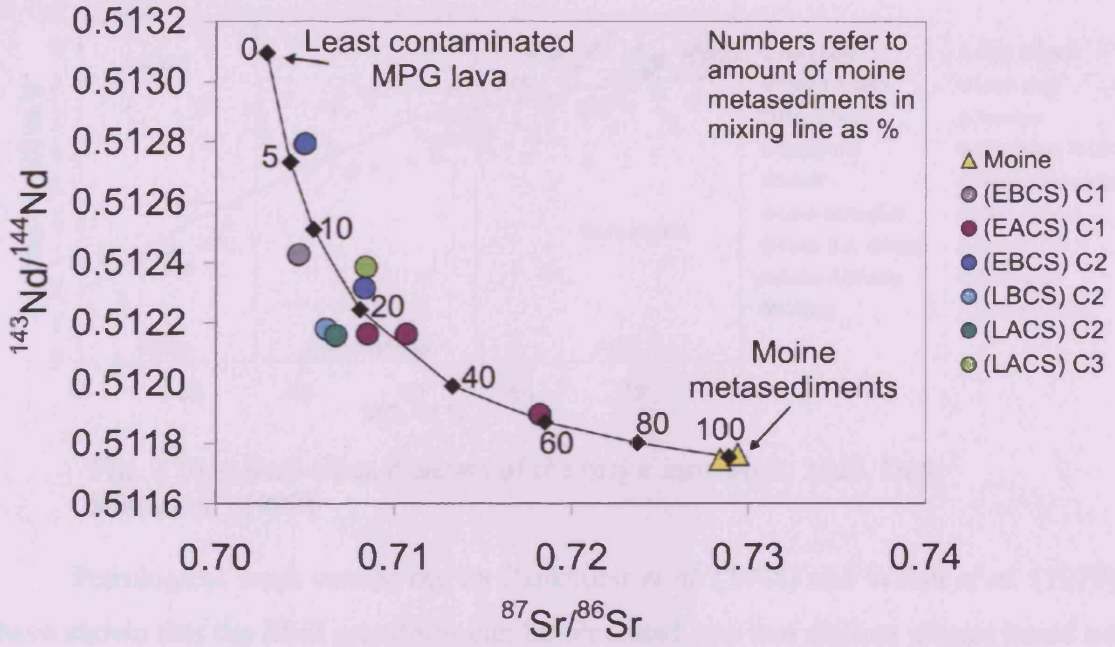

Fig. 2.29. Plot of selected isotope data for Mull cone sheets, and mixing line for depleted mantle and Moine metasediments. Cone sheet data from Thompson (1986). Moine metasediments Preston *et al.* (1998)

2.6 Major Intrusions

On Mull, the major intrusions associated with the three central complexes tend to take the form of dykes and stocks (Bailey *et al.*, 1924). In general, their compositions are granitic, or mixed bodies containing a high percentage of a granitic component Fig. 2.30. However, there are a number of exceptions including the Ben Buie, Corra-bheinn layered gabbros, and the An Cruachan and Gaodhail augite diorites. Also clear from Fig. 2.30, is that the Glen More ring dyke has a basic composition, although data is limited for this intrusion. Whereas the Beinn Chaisgidle and Loch Ba intrusions have compositions ranging from basic through intermediate to acid.

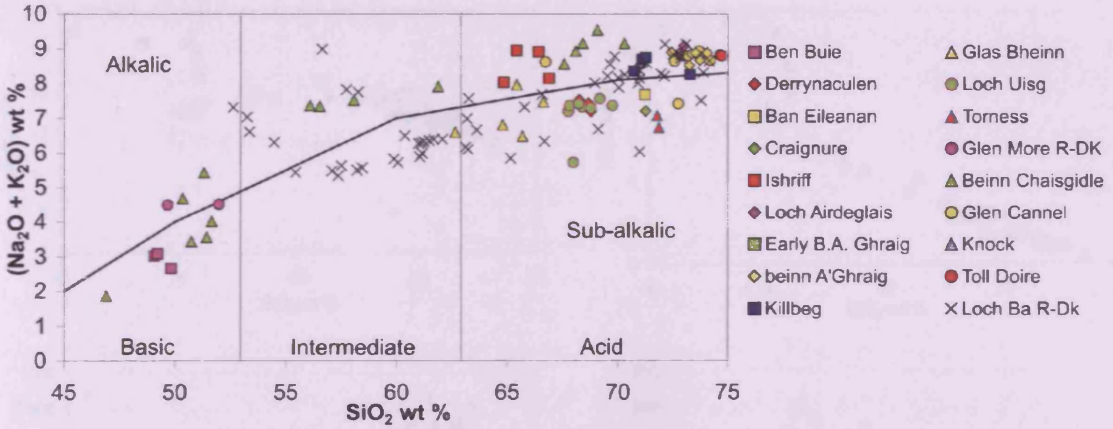

Fig. 2.30. Alkali-silica diagram of the major intrusions, Mull. Data Kerr *et al.* (1999)

Petrological work carried out by Pankhurst *et al.* (1978) and Walsh *et al.* (1979) have shown that the Mull granitoids can be separated into two distinct groups based on their composition. Early granites associated with centre 1, and late granites associated with centres 2 and 3. Selected element concentrations for the Mull granites are shown in Fig. 2.31a-d and Fig. 2.32, Kerr *et al.* (1999) points out that the late granites have higher levels of K_2O, Na_2O, Al_2O_3, MnO, Zr, Y and Nb and lower CaO, P_2O_5, TiO_2, Sr, V, $(Ce/Yb)_{cn}$ and initial $^{87}Sr/^{86}Sr$ relative to levels for the early granites. The higher levels for K_2O and Na_2O are indeed clear in Fig. 2.32, also clear is that the early granites are generally sub-alkalic, whereas the late granites are generally alkalic. An exception to this is the Loch Ba ring dyke which shows quite a wide range in (Na_2O + K_2O), being both alkalic and sub-alkalic. The higher levels of Al_2O_3 and Zr, and lower levels for CaO and Sr associated with the late granites are also clear on Fig. 2.31a-d.

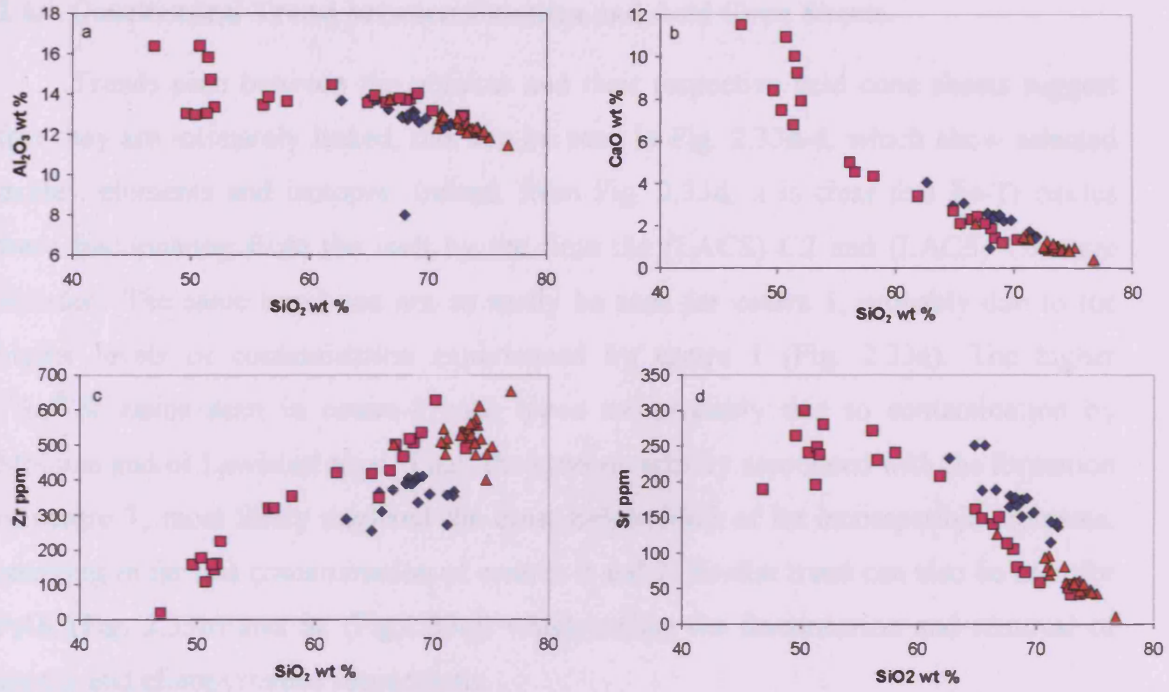

Fig. 2.31. a-d. Plots of selected major and trace elements versus SiO_2, for Mull granites. Data from Kerr *et al.* (1999)

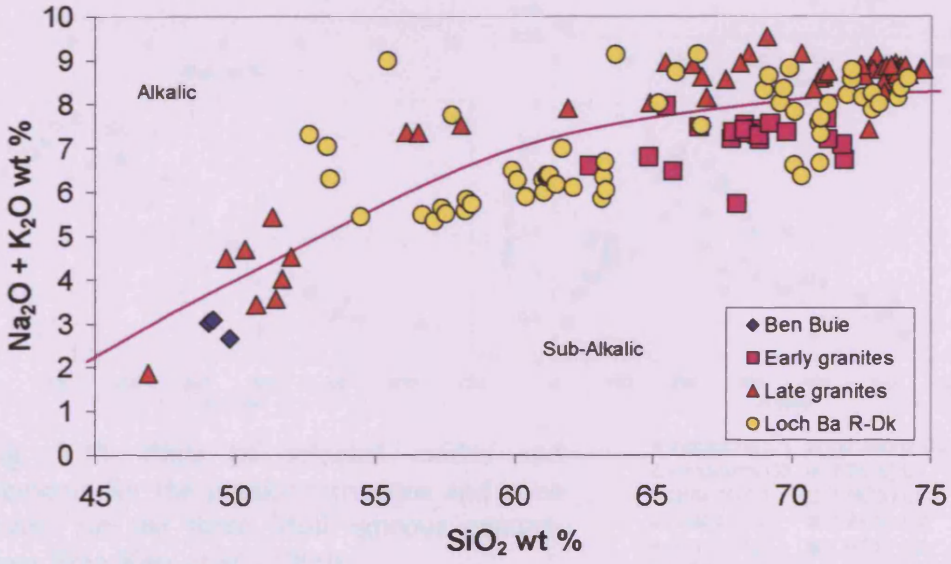

Fig. 2.32. Alkali-silica diagram of the different intrusive rock types from Mull. Data from Kerr *et al.* (1999)

2.6.1 Geochemical Trend between Granites and Acid Cone Sheets.

Trends seen between the granites and their respective acid cone sheets suggest that they are intimately linked, this can be seen in Fig. 2.33a-d, which show selected oxides, elements and isotopes. Indeed, from Fig. 2.33d, it is clear that Fe-Ti oxides were fractionating from the melt by the time the (LACS) C2 and (LACS) C3 were intruded. The same trend can not so easily be seen for centre 1, probably due to the higher levels of contamination experienced by centre 1 (Fig. 2.33a). The higher $^{87}Sr/^{86}Sr$ ratios seen in centre-1 rock types are probably due to contamination by Moinian and/or Lewisian crust. Thus, the igneous activity associated with the formation of centre 1, most likely depleted the crust below Mull of its incompatible elements, resulting in far less contamination of centres 2 and 3. Similar trend can also be seen for P_2O_5 (Fig. 2.33b) and Sc (Fig.2.33c), which reflect the fractionation and removal of apatite and clinopyroxene respectively.

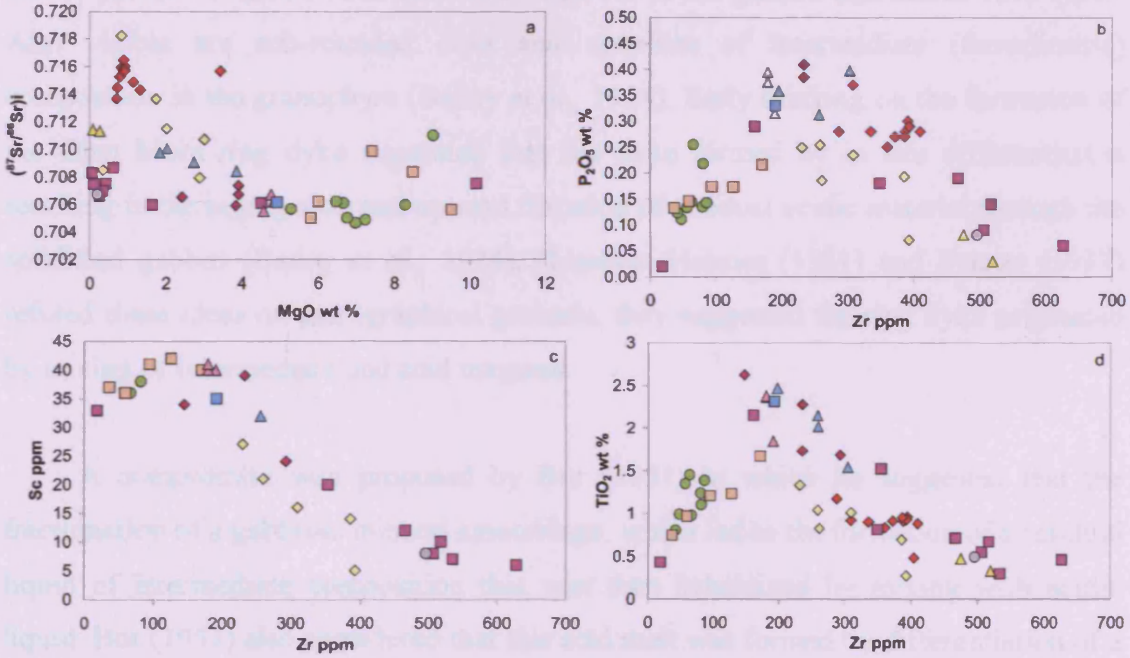

Fig. 2.33. Plots of selected oxides and elements for the granite intrusions and cone sheets for the three Mull igneous centres. Data from Kerr *et al.* (1999)

2.7 Large Scale Mixed-Magma Intrusions

There are a number of mixed-magma intrusions associated with the Mull igneous complex. Here the focus is on two, firstly the Glen More ring dyke, which is the youngest intrusion in Centre 2, and the Loch Ba Ring Dyke, which is one of the last igneous events of the Mull igneous complex, and as such is found in Centre 3.

2.7.1 Glen More Ring Dyke

The Glen More ring dyke generally consists of coarse to medium grained olivine gabbro passing upwards into quartz dolerite, diorite, granodiorite and granophyre (Bailey *et al.*, 1924; Bor, 1951). Even though the dyke is poorly exposed, there are some boundaries visible, and they appear to be gradational, magma mixing is evident due to patches of acidic rock veins and enclaves in the gabbro and diorite rock types. Also visible are sub-rounded clots and xenoliths of intermediate (ferrodioritic) composition in the granophyre (Bailey *et al.*, 1924). Early thinking on the formation of the Glen More ring dyke suggested that the dyke formed by in situ differentiation resulting in the segregation and upward filtration of residual acidic material through the solidified gabbro (Bailey *et al.*, 1924). However Holmes (1931) and Fenner (1937) refuted these ideas on petrographical grounds, they suggested the ring dyke originated by mixing of intermediate and acid magmas.

A compromise was proposed by Bor (1951) in which he suggested that the fractionation of a gabbroic mineral assemblage, which led to the formation of a residual liquid of intermediate composition that was then hybridized by mixing with acidic liquid. Bor (1951) also considered that this acid melt was formed by differentiation of a batch of basaltic magma intruding into the gabbro-dolerite after it had crystallized. Bor's hypothesis has been further backed up by the field observations of Marshall (1984), and least-squares modelling of whole rock and clinopyroxene compositions of Seedhouse (1994). Kerr *et al.* (1999) suggests that the chemical composition of the gabbros and diorites from the Glen More ring dyke are similar to those of the LBCS in that they show higher Fe_2O_3, TiO_2, P_2O_5 (Figs. 2.34, 2.35, 2.36) and are slightly more enriched in incompatible trace elements when compared to the EBCS.

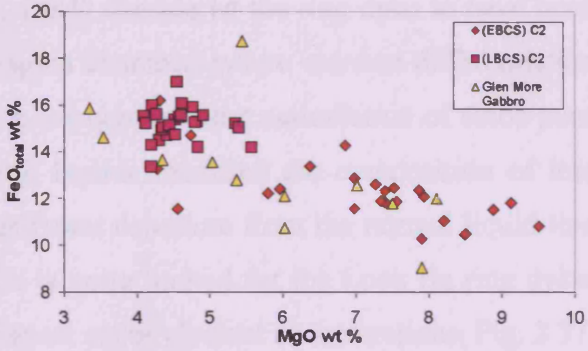

Fig. 2.34. Plot of FeO_{total} versus MgO for basaltic cone sheets (Centre 2) and Glen More gabbros.
Glen More gabbro data, Seedhouse (1994)
(EBCS + LBCS) data, Thomson (1986)

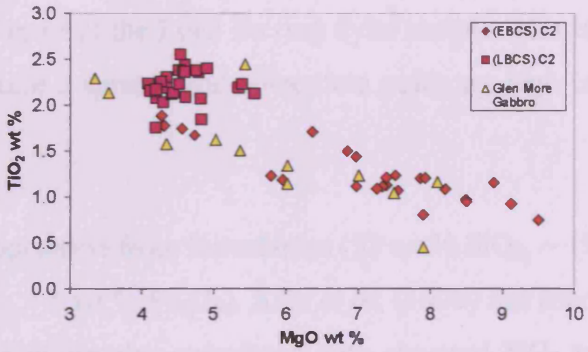

Fig. 2.35. Plot of TiO_2 versus MgO for basaltic cone sheets (Centre 2) and Glen More gabbros.
Glen More gabbro data, Seedhouse (1994)
(EBCS + LBCS) data, Thomson (1986)

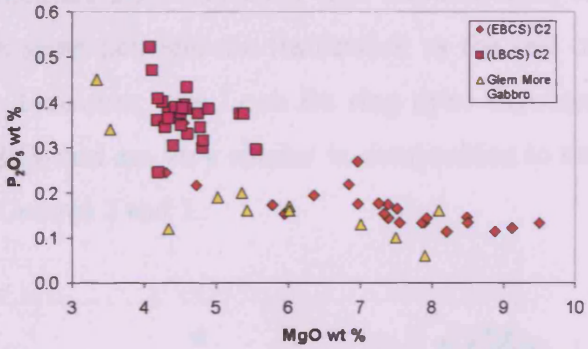

Fig. 2.36. Plot of P_2O_5 versus MgO for basaltic cone sheets (Centre 2) and Glen More gabbros.
Glen More gabbro data, Seedhouse (1994)
(EBCS + LBCS) data, Thomson (1986)

2.7.2 Loch Ba Ring Dyke

The Lock Ba ring dyke is a rhyolite body up to 400 m in thickness, approximately 8 km in diameter and consists of a fine-grained sometimes-banded rock type. The ring dyke is part of a silicic-mafic intrusive complex centred on Glen Cannel (Centre 3). The general petrology and field relationships of the ring dyke have been investigated by Bailey *et al.* (1924); Marshall (1984) and Sparks (1988), who all noted the presence of large amounts of mafic inclusions of predominantly glassy or cryptocrystalline material within the rhyolites.

The Loch Ba ring dyke was interpreted by Sparks (1988) to be a rheomorphic welded tuff emplaced during the collapse of the Centre 3 caldera. Sparks (1988)

following on from the work of (Marshall 1984) considered the ring dyke to have been derived from a compositionally zoned magma chamber, where extreme differentiation of tholeiitic magma had occurred. Thus, it is suggested that assimilation of silica poor cumulate materials derived from andesitic liquids modified the composition of less evolved magmas, therefore causing a significant departure from the normal liquid line of descent (Kerr 1999). Geochemical data is quite limited for the Lock Ba ring dyke, Sparks (1998) and Marshall (1984) only report major element concentrations. Fig. 2.37, is plotted from these data and shows that most of the Loch Ba ring dyke samples plot in the sub-alkalic field, although there is quite a spread, and some data point are high in the alkalic field.

The dark glassy rocks range in composition from ferrodiorite (53 wt % SiO_2, ~ 19 wt % Fe_2O_3) to rhyolites (~75 wt % SiO_2, ~3 wt % Fe_2O_3). Kerr *et al.* (1999) has used the occurrence of these ferrodiorites, which are also associated with elevated TiO_2 to place the Loch Ba ring dyke within the same petrogenetic framework as the rest of Centre 2 and Centre 3 igneous activity. However, the Loch Ba ring dyke rhyolites range in composition from 70-76 wt % SiO_2 and are very similar in composition to the acid cone sheets and granites from Mull Centres 2 and 3.

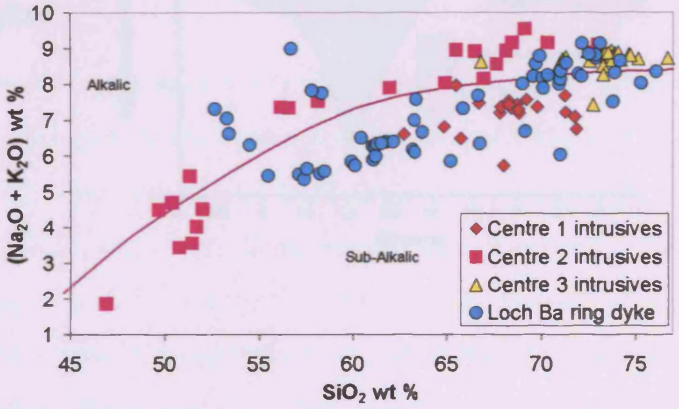

Fig. 2.37. Harker diagram of the main intrusive rocks and Loch Ba ring dyke. Data Sparks (1988)

2.7.3 Loch Ba Cross Cutting Dykes

There are a number of dykes cutting the Loch Ba ring dyke. These late cross cutting dykes are generally found along the north east edge of the Loch Ba ring dyke and represent the final pulse of igneous activity on Mull. Kerr *et al.* (1999) analysed a number of samples from these cross cutting dykes. Two sample were found to be high

Ca, low-alkali tholeiites, thus they were categorised as belonging to the Central Mull Tholeiite magma type. All other samples were found to have low to moderate MgO (~3.2-7 wt %) and are enriched in incompatible trace elements relative to the Central Mull Tholeiite type basalts Fig 2.38, thus Kerr *et al.* (1999) has classified these dykes as belonging to the Late Mull magma type Fig 2.39.

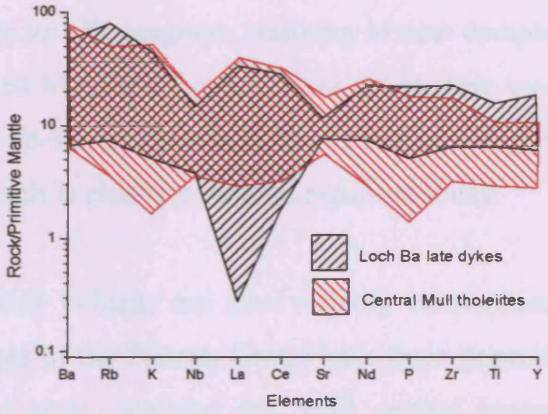

Fig. 2.38. Primitive mantle (Sun and McDonough 1989) normalised diagram of the Lock Ba late dykes and Central Mull tholeiites.

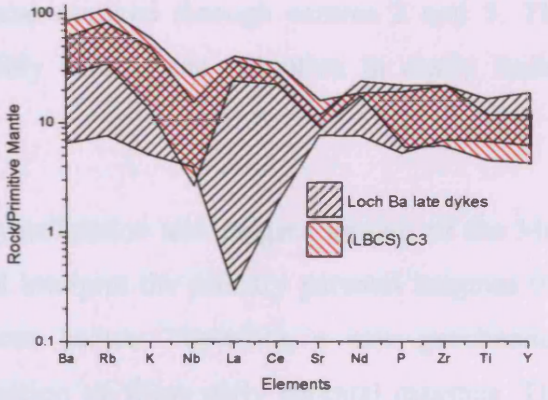

Fig. 2.39. Primitive mantle (Sun and McDonough 1989) normalised diagram of the Lock Ba late dykes and (LBCS) C3.

2.8 Conclusions

Through the work of many scientists over the last two centuries, we now have a greater understanding of the geology, petrology and geochemistry of the Mull igneous centre. Mull volcanism was associated with the break-up of the North Atlantic and the impingement below the crust of the early Icelandic mantle plume. The bulk of the volcanism occurred in two phases, phase 1 began about 62 Ma and lasted for 2-4 My, with most of the magmas being erupted onto the continental crust, including Mull.

Phase 2 began about 56 Ma with the onset of continental break-up and continues to this day in Iceland.

From the work of Kerr, Thompson and others, it is clear that magma mixing was a common process in the evolution of the Mull volcano. Two types of mixing predominate, with density being the controlling factor determining which type of mixing occurs. In the (EBCS) and CMT, there was a relatively small density difference between low MgO basalts and intermediate low Fe magmas, resulting in near complete cryptic magma mixing. Whereas in the Glen More and Loch Ba ring dykes there was a greater density contrast between high Fe-Ti intermediate and rhyolitic magmas resulting in incomplete magma mixing, which is clearly visible in exposure today.

The magmas associated with the Mull volcano are also variably contaminated with crustal components. The basic magmas of the Plateau Group have been generally contaminated with granulite-facies lower crust, whereas the Mull central igneous complex are contaminated with Moine metasediments upper crust, but this contamination reduced as the Mull volcano evolved through centres 2 and 3. This reduction in crustal contamination probably reflects the reduction in easily fusible crustal materials though time.

Due to contamination, fractional crystallisation and magma mixing of the Mull magmas, it is very difficult to sample and interpret the primary parental magmas that led to the formation of the Mull igneous centre. Therefore, a new geochemical approach is needed to glean more information on these early parental magmas. This could be achieved by the sampling of melt inclusions in early forming mineral phases such as olivine, because they should have formed before or during the processes that altered and contaminated the magmas. The remainder of this thesis interprets the results of the analysis of melt inclusions, and the implications of this study for our understanding of the early, deep-seated processes and igneous activity that led to the formation of the Mull igneous centre.

Chapter 3

Field Locations and Petrography of Samples

3.1 Introduction

The Mull-Morvern lava succession covers an area of ~840 km^2, with a maximum thickness of ~1000 m on Ben More (Fig. 3.1). Most of the succession is composed of transitional (tholeiitic-alkali) basalts, which very from picritic basalts near the base to basaltic-hawaiites near the top of the succession (Kerr, 1998). In the centre of Mull, an intrusive complex composed of cone sheets, ring dykes and large intrusive bodies cuts the lava succession. This central complex formed in the later stages of the evolution of the Mull igneous centre, and its emplacement led to the circulation of hot hydrothermal fluids within the lava succession, resulting in the alteration of the lavas closest to the central complex. Thus, the freshest lavas are found on the west and north of Mull, and on the nearby mainland of Morvern.

Since the most evolved lava types lie within the central zone of intense alteration, and contain no fresh olivine (Kerr, 1998), all of the samples for this study have been collected away from the central zone in the west and north of Mull, and the mainland of Morvern (Figs. 3.1, 3.2). All samples collected belong to the Mull Plateau Group of lavas. However, these lavas are not completely fresh, and contain variable amounts of zeolites. Thus, attempts were made to collect samples from the centres of the individual lava flows, away from the more altered margins.

Whole rock analysis was carried out by ICP-OES for major compositions, and by ICP-MS for trace element compositions, (full results are presented in Appendix 2). Analysis of olivines was carried out by SEM and LA-ICP-MS (full results are presented in appendices 3 and 4 respectively). All analyses were carried out at Cardiff University. The locations and grid references for all samples collected are shown in appendix 5.

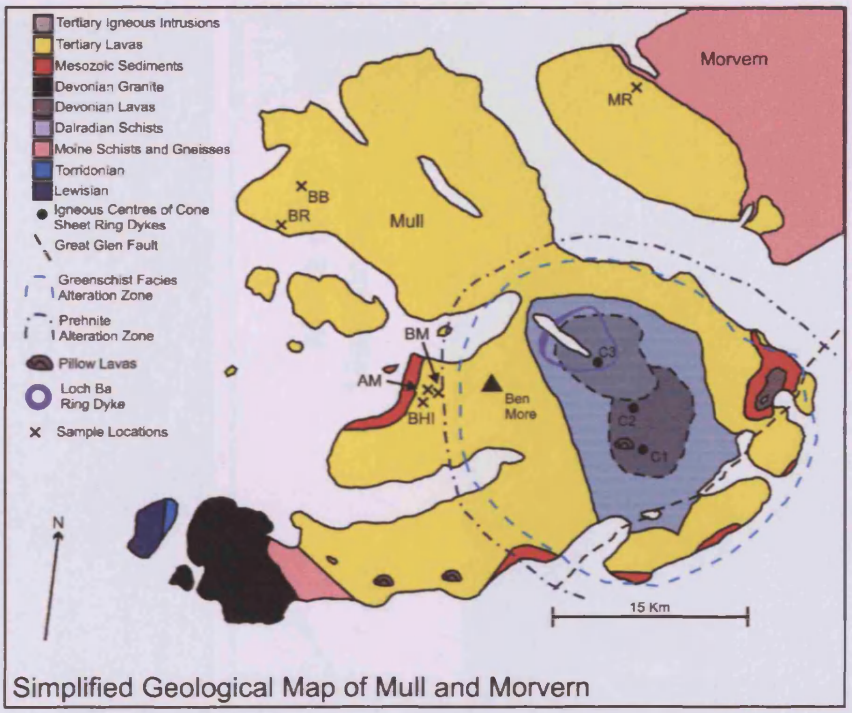

Fig. 3.1. Simplified map of the Mull-Morvern Tertiary igneous centre showing the locations of sampled lavas.

3.2 The lava flows

Originally, the tops and bottoms of the lava flows were vesicular, but these vesicles now contain numerous secondary alteration minerals; zeolites, outside the central alteration zone, and epidote, albite and calcite within the zone. Hydrothermal fluids circulating through the lava pile, during the emplacement and cooling of the central complex would have precipitated these minerals. Between these altered amygdoidal outer margins, there is usually a central, generally non-vesicular, less altered region to the lava flows.

Kerr, (1993) carried out a geochemical and petrographic study of the Mull lavas, including a series of flows (BHL series) from the basal ash deposit at Gribun (Fig. 2.10) to the top of Beinn na Iolaire (Fig. 3.3). Kerr (1993) assumed that each terrace represented a separate flow, and on this basis, the individual flows would have thicknesses in the order of 5-7m. In order to assess if this is the case, Kerr (1993) looked at the chemistry of the individual terraces to see if any which overlie each other are identical, so indicating that they belong to the same flow. Apart for a few exceptions, the geochemical evidence pointed to the individual terraces representing separate and distinct flows.

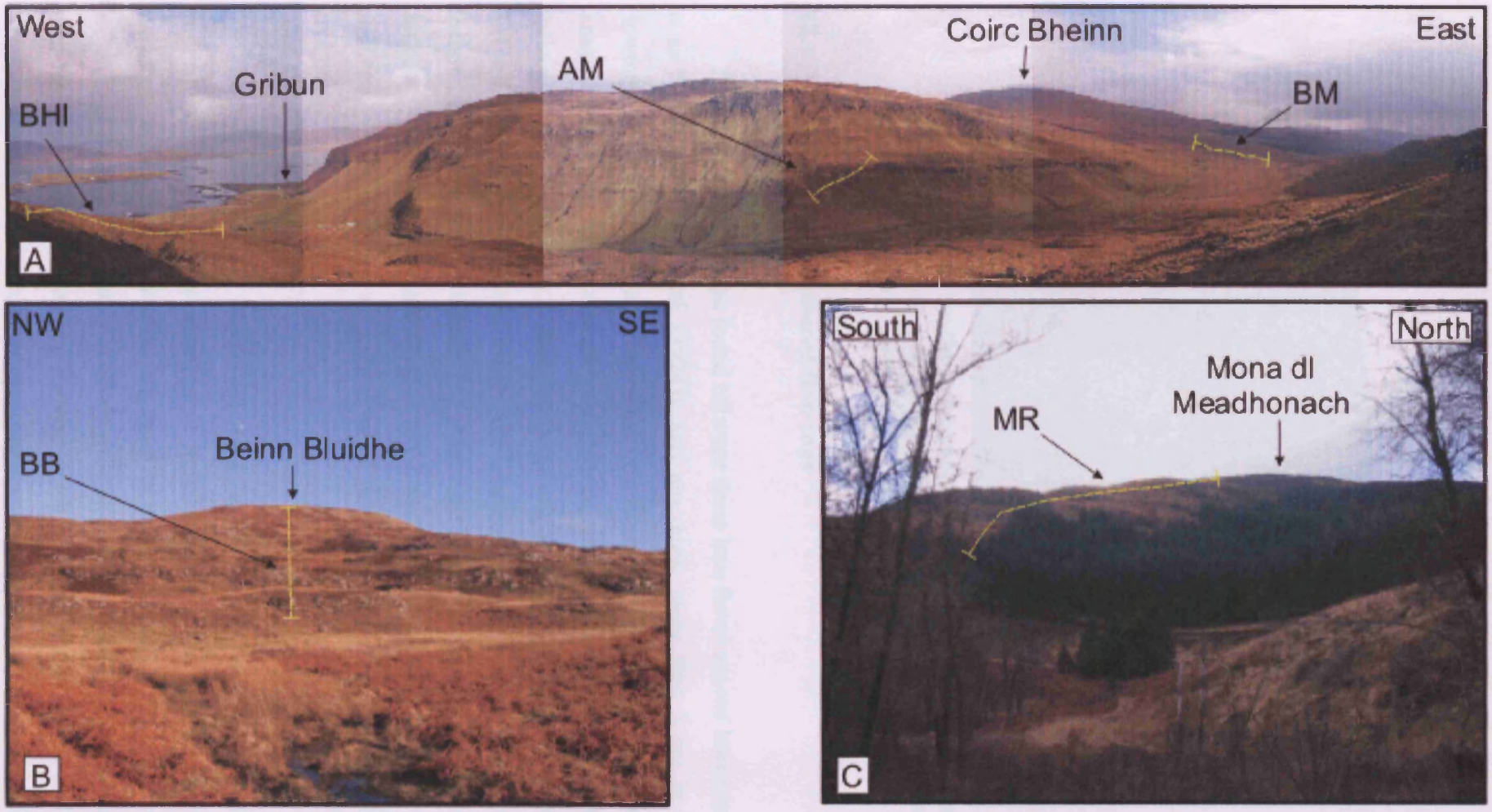

Fig. 3.2. A) mosaic of location in western Mull showing trap topography of the MPG lavas, and locations of BHI, AM and BM samples. B) location in northern Mull where BB samples where collected. C) Location in Morvern where MR samples where collected.

Fig. 3.3. Showing the trap topography of the MPG lavas at Beinn na Iolaire. Each terrace represents a distinct flow of between 5-10m in thickness. GR [NM452314]

3.2.1 Pyroclastics and weathered flow tops

The main intercalations found between these lava flows are red horizons (referred to as boles by Bailey *et al.* (1924)), and are rarely more than 5 cm in thickness. However, post-volcanic weathering of the lava flows has lead to material falling off the faces of the flows, which obscures their bases, consequently flow junctions and red horizons are not often seen. These red boles are best exposed in stream sections (e.g. BM samples), which are observed in Allt Chreaga Dubah (Fig. 3.4) on the road from Gribun to Loch Scridain (NM469318). Although most of these red boles are ~5 cm in thickness, Kerr (1993) found several red boles that are between 10 and 40 cm in thickness, whilst Bailey *et al.* (1924) noted the occurrence of a red bole of 2.5 m in thickness.

Bailey *et al.* (1924) interpreted these red boles, as fossil soils resulting from tropical weathering on the surfaces of basaltic flows. This may be true in some instances; however, examination of these boles by Kerr (1993), has revealed the presence of fragmental crystals of clinopyroxene and pseudomorphs of zeolite, possibly after feldspar. These are set in a matrix, which although badly altered and oxidised, preserves (in thin section) a ghost structure reminiscent of streaked-out and bent glass

shards. Thus, Kerr (1993) has interpreted the angular, fragmental nature of the crystals and crystal pseudomorphs, as being strongly suggestive of their derivation from an explosive eruption of pyroclasic material.

Fig. 3.4. Stream in Allt Chreaga Dubah where red boles of ~5 cm in thickness can be observed. The waterfall is ~2 m in height, and the grid reference is [NM469318].

3.3 Petrography of Samples

All of the samples collected for this study are generally basaltic in composition, having concentrations of SiO_2 between 42-50 wt %, MgO > 6 wt %, and total alkalis (Na_2O+K_2O) of less than 4 wt %. Texturally, the samples range from olivine porphyritic (Figs. 3.5 and 3.6) to very fine-grained (Fig. 3.7). The olivine phenocrysts are generally up to 3 mm in diameter, and show euhedral to anhedral texture. Occasionally plagioclase phenocrysts are also present (Fig. 3.6), with a size range up to 3 mm, but these are generally found in rocks with lower (<10 wt %) whole rock MgO values. The texture of the groundmass varies from fine-grained (<0.3 mm) (Fig. 3.7) to doleritic (>1 mm) (Fig. 3.6), with a mineralogy of clinopyroxene, plagioclase, olivine and Fe-Ti oxides.

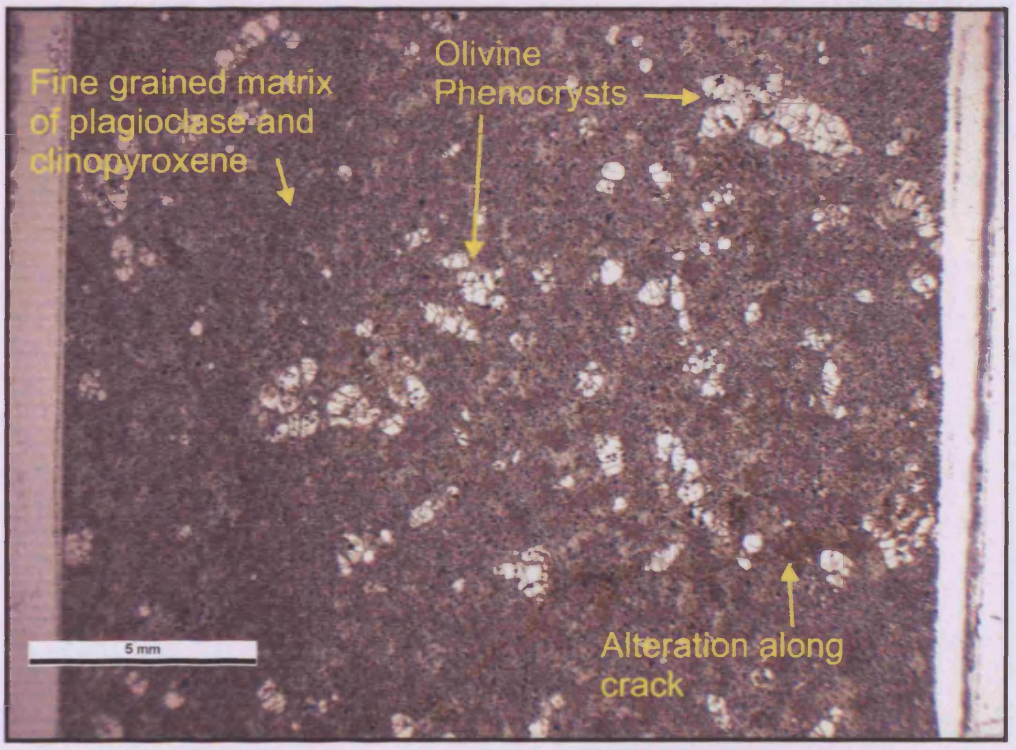

Fig. 3.5. Thin section of sample AM2 (GR NM860490, Alt 190 m), showing porphyritic texture, consisting of olivine phenocrysts in a fine grained matrix of olivine, plagioclase and clinopyroxene, and lesser amounts of Fe-Ti oxides.

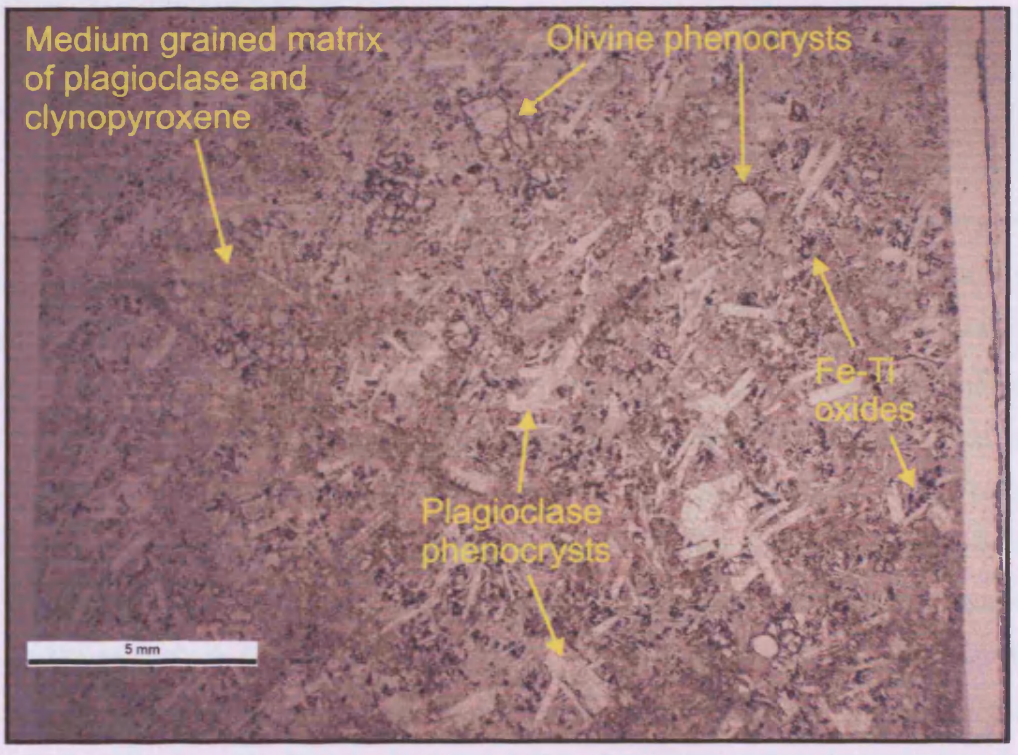

Fig. 3.6. Thin section of sample BHI 26 (GR NM245161, Alt 333 m), showing porphyritic texture, consisting of olivine and plagioclase in a medium-grained matrix of olivine, plagioclase, clinopyroxene and Fe-Ti oxides.

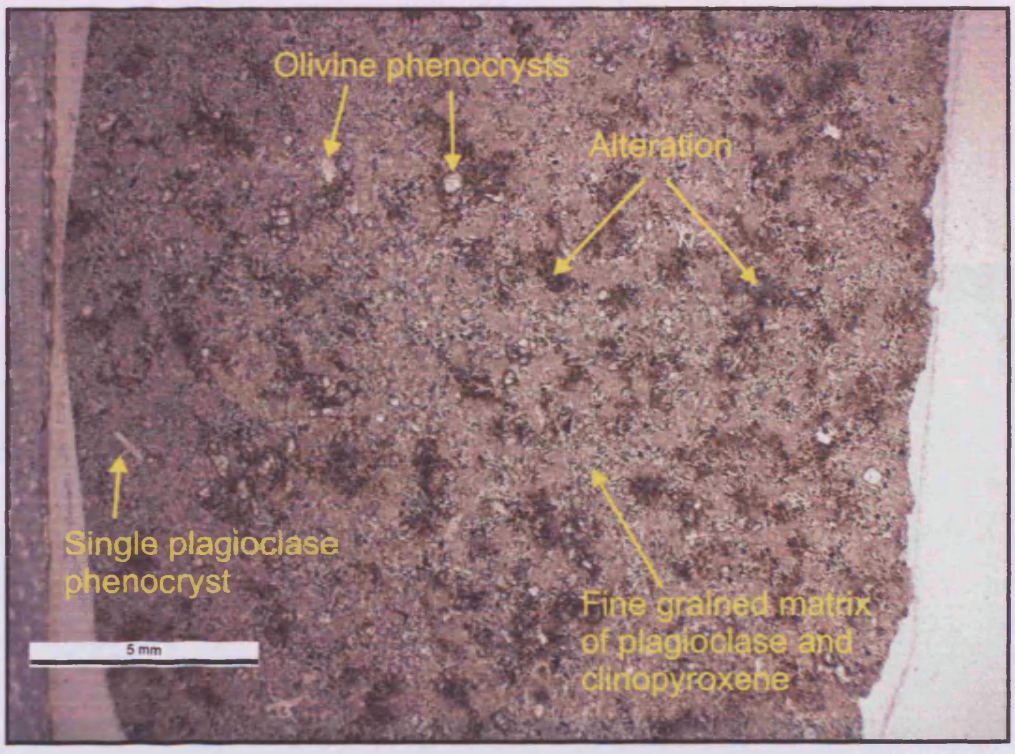

Fig. 3.7. Thin section of BM2 (GR NM874784, Alt 157 m), showing a fine grained texture of olivine, plagioclase and clinopyroxene. Also present are a number of small <0.5 mm olivine micro-phenocrysts, and a single plagioclase micro-phenocryst

3.2.1 Olivine

Olivine crystals in all samples are altered to some extent, particularly on their margins and along cracks (Fig. 3.8a), with the alteration products being serpentine, chlorite, oxides, and iddingsite. Another feature of olivine phenocrysts, particularly the larger crystals is the number of decrepitated melt inclusions that they contain (see Chapter 4). Radiating from all these decrepitated inclusions are fractures, indicating that the overall fracturing of olivines may due to their inability to contain the excessive internal pressures that these large inclusions place on the enveloping olivine crystals. Also present are undamaged melt inclusions (Fig. 3.8c), but these inclusions tend to be much smaller than their decrepitated counterparts, suggesting that there is a maximum size to the inclusions that olivine can contain without decrepitation taking place. From this study the cut-off point for the retention of whole inclusions within the olivine crystals is ~40 μm, with all inclusions larger than this experiencing decrepitation during their evolution. Most olivine crystals also contain solid inclusions of chrome-spinel

(Fig. 3.8b), indicating that chrome-spinel was the first phase to fractionate from these basaltic melts.

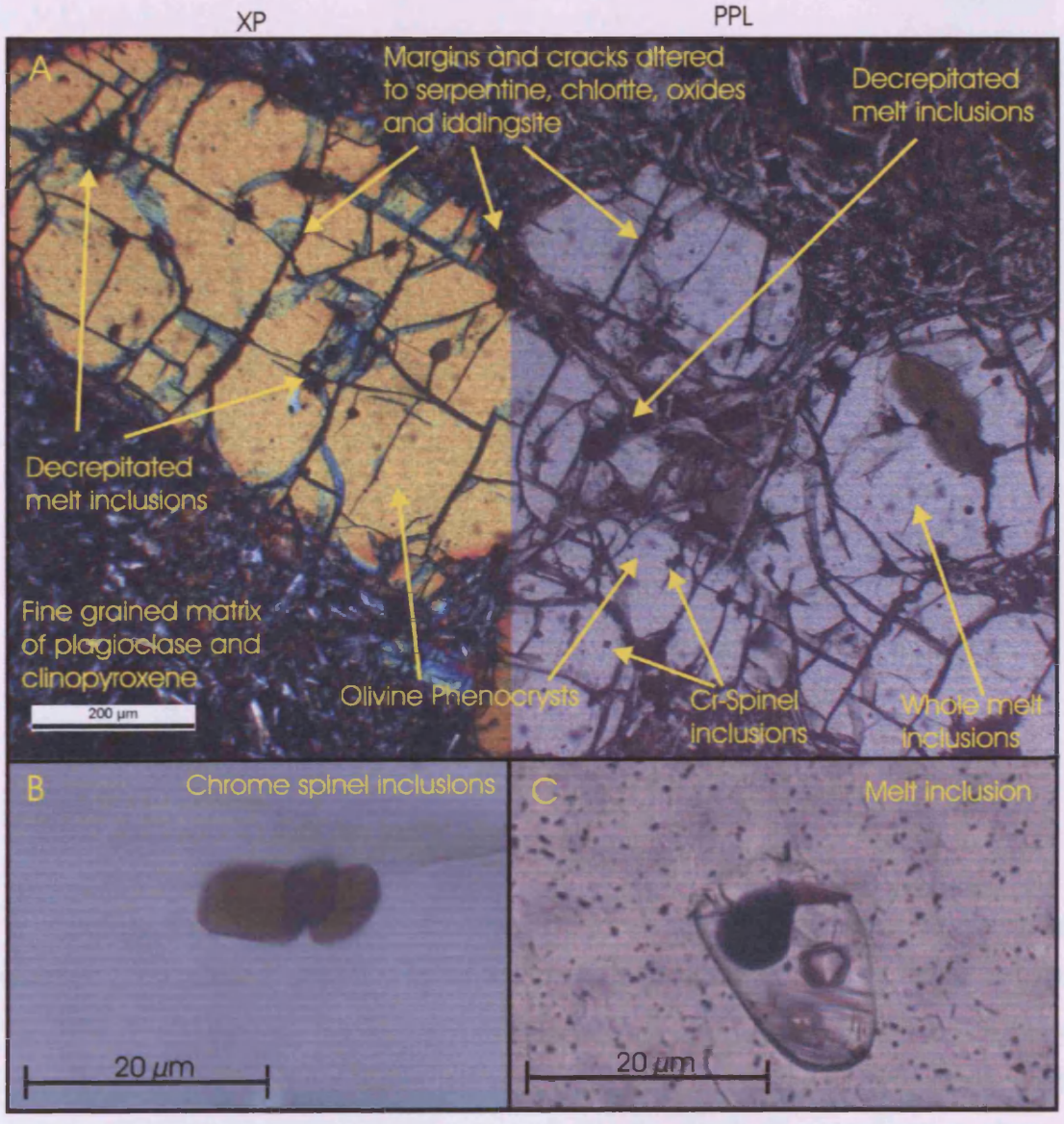

Fig. 3.8. A) Thin section of olivine phenocryst in sample AM2 (GR NM860490, Alt 190 m), showing alteration of margins and cracks. Also visible are numerous decrepitated melt inclusions, smaller whole melt inclusions and solid chrome spinel inclusions. B) Image of three solid chrome spinel inclusions. C) Image of melt inclusion, containing vapour bubble and daughter crystals.

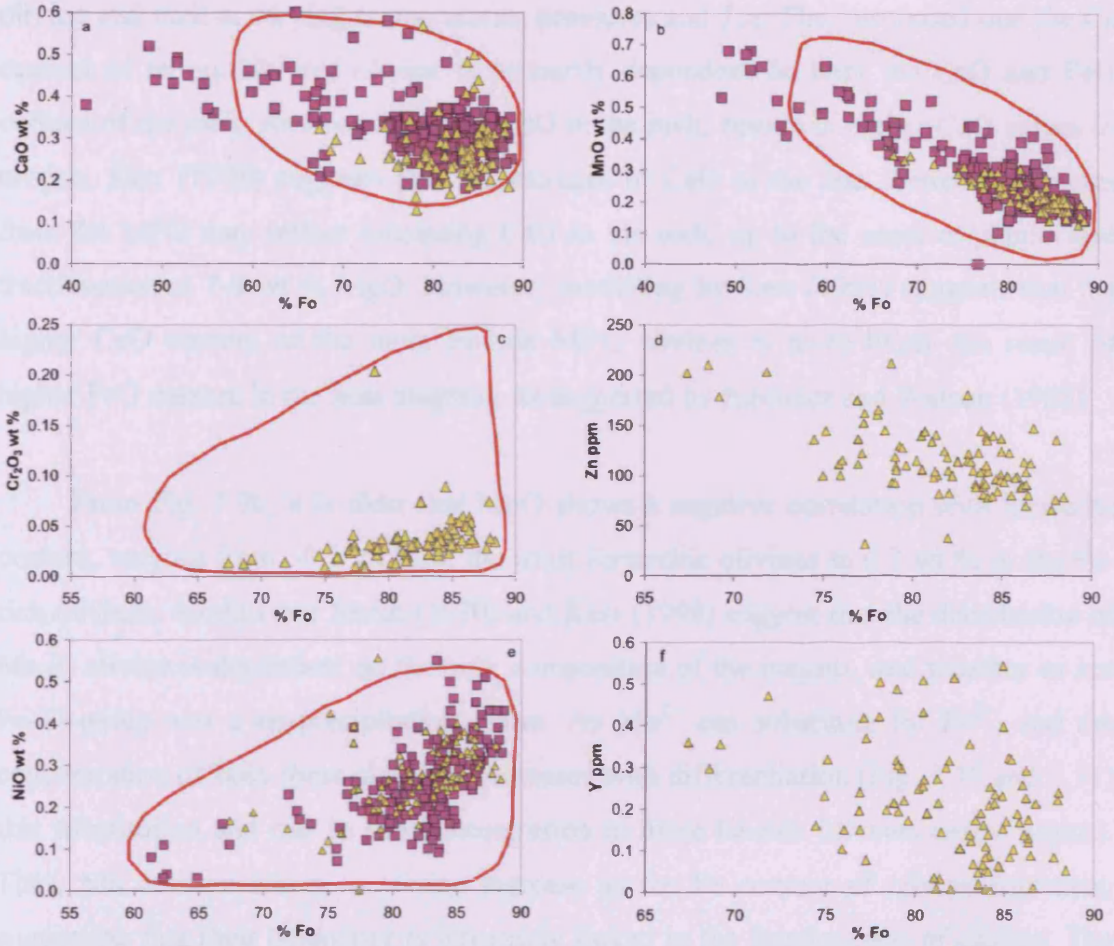

Fig. 3.9 a-f. Plots of minor element variation against forsterite content for olivines from the MPG. Electron micro probe (EMP) data Kerr (1998), SEM (Appendix 3) and LA-ICP-MS (Chapter 5 and Appendix 4) data this work.

In Fig. 3.9a-f, forsterite (Fo) content has been used as a differention index, to ascertain how minor elements very in MPG olivines as the host magmas evolve. On Fig. 3.9a it is clear that the lowest CaO values (~0.2 wt %) are found in the more forsteritic olivines, with the higher values (~0.4-0.6 wt %) found in the more Fe-rich olivines. Simkin and Smith (1970) proposed that the depth of crystallisation plays a major role in determining the Ca content of olivines. With deep crystallising plutonic rocks having lower CaO (<0.1 wt %) in their olivines, whereas, extrusive and shallow intrusive rocks contain higher CaO (>0.1 wt %) in their olivines. This implies a pressure control on the CaO content of olivines, with the larger Ca cation (1.20 Å (Å = 10^{-10}m) finding it more difficult to substitute for the smaller Mg (0.80 Å), Ni (0.77 Å), Mn (0.75 Å) and Fe^{2+} (0.86 Å) cations at higher pressures. Conversely, in experimental studies Jurewicz and Watson (1988) determined Ca partition coefficients between

olivine and melt at varying temperatures, pressures and fO_2. They proposed that the Ca content of an equilibrated olivine is primarily dependent on both the CaO and FeO content of the melt. As a result, higher FeO in the melt, results in higher CaO values in olivine. Kerr (1998) suggests that the increase in CaO in the less forsteritic olivines from the MPG may reflect increasing CaO in the melt, up to the onset of plagioclase fractionation at 7-8 wt % MgO. However, modelling by Kerr (1993) suggests that the higher CaO content of the more Fe-rich MPG olivines is more likely the result of higher FeO content in the host magmas, as suggested by Jurewicz and Watson (1988).

From Fig. 3.9b, it is clear that MnO shows a negative correlation with forsterite content, varying from ~0.1 wt % in the most forsteritic olivines to 0.7 wt % in the Fe-rich olivines. Simkin and Smith (1970) and Kerr (1998) suggest that the distribution of Mn in olivine is dependent on the bulk composition of the magma, and whether or not Fe-Ti oxide was a co-precipitating phase. As Mn^{2+} can substitute for Fe^{2+}, and the concentration of both these elements increases with differentiation (Fig. 3.10 and 3.11) this substitution and rise in Mn concentration in more Fe-rich olivines seems logical. Thus, Mn concentrations in olivine increase as the Fe content of olivine increases, suggesting that their behaviour is intimately linked in the fractionation of olivine. The behaviour of Zn also mirrors the trends seen for MnO, with a general rise in its concentration in olivine (Fig. 3.9d) and melt (Fig. 3.12) as differentiation proceeds.

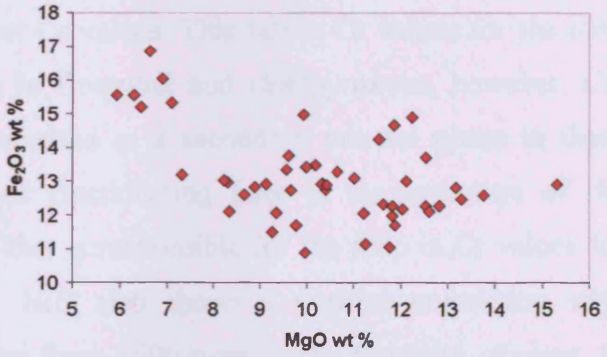

Fig. 3.10. Plot of Fe_2O_3 versus MgO for the MPG lavas. Data from this study.

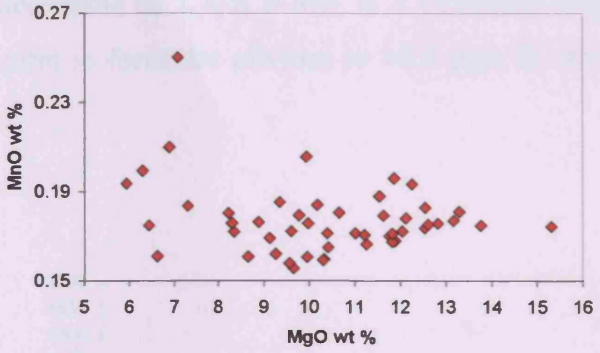

Fig. 3.11. Plot of MnO versus MgO for the MPG lavas. Data from this study.

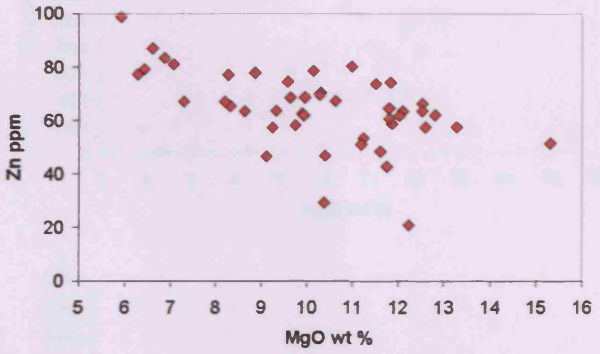

Fig. 3.12. Plot of Zn versus MgO for the MPG lavas. Data from this study.

Unlike Ca, Mn and Zn, Cr_2O_3 (Fig. 3.9c) exhibits a positive correlation when plotted against the forsterite content. The highest values (~ 0.24 wt %) are found in the most forsteritic olivines, whereas the lowest values (<0.05 wt %) are found in the Fe-rich olivines. Kerr (1998) suggests that the main control on the Cr content of olivine (in the form of exsolved chromite) is the abundance of Cr in the magma from which the olivine fractionated. From Fig. 3.13, which is Cr ppm versus MgO wt % for the MPG lavas, there does seem to be a good positive correlation. That is, lavas with the lowest Cr values, host olivines with the lowest Cr values. This fall in Cr values for the melt could be due to Cr being compatible in Cr-spinel and clinopyroxene; however, Cr-spinel only seems to have been fractionated as a secondary mineral phase in these basalts, and clinopyroxene only began fractionating later in the evolution of the magmas. Therefore, it may be olivine that is responsible for the drop in Cr values for the melt as fractionation proceeded. NiO also shows a positive correlation with forsterite content (Fig. 3.9e) and varies from 3500 ppm in the forsterite olivines, to below 500 ppm in the Fe-rich olivines. The distribution of Ni, like Cr is dependant on the bulk composition of the melt, and as fractionation of olivine proceeds, Ni becomes depleted in the melt (Fig. 3.14). The only other element in analysed olivines, which is

consistently present in concentrations detectable by LA-ICP-MS, is Y (Yttrium) (Fig. 3.9f). Concentrations range from <0.1 ppm in forsterite olivines to >0.3 ppm in more Fe-rich olivines.

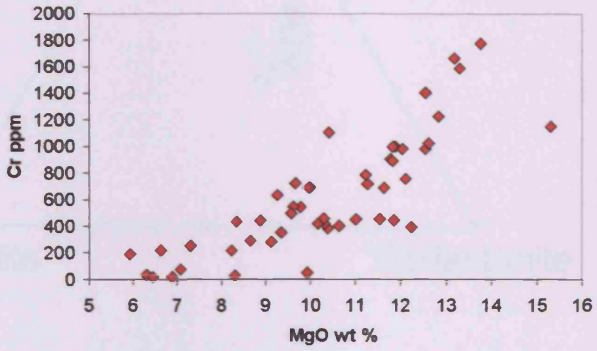

Fig. 3.13. Plot of Cr versus MgO for the MPG lavas. Data from this study.

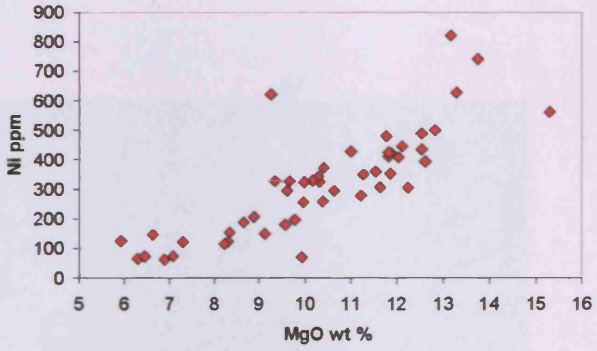

Fig. 3.14. Plot of Ni versus MgO for the MPG lavas. Data from this study.

3.2.2 Other mineral phases in MPG lavas

Clinopyroxene with chemical compositions (En_{21-49}, Fs_{10-32}, Wo_{38-49} Fig. 3.15), in the form of pale brown augite (Kerr, 1998) very rarely forms phenocrysts in the MPG lavas, but varies from poikilitic (Fig. 3.16) to ophitic (Fig. 3.17). In the poikilitic texture, the augite oikocrysts surround olivine, Fe-Ti oxides and laths of plagioclase up to 1 mm in length. Whereas, the ophitic texture, is augite surrounding plagioclase laths of less than 200 μm in length. As clinopyroxene oikocrysts tend to surround all other mineral phases in the MPG lavas, it suggests that clinopyroxene was the last major phase to crystallise from the melt.

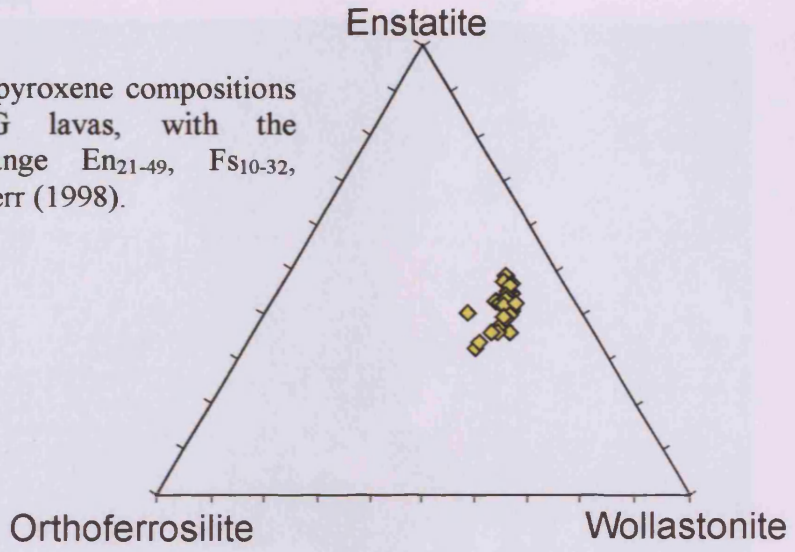

Fig. 3.15. Clinopyroxene compositions for the MPG lavas, with the composition range En_{21-49}, Fs_{10-32}, Wo_{38-49}. Data Kerr (1998).

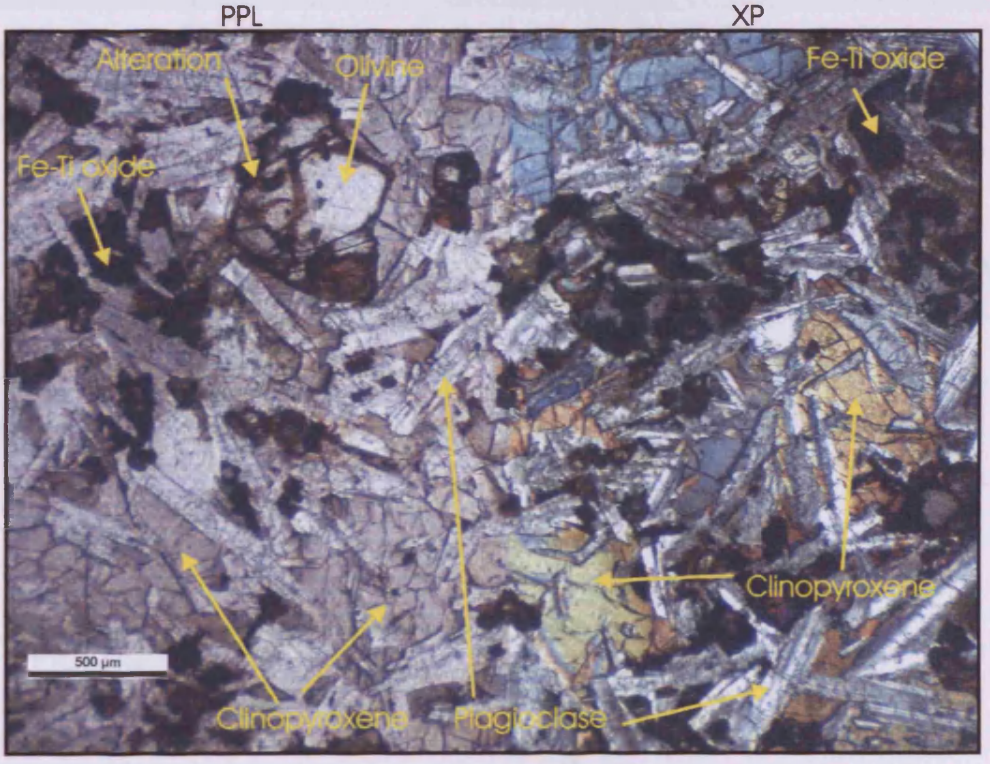

Fig. 3.16. Image of thin section, sample BM2 (GR NM874784). Showing poikilitic texture, where the chadocrysts are olivine, Fe-Ti oxides and elongated plagioclase laths generally less than 1 mm in length, and the surrounding oikocrysts are clinopyroxene.

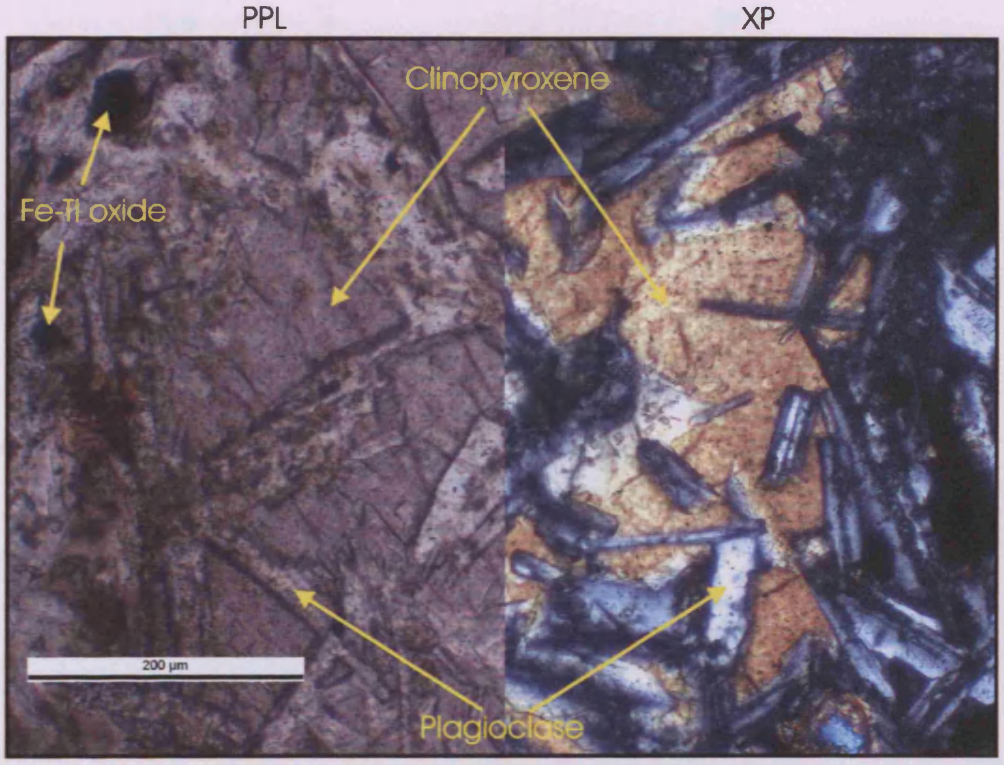

Fig. 3.17. Image of thin section, sample BM6 (GR NM956880) showing a close up of a clinopyroxene oikocryst surrounding or partially surrounding plagioclase laths of less than 200 µm in length.

Plagioclase in the MPG basalts exhibits a range of compositions from bytownite An_{70}-An_{90} through labradorite An_{50}-An_{70} to very occasionally andesine An_{30}-An_{50} (Fig. 3.18). Texturally plagioclase laths are generally subhedral to anhedral (Fig. 3.19), less than 3 mm in length (Fig. 3.6), and occasionally show trachytic texture (Fig. 3.20).

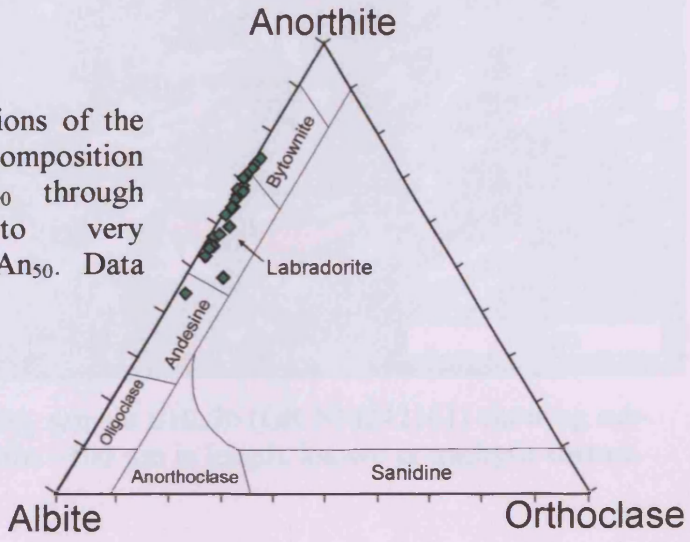

Fig. 3.18. Feldspar compositions of the MPG basaltic lavas, with the composition range, bytownite An_{70}-An_{90} through labradorite An_{50}-An_{70} to very occasionally andesine An_{30}-An_{50}. Data Kerr (1998).

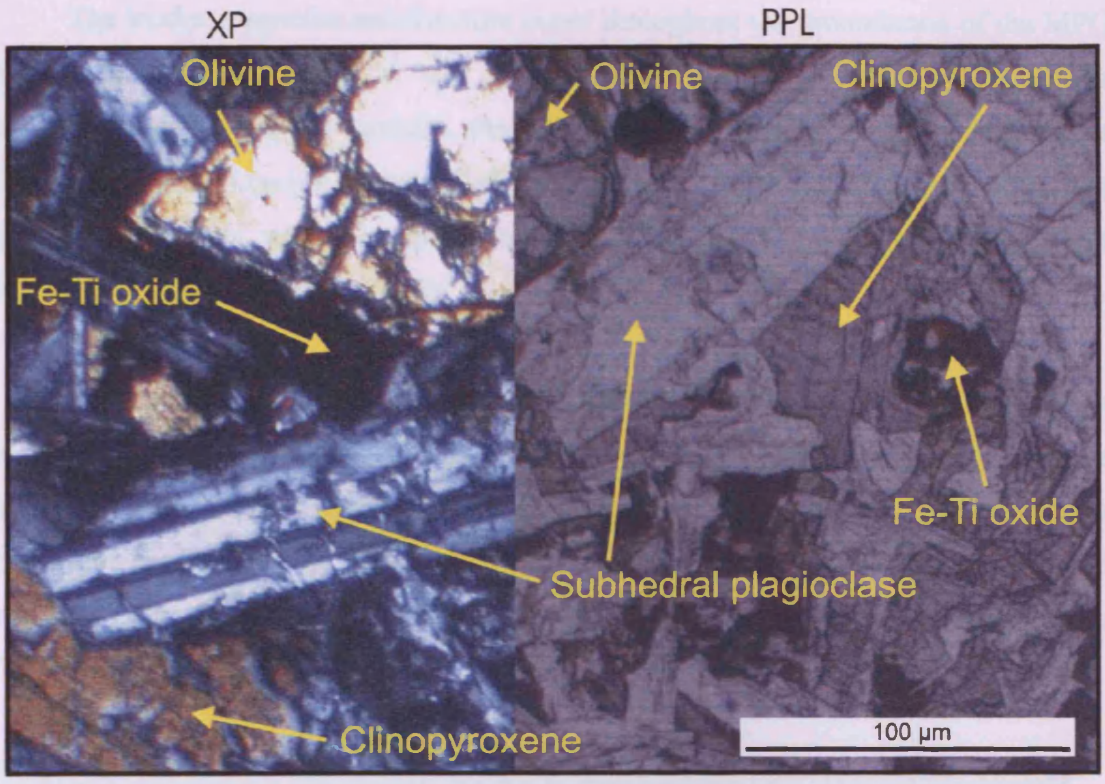

Fig. 3.19. Image of thin section, sample BM2 (GR NM874784) showing subhedral plagioclase laths of ~ 100 µm in length

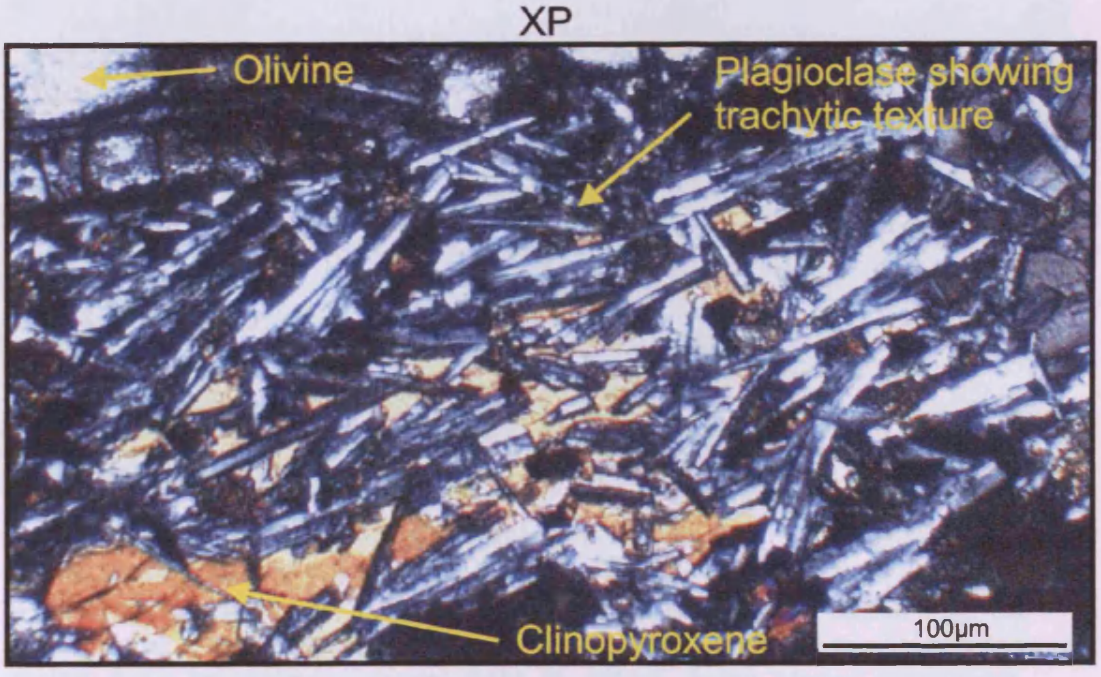

Fig. 3.20. Image of thin section, sample BHL26 (GR NM242161) showing sub-parallel aligned plagioclase laths ~100 µm in length, known as trachytic texture.

The oxides magnetite and ilmenite occur throughout the groundmass of the MPG basaltic lavas (Figs. 3.6, 3.16 and 3.17). Ilmenite generally occurs as exsolution lamellae in magnetite, and contains abundant Ti and Fe^{2+} along with variable amounts (0-10%) of Fe^{3+}. Opaque minerals of the magnetite series make up the rest of the groundmass oxides, with a composition of 20-30 wt % TiO_2, 0-12 wt % Fe_2O_3 and 0.15-0.35 wt % Cr_2O_3 (Kerr, 1998).

Cr-spinel is only found enclosed, or partially enclosed, within olivine crystals in the MPG lavas. As suggested by Kerr (1998), it is highly likely that Cr-spinel was the first phase to crystallise from these Mg-Cr rich magmas, and probably provided sites for olivine nucleation (Fig. 3.21a). As a rule, the dark coloured spinels in Fig. 3.21a are probably rich in Cr, whereas the lighter coloured spinels in Figs. 3.21b-c are probably rich in Al and possibly Mg, as Mg rich spinels are transparent (Gribble and Hall, 1992).

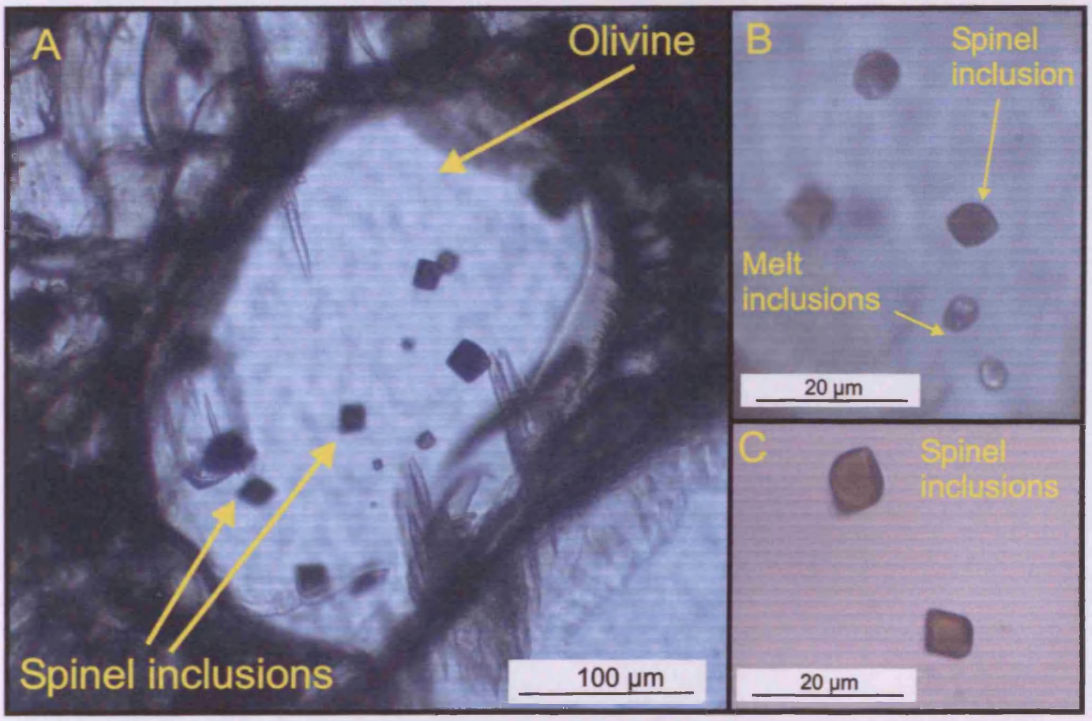

Fig. 3.21a-c. a) olivine hosting several spinel inclusions, in this sample the spinels are very dark almost opaque in colour, sample BHI18 (GR NM298391). b) Several inclusions hosted in olivine, the spinel is lighter in colour than the spinels in (a), sample MR8 (GR NM424305). c) Two spinel inclusions hosted in olivine, both inclusions are very light in colour, being almost transparent, sample BM6 (GR NM956880).

3.3 Summary

- The MPG basalts are composed predominantly of olivine, pyroxene and plagioclase in varying amounts. Opaque accessory phases included magnetite, ilmenite and spinel.
- The basalts are variably altered with secondary assemblages dominated by zeolites. Olivines are altered along margins to serpentine, chlorite, oxides, and iddingsite. Pyroxene and plagioclase do not seem to have suffered alteration.
- Textural relationships in the basalts suggest that spinel was the first mineral phase to crystallise, followed closely by olivine and then Fe-Ti oxides and plagioclase, with clinopyroxene being the last phase to crystallise.
- Olivine crystals contain a selections of inclusions including, decrepitated melt inclusions, undamaged melt inclusions and solid inclusions of chrome-spinel.
- Decrepitated melt inclusions have a minimum size of ~40 μm, whereas the undamaged inclusions have a maximum size of ~40 μm.

Chapter 4
Melt Inclusions and Methods of Analysis

4.1 Introduction

Melt inclusions are small portions of melt trapped by growing crystals during magma evolution prior to and during eruptions, and their existence has been known for many years (e.g. Anderson, 1974; Clocchiatti, 1975; Sobolev and Kostyuk, 1975; Sobolev, 1983; Roedder, 1984). Melt inclusion analysis can provide valuable information on crystallisation temperatures, the sequence of phase changes in the host magma during cooling, cooling rates, the composition and volatile content of the host magma and liquid lines of decent (Roedder, 1979). In the context of CFBs, melt inclusions also have the potential to provide information on the timing, extent and geochemical effects of crustal contamination.

4.2 Melt Inclusion Properties

Generally, silicate melt inclusions have a small volume, being <300 μm in diameter, and make up less than 0.3% of the volume of the host mineral. During ascent of the host crystal, it is assumed that the trapped melts (inclusions) are protected from degassing by the enveloping mineral phase (i.e. olivine, plagioclase). Thus, inclusions have the potential to retain high concentrations of volatile elements, which could yield estimates of gas saturation pressures (Schiano, 2003). After entrapment of the melt by overgrowth of the host mineral, a number of changes occur that may alter the composition of the trapped melt. The degree of modification will be determined by the changes in the equilibrium state between the host mineral and the trapped melt. Thus, as the host mineral rises through the magma pluming system en route to the surface it will cool slowly, and at the same time differences in the thermal expansion coefficients of the host mineral and melt will lead to the separation of volatile fluid phases (i.e. H_2O, CO_2, Fig. 4.1). The composition of the melt inclusions can also be modified by the overgrowth of the host phase on the inclusion walls and nucleation of minerals

(daughter minerals) directly from the melt (Fig. 4.2). Therefore, at the Earth's surface, silicate melt inclusions usually contain one to several vapour bubbles, daughter crystals, glass and mineral overgrowths on the inclusion wall. If the inclusion and host phase formed at the same time, the inclusion is said to be primary, but if the inclusion formed after the mineral phase it is said to be secondary, (Schiano, 2003).

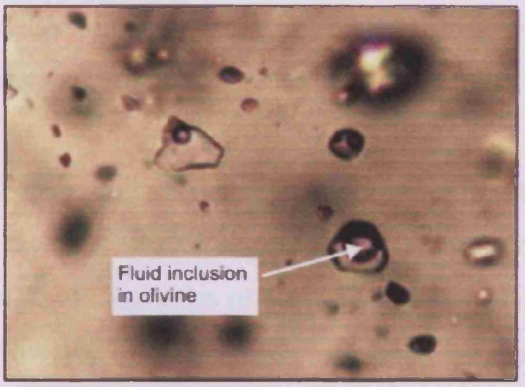

Fig. 4.1. Showing fluid phase in olivine-hosted inclusion. The arrowed inclusion is approximately 30 μm in diameter.

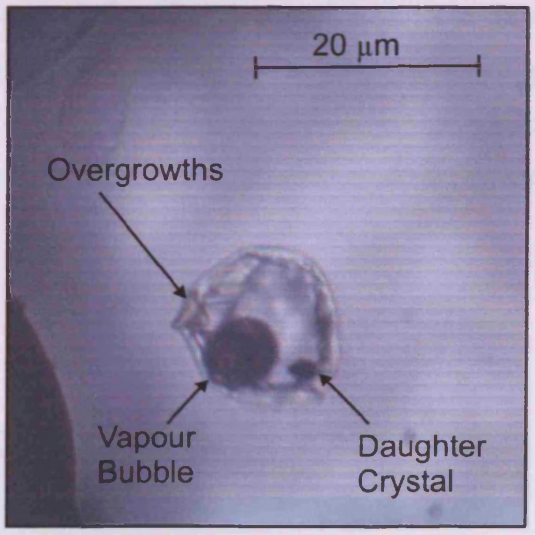

Fig. 4.2. Olivine-hosted melt inclusion, showing overgrowths, daughter crystals and vapour bubble. The sample is from the Mull Plateau Group lavas, sample BM7, Grid Reference [NM 4697331900], altitude 187 m.

4.2.1 Primary Inclusions

Lofgren and Donaldson (1975) suggest that melts are included mostly in the central part of crystals. This may be true of some mineral phases that have undergone a fast cooling rate but, in olivine-hosted inclusions studied from Mull, the inclusions are randomly spaced in the minerals. Indeed most of the phenocrysts that host inclusions, host several with no particular preference for where the inclusions are situated (Fig.

4.3). Roedder (1984) and Sobolev and Kostyuk (1975) list a variety of mechanisms by which primary inclusions may form, including: 1) non-uniform supply of nutrients to the crystal face, resulting in skeletal growth; 2) under-cooling, also resulting in skeletal growth; 3) formation of re-entrants in the crystal during resorption events, followed by subsequent crystal growth; 4) wetting by a separate immiscible phase (e.g. molten sulphide or a vapour bubble) that creates irregularities in crystal growth, resulting in entrapment of that phase as well as melt. Even though this random pattern of inclusions holds for olivine and clinopyroxene, in plagioclase, inclusions are not only random, but also form populations outlining the zones of crystal growth (Fig. 4.4).

Primary inclusions are generally round to oval in shape (Figs. 4.2 and 4.3), but can also be elongated or irregular (Fig. 4.5). Schiano (2003) suggests that the rounded shapes of the inclusions are a function of the crystallography of the host mineral, thus producing faceted negative crystal cavities. However, Mainley (1996) has shown, using experiments on natural and synthetic inclusions, that the shape of inclusions is a secondary feature, reflecting the minimisation of surface energy. The rounded shape of the inclusions is thus a product of surface diffusion within the inclusion that yields rounded inclusions with (lowest surface area for volume) and negative crystals (lowest surface energy) shapes.

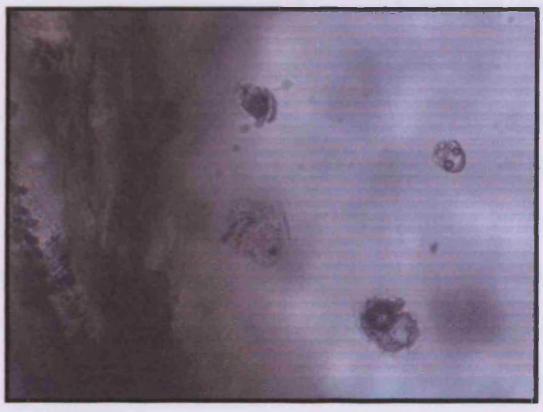

Fig. 4.3. Olivine mineral with several melt inclusions randomly spaced near the edge of the phenocryst. The inclusions are between 10 and 20 μm in diameter. The sample is from the Mull Plateau Group lavas, sample BM7, Grid Reference [NM 973900], altitude 187 m.

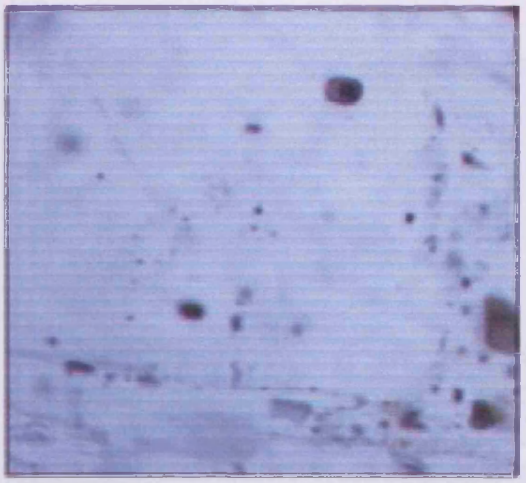

Fig. 4.4. Plagioclase-hosted inclusions outlining the planes of crystal growth; the largest inclusion is ~10 μm in diameter. The sample is from the Deccan Traps, India.

Fig. 4.5. Several inclusions hosted in olivine, the larger inclusions have elongated to irregular shapes being ~30 μm in length and 5-15 μm in width. The sample is from the Mull Plateau Group lavas; sample BM2, Grid Reference [NM 874784], altitude 157m.

4.2.2 Secondary Inclusions

As well as hosting primary inclusions, many phenocrysts host secondary inclusions, the main difference being that primary inclusions are derived from the melt from which the host crystal fractionated, whereas secondary inclusions are derived from a younger melt after the host phenocryst has formed. Secondary inclusions are generally located in fracture planes that cut the growth zones and cleavage planes of the host mineral (Fig. 4.6a-c), indicating that the crystals have undergone shear deformation events, with injection of melt into the fractures. Very often, the only evidence of these deformation events are the secondary inclusions. This is because the fracture zones often heal (Fig. 4.7). The secondary melt inclusions are generally spherical or sub-spherical in shape, but are often deformed before they pass the glass transition temperature, leading to ellipsoidal or flat and elongated inclusions (Fig. 4.6c).

Fig. 4.6a. Olivine phenocryst that has undergone shear forces, leading to the fracturing of the crystal. Magma has been injected into the fractures creating secondary melt inclusions. Microscope focused on sample surface. The sample is from the Mull Plateau Group lavas, sample BM2, Grid Reference [NM 874784], altitude 157 m.

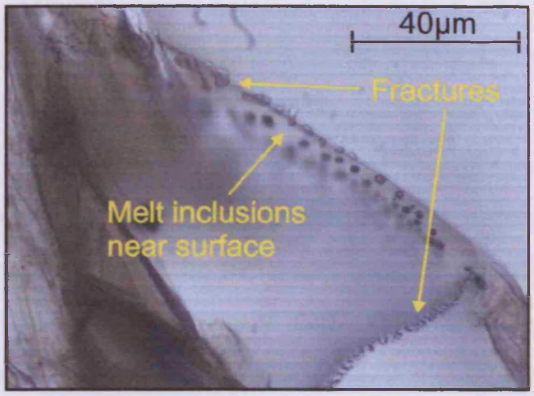

Fig. 4.6b. Focusing into the olivine crystal, it is possible to see the secondary melt inclusions tracing the direction and orientation of the fracture zones.

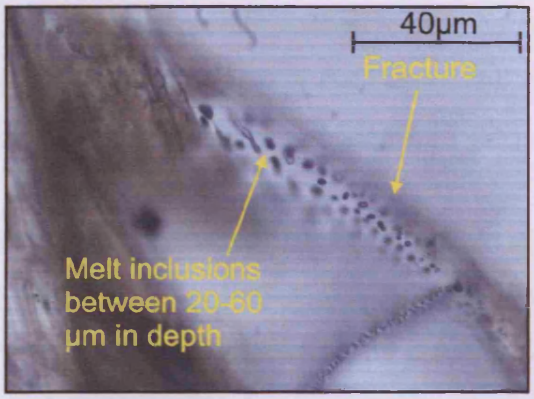

Fig. 4.6c. Focusing near the bottom of the olivine crystal (~100 µm thick). The inclusions are mostly round to oval in shape, but in the centre of the photo there are a number of elongated inclusions.

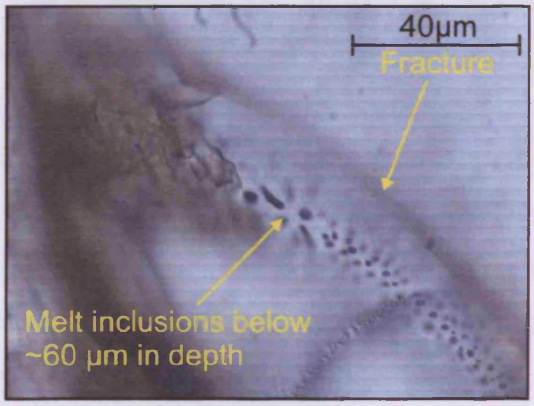

Fig. 4.7. Lined-up melt inclusions in olivine crystal, indicating that the olivine has undergone shear forces. The fracture as long since healed, leaving the inclusions as the only evidence of the earlier deformation event. The sample is from the Mull Plateau Group lavas, sample BM2, Grid Reference [NM 874784], altitude 157 m.

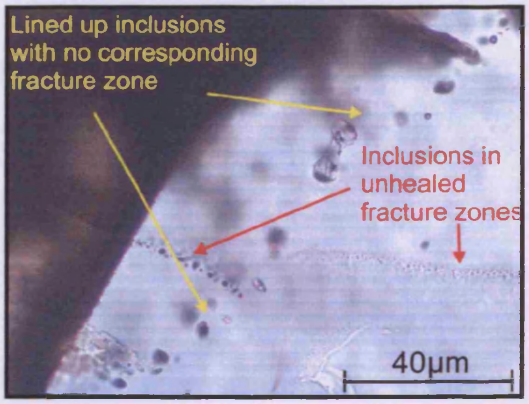

4.2.3 Mechanical Aspects of Melt Inclusions during Decompression

It has been shown by several workers (Gillet *et al.*, 1984; Tait 1992; Zhang 1998) that when a melt inclusion forms within a crystal, the internal pressure of the inclusion (P_{in}) is equal to the outside confining pressure (P_{out}) at the surface of the host mineral. If the host mineral undergoes changes in pressure (P) and/or temperature (T), it may lead to a large difference between the internal pressure of the inclusion, and the outside confining pressure. These differences are a consequence of the different incompressibilities (bulk modulus, K) between inclusion and host mineral. Generally melts that form the inclusions tend to have lower incompressibilities than the confining mineral, so that inclusions expand more than the host mineral upon decompression of the system, therefore resulting in an overpressure inside the inclusions (Zhang, 1998).

Schiano (1999), has taken the physical model of Zhang (1998), in which the mechanical equilibria of an inclusion-host system are considered during P-T changes, and applied it to felsic and basaltic melt inclusions that were trapped at 1.0 GPa inside an olivine crystal host and brought up to the surface. Fig 4.8 shows that, during adiabatic ascent, the pressure inside the melt inclusion will be almost completely preserved compared with the case of interstitial melt/glass, which follows the external pressure P_{out}. However, there is a difference between the initial pressure of trapping and the internal pressure of the inclusion for an external pressure of 1 atmosphere. This difference is a function of the bulk modulus of the inclusions and may vary by a factor of two between felsic and mafic inclusions. The ultimate drop in pressure of the inclusions is a result of the final cooling stage associated with reaching the Earth's surface. Nevertheless, even with this last drop in pressure, the inclusions retain a large proportion of their initial pressure when compared to interstitial melt/glass, which is now at atmospheric pressure.

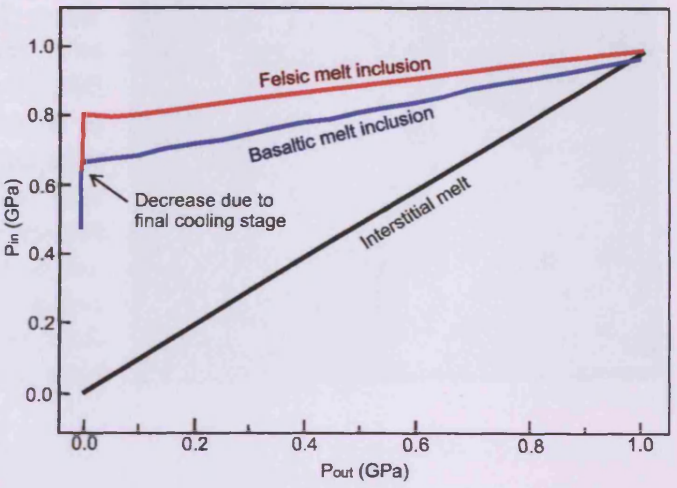

Fig. 4.8. Internal pressures (P_{in}) for melt inclusions as a function of the applied external pressure (P_{out}) during decompression and cooling, for inclusions of felsic and mafic melts trapped inside a olivine crystal at T = 1200°C and P = 1.0 GPa. The evolution of the internal pressure for an interstitial melt is also shown for comparison, Modified from Schiano (1999).

4.2.4 Decrepitation of Inclusions

The above arguments all refer to perfect conditions; however, this is not always the case. As Tait (1992) points out, phenocrysts that contain melt/volatile inclusions experience dilational stresses during eruptions, because the bulk modulus of silicate melt is an order of magnitude less than the elastic moduli of crystals (olivine, clinopyroxene), and because dissolved volatile components can exsolve in response to decompression. Thus, when the dilatational stress caused by melt decompression exceeds a critical value, the inclusion decrepitates (Fig. 4.9a-b), i.e. the host mineral surrounding the inclusion fractures, and material once confined in the inclusion is injected into the fractures. These fractures only develop when K_i (bulk modulus of inclusion) is less that K_h (bulk modulus of host mineral), and not when $K_i > K_h$, thus P_{in} must be grater than P_{out}, therefore proving these are decompression events. However, calculations by Zhang (1998) have shown that the decompression is approximately adiabatic or isothermal. If this decompression is accompanied by temperature decrease along a typical geotherm (slow rise to the surface), then the pressure and temperature would cancel each other out, and P_{in} would be equal to P_{out}, with no fracturing of host crystals surrounding inclusions. Therefore, it is possible to infer from the presence of decrepitated inclusions, that the host phase decompressed rapidly with no corresponding drop in temperature (i.e. rapid rise to the surface).

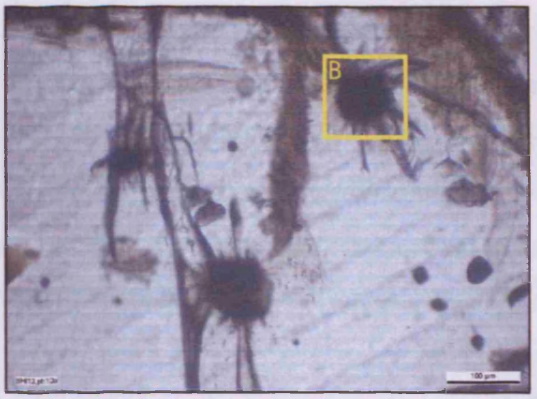

Fig. 4.9a, Three decrepitated melt inclusions in a olivine phenocryst. The decrepit inclusions are all between 70-100 μm in diameter, suggesting there is a upper size to pristine melt inclusions after which the elastic moduli of the host crystal can no longer contain the excess pressure of the melt inclusion due to de-pressurisation, and the inclusion decrepitates. The sample is from the Mull Plateau Group lavas, sample BHI 3, Grid Reference [NM 421832].

Fig. 4.9b, Close-up of a decrepitated inclusion, showing the fracture radiating away from the surface. These fractures follow pre-existing weaknesses in the host crystal. The sample is from the Mull Plateau Group lavas, sample BHI 3, Grid Reference [NM 421832].

4.2.5 Do Trapped Melt Inclusions Represent Liquid

The capacity of melt inclusions to preserve information about the original composition of the trapped melt is conditional on the efficiency of their isolation since entrapment. Post-entrapment reactions between inclusion, host and external melt have been studied extensively (Quin *et al.*,1992; Sobolev and Danyushevsky, 1994; Danyushevsky *et al.*, 2000; Gaetani and Watson, 2000). Investigations by Quin *et al.* (1992) show that, for a given element, the extent of re-equilibration increases as the diffusivity and crystal/melt partition coefficient of the element increase, and as the inclusion and host crystal size decrease. Thus, for trace elements excluded from the structure of the host mineral, the capability of transport via diffusion appears limited. Therefore, for olivine hosted melt inclusions, incompatible trace elements are preserved in the melt and are available for analysis and interpretation of magmatic processes. However, for olivine, readily exchanged major elements such as Fe and Mg are susceptible to post-entrapment modification. Gaetani and Watson (2000) showed that

olivine-hosted melt inclusions could undergo a high degree of compositional change in order to maintain Fe-Mg exchange equilibrium with a fractionating external melt. Even when equilibration is limited to the host-mineral inclusion system, diffusive re-equilibration of Fe and Mg may occur, and seems to be controlled by the cooling rate of the host crystal in the magma chamber and by the temperature difference between trapping and quenching of the inclusion during eruption (Danyushevsky *et al.*, 2000).

Although H_2O has lower diffusivity than major elements in olivine, H_2O (hydroxyl group, OH^-, OH^+) in melt inclusions could also re-equilibrate with external melt over geological time scales (Quin *et al.*, 1992). For inclusions hosted in olivine, dehydration of the trapped melt is facilitated by diffusion along plane of dislocation or propagation of defect points in the host olivine (Massare *et al.*, 2002). Hauri (2002) has also invoked diffusive hydrogen (D/H) loss during slow cooling after eruption to explain the D/H ratios measured in melt inclusions found in Hawaiian basalts. Diffusion of hydrogen driven by hydrogen fugacity gradients has also been suggested by Sobolev and Danyushevsky (1994) and Danyushevsky *et al.* (2002) to account for the appearance of minute magnetite crystals in some naturally quenched inclusions at temperatures higher than magnetite stability. i.e.

$$2H_2O_{melt} + 6FeO_{melt} \longrightarrow 2H_2 + 2Fe_3O_4 \quad \text{or} \quad H_2O_{melt} + 2FeO_{melt} \longrightarrow H_2 + Fe_2O_{3melt}$$

Thus the possibility of H_2O loss must be taken into account before the volatile content of melt inclusions can be used to make inferences about the amount of volatiles dissolved in the parent magma, and therefore estimates of gas saturation pressures prior to eruption (Wallace, 1998; Schiano, 2003).

4.2.6 Crystallisation

If allowed to cool slowly, melt inclusions have the potential to crystallise. Crystallised melt inclusions are usually described as 'devitrified', though it is not always evident that the crystals grew from a glass rather than a still-molten liquid (in which case, the inclusions are not technically devitrified) (Watson, 1976). Generally, crystallisation begins with precipitation of the host mineral onto the inclusion wall (Fig. 4.2 and 4.10), although some workers have concluded that melt inclusion compositions change little post-entrapment (Beddoe-Stephens *et al.*, 1983; Dunbar and Hervig, 1992; Bacon *et al.*, 1992). However, other studies have found evidence for limited post-entrapment crystallisation of melt inclusions. Sisson and Layne (1993) reported that olivine-hosted melt inclusions from Fuego volcano were affected by post-entrapment crystallisation, representing up to 11% of the inclusion mass. This finding was borne out during the present study of melt inclusions, where more that half the olivine-hosted melt inclusions studied contain crystallised daughter phases (Fig. 4.2 and 4.10). The heterogeneous precipitation of olivine onto the inclusion wall should stop when the trapped melt becomes saturated with respect to the host phase. However, if other crystalline phase begin to form, the entire melt may crystallise (Fig. 4.10).

Skirius *et al.* (1990) suggests that the degree of crystallisation is correlated to cooling rates. From their work on melt inclusions, they found that inclusions from slowly-cooled pyroclasic flows were commonly crystallised whereas those from more rapidly-emplaced Plinian units remained glassy (Fig. 4.11). However, this study shows no correlation between the crystallisation of inclusions and cooling rates. This can be surmised from the fact that glassy and crystalline inclusions coexist in the same olivine crystals (Fig 4.10), which should indicate that they have undergone cooling at the same rate. There is, however, a correlation between the crystallisation of inclusions and the size of the inclusions. Even though there is an overlap in the sizes of glassy and crystallised inclusions, generally glassy inclusions tend to be between 5-15μm, whereas crystallised inclusions tend to be 10-30μm. This could be evidence for cooling rate being the controlling factor in their formation (i.e. larger objects cool slower), but the overall cooling rate should be controlled by the host crystal unless the inclusions and olivine have different thermal properties.

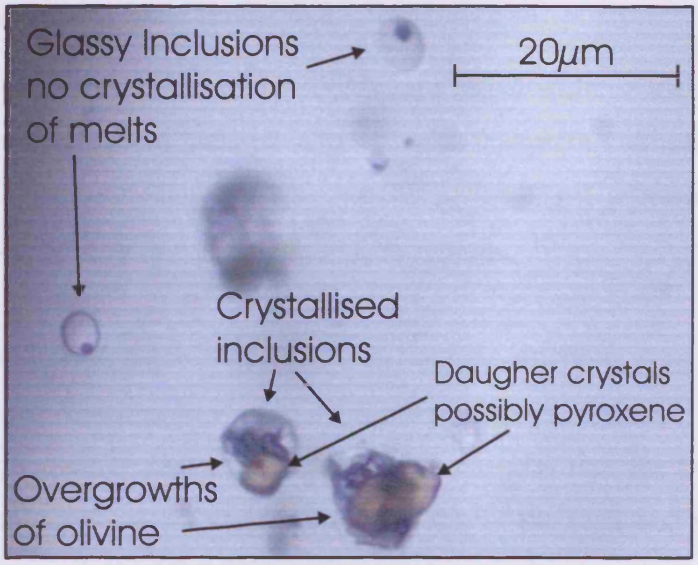

Fig. 4.10. Several inclusions hosted in the same olivine crystal. The two smaller inclusions are glassy, and have not undergoes crystallisation, but they do contain vapour bubbles. The larger inclusions have undergone crystallisation with olivine being precipitated onto the inclusion walls, and large daughter crystals (possibly pyroxene) forming in their centres. Sample from the Mull Plateau Group lavas, sample BM7, Grid Reference [NM 973900], altitude 187 m.

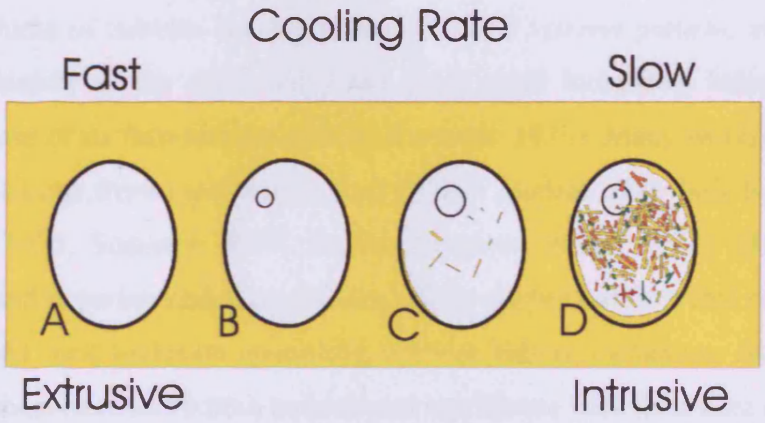

Fig. 4.11. Schematic diagram of four crystal-hosted melt inclusions that undergo different cooling rates. **(A)** During rapid cooling, neither crystals nor bubble form prior to cooling to the glass transition. **(B)** A bubble may nucleate during less rapid cooling. **(C)** Diffusion during slow cooling allows the bubble to grow and the melt to partly crystallise. **(D)** Very slow cooling permits nearly full crystallisation of the inclusion and growth of a layer of host mineral on the melt inclusion wall. Time-scales for bubble nucleation and crystallisation are composition dependant. Low-viscosity basaltic melt inclusions may fully crystallise within minutes, whereas more viscous rhyolitic melt inclusions may not crystallise even if kept at high (but sub-liquidus) temperature for years. Modified from Skirius *et al.* (1990)

4.2.7 Origins of Bubbles in Melt Inclusions

There are at least three reasons why bubbles are found within a melt inclusion: 1) it formed during near constant volume cooling of homogenous silicate melt, 2) it formed during decrepitation/leakage of the melt inclusion, 3) it represents magmatic vapour that was co-trapped with melt in a mixed inclusion.

Shrinkage Bubbles: A bubble can nucleate because isochoric (constant volume) cooling of a trapped homogenous liquid, causing depressurisation and resultant saturation with a low-density phase. Roedder (1984) suggests that the bubbles should be considered a separate phase formed by immiscibility of the melt and vapour. When equilibrium is maintained, the internal pressure of the bubble should equal that of the melt. However, melt-vapour equilibration should cease at temperatures below the glass transition temperature, after which the bubble contents may cool isochorically. This should result in high pressure (high density) fluids in the shrinkage bubble, if the melt was oversaturated with volatile phases, or a low pressure vacuum if the melt was undersaturated with a volatile phase (Fig. 4.12) (Lowenstern, 1995).

The volume of bubbles can range from 0.1 to 5 volume percent, and depends on the cooling history of the melt inclusions, with small inclusions failing to nucleate bubbles because of surface-tension effects (Roedder, 1979). Many workers have shown that melt inclusions from rapidly-quenched Plinian pumice often lack bubbles entirely (Clocchiatti, 1975; Sommer, 1977; Beddoe-Stephens *et al.*, 1983). Both theoretical (Tait, 1992) and experimental (Lowenstern, 1994) studies confirm that rapid cooling is likely to permit melt inclusion quenching without bubble formation. As cooling rates decrease, bubbles have more time to form and equilibrate with their host melts and thus to grow and partially crystallise (Skirius *et al.*, 1990). In intrusions or slow cooling magmas, crystallisation of the melt at near-magmatic temperatures will allow bubble within the melt inclusion to reach as much as 15-30 % of the total inclusion volume (Student and Bodnar, 1996). This volume of bubble is clearly reached in some of the inclusions shown in Fig. 4.12, suggesting that they cooled very slowly after entrapment in their host olivine crystals.

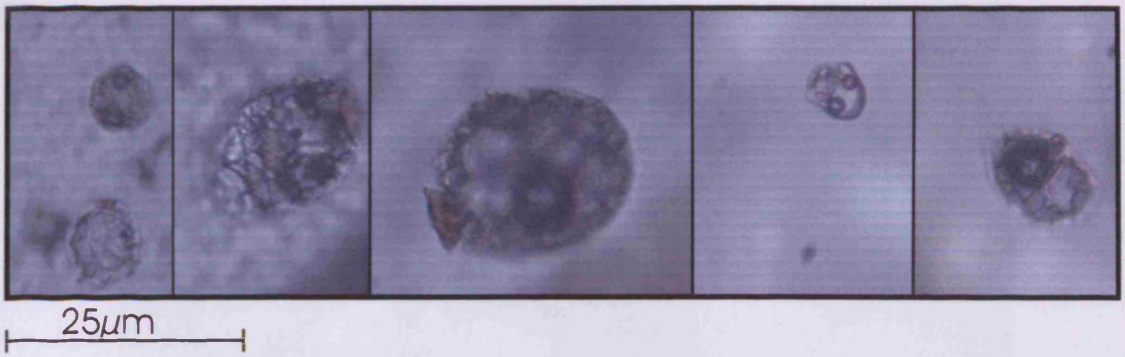

Fig. 4.12. Several images of melt inclusions with shrinkage bubbles. On examination the bubbles do not seem to contain any fluids, thus they probably approximate low pressure vacuums, due to the melts being under saturated with a volatile phase. . Sample from the Mull Plateau Group lavas, sample BM7, Grid Reference [NM 973900], altitude 187 m.

Decrepitation or leakage through capillaries: When the host crystals cool more slowly within a lava or dense pyroclastic flow, the bubbles have time to form, causing the internal pressure of the melt inclusion to rise (Tait, 1992). Often these slowly cooled rocks have cracked crystals containing melt inclusions with numerous large bubbles (Lowenstern, 1995; Best and Christiansen, 1997). An example of this fracturing of a crystal can be seen in Fig. 4.13, which is an olivine phenocryst from the Mull Plateau Group lavas. Several large inclusions have decrepitated, leading to fractures developing in the crystal. Also visible in the image are two coplanar 2-phase fluid inclusions (ringed). Skirius *et al.* (1990) have interpreted such inclusions as forming along fractures created when the inclusion decrepitates, prior to or during eruption. They appear to consist of vapour degassed from the inclusion at high temperature and pressure.

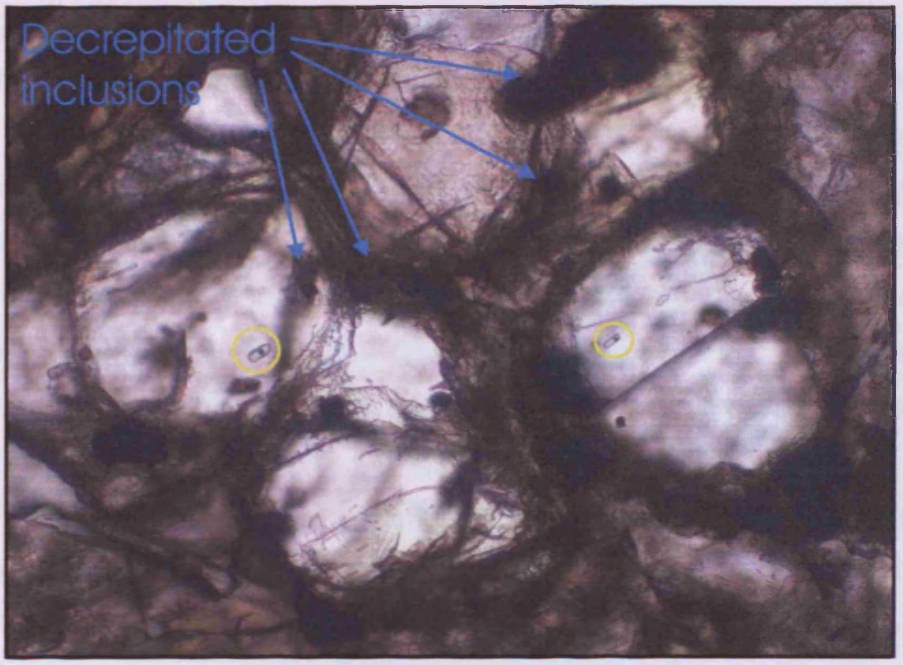

Fig. 4.13. A large olivine phenocryst (~1mm across) that has undergone fracturing due to the decrepitation of melt inclusions (arrowed). Also present are two coplanar, 2-phase fluid inclusions (ringed), which probably formed by the release of volatiles from the decrepitated inclusions, and subsequently trapped in fractures. Sample from the Mull Plateau Group lavas, sample MR10, Grid Reference [NM 340266].

Presence of a separate vapour phase in mixed inclusions: The commonest evidence for the presence of vapours or other non-silicate fluids is their entrapment either as fluid inclusions or as a phase within mixed inclusions (non-silicate fluid + silicate magma) in igneous phenocrysts. These are common in intrusive rocks (Lowenstern *et al.*, 1997; Dietrich *et al.*, 2000; Frezzotti, 2001). Tuttle (1952) noted that, whereas intrusive rocks often contained inclusions, they were rare in volcanic rocks, which instead contained melt inclusions. Anderson (1991) outlines a number of possible reasons why vapour-rich fluid inclusions are rarely present in the crystals of volcanic rocks. He concluded that any melt inclusions with a trapped vapour bubble would create a pressure gradient during magma ascent, preventing the inclusion from sealing. However, Tait (1992) postulated that melt inclusions with co-trapped vapour would be more likely to rupture (decrepitate) during eruption.

Other support for entrapped vapours comes from strange bubbles within melt inclusions that cannot be explained by either shrinkage or leakage. Lowenstern *et al.* (1991) discovered that bubbles within some quartz-hosted melt inclusions in peralkaline rhyolites had anomalous Cu concentrations, and that the Cu was located in Cu sulphides associated with salts precipitated on the bubble walls. The heterogeneous nature of the enrichment and association with large bubbles was consistent with occasional trapping of Cu-rich magmatic vapour. Yang and Scott (1996) found metal-rich bubbles in melt inclusions from submarine basalts of the Manus back-arc basin offshore in the western Pacific. Mineralization in melt inclusion-hosted bubbles included sulphides and chlorides of Cu, Zn and Fe. Kamenetsky *et al.* (2002) analysed small crystals in fluid inclusions, bubbles in melt inclusions and bubbles in matrix glass from a variety of young submarine rocks. They documented high mobility of a variety of metals and anions in low-pressure vapours exsolved from mafic magmas, and interpreted many of the bubbles in melt inclusions as magmatic vapour trapped along with melt in mixed inclusions.

4.3 Methods of Analysis

Since the first analysis (electron microprobe EMP) of melt inclusions (Clocchiatti, 1975), the study of these little droplets of melt has provided important insight into igneous processes. Thus, during the past twenty years scientists have searched for new analytical tools to analyse melt inclusions, with particular emphasis on the trace element concentrations. Examples of such tools are Secondary Ion microprobe Mass Spectrometry (SIMS) and Proton Induced X-ray Emission (PIXE), which have provided a growing number of high quality data in recent years (Webster and Duffield, 1991, 1994; Sobolev and Shimizu, 1993; Dietrich *et al.*, 2000). However, there are a number of limitations to these techniques as they can only be applied to homogeneous melt inclusions exposed to the sample surface (e.g. SIMS, EMP), or to inclusions in chemically-simple host minerals such as quartz (PIXE). Few inclusions (Fig. 4.14) fulfil these requirements a priori and all others need to be homogenised through heating to the trapping temperature.

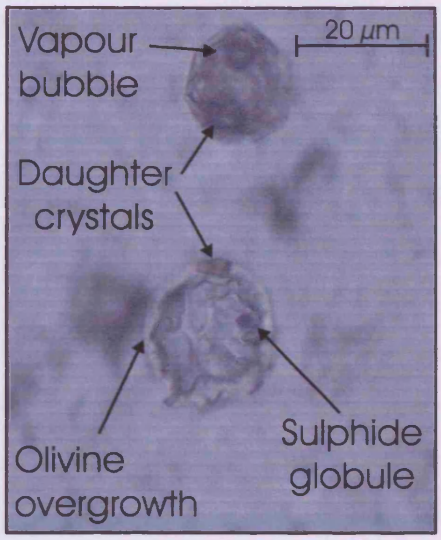

Fig. 4.14. Showing two inclusions within an olivine host crystal. Clearly visible are the heterogeneities within these inclusions, with the top inclusion containing a vapour bubble and daughter crystals, whilst the bottom inclusions contains daughter crystals and sulphide globule. The sample is from the Mull Plateau Group lavas, sample BM7, Grid Reference [NM 973900], Altitude 187m.

4.3.1 Heating Experiments

The experimental study of melt inclusions aims to reverse post-entrapment reactions inside the inclusion during cooling, by reheating and homogenising the contents trapped inside the inclusion. Generally, there are two methods for the reheating of the inclusions, a 1-atm vertical quenching furnace under controlled oxygen fugacity or a microscope heating stage.

In the standard quenching technique, the samples are suspended in Pt capsules in a furnace, heated to a pre-determined temperature and maintained for a defined time at that temperature to ensure equilibrium. A gas mixture usually CO-CO_2 corresponding to the Quartz-Fayalite-Magnetite (QFM) buffer controls oxygen fugacity in the furnace. This type of apparatus has a drop-quenching system, with which samples are dropped from heated area into cold area at the end of each heating run, thus ensuring the samples are quenched at high cooling rates. Once a sample is removed from the furnace, it is examined under a microscope to record changes from the previous lower temperature run. The runs are undertaken at 2-50°C temperature increments until homogenisation is reached (Schiano, 2003). The main disadvantage with this technique is that it does not allow observations of the phase changes taking place within the

inclusions on heating. Thus, it would be very easy not to melt the entire inclusions, or melt some of the host mineral, producing imprecise homogenisation.

With the heating stage technique, the sample is placed in a heating stage attached to a petrological microscope, thus allowing monitoring by direct observation of melting phenomena and temperature during a single run. One of the most commonly used heating stages is that of Sobolev *et al.* (1980) (Fig. 4.15). Even though there are distinct advantages to using a heat stage to homogenise inclusions, there remains many disadvantages. Only very small samples may be placed into the apparatus at any given time, thus limiting the number of inclusions that can be analysed. Even with careful observations, inclusions may not be homogenised correctly (Fig. 4.16) leading to erroneous analyses. In addition, before an inclusion can be analysed it has to be brought to the sample surface. During this process, many inclusions may be lost simply to glean information from one.

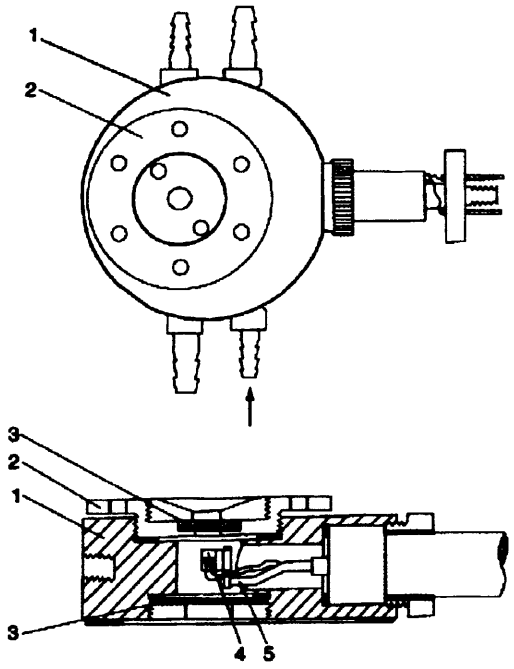

Fig. 4.15. Microscope heating stage designed by Sobolev *et al.* (1980)
1. Gas-tight sealed body cooled by water.
2. Screwed lid.
3. Optical quartz glass window.
4. $Pt_{90}Rh_{10}$ heating element and ring-shaped metallic sample holder with Pt-$Pt_{90}Rh_{10}$ thermocouple.
5. Electrode

After Schiano (2003)

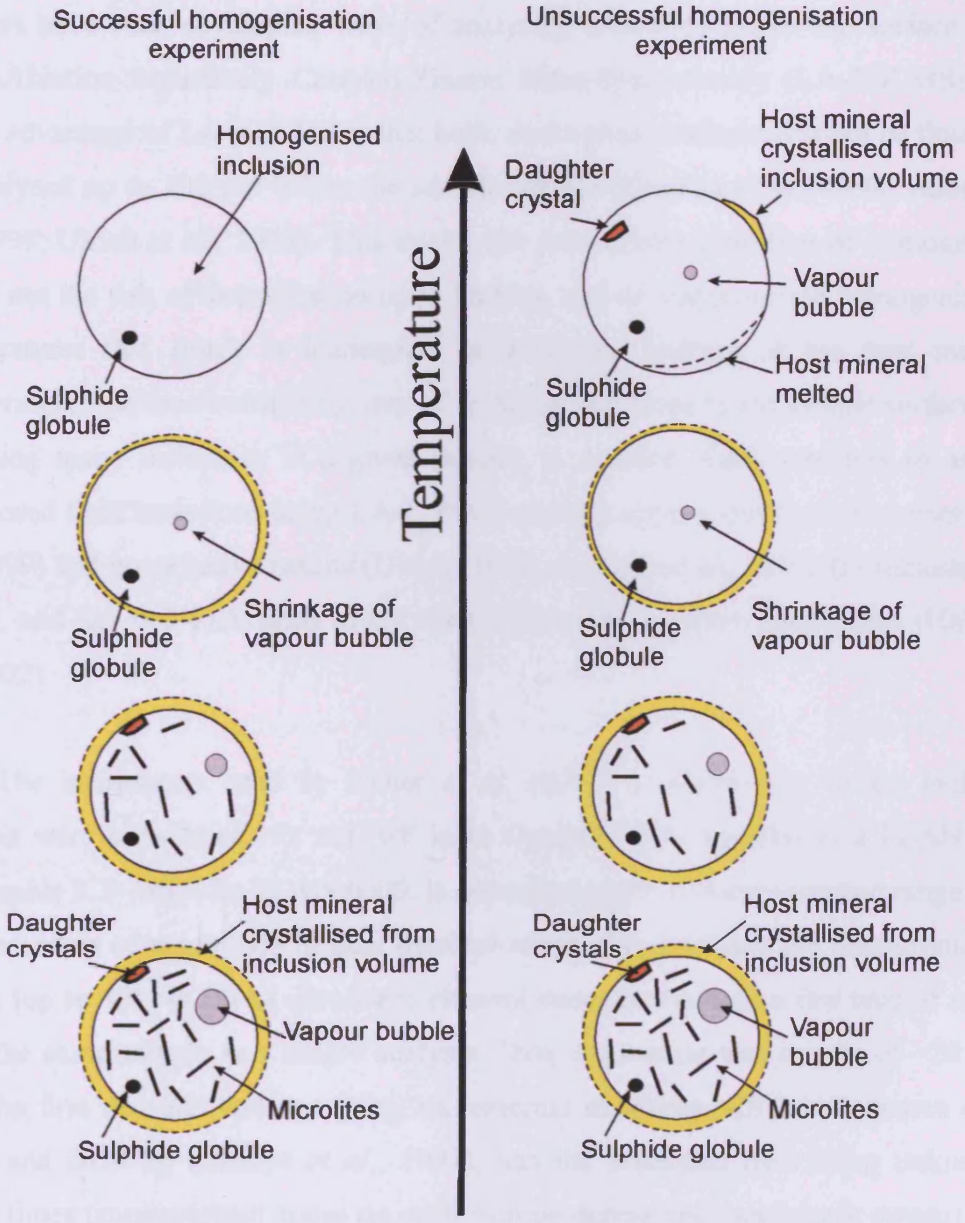

Fig. 4.16. Illustrations showing an ideal and unsuccessful melt inclusion experiments. In the ideal experiment, the inclusion is completely homogenised except for the sulphide globule (which never homogenise). In contrast the unsuccessful experiment, daughter crystals, vapour bubble and sulphide globule remain, and some of the host mineral has be melted and incorporated into the homogenised inclusion

4.3.2 In-situ analysis of inclusions

To overcome the problems associated with the homogenisation of inclusions, workers have been developing ways of analysing inclusions below the surface using Laser-Ablation Inductively Coupled-Plasma Mass-Spectrometry (LA-ICP-MS). The major advantage of LA-ICP-MS is that bulk, multi-phase inclusions (melt of fluid) can be analysed up to 100 μm below the sample surface (Gunther *et al.*, 1998; Audetat *et al.*, 1998; Ulrich *et al.*, 1999). This avoids the prerequisite condition of homogeneity, ruling out the risk of decrepitation upon heating, and of inappropriate homogenisation temperatures that result in inadequate or excessive melting of the host mineral. Furthermore, the time-consuming step of bringing inclusions to the sample surface, and so losing many inclusions in a given sample, is avoided. Early attempts to analyse unexposed fluid inclusions using LA-ICP-MS yielded some qualitative (Kamenetsky *et al.*, 1999) and quantitative results (Ulrich, 1999; Audetat *et al.*, 2000) for inclusions in quartz, and for melt inclusions in the chemically more complex plagioclase (Halter *et al.*, 2002).

The instruments used by Halter *et al.* (2002) in developing in-situ inclusion analysis were a Excimer 193 nm ArF laser Compex 1101, coupled to a ELAN 6000 quadrupole ICP-MS. The ELAN 6000, is characterized by a linear dynamic range of up to nine orders of magnitude in dual detector mode, thus enabling the measurement of matrix (up to 100 wt %) to ultra-trace element concentrations ($\geq$ a few tens of ng g^{-1}) from the same sample in a single analysis. Data acquisition was in sets of ~20 runs, with the first two and last two being the external standards NIST 610 (Pearce *et al.*, 1997) and BCR-2g (Lahaye *et al.*, 1997), and the bracketed runs being unknowns. Dwell times (measurement times on each isotope during one quadrupole sweep) were set to 10 ms, and the settling time between measurements was 3 ms (for full analytical setup see Halter *et al.*, 2002).

Each analysis starts with the monitoring of the gas blank (segment 1 in Fig. 4.18), usually for approximately the same period of time as ablation lasts. Once the laser is turned on, the ablation signal corresponds to pure host mineral until the inclusion is reached (segment 2 in Fig. 4.17 and 4.18). As the inclusion is reached, mixed material from the host and inclusion are analysed simultaneously in unknown, evolving

proportions (segment 3 in Fig. 4.17 and 4.18). After the inclusion has been ablated, the element ratios return to those of pure host mineral (segment 4 in Fig. 4.17 and 4.18). Identification of where ablation of the inclusion starts and finishes can be gleaned from the signals of incompatible and compatible elements (with respect to the host mineral phase). Incompatible elements show a sharp rise in counts per second (CPS), whereas compatible elements show a drop in CPS when the inclusion is reached, and vice-versa when the inclusion is past (Fig 4.18), thus establishing the parameters for the mixed portion (inclusion + host) in the transient signal.

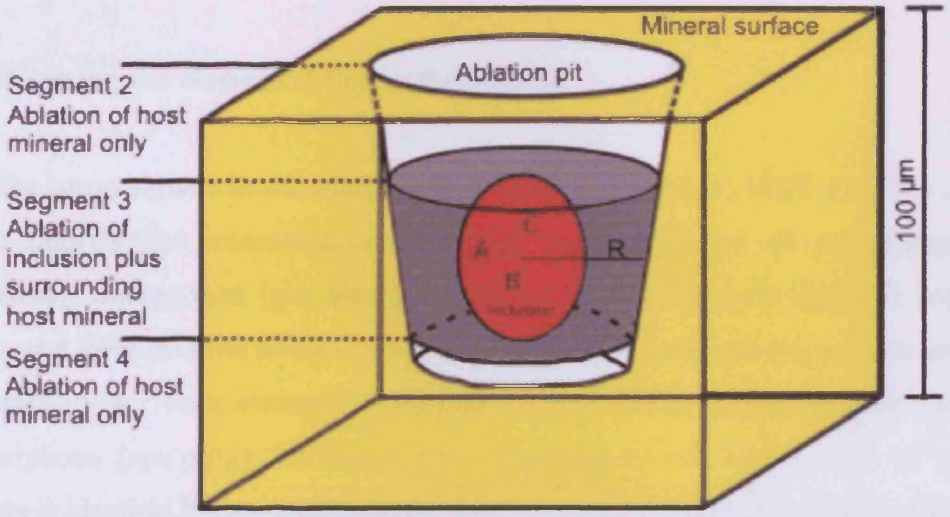

Fig. 4.17. Schematic representation of a melt inclusion and the ablation pit. The inclusion is approximated by an ellipsoid with its three axes A, B and C. The pit is approximated by a cylinder of radius R. Amended from Halter *et al.* (2002).

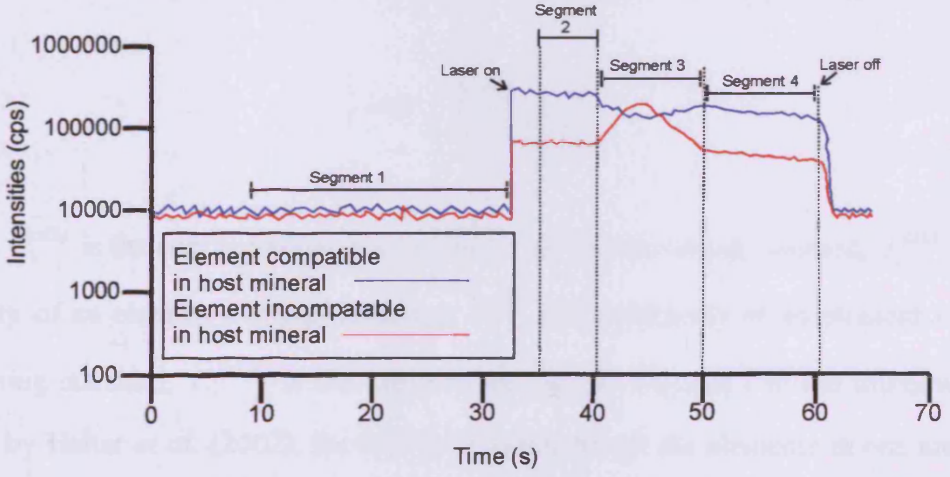

Fig. 4.18. Schematic diagram of a typical transient signal obtained from the ablation of a melt inclusion in a host mineral phase (i.e. olivine, plagioclase). Segment 1 is the gas blank, segment 2 is pure host mineral, segment 3 is host mineral and inclusion ablated together, segment 4 is pure host

4.3.3 Methods of quantification

The methods of quantification developed by Halter *et al.* (2002) for the interpretation of the analytical signal into quantitative element concentrations in the melt inclusion consist of a three-step process. First, analytical signal is converted into element ratios through the use of an external standard, second, the element concentrations are calculated by means of an internal standard, and third, the host contribution to the element concentration in the mixed host-inclusion signal (segment 3 in Fig. 4.17 and 4.18) is subtracted.

4.3.4 Resolving the element ratios in the analysis

The mean signals in the bracketing standards (NIST 614, NIST 612) are used to correct linearly for instrument drift during the acquisition of one sample set (unknowns). Background (gas blank) signals are subtracted form the drift corrected signals, and these and the known concentrations for the standards are used to calculate the sensitivity for each element individually, expressed as counts per unit time and concentrations (cps/µg/g). However, the ratio between the sensitivities of various elements is identical between measurements of the bracketing standards and unknowns, i.e. there are no ablation related changes in the element ratios during the analysis (Halter *et al.*, 2002). In this way, the determination of element concentrations in the unknown can be acquired as a function of the relative sensitivity factor RSF.

$$C_i^{SAMP} = \frac{C_i^{STD} \cdot I_i^{SAMP}}{I_i^{STD} \cdot RSF} \tag{1a}$$

Where C_i^{STD} is the concentration of an element *i* in the bracketing standard, I_i^{SAMP} is the intensity of an element *i* in the unknown, I_i^{STD} is the intensity of an element *i* in the bracketing standard, C_i^{SAMP} is the concentration of an element *i* in the unknown. As shown by Halter *et al.* (2002), the RSF is identical for all the elements in one analysis. Therefore, the ratios between element concentrations in the sample are uniquely determined even if the RFS is unknown.

4.3.5 Quantification of element concentrations

The identification of an element that can be analysed independently in the unknown sample (C_{is}^{SAMP}) must first be found. The known concentration of this element can then be used as an internal standard, and establish the RSF for each analysis by rearranging Eq (1a)

$$RSF = \frac{C_{is}^{STD} \cdot I_{is}^{SAMP}}{I_{is}^{STD} \cdot C_{is}^{SAMP}} \quad (1b)$$

The concentration of all other elements is then obtained by Eq 1a.

In the mixed signal (segment 3 in Fig. 4.17 and 4.18), the concentrations of all elements changes with the host/melt ratio, so no internal standard can be applied directly. To overcome this problem, Halter *et al.* (2002) assumed that the sum of the concentration of all the element oxides is 100% (less if undetectable elements are present i.e. Hydrogen), in order to calculate the concentrations in the host and mixed (host + inclusion) signals.

4.3.6 Concentrations of Elements in Melt Inclusions

Quantification of element concentrations in the melt inclusions requires that the relative contributions of inclusion and host to the mixed signal (segment 3 in Figs 4.17 and 4.18) is known. Halter *et al.* (2002) represent these contributions by a mass ratio, x, defined as the ratio of the mass of the inclusion over the total mass ablated during the time segment 3. Once determined, x relates element concentrations in the host, the mixed signal and the inclusion as represented graphically in Fig. 4.19. Thus, from this Figure, x can be defined from the following equation (2a), where m refers to the masses of the inclusion and the total ablated mixture, and C_i^{HOST}, C_i^{MIX} and C_i^{INCL} are the concentrations of an element I in the host, in the mixture of host plus inclusion, and inclusion respectively.

$$x = \frac{m^{INCL}}{m^{MIX}} = \frac{C_i^{HOST} - C_i^{MIX}}{C_i^{HOST} - C_i^{INCL}} \quad (2a)$$

Once x is uniquely determined, the concentrations of all other elements, including elements in the host mineral, can be determined by rearranging Eq (2a) into (Eq2b).

$$C_i^{INCL} = C_i^{HOST} - \frac{(C_i^{HOST} - C_i^{MIX})}{x} \quad (2b)$$

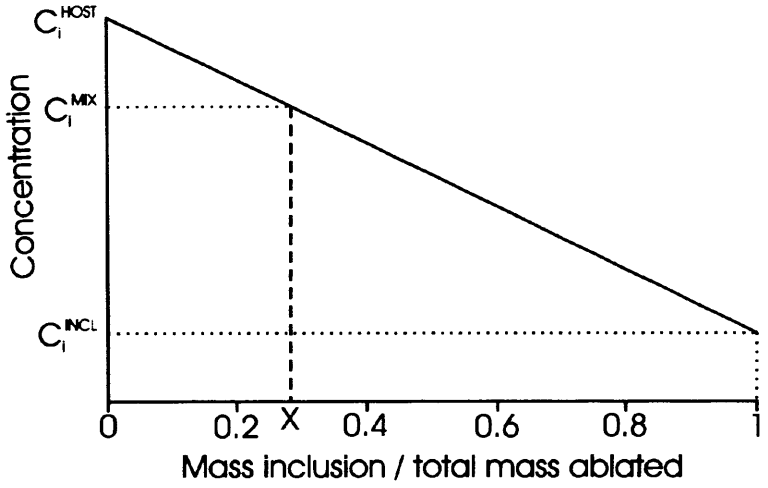

Fig. 4.19. Plot of the concentration C of an element *I* as a function of the mass ratio x between the inclusion and the total ablated material in the mixed signal section. C_i^{HOST}, C_i^{MIX} and C_i^{INCL} are the concentrations of an element *I* in the host(analysed), in the mixed signal of the host and signal (analyed), and the inclusion (extrapolated), respectively. Amended from Halter *et al.* (2002).

4.3.7 Determination of the Mass Factor x

Halter *et al.* (2002), outlines four ways of determining the mass factor x. These are based on: 1) a constant internal standard for the melt inclusion, 2) whole rock differentiation trends, 3) a constant distribution coefficient of an element between the host and the melt, 4) volume measurements of the inclusion and the ablated pit. The different methods each have advantages and disadvantages, and any method may be more advantageous than the others, depending on the compositions of the host phase and melt inclusion. The most attractive methods for the analysis of olivine hosted melt inclusions (this study) are *constant internal standard for the melt inclusions* and *constant distribution coefficient of an element between mineral and melt.*

Constant internal standard for the melt inclusion: Some elemental concentrations differ little during igneous differentiation and can, to a first approximation, be taken as constant in a set of coeval melt inclusions. Therefore, it is sufficient to estimate (from whole rock analysis) or to determine the absolute concentration of such an element in one or several inclusions, and take this value (or averaged value) as the internal standard for the quantification of all coexisting inclusions.

The problems with this approach are two-fold. First, the possible variability of the element that serves as the internal standard. This would yield incorrect values for x, and thus for the concentrations of all other elements. Second, x is best determined with highly compatible or highly incompatible elements (i.e. elements with concentrations much higher or much lower in the melt as compared to the host crystal). This is shown graphically in Fig. 4.20, where highly incompatible or highly compatible elements have a small uncertainty on x. However, these elements could not be used in this method because their concentrations would increase or decrease considerably in the melt as fractionation proceeds. For an element to be used as an internal standard in a set of coeval melt inclusions, it would have to be weakly compatible or weakly incompatible, but this would lead to large uncertainties to the value of x.

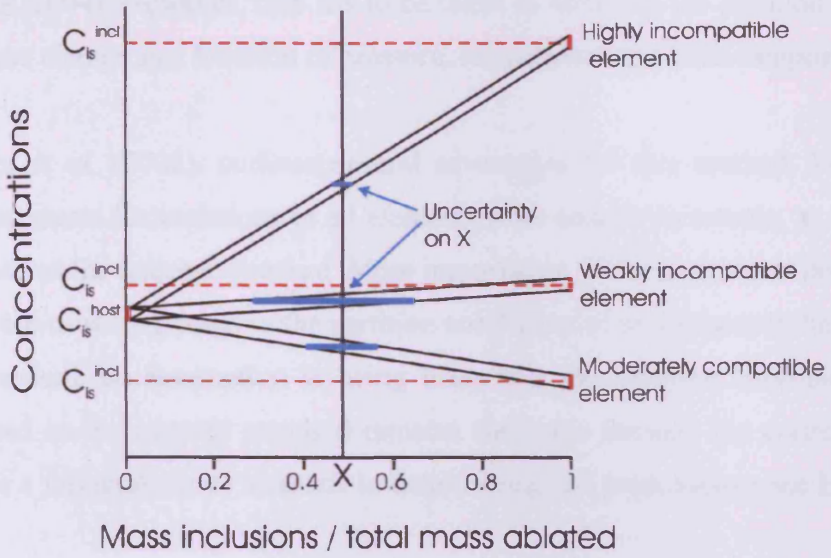

Fig. 4.20. Plot of concentrations versus x, showing the importance of using highly incompatible (or compatible) elements to determine the mass ratio x. Given the same uncertainty on the analysis, the uncertainty on x is much larger if the difference in concentrations of an element between host and inclusion is small. Indicated on the ordinate are the concentrations of a reference element (internal standard) in the inclusion C_{is}^{INCL} and the host C_{is}^{HOST}. Amended after Halter *et al.* (2002).

Constant distribution coefficient of an element between mineral and melt: Whereas absolute concentrations of all elements very to lesser or greater degrees during magmatic evolution, distribution coefficients of trace elements between a mineral and the melt are either constant over a much wider compositional range, or can be reliably predicted. The distribution coefficient D_i is defined by the relationship

$$C_i^{MIN} = Di \times C_i^{MELT} \qquad (3)$$

Where C_i^{MIN} and C_i^{MELT} are the concentrations of an element i in the mineral and melt respectively. Therefore, if the concentration of an element in the immediate host of an inclusion, and the partition coefficient of that element (for the host phase) are known, the concentration of that element in the melt (inclusion) can be calculated. This value can then be used in equation 2b to calculate the mass factor x. The distribution coefficient can be determined by the analysis of a few homogenised inclusions, or be taken from the large dataset reported in the literature (e.g. McDade *et al.*, 2003; Salters

and Stracke, 2004). However, care has to be taken in selecting the partition coefficient used as it can change as a function of pressure, temperature and bulk composition.

Halter *et al.* (2002), outlines several advantages for this method. Including, it explicitly accounts for variations in all elements from sample to sample, as well as the element used as the internal standard. More importantly, if the analysis of homogenised inclusions are used to determine the partition coefficient of an element to be used as an internal standard, an assumption is being made that the partition coefficient for the element used as the internal standard remains the same through the entire magmatic system. For a full analysis of methods in determining, the mass factors see Halter *et al.* (2002).

4.3.8 Accuracy of Melt Inclusion Analysis by LA-ICP-MS

Pettke *et al.* (2004) has undertaken a thorough examination of the accuracy of the mathematical deconvolution procedure of analytical data obtained by LA-ICP-MS for melt inclusions included in chemically complex host minerals. The accuracy tests are based on a comparison of methods between LA-ICP-MS, SIMS and EMP, when applied to three different types of melt inclusions, namely, 1) natural glassy untreated, 2) natural crystallised untreated and 3) natural crystallised but reheated to a homogenous glass.

From this work, Pettke *et al.* (2004) suggests that the precisions for average element concentrations of melt inclusion assemblages (individual melt inclusions trapped coevally along a petrographically defined growth zone of the host mineral) are comparable between the three analytical methods. However, Pettke *et al.* (2004) does point out that LA-ICP-MS is inferior to EMP and SIMS in its spatial resolution, in the limits of detection (LOD) for some trace elements in melt inclusions less than 10 μm in diameter, and the fact that it cannot yet analyse H_2O, F, S and Cl reliably. Thus, Pettke *et al.* (2004) suggests that the analysis of entire melt inclusions drilled out of the sample/s by LA-ICP-MS enables the accurate quantification of melt inclusion chemistry for samples that cannot be homogenised in the lab. The main reasons that prevent the homogenisation of inclusions are: 1) The loss of volatile species (i.e. H_2O, CO_2) during the evolution of the sample, thus preventing the inclusions reaching their homogenisation temperatures. 2) Inclusions that are hosted in mineral phases with

strong cleavage (i.e. plagioclase) are prone to decrepitation during homogenisation experiments. 3) Inclusions that contain sulphides cannot be homogenised, as the temperatures needed to melt sulphides, would also melt the host mineral phase. Any of these factors would lead to the inclusions remaining heterogeneous, and any sampling of the inclusions would be inaccurate.

The most important limitation of this approach is the requirement of an independently known internal standard for the quantification of melt inclusion measurements by LA-ICP-MS. The choice of an internal standard element is delicate and currently sufferers most from the limited knowledge of the existence and extent of post-entrapment diffusional re-equilibration of potential internal standard elements between host and melt inclusion (Pettke *et al.*, 2004). Therefore, analysts have to choose between the problems (Section 4.3.1) innate to the thermal homogenisation procedures required for melt inclusion analysis by EMP and SIMS, or the uncertainties associated with internal standardisation (Section 4.3.7) required for the quantification of LA-ICP-MS data.

4.4 Summery

Melt inclusions

- Primary melt inclusions hosted within olivine crystals are generally less than 40 μm in diameter. The inclusions are randomly included within the crystals, and often contain vapour bubbles and daughter crystals. The inclusions are round to oval in shape.
- Secondary melt inclusions are generally found in fracture zones within the crystals. However, some secondary melt inclusions form strings, indicating that the fractures have annealed since the injection of magma into these fractures.
- All melt inclusions over 40 μm in diameter have decrepitated, indicating a rapid decrease in pressure, probably due to a fast rise to the surface.

Methods of analysis

- There are two methods of analysis of melt inclusions: 1) homogenisation of inclusions, which are then brought to the surface for analysis; 2) in-situ analysis of inclusions along with a quantity of the host mineral phase, and the subsequent deconvolution of the inclusion signal from the mixed (inclusion + host) signal.
- Both methods of analysis have advantages and disadvantages, but nether has clear advantages over the other.
- Heating experiments can suffer from incomplete homogenisation, due to changes to the internal pressure of the inclusions, or due to the presence of sulphides in the inclusions that can never be homogenised. The main advantage of this method is that the inclusions are brought to the surface, where they can be sampled directly.
- In-situ analysis of inclusions by LA-ICP-MS, samples the inclusions as a proportion of a mixed signal (host + inclusion). Its main drawback is that an independent internal standard for the inclusions is needed for the quantification of the melt inclusions. The main advantage of this approach, is that many inclusion, even in the same crystal can be sampled, without prior homogenisation.

Chapter 5
Melt Inclusion Analysis by LA-ICP-MS

5.1 Introduction

During the summer of 2002, Cardiff University acquired a 213 nm (ultra violet) laser, supplied by New Wave Industries, which is coupled to an X-series mass spectrometer supplied by Thermo Elemental. As Cardiff University does not have the equipment to run heating experiments on melt inclusions, it was decided that all analysis on inclusions would follow the methodologies developed by Halter *el al.* (2002), but with further developments, where necessary, to augment these processes.

5.2 Instrument Parameters

Fig. 5.1 provides a compilation of instrument and data acquisition parameters. A pulsed 213 nm Nd-YAG laser with homogenised beam profile was used. This system is characterised by a laterally homogeneous energy distribution, allowing depth-controlled ablation of material at a rate of 0.1-0.2 μm per shot, depending on laser energy and matrix chemistry. A constant energy density over the entire pit area is a prerequisite for controlled ablation over variable pit sizes during crater drilling. The resulting ablation craters were nearly cylindrical and could be varied in diameter between 5 and 100 μm (Fig. 5.2). Samples to be analysed, are loaded into the ablation cell along with external reference materials, and placed within a sealed unit below the laser. The equipment is also coupled to a video monitoring system, thus enabling visual inspection of the ablation progress on a computer screen, which is essential for controlled sample ablation. Laser ablation aerosols are carried to the ICP-MS by Ar or He carrier gas. A quadrupole mass spectrometer is used for the analyses, the X-series ICP-MS characterised by a linear dynamic range of up to nine orders of magnitude in dual detector mode. This enables the measurement of matrix (up to 100 wt %) to ultra-trace element concentrations ($< \mu g\ g^{-1}$) from the same sample in a single analysis.

New Wave 197 nm laser system

Output energy	Adjusted to between 180 and 240 mJ at 213 nm
Pulse duration	15 ns
Repetition rate	20 Hz
Pit size	Adjustable between 5 and 100 µm
Ablation cell	Plexiglas with anti-reflection coated silica glass window
Cell Ar or He gas flow	Optimised between 0.5 and 1.1 l min^{-1}

Quadrupole ICP-MS

Nebuliser gas flow	Optimised to between 0.6 and 0.7 l min^{-1}
Auxiliary gas flow	Optimised to between 0.65 and 0.75 l min^{-1}
Cool gas flow	Optimised to between 12.5 and 13.5 l min^{-1}
rf Power	1250 W
Detector mode	Duel, up to nine orders of magnitude linear dynamic range
Quadrupole settling time	3 ms
Detector housing vacuum	Between 1.5 and 2.8 x 10^{-5} Torr during analysis

Data acquisition parameters

Sweeps per reading	1
Readings per replicate	200-1000 as a function of number of isotopes
Replicates	1
Dwell time per isotope	Adjusted to between 10 ms (standard) and 30 ms (to lower LOD)
Isotopes	^{23}Na, ^{24}Mg, ^{27}Al, ^{29}Si, ^{31}P, ^{39}K, ^{44}Ca, ^{47}Ti, ^{52}Cr, ^{56}Mn, ^{56}Fe, ^{59}Co, ^{60}Ni, ^{65}Cu, ^{66}Zn, ^{85}Rb, ^{88}Sr, ^{89}Y, ^{90}Zr, ^{93}Nb, ^{137}Ba, ^{139}La, ^{140}Ce, ^{146}Nd, ^{147}Sm, ^{153}Eu, ^{157}Gd, ^{159}Tb, ^{172}Yb, ^{208}Pb, ^{232}Th, ^{238}U

Fig. 5.1. Table of LA-ICP-MS machine and data acquisition parameters

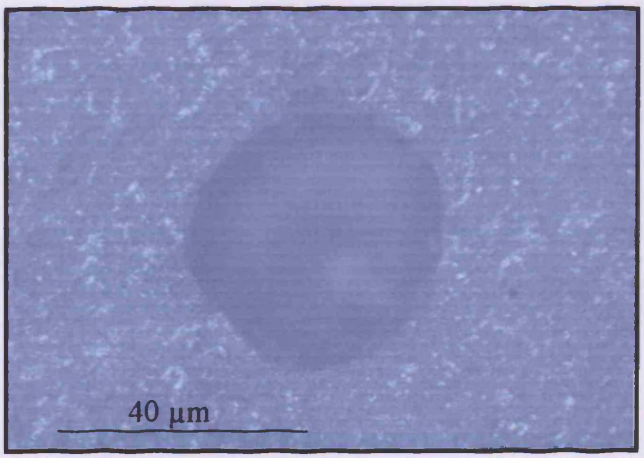

Fig. 5.2. Visible light image of the pit ablated into the NIST 610 reference glass. All sputter surrounding the ablation pit has been removed, thus revealing the geometry of the pit, which is not perfectly circular, but still has a reasonable profile.

5.3 External Standards

Halter *et al.* (2002) used the certified glass standards SRM 610 from NIST (hereafter NIST 610; Pearce *et al.*, 1997) and BCR-2g from the United States Geological Survey (USGS) (Lahaye *et al.*, 1997) as external standards. However, the chemical composition of the NIST reference glasses do not make them suitable as external standards for the analysis of olivine-hosted melt inclusions found in the MPG lavas. Fig. 5.3 is a Table of the ICP-OES (Appendix 2, MPG basalts, major element data) data for 12 MPG lavas (BHI samples) and NIST reference materials. It is clear that there are considerable differences in the chemical compositions of the MPG basalts and NIST glasses. The greatest differences are for Fe_2O_3 and MgO, which have concentrations in the MPG basalts that are two orders of magnitude greater than for the NIST glasses, whereas Al_2O_3 and TiO_2 are approximately one order of magnitude greater. In contrast, the SiO_2 concentrations in the NIST glasses are double that in the MPG basalts (Fig. 5.4). In an attempt to overcome the problem of vastly different concentrations between NIST glasses and MPG basalts, a number of artificial glass rock standards have been acquired from the USGS.

	SiO_2	TiO_2	Al_2O_3	Fe_2O_3	MnO	MgO	CaO	Na_2O	K_2O	P_2O_5
BHI2	43.09	2.09	14.05	14.24	0.19	11.53	8.85	2.27	0.28	0.19
BHI3	43.64	2.02	14.40	13.28	0.18	10.64	8.31	2.64	0.50	0.20
BHI17	43.91	1.71	15.11	13.09	0.17	11.01	9.59	2.62	0.23	0.20
BHI18	43.34	1.65	14.81	12.76	0.17	10.39	9.39	2.81	0.23	0.17
BHI19	45.73	1.14	13.51	11.05	0.17	11.76	10.25	2.09	0.30	0.12
BHI20	44.96	1.22	14.14	11.69	0.17	11.87	10.11	2.07	0.19	0.13
BHI26	45.93	1.36	14.73	11.70	0.18	9.77	10.90	2.29	0.25	0.15
BHI27	45.05	1.43	15.49	12.07	0.19	9.35	9.80	2.28	0.37	0.15
BHI28A	47.74	1.42	13.09	15.32	0.25	7.08	11.60	2.35	0.12	0.12
BHI28B	46.74	1.41	14.93	12.11	0.17	8.34	11.16	2.53	0.29	0.14
BHI30	44.81	1.25	13.43	12.46	0.18	13.28	10.03	1.83	0.23	0.14
NIST 610	72.71	0.10	2.08	0.09	0.06	0.11	12.00	12.74	0.01	0.10
NIST 612	72.75	0.02	2.12	0.03	0.01	0.03	12.23	12.82	<LOD	0.01
NIST 614	72.85	0.01	2.13	0.03	0.00	0.03	12.19	12.78	<LOD	0.00

Fig. 5.3. Table showing the major oxide compositions (values in wt %) for MPG lavas (BHI samples) and the NIST (610, 612, 614) reference glasses.

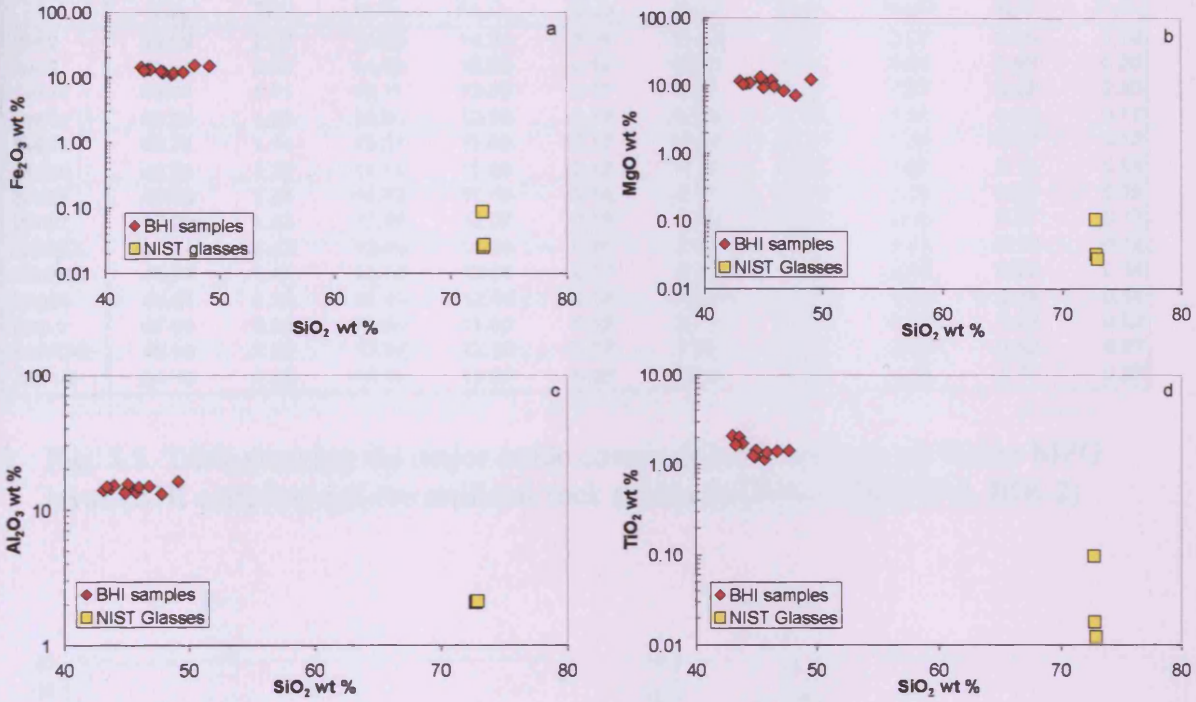

Fig. 5.4a-d. Plots showing differences in major oxide concentrations between selected MPG basalts (BHI samples) and NIST (610, 612, 614) reference glasses. The BHI samples have Fe_2O_3 and MgO concentrations two orders of magnitude greater than the NIST glasses, and approximately one order of magnitude greater for Al_2O_3 and TiO_2. In contrast, the SiO_2 concentrations in the NIST glasses are approximately double, what they are in the BHI samples.

5.3.1 USGS glass rock standards (major oxides)

Three artificial rock standards (BIR-1, BHVO-2, BCR-2) have been acquired from the USGS. These standards have concentrations closer to those of the MPG basalts than the NIST glasses. The major oxide concentrations for selected MPG basalts (BHI samples) and the rock reference materials BIR-1, BHVO-2 and BCR-2 are shown in Figs 5.5 and 5.6. For all the major oxides, there is overlap between the MPG basalts and rock standards. This makes them more acceptable as standards for the analysis of olivine hosted melt inclusions, where the inclusions have similar compositions to the host basalts.

	SiO_2	TiO_2	Al_2O_3	Fe_2O_3	MnO	MgO	CaO	Na_2O	K_2O	P_2O_5
BHI2	43.09	2.09	14.05	14.24	0.19	11.53	8.85	2.27	0.28	0.19
BHI3	43.64	2.02	14.40	13.28	0.18	10.64	8.31	2.64	0.50	0.20
BHI17	43.91	1.71	15.11	13.09	0.17	11.01	9.59	2.62	0.23	0.20
BHI18	43.34	1.65	14.81	12.76	0.17	10.39	9.39	2.81	0.23	0.17
BHI19	45.73	1.14	13.51	11.05	0.17	11.76	10.25	2.09	0.30	0.12
BHI20	44.96	1.22	14.14	11.69	0.17	11.87	10.11	2.07	0.19	0.13
BHI26	45.93	1.36	14.73	11.70	0.18	9.77	10.90	2.29	0.25	0.15
BHI27	45.05	1.43	15.49	12.07	0.19	9.35	9.80	2.28	0.37	0.15
BHI28A	47.74	1.42	13.09	15.32	0.25	7.08	11.60	2.35	0.12	0.12
BHI28B	46.74	1.41	14.93	12.11	0.17	8.34	11.16	2.53	0.29	0.14
BHI30	44.81	1.25	13.43	12.46	0.18	13.28	10.03	1.83	0.23	0.14
BIR-1	47.96	0.96	15.50	11.30	0.18	9.70	13.30	1.82	0.03	0.02
BHVO-2	49.90	2.73	13.50	12.30	0.17	7.23	11.40	2.22	0.52	0.27
BCR-2	54.10	2.26	13.50	13.80	0.20	3.59	7.12	3.16	1.79	0.35

Fig. 5.5. Table showing the major oxide compositions (values in wt %) for MPG lavas (BHI samples) and the artificial rock standards (BIR-1, BHVO-2, BIR-2)

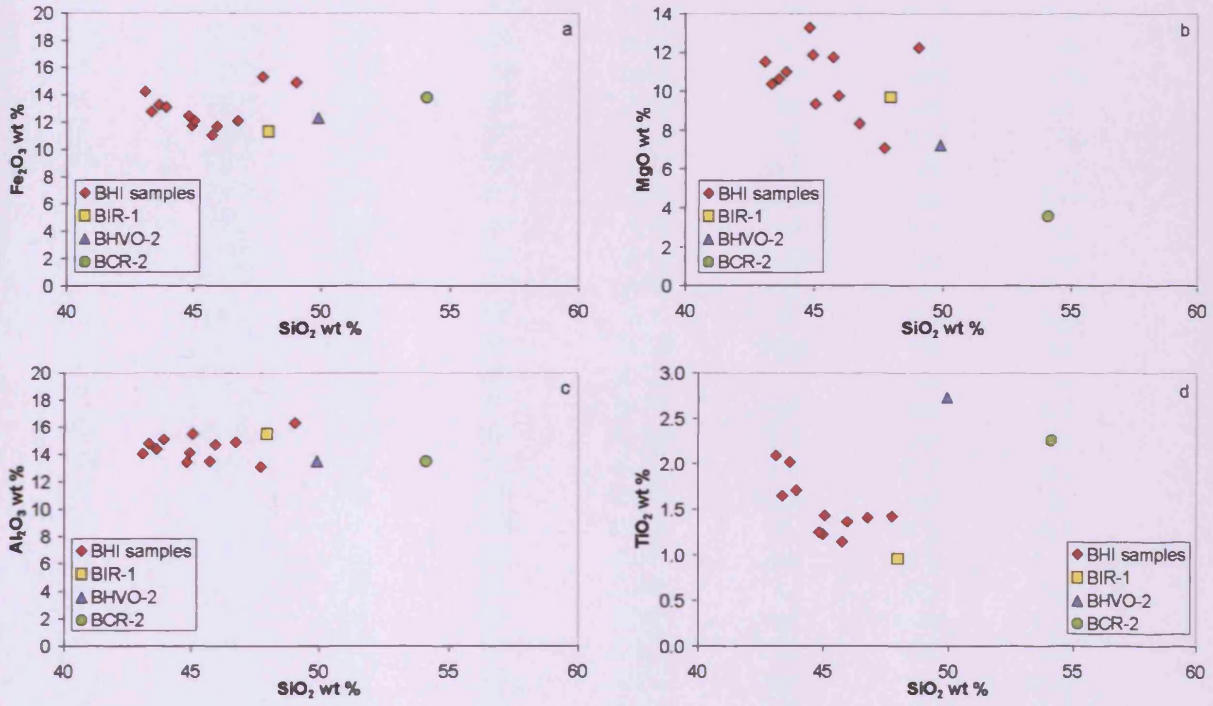

Fig. 5.6a-d. Plots showing the differences in major oxide concentrations between selected MPG basalts (BHI samples) and rock standards (BIR-1, BHVO-2, BIR-2) reference glasses. For all major oxides, there is considerable overlap between the MPG basalts and rock standards. This indicates that the rock standards are preferable to the NIST glasses as standards for the analysis of olivine-hosted melt inclusions located in the MPG basalts.

5.3.2 USGS glass rock standards (trace elements)

Even though the major element concentrations make the rock standards more compatible than the NIST glasses as external standards for the analysis of olivine-hosted inclusions. The same cannot be said for their trace element concentrations. This is because the NIST glasses were produced primarily as standards for trace elements, and as such have a wider range of concentrations than the rock standards (Fig. 5.7). This makes them superior to the BIR-1, BHVO-2 and BCR-2, as external standard for the analysis of trace element concentrations.

		NIST 610	NIST 612	NIST 614	BIR-1	BHVO-2	BCR-2
SiO_2	%	72.71	72.75	72.85	47.96	49.90	54.10
Al_2O_3	%	2.08	2.12	2.13	15.50	13.50	13.50
CaO	%	12.00	12.23	12.19	13.30	11.40	7.12
MgO	%	0.11	0.03	0.03	9.70	7.23	3.59
Na_2O	%	12.74	12.82	12.78	1.82	2.22	3.16
K_2O	%	0.01	0.02	0.02	0.03	0.52	1.79
MnO	%	0.06	0.01	0.00	0.18	0.17	0.20
P_2O_5	%	0.10	0.01	0.00	0.02	0.27	0.35
TiO_2	%	0.10	0.02	0.01	0.96	2.73	2.26
Fe_2O_3	%	0.09	0.03	0.03	11.30	12.30	13.80
Li	ppm	484	41	1.7	3.6	5	9
Sc	ppm	442	40	2.2	44	32	33
V	ppm	442	38.3	1.09	310	317	416
Cr	ppm	404	39	3.3	370	280	18
Co	ppm	405	35	0.71	52	45	37
Ni	ppm	445	38	0.9	170	119	na
Cu	ppm	430	37	1.3	125	127	19
Zn	ppm	455	38	1.9	70	103	127
Ga	ppm	437	37	1.12	16	21.7	23
Rb	ppm	431	32	0.87	nd	9.8	48
Sr	ppm	497	75	44.3	110	389	346
Y	ppm	450	38	0.77	16	26	37
Zr	ppm	439	37	0.8	18	172	188
Nb	ppm	420	36	0.78	0.6	18	nd
Mo	ppm	378	35	0.7	nd	nd	248
Sn	ppm	400	40	1.4	nd	1.9	nd
Sb	ppm	377	34	0.73	0.58	nd	nd
Cs	ppm	360	41	0.68	nd	nd	1.1
Ba	ppm	425	37	3.1	6	130	683
La	ppm	457	37	0.72	0.63	15	25
Ce	ppm	448	38	0.79	2	38	53
Pr	ppm	430	37	0.75	nd	nd	6.8
Nd	ppm	430	35	0.74	2.5	25	28
Sm	ppm	449	37	0.77	1.1	6.2	6.7
Eu	ppm	460	35	0.75	0.55	nd	2
Gd	ppm	420	36	0.75	2	6.3	6.8
Tb	ppm	442	36	0.74	nd	0.9	1.07
Dy	ppm	426	36	0.74	4	nd	nd
Ho	ppm	448	38	0.76	nd	1.04	1.33
Er	ppm	426	37	0.73	nd	nd	nd
Tm	ppm	420	37	0.72	nd	nd	0.54
Yb	ppm	460	40	0.81	1.7	2	3.5
Lu	ppm	435	37	0.72	3.6	0.28	0.51
Hf	ppm	418	35	0.67	0.6	4.1	4.8
Ta	ppm	376	36	0.77	nd	1.4	nd
Pb	ppm	413	38	2.4	3	nd	11
Th	ppm	451	37	0.74	nd	1.2	6.2
U	ppm	457	37	0.83	nd	nd	1.69

Fig. 5.7. Major and trace element concentrations for the NIST glasses and rock standards. NIST glasses – Geo *et al.* (2002), BIR-1 – Govindaraju, (1994), BHVO-2 – Wilson, (1997a), BCR-2 – Wilson, (1997b). (nd – no data).

5.3.3 Using NIST (610, 612, 614) glasses and rock standards (BIR-1, BHVO-2, BCR-2) in calibration curves

There is the potential to use both NIST glasses (610, 612, 614) and rock standards (BIR-1, BHVO-2, BCR-2) as external standards for analyses carried out by LA-ICP-MS. However, for this to work, the different standards would have to behave similarly under the same LA-ICP-MS operating parameters. Fig. 5.8a-b. shows the calibration curves produced for the isotopes ^{88}Sr and ^{66}Zn under controlled and unchanging LA-ICP-MS conditions. It is clear that the NIST glasses and rock standards produce different calibration curves, suggesting that they behave differently under set operating parameters. These differing calibration curves probably reflect the different chemical makeup of the standards, particularly their concentrations of SiO_2, Fe_2O_3, MgO and Al_2O_3 (Figs. 5.4 and 5.6).

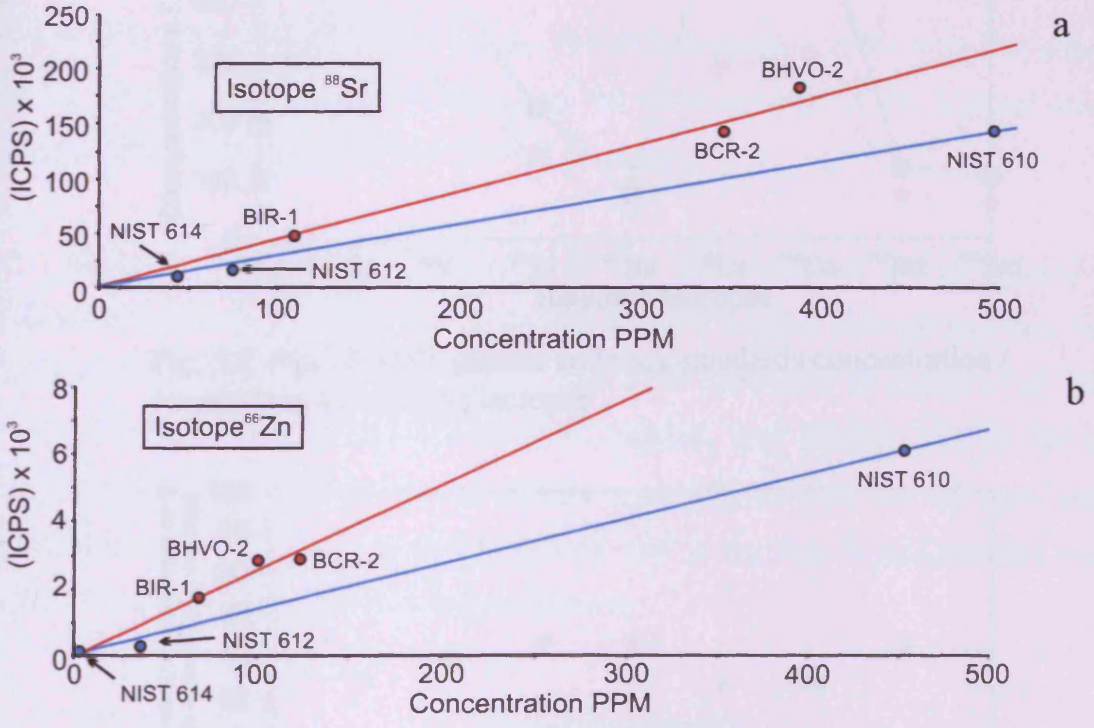

Fig. 5.8a-b. Calibration curves for the isotopes ^{88}Sr and ^{66}Zn for the NIST glasses (610, 612, 614) and rock standards (BIR-1, BHVO-2, BCR-2). It can be seen that different standards define different calibration curves, reflecting their different chemistry and behaviour under controlled LA-ICP-MS conditions.

In Fig. 5.9, the (concentration/ICP counts s) ratios are plotted for selected elements. The rock standards consistently plot higher than the NIST glasses, suggesting that there is more ablated aerosol reaching the ICP-MS for the rock standards. Fig 5.10, shows the NIST glasses (concentrations/counts s) ratios plotted as a percentage of the rock standards (concentrations/counts s) ratios. From this, it is obvious that the amount of ablated NIST aerosols reaching the ICP-MS lies between ~50-60 % of the rock standard values. The most likely cause for this difference in concentration count ratios is the ablation rates of the different materials, i.e. the rock standards are ablating ~ 45 ± 5 % faster than the NIST glasses.

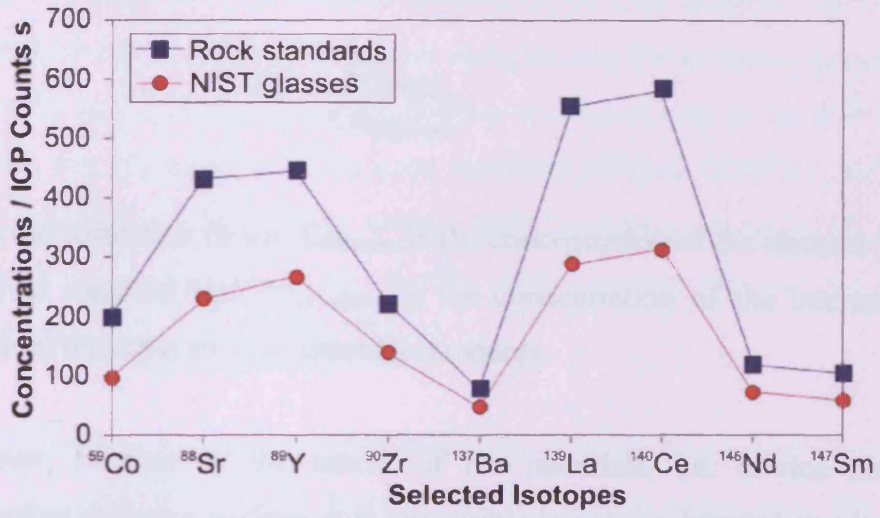

Fig. 5.9. Plot of NIST glasses and rock standards concentration / count ratios for selected isotopes

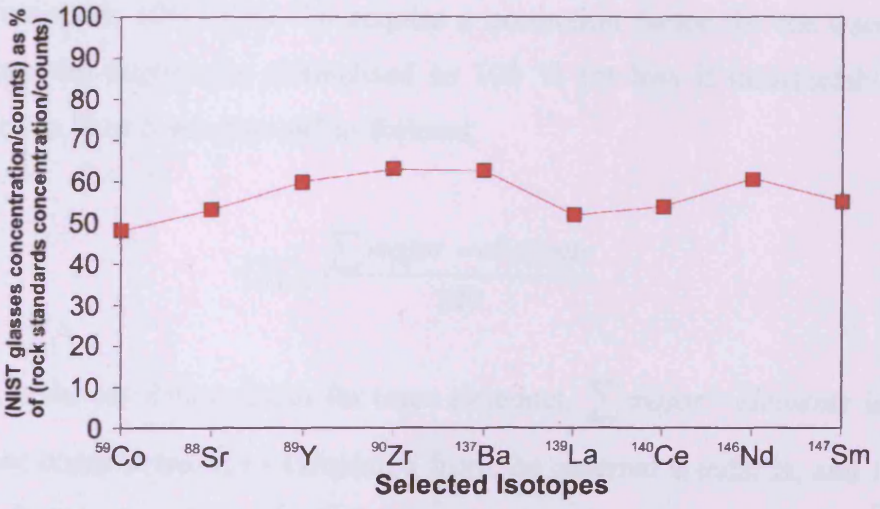

Fig. 5.10. Plot of NIST concentration / count ratios as a % of the rock standard concentration / count ratios

5.4 Calculating elemental concentrations in unknowns

All materials supply aerosols to the ICP-MS at differing rates, due to changes in ablation rates, chemical composition, position in ablation cell and possibly changes in the operating parameters of the equipment over time, thus there is a need to correct for these changes in ablation rates between unknowns and external reference materials. Normally this is done by acquiring an internal standard for the unknown. This can be achieved by analysis of the unknown by methods that do not need an internal standard, such as ion microprobe (IMP), electron microprobe (EMP) or scanning electron microscope (SEM). Once the concentration of an element is known in the unknown, a correction factor can be calculated as follows

$$Cf = \frac{Co_{known}}{Co_{calculated}}$$

where Cf is the correction factor, Co_{known} is the concentration of the element being used as the internal standard and $Co_{calculated}$ is the concentration of the internal standard calculated from the calibration of external standards.

However, because of the nature of the materials, i.e. olivine hosted melt inclusions below the same surface, it is impossible to acquire internal standards for the unknowns. Therefore, a different method has been developed by Halter *et al.* (2002), which dispenses with an internal standard. Instead, they assume that all the major oxides approximates 100 wt %. To acquire a correction factor for the trace element concentrations the majors are normalised to 100 % (or less if undetectable volatile elements such as H or S are present) as follows;

$$Cf_{trace} \frac{\sum major - elements}{100}$$

where Cf_{trace} is the correction factor for trace elements, $\sum major - elements$ is the total major element concentrations as calculated from the external standards, and 100 is the normalising factor. As major element concentrations in the rock standards (BIR-1, BHVO-2, BCR-2) that are being used to calculate the major element concentrations in

the unknowns (i.e. olivine and inclusions) the correction factor calculated by normalisation of the resultant unknown major element concentrations will only apply to the trace element concentrations calculated from the same external standards. Therefore, the correction factor will not apply to calibration curves calculated from the NIST glass or combination of NIST glasses and rock standards. Consequently, for all analyses of olivine and inclusions in this work, only the rock standards will be used as external standards.

5.5 Ar versus He as carrier gas

In order to determine the transport efficiencies of laser ablation induced aerosols, measurements of the count rates over time, using Ar and He as carrier gasses has been carried out (this study). The transport efficiency is defined here as the ICP-MS counts per unit time. The count rates for the rock standards (BIR-1, BHVO-2, BCR-2) were determined in an Ar or He gas flow, using a laser repetition rate of 20 Hz and a spot size of 40 µm at a laser power output of 40%, whilst ablating pits into the surfaces of the rock standards (BIR-1, BHVO-2, BIR-2).

Fig. 5.11 shows the count profile through an entire experiment for Mg in sample BIR-1. The first 14 s monitor the background (gas blank) count rates, the laser then starts firing, and keeps firing until 66 s into the experiment, at which point the laser turns off. Between 66 and 70 s there is a sharp decline in the count rate, until it reaches the background levels.

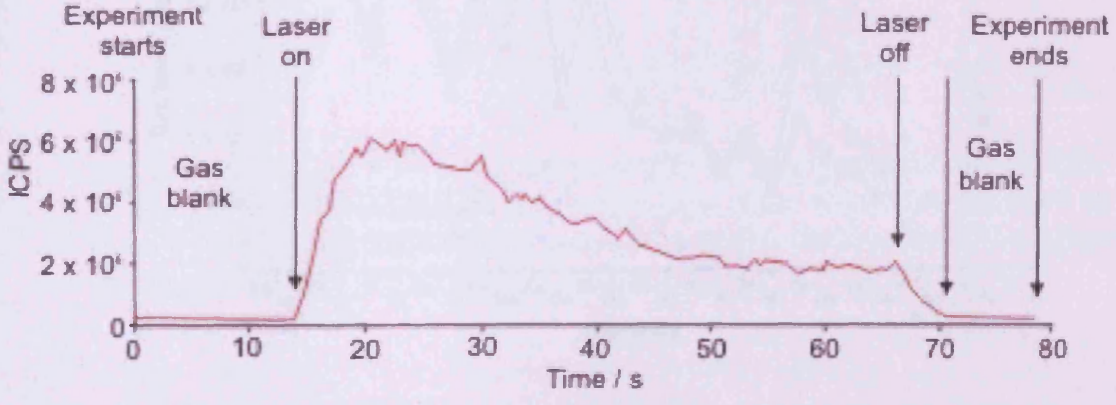

Fig. 5.11. Diagram showing a typical count profile for Mg in sample BIR-1, during an ablation experiment.

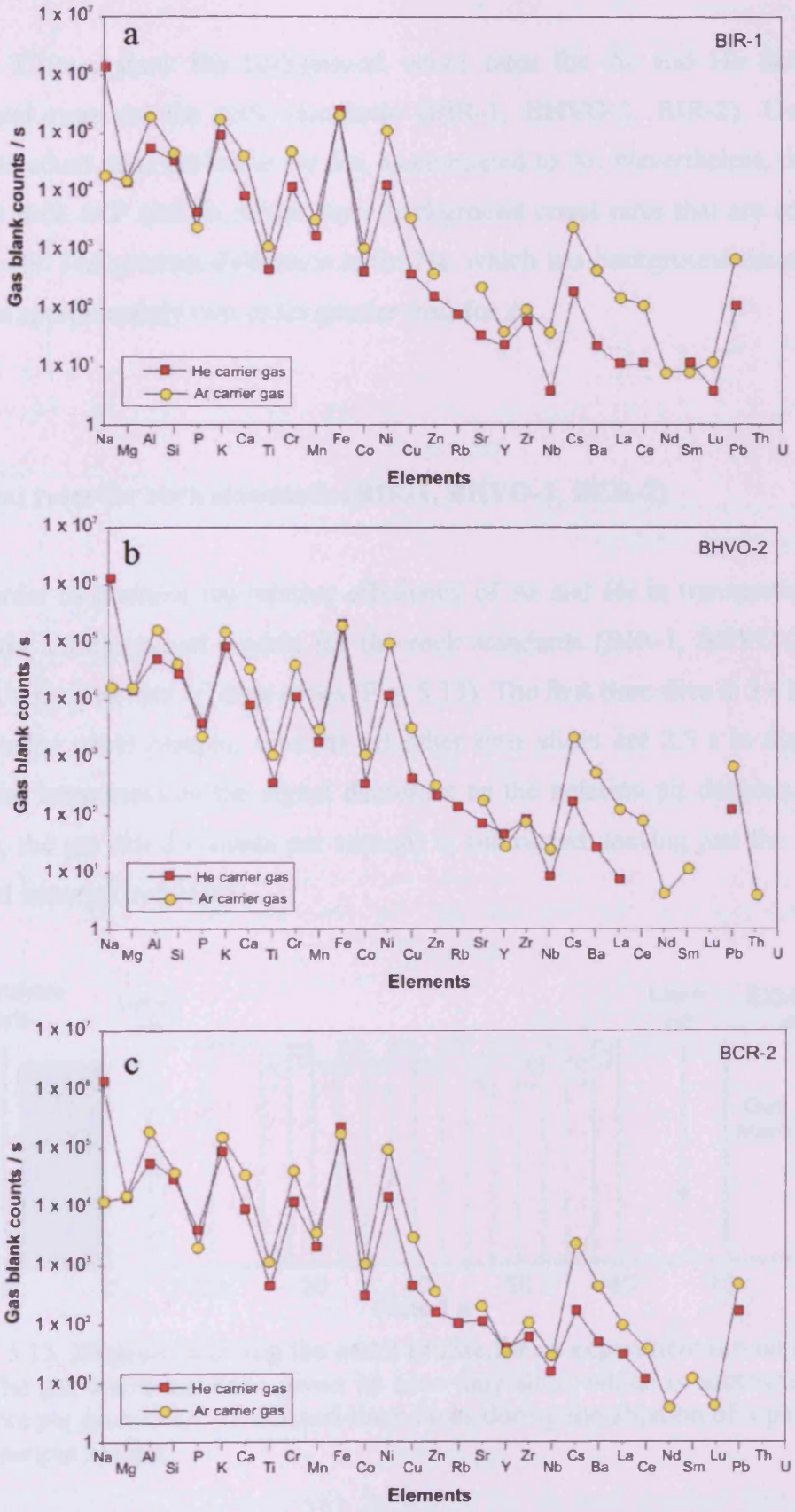

Fig. 5.12c. Plots of the background count rates for Ar and He, for three experiment runs on the rock standards (BIR-1, BHVO-2, BCR-2). Except for Na, P and Fe, the background count rates are lower for He as compared to Ar

5.5.1 Gas blank (background) counts for Ar and He

Fig. 5.12a-c show the background count rates for Ar and He during three experimental runs on the rock standards (BIR-1, BHVO-2, BIR-2). Overall, the background count rates are lower for He, as compared to Ar. Nevertheless, there a few exceptions such as P and Fe, which have background count rates that are consistently higher for He. The greatest difference is for Na, which has background count rates for He that are approximately two order greater than for Ar.

5.5.2 Count rates for rock standards (BIR-1, BHVO-2, BCR-2)

In order to examine the relative efficiency of Ar and He in transporting ablated aerosols, the time-resolved signals for the rock standards (BIR-1, BHVO-2, BCR-2) have been separated into 15 time slices (Fig. 5.13). The first time slice is 5 s in duration and covers the count plateau, whereas all other time slices are 2.5 s in duration and cover count increments as the signal decreases as the ablation pit deepens. For each time slice, the gas blank (counts per second) is subtracted, leaving just the counts for the ablated material over time.

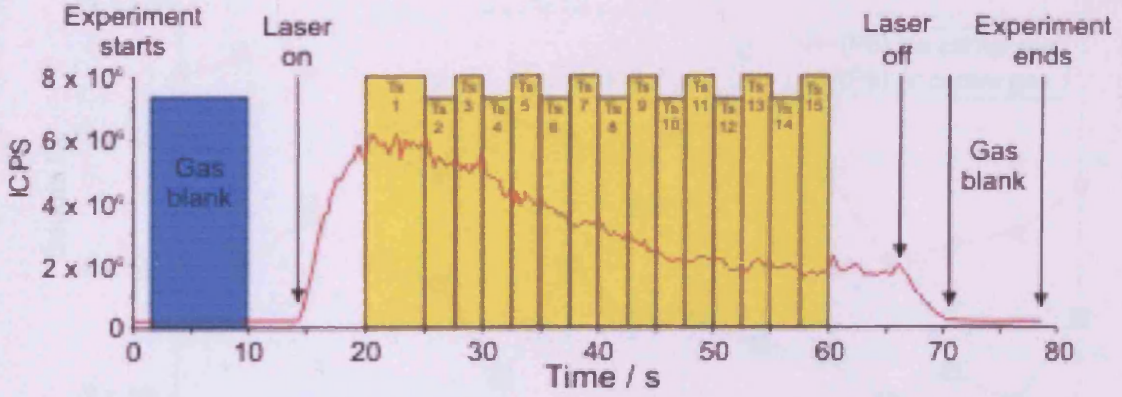

Fig. 5.13. Diagram showing the count profile for an experiment run on BIR-1. The gas blank has been given its own time slice, which is subtracted as counts per second for 15 defined time slices during the ablation of a pit into the sample surface.

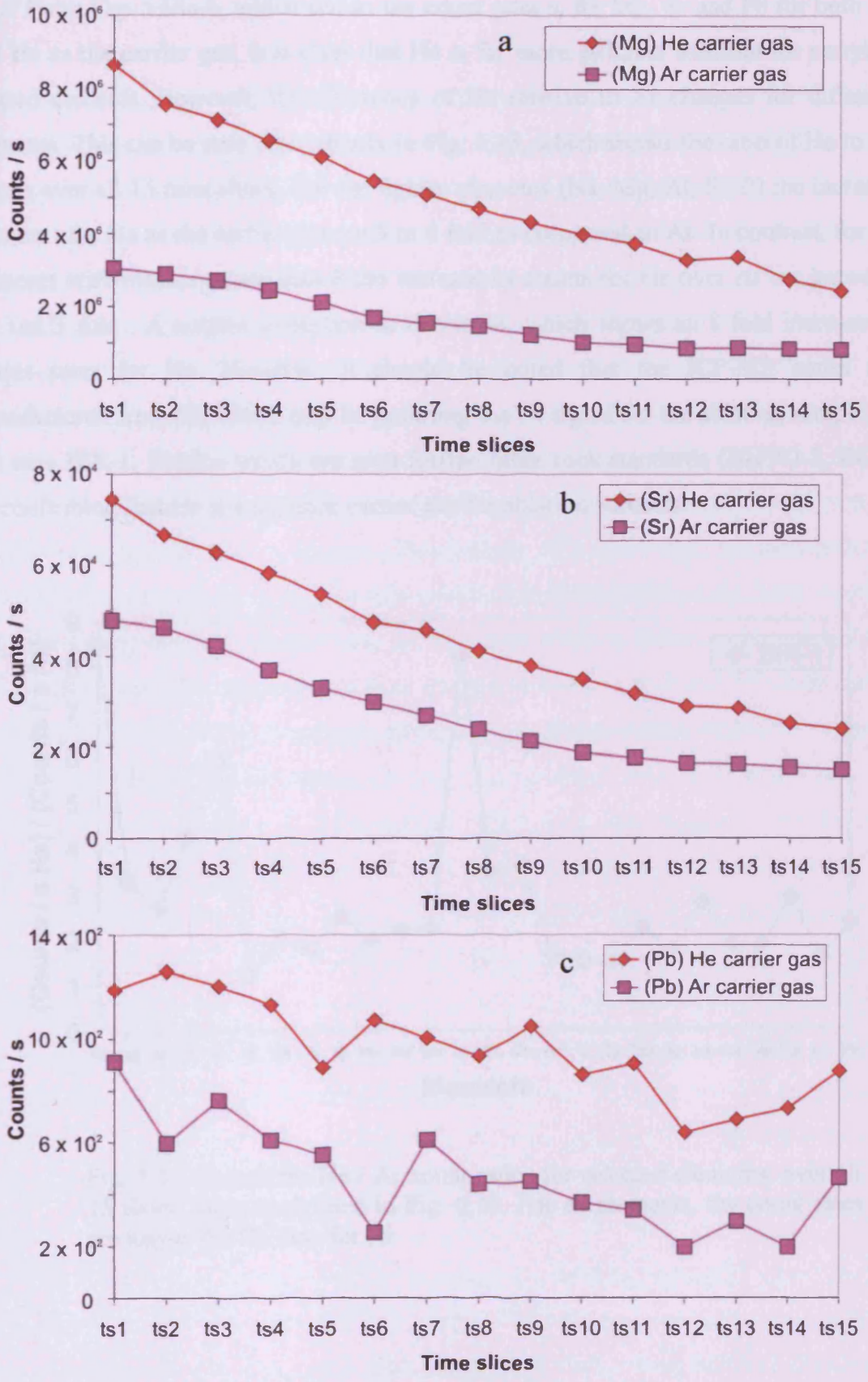

Fig. 5.14a-c. Plots of counts s for Mg, Sr and Pb for the rock standard BIR-1, across the 15 time slices defined in Fig. 6.13. For all three elements and across all time slices, He is shown to be a better carrier gas than Ar. The count rates for BHVO-2 and BCR-2, are consistent with the results seen here for BIR-1.

From Fig. 5.14a-b, which shows the count rates s, for Mg, Sr and Pb for both Ar and He as the carrier gas, it is clear that He is far more efficient medium for carrying ablated aerosols. However, the efficiency of He relative to Ar changes for different elements. This can be seen most clearly in Fig. 5.15, which shows the ratio of He to Ar counts over all 15 time slices. For the lighter elements (Na, Mg, Al, Si, P) the increase in counts for He as the carrier gas are 3 to 8 fold as compared to Ar. In contrast, for all elements with masses grater than P the increase in counts for He over Ar are between 0.5 and 3 fold . A notable exception to this is Ni, which shows an 8 fold increase in counts rates for He. However, it should be noted that the ICP-MS cones are manufactured from Ni, which may be polluting the Ni signal for the ablating sample, in this case BIR-1. Similar trends are seen for the other rock standards (BHVO-2, BCR-2), confirming that He is a superior carrier gas for ablation aerosols.

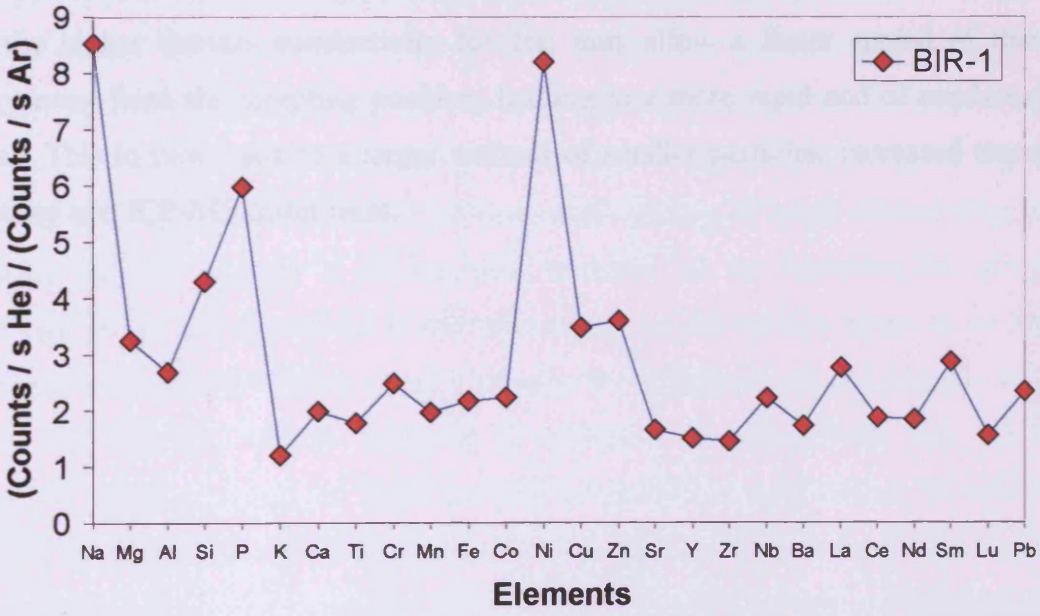

Fig. 5.15. Plot of the He / Ar count ratios for selected elements, over all 15 times slices as defined in Fig. 6.13. For all elements, the count rates are higher for He than for Ar.

5.5.3 Transport efficiency

Horn and Günther (2003) have shown that there are differences in the particle size distribution for aerosols transported in Ar and He atmosphere using 266 and 193 nm lasers for ablation. Ablation in He produces significantly smaller particles in comparison to Ar for all materials and laser wavelengths. This shift in the particle size distribution towards smaller particle sizes may partially explain the increased sensitivities seen in ICP-MS when using He as the carrier gas. Horn and Günther (2003) also suggest that the gas environment at the ablation site may contribute to the control of condensation or coagulation growth of particles after the laser impact. This is because Ar and He have different physical properties such as thermal conductivity, molecular weight and first ionisation potential, thus possibly influencing the growth of particles condensing from a vapour. Observations also show that the laser-induced plasma in He atmosphere is significantly smaller when compared to Ar. This, together with the higher thermal conductivity for He, may allow a faster spread of thermal energy away from the sampling position, leading to a more rapid end of condensation growth. This in turn leads to a larger amount of smaller particles, increased transport efficiency and ICP-MS count rates.

5.6 Fractionation processes

Pulsed laser ablation micro-sampling, coupled with analysis of the ablation products by LA-ICP-MS, is an analytical technique, which has undergone rapid development, and has growing applications in many diverse fields (Sylvester, 2001). To fully utilise the full potential of this technique, the ablation sampling and transport of material to the plasma must be as close to quantitative as possible. Many early studies in LA-ICP-MS were conducted using ruby lasers, with wavelengths in the infrared (λ = 694 nm), this also being the fundamental wavelength of the Nd:YAG laser. For bulk sampling applications, where high spatial resolution and controlled ablation are not critical requirements, visible and infrared lasers are reasonably well suited. However, although infrared lasers could achieve controlled ablation of minerals with high absorptivity (mostly minerals with strong body colour), it often resulted in poor ablation of minerals that are weakly absorbent, typically the colourless minerals (quartz, calcite, feldspars, apatite, etc). This is because colourless minerals do not attenuate incident infrared energy, however energy can be absorbed by defects within the crystal, or by the epoxy cement that bonds the mineral wafer to the glass slides. In either case the result can be sudden, uncontrolled spalling of large mineral fragments, or entire mineral grains, a phenomenon referred to as "catastrophic ablation" (Sylvester, 2001). As absorption of the laser energy in the surface layers is the key to controlled ablation, this affect clearly reduces the efficiency of the system, and the quantitative accuracy of the analysis in question. To circumvent this problem, ultraviolet lasers are used, as these are just as absorbent with respect to colourless minerals as they are to coloured minerals (Sylvester, 2001). However, there are other fundamental processes, which affect and influence LA-ICP-MS that are independent of the laser wavelength, and these must be taken into account if this system is to be used to its full potential.

The ICP-MS is an atmospheric pressure ion source; therefore, laser ablation sampling must also be carried out in an atmospheric pressure ambient gas in order to ensure contamination-free transport of the ablation products to the ICP-MS. Because of these conditions, expansion of the laser-induced plasma above the ablation site is constrained by the ambient gas to a volume of only a few mm^3. The confinement of this

plasma promotes redeposition of ablated material onto the sample surface following the laser light pulse (Fig. 5.16). This condensation, plus other possible transport losses and condensation onto the ablation pit sidewalls as the plasma plume exits the ablation hole, reduces the ablation yield and may influence measured elemental concentrations due to fractionation trends.

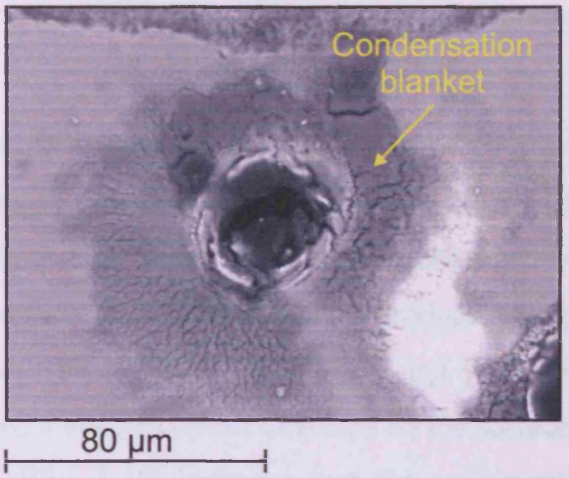

Fig. 5.16. Image showing condensation of ablated material onto the sample surface around the ablation pit. The carrier gas was Ar, with a flow rate of 1 l/minute.

5.6.1 Experimental

The LA-ICP-MS has been used to investigate the time-dependent signal behaviour of the rock standards (BIR-1, BHVO-2, BCR-2) and the mineral olivine. The rock standards have been acquired from the USGS, and have only seen limited use as external standards for LA-ICP-MS. The olivine phenocrysts used in this work are from the MPG basalts, so it is of importance to determine whether they fractionate at similar rates to the rock standards. The laser-operating parameters were the same for all experiments, except for the carrier gas, which was alternated between Ar and He (Fig. 5.17). The sensitivity of the ICP-MS was typically between 6.4 x 10^4 and 5 x 10^4 cps (counts per second) near the top of the pits, and 2.2 x 10^4 and 1.5 x 10^4 cps near the bottom of the pits for He and Ar respectively, for the element Sr in the rock standard BIR-1. A suite of elements spanning a wide range of vaporisation temperatures (Lodders, 1995), was measured with 5 s and 2.5 s (Fig 5.13) resolution as the pit deepened into the sample. No pre-ablation was carried out.

Fig. 5.17. Table of the operating parameters for the laser ablation of pits in the rock standards (BIR-1, BHVO-2, BCR-2) and olivine phenocrysts, to determine the fractionation of elements in these materials.

Spot size 40 µm	Energy output 40%
Rep rate 20 Hz	Dwell time 5 s
Number of passes 10	Depth of pass 10 µm
No pre-ablation	Carrier gas Ar 1/Lmin or He 0.5/Lmin

Ablation pits produced in these experiments exhibit good imaging of circular masks (Fig. 5.2). The rate of material removal is estimated from optical microscopy to be ~ 0.1 µm / pulse (2 µm / s at 20Hz). Each laser pulse in principle results in the quantitative removal of material from the sample site, with the ablation products being no larger in size than the depth ablated with each pulse of the laser, and with no discernable residual melt. As the hole deepens, a visible deposit develops on the surface surrounding the ablation pit. SEM analysis (Fig. 5.18) indicates that the constituent material forms particles that are less than 1µm in diameter; however, as ablation continues, the fringe of this material migrates outwards as the deposit thickens to more than several microns in thickness at the edge of the ablation site (Fig. 5.18).

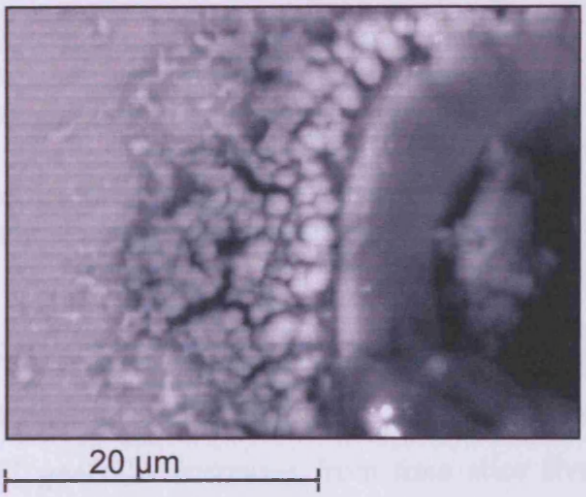

Fig. 5.18. SEM image of the deposit developed around the edge of the ablation pit during analysis. The general size of the constituent material is less than 1 µm in diameter, but has a total thickness near the pit rim of several microns.

5.6.2 Elemental fractionation rock standards

The count rates for individual elements drop considerably through time, as pits are ablated into sample surfaces (Fig. 5.19). Therefore, to investigate the time evolution of signal intensities and the ratios between elements through time, the count rates for all elements in each time slice (Fig. 5.13) are normalised to 100%. The normalised count rates for each time slice are then divided by the normalised count rate in time slice one. The ratios of two elements that display volatile and refractory behaviour (generally associated with lower and higher elemental condensation temperatures), and ablated in an Ar atmosphere, are shown in Fig. 5.20.

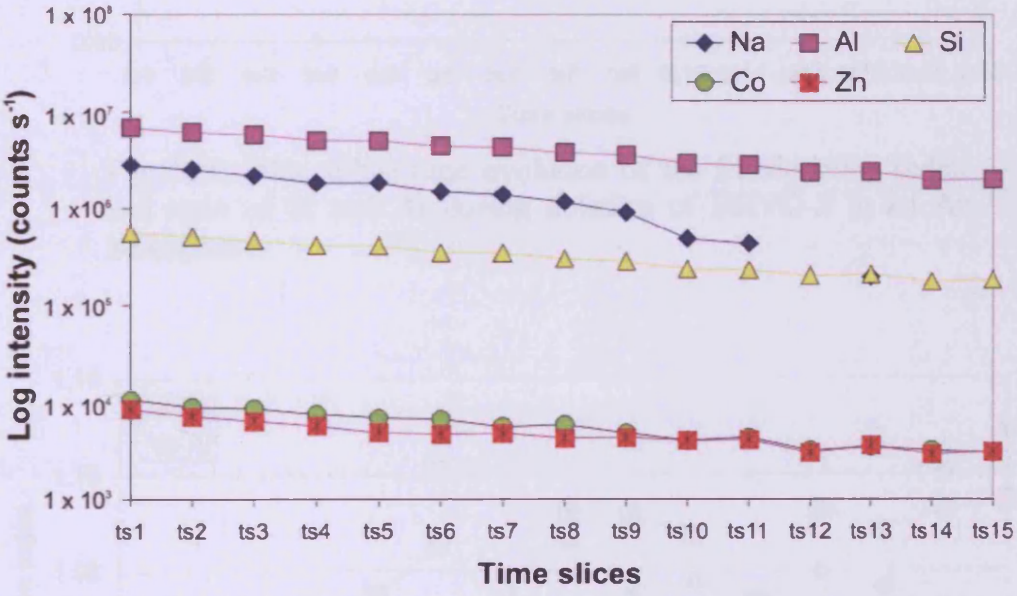

Fig. 5.19. Plot showing the counts s for selected elements, from the analysis of BCR-2, synthetic rock standard, using He as the carrier gas.

The fractionation index (FI) for both the refractory Al and more volatile Si are very similar between time slice one and time slice five. However, from this point onwards their FI diverge. For Al, the FI generally increases from time slice five onwards, with a maximum value of ~1.10, whereas the opposite is true for Si, which has an ever decreasing FI and a minimum value of ~0.93. When the FI, for Al and Si are plotted for ablation in an He atmosphere (Fig. 5.21), their values through the fifteen time slices are far more similar. For Al the pattern of change over time is very similar to that seen for ablation in a Ar atmosphere that is there is a general rise to a maximum

value of ~1.10. For Si the divergence observed during ablation under Ar is not present. Instead, the fractionation of Si over time is very similar to that seen for Al, with a maximum value of ~1.10.

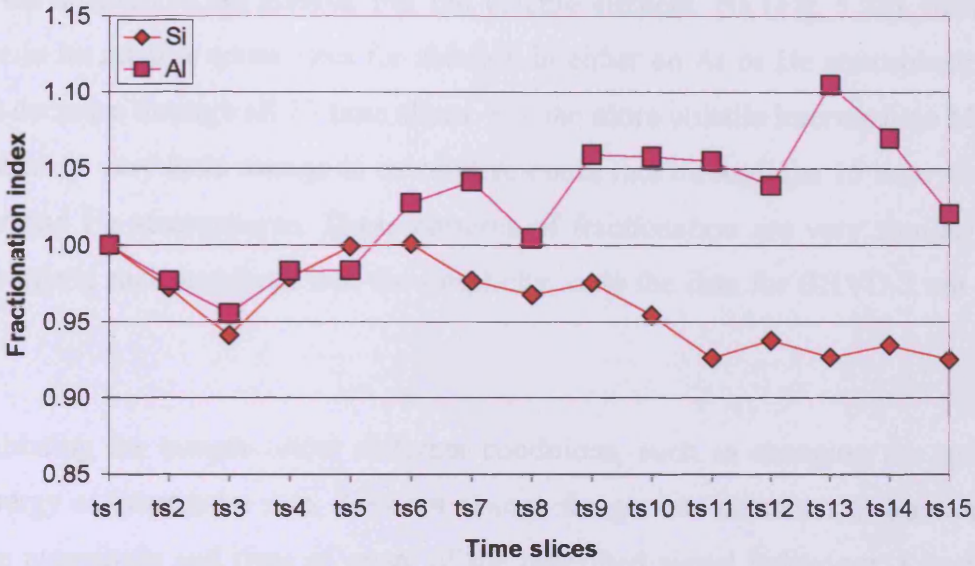

Fig. 5.20. Plot of the time evolution of the fractionation index and ratio of Si and Al during ablation of BHVO-2 in an Ar atmosphere.

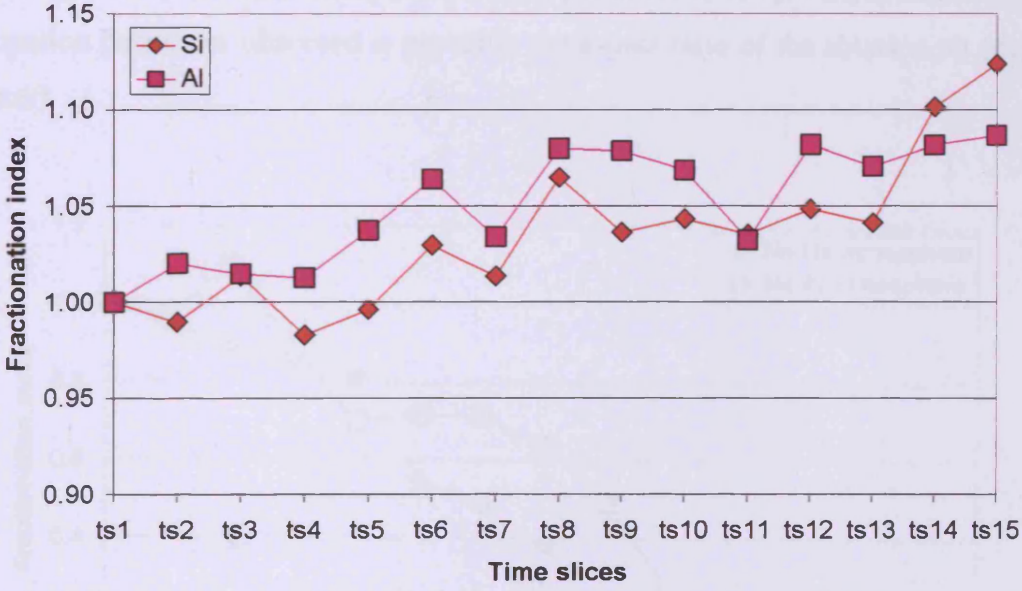

Fig. 5.21. Plot of the time evolution of the fractionation index and ratio of Si and Al during ablation of BHVO-2 in an He atmosphere.

The fractionation patterns observed for Al and Si are not the only types of fractionation pattern observed in the analysis of the synthetic rock glasses. From Figs. 5.22 and 5.23, it is clear that there are several differing fractional trends operating during the ablation of the glasses. For the volatile element, Na (Fig. 5.22), there is no increase in its relative count rates for ablation in either an Ar or He atmosphere, just a gradual decrease through all 15 time slices. For the more volatile intermediate Mn (Fig. 5.23), there is very little change in its relative count rate through the 15 time slices for both Ar and He atmospheres. These patterns of fractionation are very similar for all three synthetic rock standards but, for simplicity, only the data for BHVO-2 are shown here.

Ablating the sample under different conditions, such as changing the spot size, laser energy or laser pulse rate, does not change the general character of fractionation, only the magnitude and time of onset of the described signal behaviour. Lower laser repetition rate simply results in the observed behaviour occurring correspondingly later (i.e. probably corresponding to the same number of laser pulses). In contrast, smaller spot sizes accelerate the onset of fractional reversal seen in Fig. 5.20, as does lower laser energy levels. Thus, at constant operating parameters, the principal control on the fractionation behaviour observed is probably the aspect ratio of the ablation pit (depth / diameter).

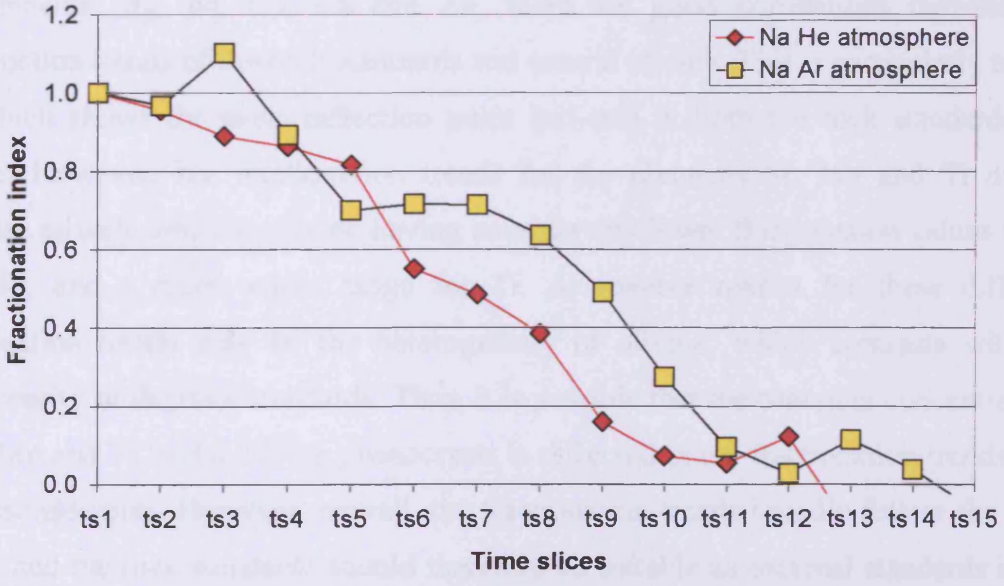

Fig. 5.22. Plot of the time evolution of the fractionation index for Na during ablation of BHVO-2 in both He and Ar atmospheres.

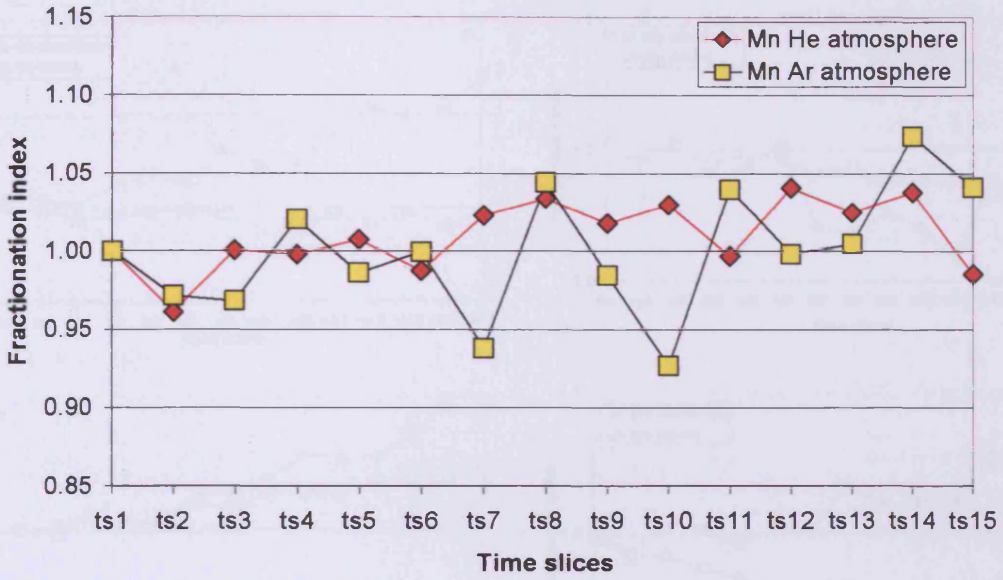

Fig. 5.23. Plot of the time evolution of the fractionation index for Mn during ablation of BHVO-2 in both He and Ar atmospheres.

5.6.3 Elemental fractionation in olivine

Several ablation experiments have been carried out on the olivine phenocrysts hosted in Mull basalts, using the same laser parameters as used on the rock standards (Fig. 5.17) in a He atmosphere. The averaged results are shown graphically in Fig. 5.24a-h together with the average fractionation trends for the three rock standards. For the elements Mg, Fe, Co, Ca and Zn, there are good correlations between the fractionation trends of the rock standards and natural olivine. This is particularly true of Zn, which shows the same inflection point (ts5-ts6) in both the rock standards and olivine. However, the fractionation trends for the elements Si, Mn and Ti do not correlate as well, with the olivine having considerably lower fractionation values for Si and Mn, and a much wider range for Ti. A possible reason for these differing fractionation trends may be the heterogeneity of olivine, which contrasts with the homogeneity of the rock standards. Thus, it is possible that the changing concentrations of Si, Mn and Ti in the olivine phenocrysts is reflected in the fractionation trends seen for these elements. However, overall, the fractionation trends broadly follow the same trends, and the rock standards should therefore be suitable as external standards in the LA-ICP-MS analysis of olivine and olivine-hosted melt inclusions.

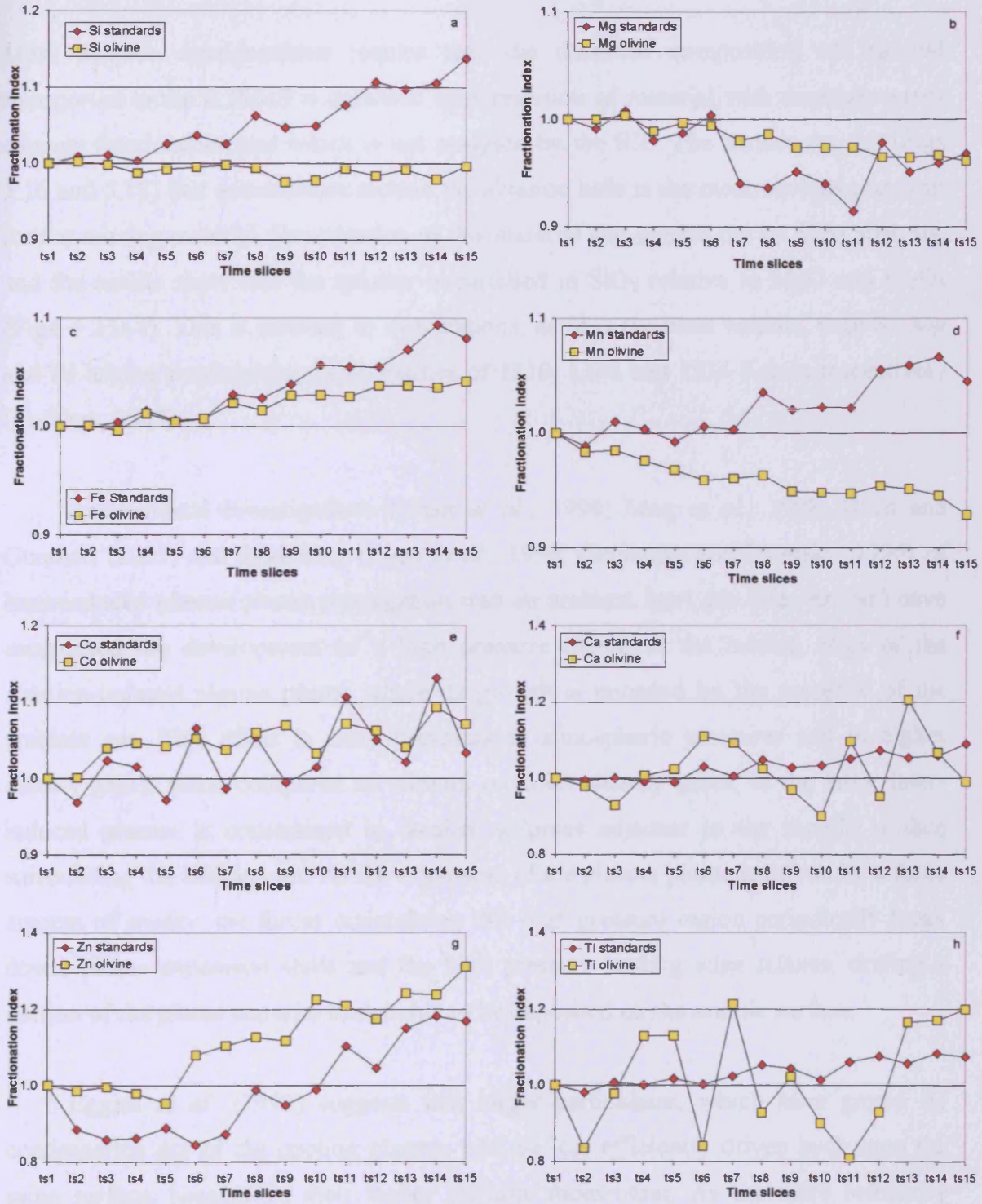

Fig. 5.24. Plots of the average fractionation indexes for selected elements from the analysis of the synthetic rock standards (BHVO-2, BIR-1, BCR-2) and olivine phenocrysts from the Mull basalts. Overall, the general fractionation of elements is broadly similar indicting that the synthetic rock standards can be used as external standards for the analysis of olivine.

5.6.4 Condensation processes during ablation

Mass balance considerations require that the chemical composition of material transported to the ICP-MS is balanced by a reservoir of material with complementary element fractionation and which is not analysed by the ICP. The surface deposit (Figs 5.16 and 5.18) that accumulates around the ablation hole is the most obvious reservoir for the missing material. Examination of this material was carried out by SEM analysis, and the results show that the splutter is enriched in SiO_2 relative to MgO and Fe_2O_3 (Figs. 5.25a-f). This is contrary to expectations, as Si is the most volatile, with Si, Mg and Fe having condensation temperatures of 1310, 1336 and 1334 Kelvin respectively (Lodders, 2003).

Experimental investigations (Chan *et al.*, 1998; Mao *et al.*, 1998; Horn and Gunther, (2003) and modelling (Chen *et al.*, 1996; Geohegan and Puretsky, 1996) of laser-induced plasma plume propagation into an ambient inert gas (He, Ar, Ne) have established the development of a high pressure region at the leading edge of the ablation-induced plasma plume where its growth is impeded by the presence of the ambient gas. This effect is more prevalent at atmospheric pressures and in higher density gases, when compared to vacuum or lower density gases, in the latter laser-induced plasma is constrained to smaller volumes adjacent to the sample surface surrounding the ablation pit. As the expansion of the plasma plume is driven by a finite amount of energy, the forces maintaining this high pressure region periodically break down, plume expansion stalls and the high pressure leading edge relaxes, driving a portion of the plume material backwards to be deposited on the sample surface.

Eggins *et al.* (1998) suggests that larger particulates, which have grown by condensation out of the cooling plasma, will be less efficiently driven back onto the same surface, because of their higher intrinsic momentum. As the more refractory elements condense out of the cooling plasma before the more volatile elements, the refractory elements escape the plasma plume, leading to the deposition of more volatile elements on the sample surface.

This on its own does not explain the fractionation seen by the ICP-MS, but it does highlight the importance of the sequence of condensation of materials out of the

cooling plasma plume, with refractory phases condensing before volatile phases. There is evidence from SEM images (Fig 5.25.) for a condensate/melt layer within the ablation pit itself, suggesting that the faster decay of the ICP-MS signal (early time slices in Figs 5.20 and 5.24f) for refractory elements (Al and Ca) is due to the preferential condensation of refractory phases onto the sidewalls of the ablation pit as the plasma plume propagates out of the hole. In addition, this condensed material presents a source of the refractory element-enriched material, which is sampled at later stages of ablation (Late time slices Figs 5.20 and 5.24f).

As indicated by Eggins *et al.* 1998, and shown here, condensed material in the inner pit, is inefficiently sampled by the laser pulses directly, because of the high inclination with respect to the incoming laser light. It is therefore likely to be resampled and partially re-condensed onto the pit walls, through thermal interactions with the hot plasma plume. From these observations, it is clear that plasma-sampling process only becomes dominant when the signal intensity has dropped considerably from their initial high.

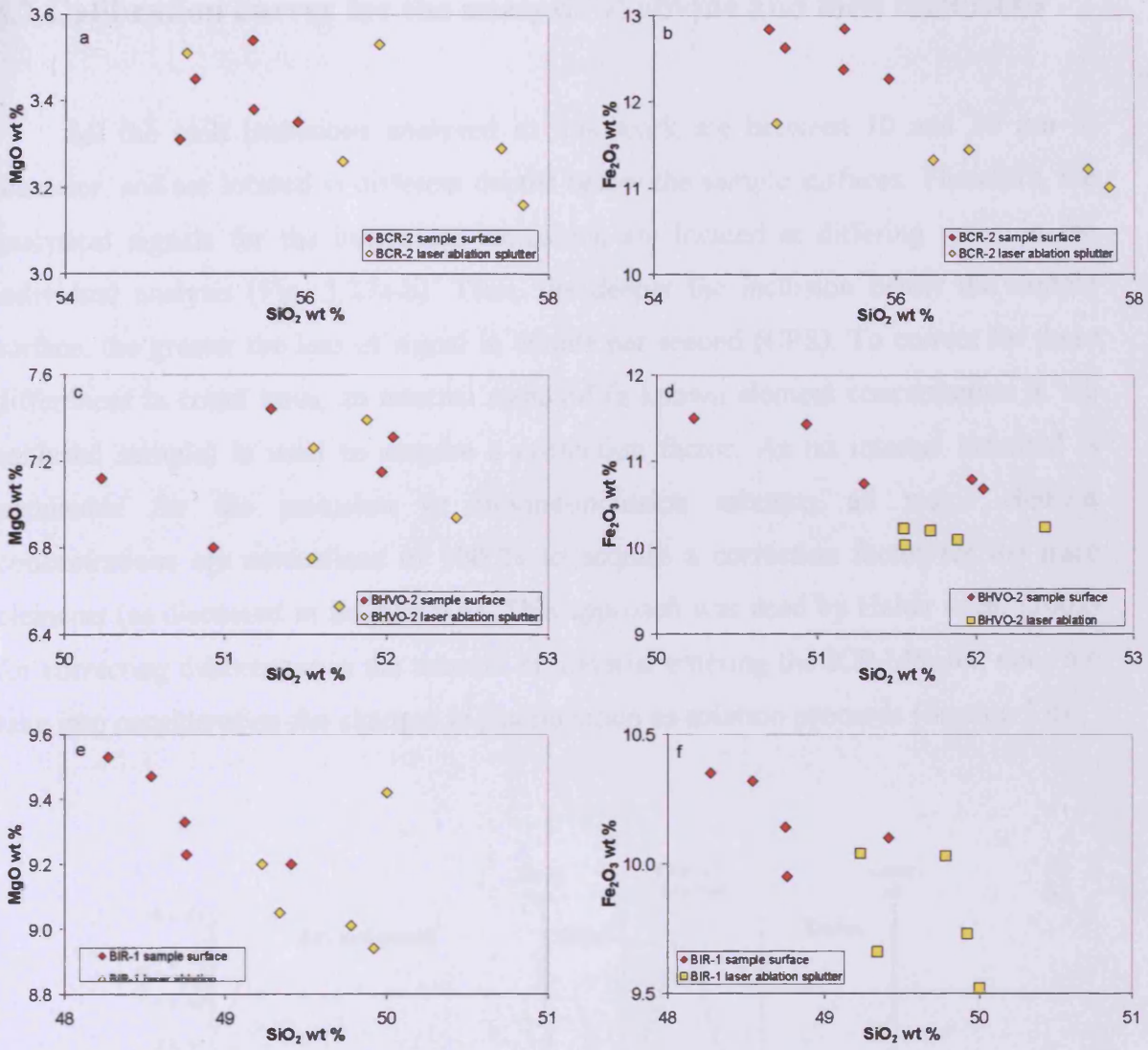

Figs. 5.25a-f. Plots showing the results of SEM analysis for SiO_2, MgO and Fe_2O_3 on the surface of the rock standards, and laser ablation splutter on the surface of the standards.

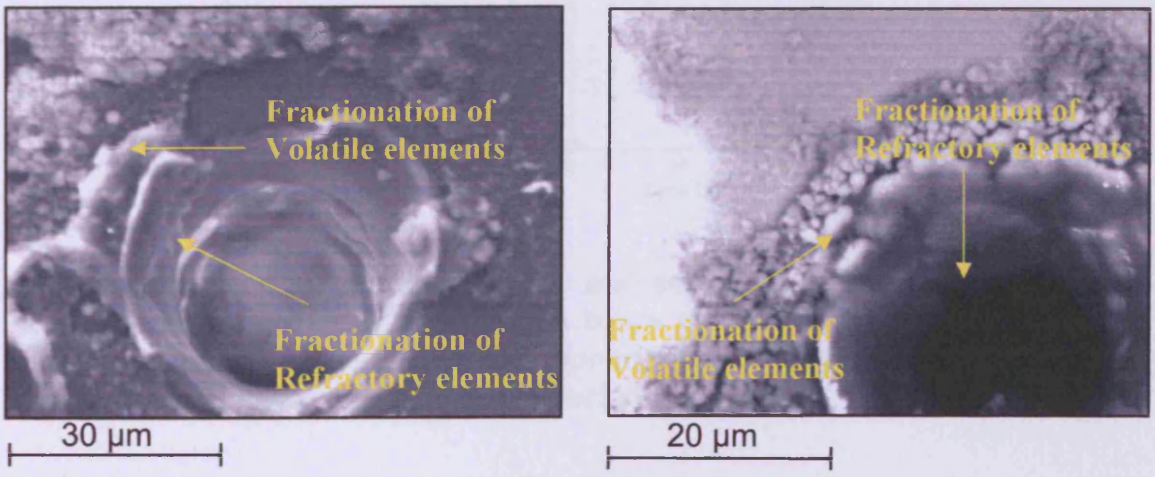

Fig 5.26. SEM images of two ablation pits in sample BHVO-2, showing condensation of material in and surrounding the ablation pits. As refractory elements condense first, they should be found in the ablation pit, whereas the volatile elements condense on the surface surrounding the ablation pit.

5.7 Calibration curves for the analysis of olivine and melt inclusions

All the melt inclusions analysed in this work are between 10 and 30 μm in diameter, and are located at different depths below the sample surfaces. Therefore, the analytical signals for the individual inclusions are located at differing times in the individual analysis (Fig. 5.27a-b). Thus, the deeper the inclusion below the sample surface, the greater the loss of signal in counts per second (CPS). To correct for these differences in count rates, an internal standard (a known element concentration in the analysed sample) is used to acquire a correction factor. As no internal standard is obtainable for the inclusion or olivine-inclusion mixture, all major element concentrations are normalised to 100 % to acquire a correction factor for the trace elements (as discussed in Section 5.4). This approach was used by Halter *et al.* (2002) for correcting differences in the amount of material entering the ICP-MS, but does not take into consideration the changes in fractionation as ablation proceeds (Section 5.6).

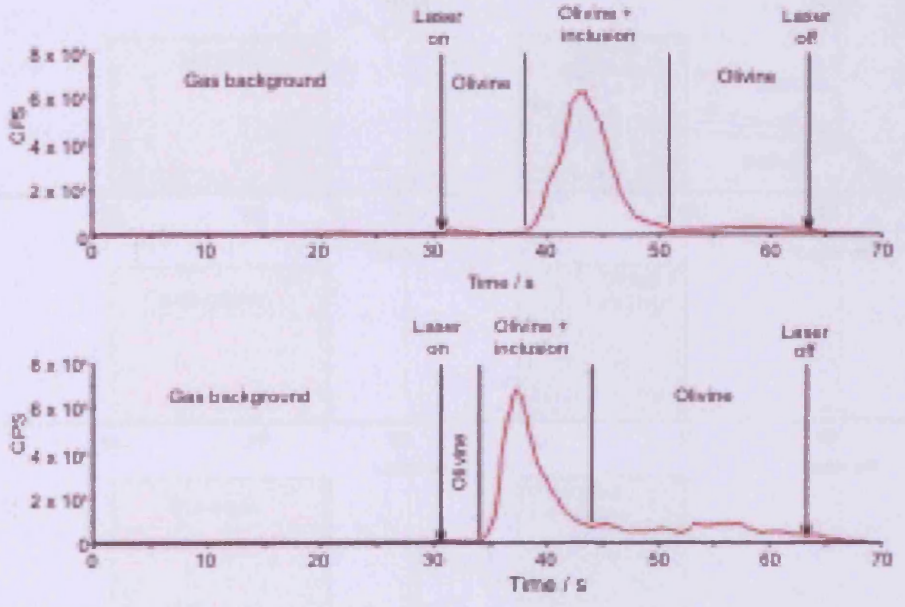

Fig. 5.27a-b. Time profiles for the analysis of Al in two olivine-hosted inclusions, located at different depths below the sample surface. The loss of counts would be greater for the inclusion in (a) as compared to the inclusion in (b), due to its greater depth below the surface.

As all the analysed inclusions are at differing depths below the sample surface, the amount of fractionation affecting the individual inclusions will be different. To correct for these fractionation trends, each analysed inclusion is considered on its own, and has its own calibration curve. This means that if the inclusion in question is defined by a signal between 4 and 5 seconds after the start of ablation, then the same time segments in the ablation of the external standards define the calibration curve (Fig. 5.28). As the host olivine composition is also needed to calculate the composition of the inclusion, a second pit is ablated into the host olivine as close to the inclusion as possible. As with the external standards, the region defined for analysis is the same as defined for the inclusion (Chapter 4). Therefore, to acquire the data needed for the analysis of olivine hosted inclusions, two pits are ablated into the host olivine, one for the composition of the olivine, a second for the mixed composition (olivine + inclusion), and one pit each in the three external standards (BIR-1, BHVO-2, BCR-2). The time slices used in all ablated pits are then defined by the depth of the inclusion below the sample surface, leading to each analysis having its own calibration curve.

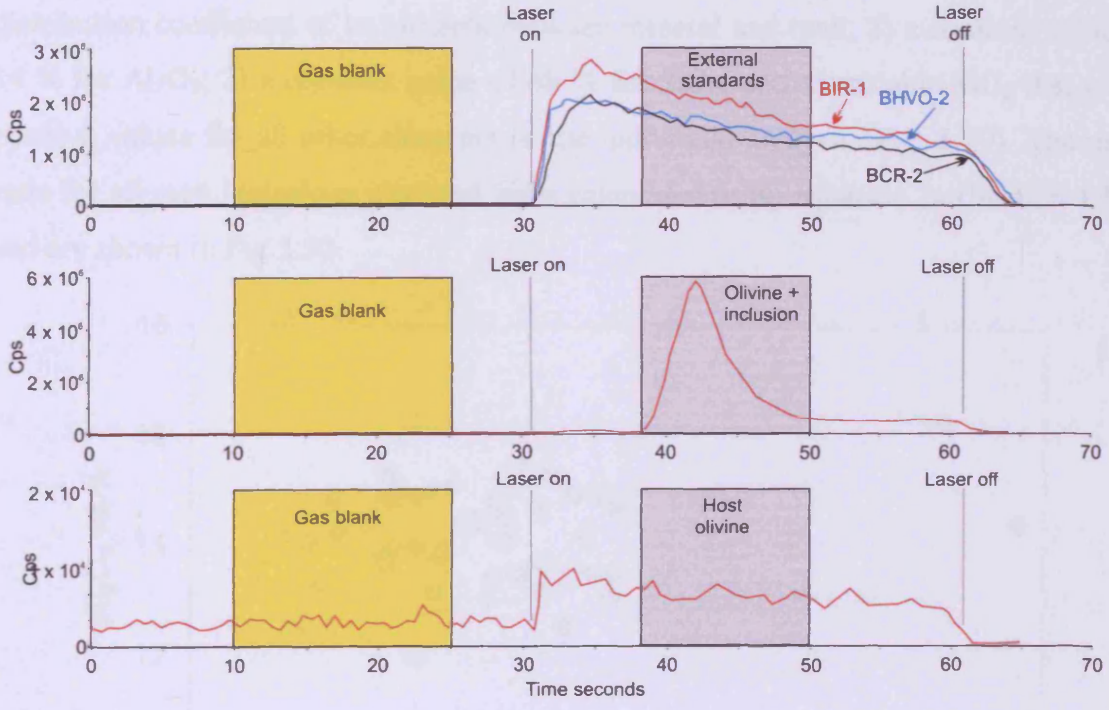

Fig. 5.28. Diagram showing the time slices defined for the analysis of the mixed (olivine + inclusion) and host olivine signals. All the external standards are given the same time slices, thus reducing the effects of fractionation on the analysis of the unknowns.

5.8 Determination of the mass ratio *x*

The following section describes two methods through which the ratio between the mass of the inclusion and the total mass of material ablated can be obtained (Section 4.3.6). These methods are based on 1) a constant internal standard for the melt inclusions, and 2) a constant distribution coefficient of an element between the host and melt (melt inclusion).

5.8.1 Constant internal standard for the melt inclusions

As shown by Halter *et al.* (2002), some elements vary little during igneous differentiation and can, to a first approximation be taken as constant in a set of coeval melt inclusions. Thus, it is sufficient to estimate the concentration of that element from the whole rock analysis, or to determine the absolute concentration of such an element from homogenised inclusions by microprobe analysis. For the analysis of olivine-hosted melt inclusions from Mull basalts, four methods were used: 1) constant distribution coefficient of an element between mineral and melt; 2) a constant value of 14 % for Al_2O_3; 3) a constant value of 48 % for SiO_2; and 4) variable SiO_2 that gives positive values for all other elements in the individual analysis (Fig. 5.29). The mass ratio for all melt inclusions analysed were calculated using equation 2a (Section 4.3.6) and are shown in Fig.5.30.

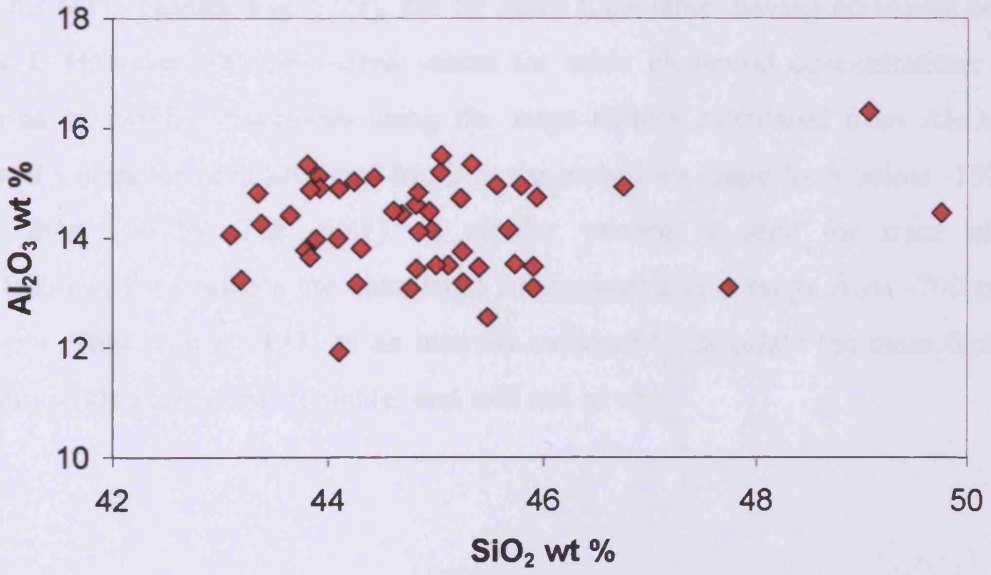

Fig. 5.29. Plot of Al_2O_3 versus SiO_2 for the whole rock analysis of all the MPG basalts analysed in this work

5.8.2 Constant distribution coefficient of an element between mineral and melt

For the olivine-hosted melt inclusions for the Mull basalts, an average distribution coefficient D_Y of 0.0038 for Y between the olivine and melt was obtained from Zanetti *et al.* (2004). The Y concentration of the host was determined for each run from the pit ablated into the olivine (Fig. 5.27). This value was used to calculate the Y concentration for each inclusion individually and in turn the mass factor using equation 2a. Values for the mass factor using this method are shown in Fig. 5.30.

As the inclusions are ablated as a proportion of the total material ablated (olivine + inclusion, section 4.3.2), the mass factor should, in theory, be between 0 (0 = only host olivine) and 1 (1 = only melt inclusion). For the mass factors calculated using a constant distribution coefficient for Y, the values are generally far greater than 1. This suggests that the published partition coefficients for Y are not very accurate for olivine-melt partitioning associated with the MPG basalts. There are published partition coefficients for other elements in basaltic systems, but all other elements detected in the host olivines tend to be compatible in the olivine, and as such, are not acceptable in calculating the mass factor (Fig. 4.20).

5.8.3 Constant value of 14 wt% Al_2O_3

The mass factors calculated using a constant value of 14 % for Al_2O_3 (average Al_2O_3 for MPG basalts, Fig. 5.29), are far more acceptable, having no values below 0 or over 1. However, the calculated values for other elemental concentrations in the inclusions are wildly inaccurate using the mass factors calculated from Al_2O_3. The calculated values for both SiO_2 and MgO in the inclusions range from below -150 % to greater than 100 % (Fig. 5.31). A similar pattern is seen for trace element concentrations, for example the calculated Zn concentrations range from -700 ppm to >800 ppm. Thus, using Al_2O_3 as an internal standard to calculate the mass factor for inclusions again seems unacceptable, and will not be used.

Sample	Inclusion	Al_2O_3 = 14%	SiO_2 = 48%	SiO_2 = var	Y D=0.0038
Am10b	Ph12 In1	0.10	0.35	0.35	4.70
Am10b	Ph12 In2	0.07	0.14	0.14	5.51
Am10b	Ph11 In2	0.06	0.09	0.09	16.09
Am10b	Ph11 In1	0.14	0.19	0.34	19.26
Am10b	Ph10 In1	0.04	0.02	0.07	8.17
Am10b	Ph8 In1	0.04	0.05	0.17	3.24
Am10b	Ph7 In1	0.19	0.32	0.32	5.32
Am10b	Ph7 In2	0.19	-0.04	0.40	7.95
Am10b	Ph7 In3	0.45	0.04	0.33	3.30
Am10b	Ph7 In4	0.31	0.44	0.44	3.21
Am10b	Ph6 In1	0.70	1.46	1.46	1.80
Am10b	Ph6 In2	0.35	0.47	0.47	7.26
AM10c	Ph1 In1	0.78	-0.44	48.33	4.19
AM10c	Ph1 In2	0.33	0.64	0.64	2.07
AM10c	Ph2 In1	0.29	0.84	0.84	2.26
AM10c	Ph2 In2	0.06	0.19	0.19	9.52
AM10c	Ph3 In1	0.04	0.05	1.13	9.65
AM10c	Ph4 In1	0.10	0.37	0.37	0.32
AM10c	Ph5 In1	0.01	0.04	0.04	1.21
BHI2	Ph5 In1	0.12	0.27	0.27	10.33
BHI2	Ph5 In2	0.07	0.20	0.20	10.33
BHI2	Ph7 In1	0.23	-0.53	1.98	8.19
BHI2	Ph4 In1	1.84	-1.96	139.89	8.19
BHI3	Ph6 In1	0.42	0.26	0.31	117.65
BHI3	Ph6 In2	0.07	0.13	0.13	16.04
BHI3	Ph8a In1	0.42	0.08	1.33	75.54
BHI3	Ph8b In1	0.04	-0.12	1.66	5.79
BHI3	Ph3 In3	0.08	-0.03	5.40	12.13
BHI3	Ph11 In2	0.04	0.18	1.52	9.21
BHI3	Ph11 In 3	0.15	0.11	0.40	9.21
BHI16	Ph3 In2	0.70	1.81	1.81	8.96
BHI18	Ph7 In3	0.04	0.01	19.30	7.51
BHI18	PH7 In1	0.26	0.75	1.01	7.51
BHI18	Ph7 In2	0.10	0.14	2.08	7.51
BHI18	Ph1 In1	0.01	-0.07	3.77	7.51
BM2	Ph2 In1	0.24	0.20	0.87	9.73
BM2	Ph2 In2	0.21	0.32	0.37	16.54
BM2	Ph2 In3	0.06	0.13	1.22	19.46
BM2	Ph3 In1	0.25	-0.77	2.06	4.04
BM2	PH3 In2	0.38	0.10	0.32	4.04
BM2	Ph3 In3	0.25	0.22	1.58	4.04
BM2	Ph3 In4	0.24	0.32	1.03	4.04
BM2	Ph3 In5	0.38	-0.10	3.14	4.04
BM2	Ph5 In1	0.21	0.28	1.54	2.97
BM2	Ph5 In2	0.04	0.14	2.19	2.97
BM2	Ph12 In1	0.12	0.15	1.29	18.62
BM2	Ph11 In1	0.09	0.06	1.09	213.61
BM2	Ph10 In1	0.16	0.37	1.41	14.18
BM2	Ph8 In1	0.08	0.27	8.79	79.81
BM2	Ph8 in2	0.30	0.57	1.04	110.27
BM6a	Ph1 In1	0.16	0.38	0.38	0.73
BM6a	Ph4 In1	0.02	0.14	1.28	0.32
BM6a	Ph4 In2	0.02	0.10	2.04	0.31
BM6a	Ph6 In1	0.06	0.00	7.02	19.68
BM6a	Ph6 In2	0.03	0.13	2.92	19.68

Fig. 5.30a. Table of the mass factors for inclusions using the differing methods of calculation

Sample	Inclusion	Al_2O_3 = 14%	SiO_2 = 48%	SiO_2 = var	Y D=0.0038
BM6a	Ph7 In3	0.03	0.00	0.69	6.39
BM6a	Ph8 In4	0.08	0.11	2.24	8.43
BM6a	Ph9 In1	0.48	1.30	1.30	1.33
BM6a	Ph9 In2	0.04	0.10	1.03	1.33
MR9	Ph1 In1	0.05	0.20	0.34	5.75
MR9	Ph2 In3	0.03	0.23	0.23	6.12
MR9	Ph3 In1	0.03	0.21	0.21	8.79
MR9	Ph5 In1	0.02	-0.20	1.44	3.99
MR10	Ph1 In1	0.04	0.11	2.13	12.04
MR10	Ph1 In2	0.12	0.27	2.35	6.62
MR10	Ph2 In1	0.17	0.46	0.46	2.54
MR10	Ph3 In1	0.40	0.81	0.81	12.31
MR10	Ph4 In1	0.16	0.28	0.32	5.83
MR10	Ph4 In2	0.36	0.82	0.82	8.14
MR10	Ph5 In1	0.06	0.38	0.89	2.42
MR10	Ph5 In2	0.04	-0.04	0.87	2.59
MR10	Ph7 In1	0.30	0.56	0.56	4.57
MR10	Ph8 In1	0.44	1.29	1.29	1.90
MR10	Ph11 In1	0.03	0.07	0.08	0.19
MR10	Ph11 In2	0.12	0.29	0.29	5.30
MR12a	Ph1 In1	0.35	0.69	0.69	12.05
MR12a	Ph1 In2	0.10	0.25	0.32	11.39
MR12a	Ph1 In3	0.07	-0.01	0.22	6.60
MR12a	Ph2 In1	0.67	-1.05	8.86	4.99
MR12a	Ph4 In1	0.01	0.09	0.12	13.76
MR12a	Ph4 In2	0.03	0.24	0.24	11.35
MR12a	Ph6 In1	0.19	0.50	0.50	13.59
MR12a	Ph7 In1	0.42	1.22	1.22	17.99
MR12a	Ph8 In1	0.10	0.30	0.30	3.22
MR12a	Ph9 In1	0.04	0.07	0.15	8.45
MR12a	Ph9 In2	0.01	0.12	1.92	11.43
MR12a	Ph12 In1	0.11	0.37	0.37	7.52
MR12a	Ph11 In1	0.17	0.43	0.43	11.66
MR12a	Ph11 In2	0.42	1.42	1.42	7.41
MR12a	Ph14 In1	0.13	0.44	0.44	3.17
AM7a	Ph1 In1	0.04	0.12	0.12	7.23
AM7a	Ph1 In3	0.06	0.09	1.22	7.23
AM7a	Ph1 In4	0.15	0.34	1.30	7.23
AM7a	Ph2 In1	0.12	0.47	0.47	1.97
AM7a	Ph3 In1	0.03	0.09	1.45	8.13
AM7a	Ph3 In2	0.07	0.12	0.43	9.13
AM7a	Ph4 In1	0.18	0.29	0.29	11.16
AM7a	Ph4 In2	0.02	0.85	0.85	0.40
AM7a	Ph5 In1	0.02	0.07	1.19	13.60
AM7a	Ph5 In2	0.03	0.36	0.36	6.17
AM7a	Ph6 In1	0.05	0.12	1.25	12.17
AM7a	Ph7 In1	0.31	0.37	1.13	15.16
AM7a	Ph8 In1	0.04	0.31	1.48	20.75
AM7b	Ph3 In1	0.70	-1.23	15.74	3.38
AM7b	Ph4 In1	0.96	-1.41	13.56	7.21
AM7b	Ph5 In1	0.16	0.28	0.57	3.92
AM7b	Ph6 In1	0.20	0.31	0.48	9.82
AM7b	Ph6 In2	0.22	0.15	0.23	8.65
AM7b	Ph6 In3	0.11	0.07	0.10	5.26
AM7b	Ph7 In1	0.16	0.21	0.21	8.79
AM7b	Ph7 In2	0.31	0.31	0.94	6.65
AM7b	Ph7 In3	0.18	0.08	0.54	6.46
AM7b	Ph10 In1	0.02	0.00	1.89	10.39

Fig. 5.30b. Table of the mass factors for inclusions using the differing methods of calculation

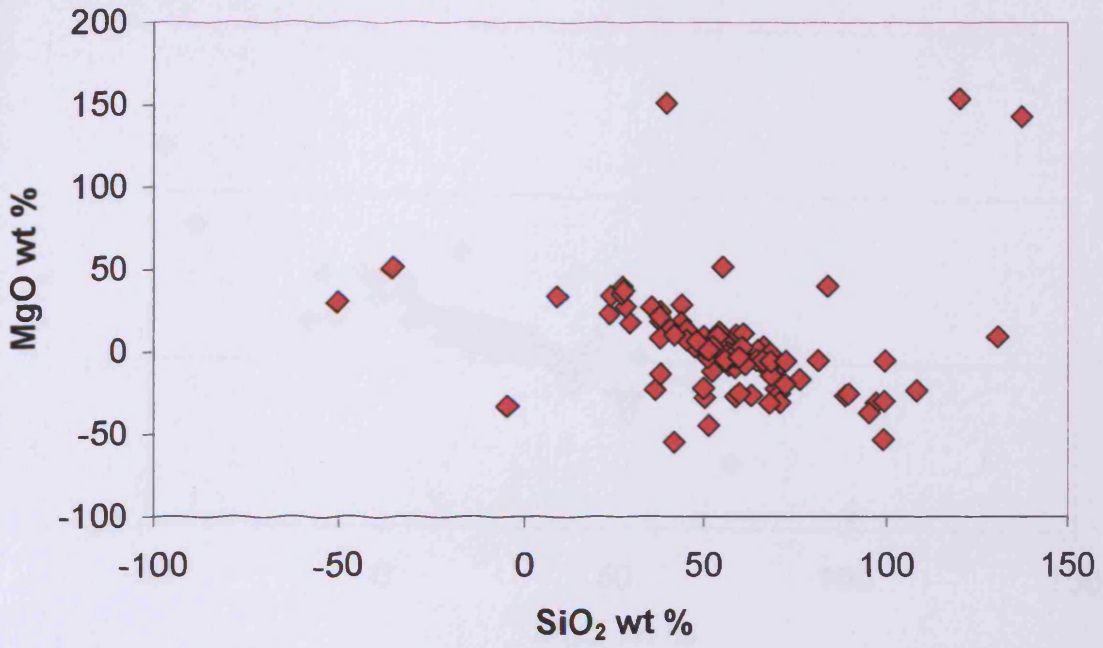

Fig. 5.31. Plot showing the concentrations of MgO and SiO_2 in the inclusions as calculated using a constant value of 14 % for Al_2O_3 to calculate the mass factors of the inclusions. Both SiO_2 and MgO show concentrations ranging from -50 wt % to greater than 100 wt %.

5.8.4 Constant value of 48 wt % SiO_2

The mass factors calculated from using a constant value of 48 wt % SiO_2 (higher value for MPG basalts Fig. 5.29) have values mostly between 0 and 1, but there are a few values that are negative or above 1 (Fig. 5.30). However, like the inclusion concentrations calculated using Al_2O_3 as an internal standard, the SiO_2 values have an extreme range for major (Fig. 5.32) and trace element concentrations in the inclusions. The MgO concentrations range from -50 to over 100 wt %, whereas the Al_2O_3 concentrations range from -50 to over 50 wt %, and the trace element, Zn, has a range from -5000 to >6000 ppm. Therefore using a constant value of 48 wt % SiO_2 to calculate the mass factor is unacceptable and will not be used.

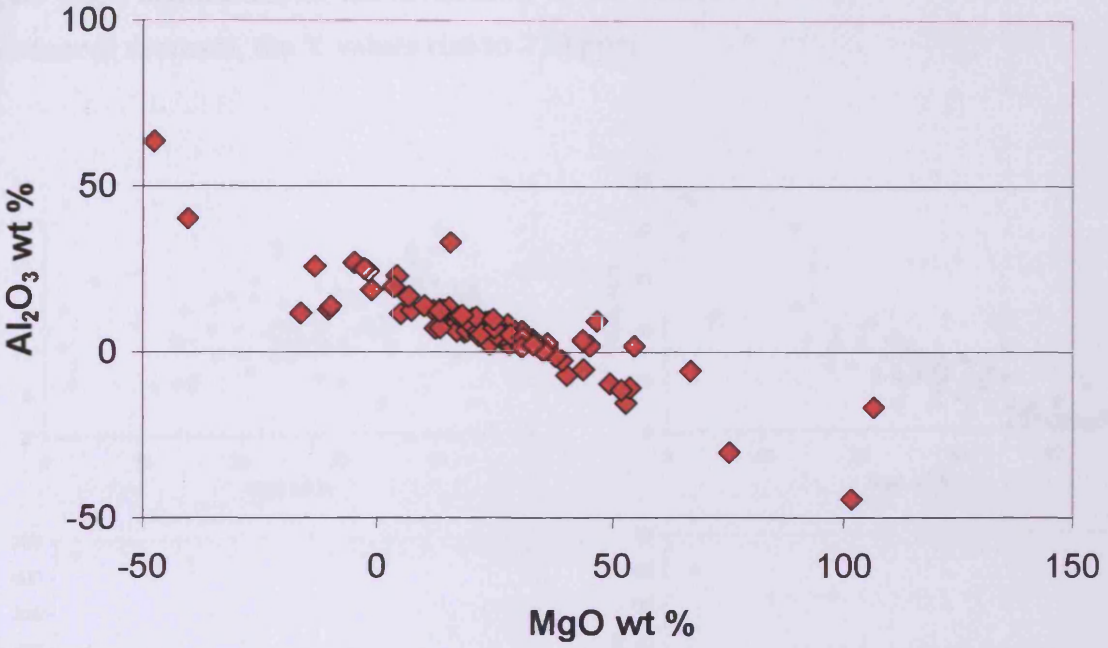

Fig. 5.32. Plot showing the concentrations of Al_2O_3 and MgO in the inclusions as calculated using a constant value of 48 % for SiO_2 to calculate the mass factors of the inclusions. Both MgO and Al_2O_3 show concentrations ranging from -50 wt % to greater than 50 wt %.

5.8.5 Variable SiO_2 concentrations

To try to increase the accuracy of the concentrations in the inclusions, all the mass factors for the inclusions have been calculated using SiO_2 values that are as near to 48 wt % as possible without producing negative values in the inclusions. The mass factors using this approach are all positive, but some values are far greater than 1, so this method is not without its problems. The main advantage of this approach is that the concentrations in the inclusions all have positive values. From Fig. 5.33a-d, it is clear that the MgO values are generally too high, and the Al_2O_3 values are too low, although the trend between the two oxides is what might be expected, i.e. as the MgO concentrations decrease, the Al_2O_3 concentrations increase. The Fe_2O_3 concentrations are more tightly constrained, having values that are generally between 5 and 20 wt %, but again this is probably greater than expected. Zn concentrations in the inclusions do not change significantly as the MgO concentration decreases, and average ~100 ppm (Fig. 5.33c). This trend is expected as Zn has a partition coefficient of ~1 in olivine. Y, is highly incompatible in olivine, so there should be a gradual increase in its abundance in the inclusions as MgO decreases, and this is what is observed in Fig. 5.33d. At

higher MgO abundances in the inclusions, Y has values of <10 ppm but, as the MgO abundances decrease, the Y values rise to >20 ppm.

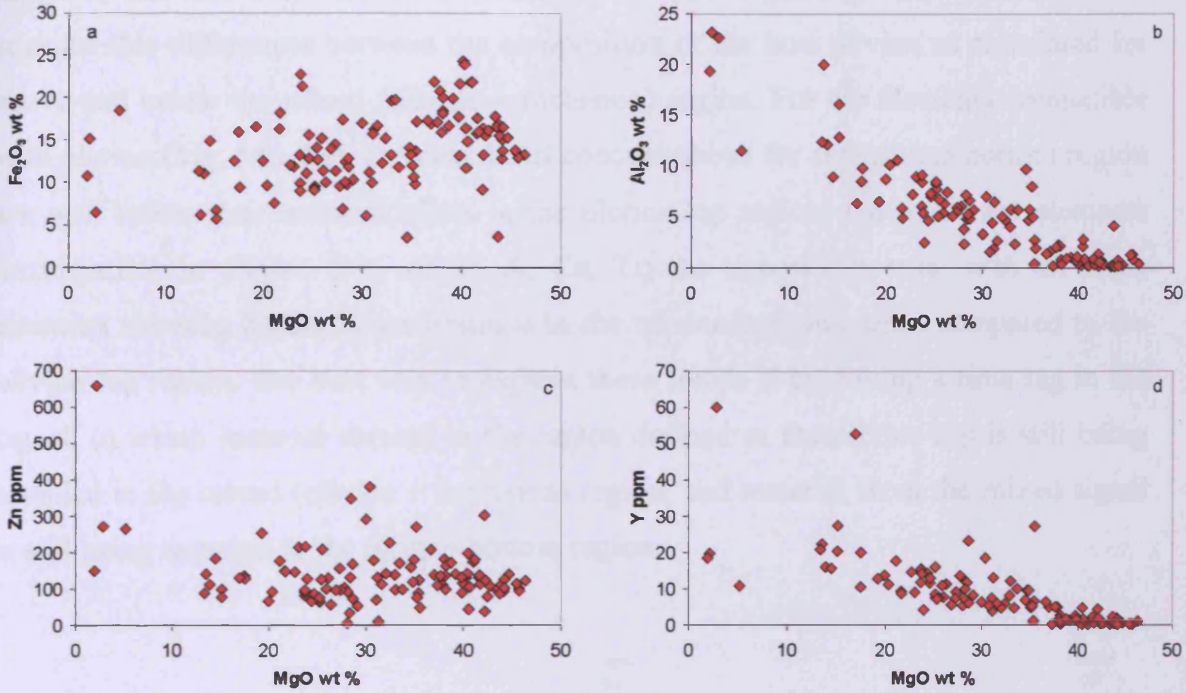

Fig. 5.33a-d. Plots of selected oxides and elements calculated using a variable concentration of SiO_2 in the inclusions to calculate the mass factor. There is still a considerable spread in concentration, particularly for MgO and Al_2O_3, but it is by far the best method for the calculation of concentrations in the inclusions.

5.9 Problems with analysis

Even though the techniques developed here are slightly different to Halter *et al.* (2002), the essentials are the same in that segments are defined according to whether they contain host olivine or a mixture of olivine and inclusion (Fig. 5.27). However, there are problems with the ratios between oxides and/or elements (Fig 5.32a-d). Fig. 5.34 shows the time-resolved signal (counts per second) for Mg and Al during the ablation of a pit into an olivine containing a melt inclusion. Three areas for analysis have been defined: 1) olivine-top (host olivine above the inclusion); 2) olivine + inclusion (host olivine and melt inclusion); 3) olivine-bottom (host olivine below inclusion).

In principle and practice, it is therefore possible to define regions as host material and mixed (host + inclusion) material. However, the calculated concentrations for oxides from the three defined areas in the experimental run shown in Fig. 5.34, suggests that this may not be the case. It is clear from Fig. 5.35 that there are considerable differences between the composition of the host olivine as calculated for above and below the mixed (olivine + inclusion) region. For the elements compatible with olivine (Mg, Mn, Fe), the calculated concentrations for the olivine-bottom region are well below their concentrations in the olivine-top region. However, for elements incompatible in olivine (Na, Al, P, K, Ca, Ti) the opposite is true, with all these elements showing higher concentrations in the olivine-bottom region compared to the olivine-top region. The best way to explain these trends is by having a time lag in the signal, in which material ablated in the region defined as the olivine-top is still being sampled in the mixed (olivine + inclusion) region, and material from the mixed signal is still being sampled in the olivine-bottom region.

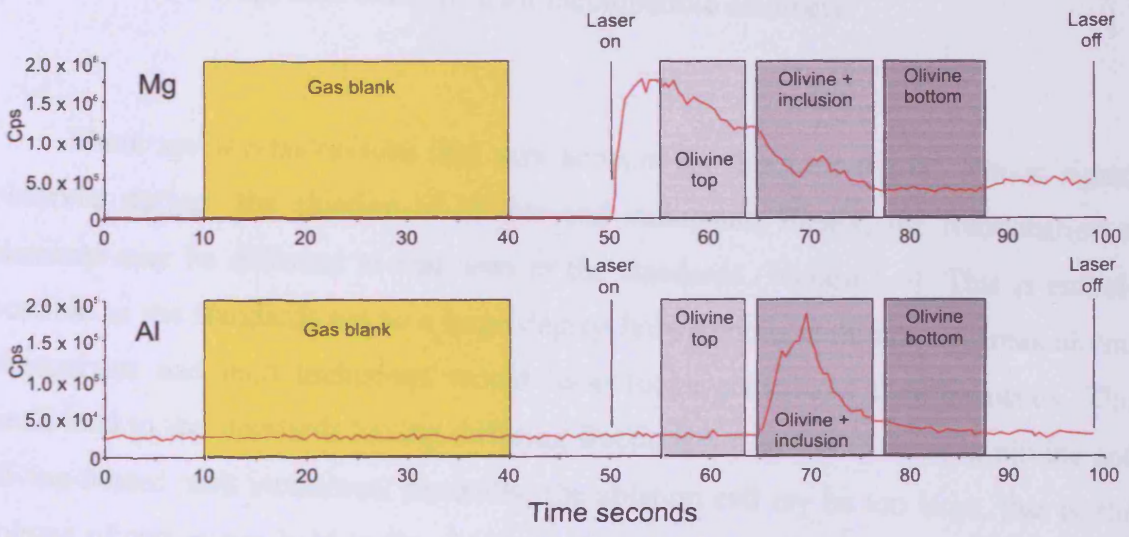

Fig. 5.34. Diagrams showing the Mg and Al signal profiles (counts per second) and time-slices defined for the analysis of olivine and mixed (olivine + inclusion) regions, during the ablation of a olivine phenocryst hosting an inclusion.

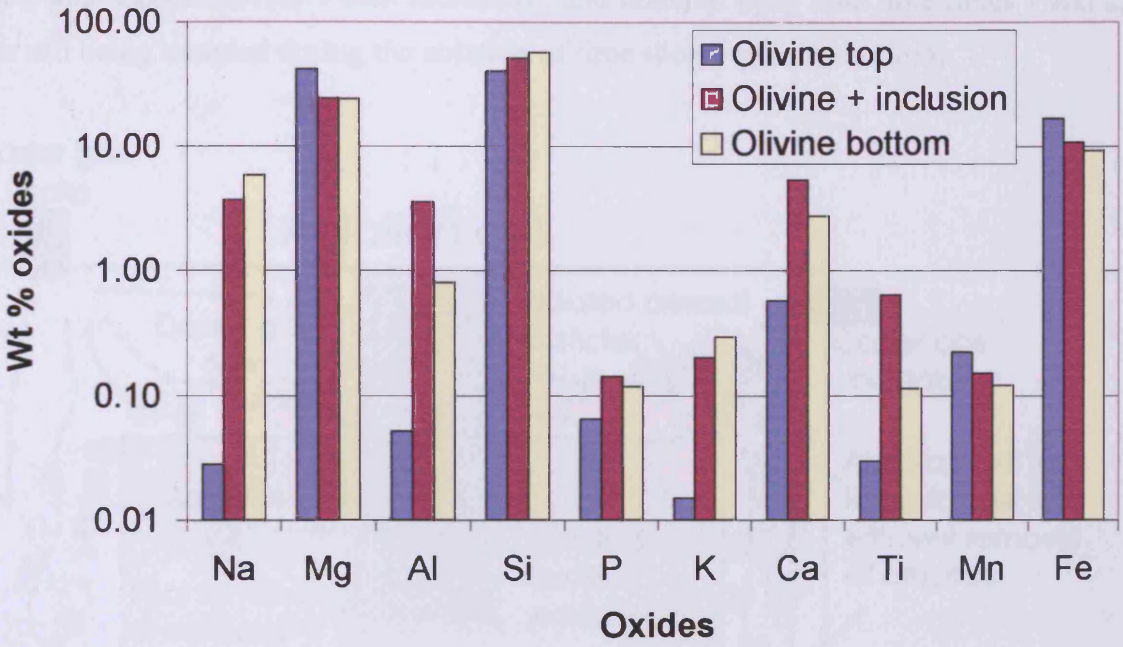

Fig. 5.35. Diagram showing the calculated composition of the three time slices in Fig. 5.34 (all elements are reported as oxides). All olivine-compatible elements show lower concentration in the olivine-bottom region, with the opposite being true for incompatible elements.

There are several reasons that may account for this time lag in element signals observed during the ablation of olivine and inclusions. Firstly, the fractionation of elements may be different to that seen in the standards (section 5.6). This is entirely possible as the standards are to a large degree homogenous materials, whereas olivine phenocrysts and melt inclusions would have to be considered heterogeneous. This could lead to the standards having differing fractionation trends to those in olivine and olivine-hosted melt inclusions. Secondly, the ablation cell my be too large, that is, the volume of carrier gas held in the ablation cell is too large for the efficient removal of ablated material (Fig. 5.36). As a matter of reference, the size of the ablation cell used by Halter *et al.* (2002) is considerably smaller than the one used during this study. Thirdly, and probably the most fundamental reason for the time lag signal, is the inability of the carrier gas to remove ablated aerosols from the ablation pit (Fig. 5.36). Leading to ablated material remaining in the ablation pit, this is then sampled at a later point in the analysis. This tail-off in analytical signals is illustrated in Fig. 5.37. Where material ablated in time slice 1 (olivine top) is still being sampled during the ablation of

time slice 2 (host olivine + melt inclusion), and material from both time slices 1 and 2, are still being sampled during the ablation of time slice 3 (olivine bottom).

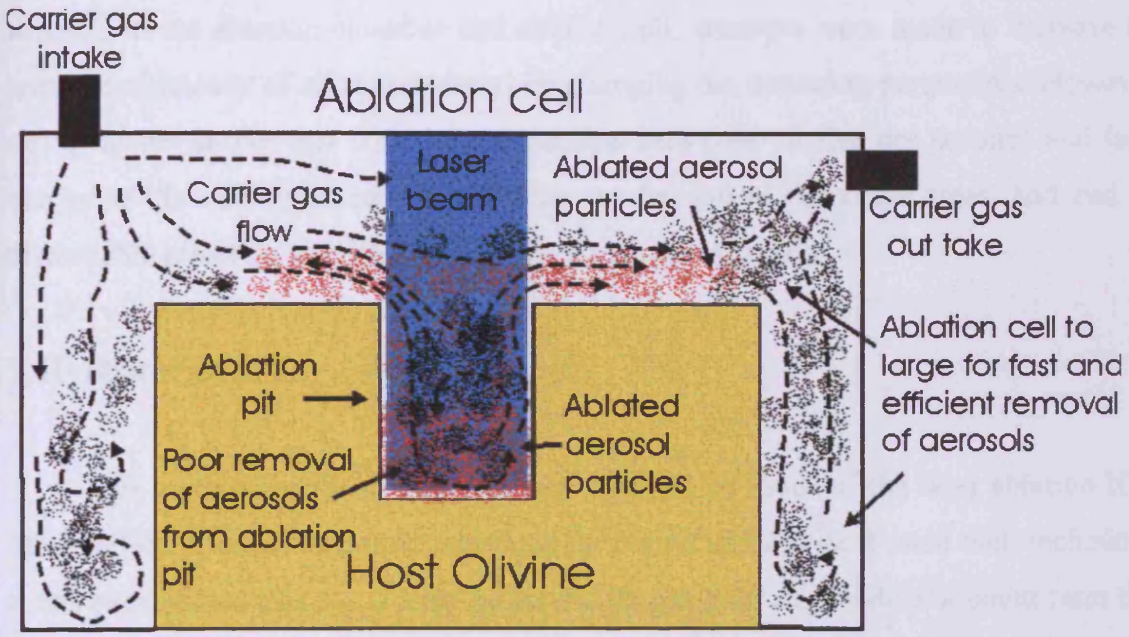

Fig. 5.36. Schematic diagram (not to scale) of ablation cell, showing the difficulties associated with the removal of ablated aerosol particles from ablation pit and ablation cell.

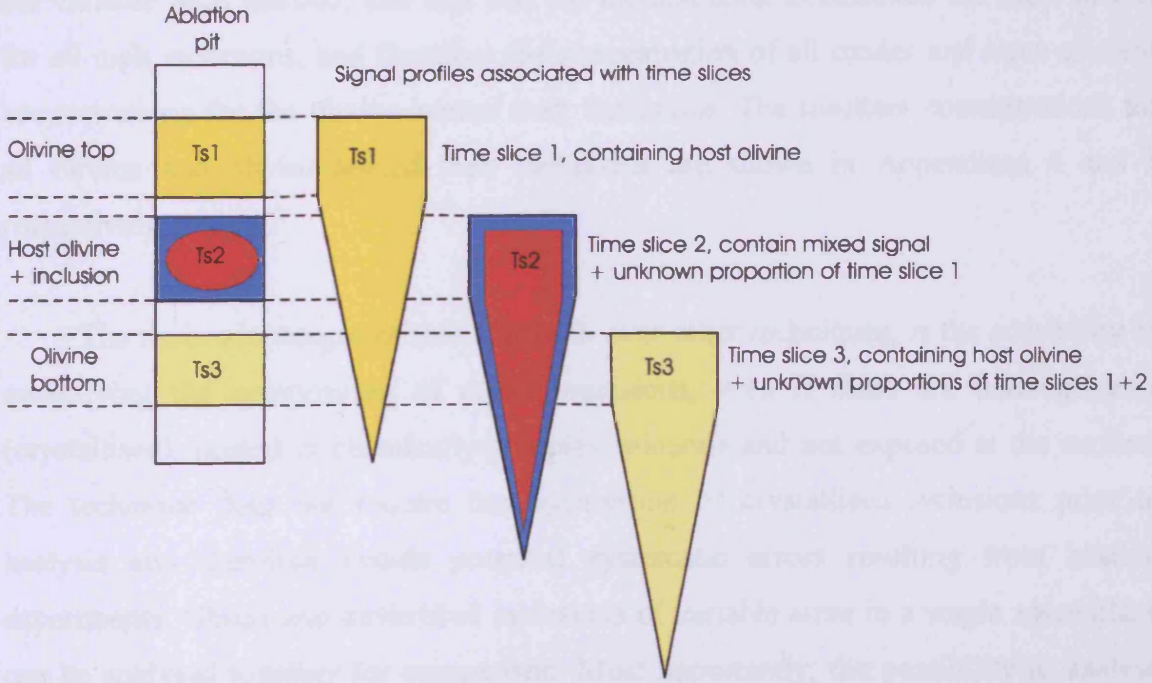

Fig. 5.37. Diagram showing the tail off in signal after the defined area for analysis has been passes

5.9.1 Changing laser parameter

As the tail off in counts is probably due to some extent, to the retention of ablated aerosols in the ablation chamber and ablation pit, attempts were made to increase the removal efficiency of ablated material by changing the operating parameters. However, changing the carrier gas rate, laser repetition rate (rate of fire per second) and laser energy levels only resulted in increasing or decreasing the count rates, and had no discernable affect on the time lag signals of ablated materials.

5.10 Discussion

This work presents an evaluation of different methods of the laser ablation ICP-MS analysis of major and trace elements in olivine and olivine-hosted melt inclusions. It has been shown that He is a far better carrier gas than Ar, producing count rates that are up to 8 fold that of Ar, and therefore He was used as the carrier gas in all experiments of olivine and olivine hosted melt inclusions. Determination of the mass ratio x (mass of inclusion/mass of mixture (inclusion + olivine)) proved to be very problematic, probably due to poor removal of ablated material for the ablation site and ablation cell. Although far from perfect, the method that produced the best results was the variable SiO_2 method, and this was the method used to calculate the mass factors for all melt inclusions, and therefore the concentration of all oxides and trace element concentrations for the olivine-hosted melt inclusions. The resultant concentrations for all olivine and olivine-hosted melt inclusions are shown in Appendices 4 and 5 respectively.

The main advantages of this approach over other techniques, is the possibility of quantifying the composition of entire inclusions, even if these are heterogeneous (crystallised), hosted in chemically-complex minerals and not exposed at the surface. The technique does not require homogenisation of crystallised inclusions prior to analysis and therefore avoids potential systematic errors resulting from heating experiments. Glassy and devitrified inclusions of variable sizes in a single assemblage can be analysed together for comparison. Most importantly, the possibility to analyse

crystallised inclusions avoids a likely sampling bias inherent to conventional studies, which are systematically restricted to glassy inclusions.

The disadvantages of this method of analysis are the uncertainties with acquiring an internal standard for the inclusions, therefore increasing the uncertainties of the final compositions. However, this could be improved by homogenising several inclusions from the same samples, and analysing them by conventional means (EMP, SIMS, PIXE). Therefore, absolute concentrations and partition coefficients could be acquired for the mineral-melt system, which in turn would improve the calculation of the mass factors needed for this method of melt inclusion analysis. The other main problem with this method of analysis is the fractionation and retention of ablated aerosols in and around the ablation sit, leading to difficulties in defining areas for analysis in the analytic signal. It may be possible to mitigate these problems to a lesser or greater degree by redesigning the ablation cell, so that the volume of carrier gas held in the ablation cell is less. This should it theory improve the efficiency of the carrier gas to remove aerosols from the ablation sit.

Chapter 6
Whole Rock and Melt Inclusions Data Interpretation

6.1 Introduction

This chapter examines the whole rock and melt inclusion geochemistry, in order to evaluate the processes that have influenced the composition of the MPG basalts. A number of processes and variables control the composition of a suite of basaltic rocks such as this. Firstly, it is necessary to assess how post-emplacement processes such as hydrothermal alteration have changed the observed compositions. Second, the processes that modified the parental magmas between the time of their extraction from their source region, and their eruption at the surface. These processes potentially include fractional crystallisation and assimilation of pre-existing crustal rock during magma assent, as well as mixing with other magma batches. Finally, the composition of the source region for the parental magmas, and the melting processes involved. The approach used here is "youngest first", that is, in a study of this nature, it is vital to consider the effects of the younger processes before deciding which data can reasonably be used to model the petrogenetic history of the MPG lavas.

6.2 Secondary element mobilisation affecting the MPG basalts

Before a detailed study of the magmatic geochemistry of the MPG basalts can be undertaken, the effect of secondary alteration processes need to be assessed. The original composition of the lavas may have been altered because of element mobilisation, with far-reaching consequences for establishing primary magmatic and tectonic processes.

As shown by Bailey *et al.* (1924), Walker (1970) and Morrison (1979) lavas on Mull have been altered by the circulation of hot hydrothermal fluids, because of the emplacement of the Central Intrusive Complex. Towards the western and northern fringes of the island, the lavas remain reasonably fresh, whereas the central zones are

altered to greenschist and prehnite facies (Fig. 2.8). Olivines in the MPG basalts have, to varying extents, been altered to serpentine, chlorite, iddingsite and oxides (Section 3.2.1), while the clinopyroxenes and feldspars (both phenocrysts and groundmass phases) show no alteration. It therefore appears that the MPG basalts used in this study only reached the lowest (zeolite) alteration grades. The following sections are subdivided, on the basis of elemental groups that behave similarly when affected by secondary alteration.

6.2.1 High field strength elements (i.e. Nb, Zr, Y, P, Ti, Ta, Hf)

There is a consensus that high field strength elements (HFSE) are relatively immobile at low to moderate alteration grades (e.g. Cann, 1970; Walker, 1970; Hart *et al.*, 1974; Wood *et al.*, 1976; Floyd and Tarney, 1978; Morrison, 1978; Ludden *et al.*, 1982; Gibson *et al.*, 1982). For example, in the Icelandic Research Drilling Programme (IRDP), the deepest lavas recovered, which were extensively epidotized and metamorphosed to greenschist facies, have retained their original magmatic HFSE concentrations (Gibson *et al.*, 1982). Although the Icelandic lavas can be considered geologically young, comparisons can also be made with far more ancient complexes, For example, the Abitibi Greenstone Belt contains lavas that have been metamorphosed to zeolite-lower amphibolite facies, and represent a far more extreme case of element mobility . At lower grades of metamorphism (i.e. zeolite facies), HFSE and rare-earth elements (REE) were found to be immobile in the Abitibi Greenstone Belt basalts (Ludden *et al.*, 1982). Even at amphibolite grade, the lavas have retained their magmatic Zr/Y and Zr/Ti ratios, although the REE have been leached and redeposited. The epidotization, which has affected the Icelandic basalts, and the amphibolite facies metamorphic grades within the Abitibi greenstone lavas, both represent far more extreme alteration than have affected the MPG basalts of this study.

Bivariate plots of HFSE for the MPG basalts are shown in Fig. 6.1. The highly significant correlations between pairs of incompatible HFSE shown by the MPG basalts indicate that the HFSE have remained unaffected by alteration and, as such, represent primary igneous values. Zr has been used as an index of fractionation because of its incompatibility in the MPG basalts, immobility during alteration, and relatively high

abundances. Concentrations of all the HFSE increase with increasing Zr values, indicating that the HFSE are all incompatible in the MPG basalts

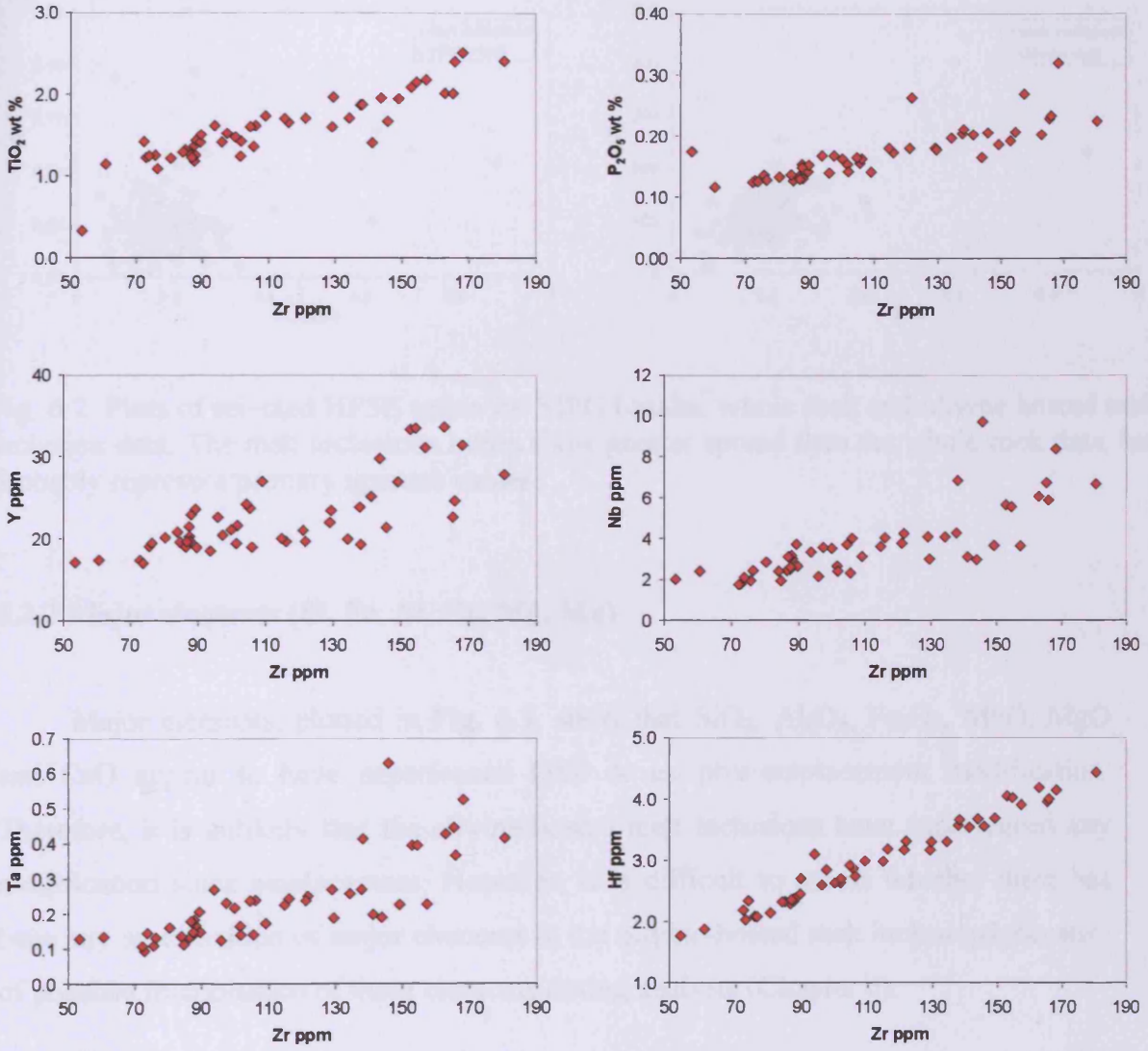

Fig. 6.1. Plots of HFS elements for the MPG basalts. The highly significant correlations indicate that the HFSE are immobile, and have not been affected by low grade alteration. All the HFSE act incompatibly and increase in concentration as the magma evolves.

As the HFSE seem to be immobile in the MPG basalts (this study), it is unlikely that the concentrations of the HFSE behave differently in the olivine-hosted melt inclusions. There are significant correlations between the whole rock and melt inclusion values for selected HFSE pairs (Fig. 6.2). However, there is greater spread in the HFSE ratios in the melt inclusions. This could be due to greater heterogeneity in the melt inclusions, or to the limitations of the method of analysis, rather than alteration.

Thus, there is good evidence that the HFSE ratios in the inclusions represent the primary igneous values.

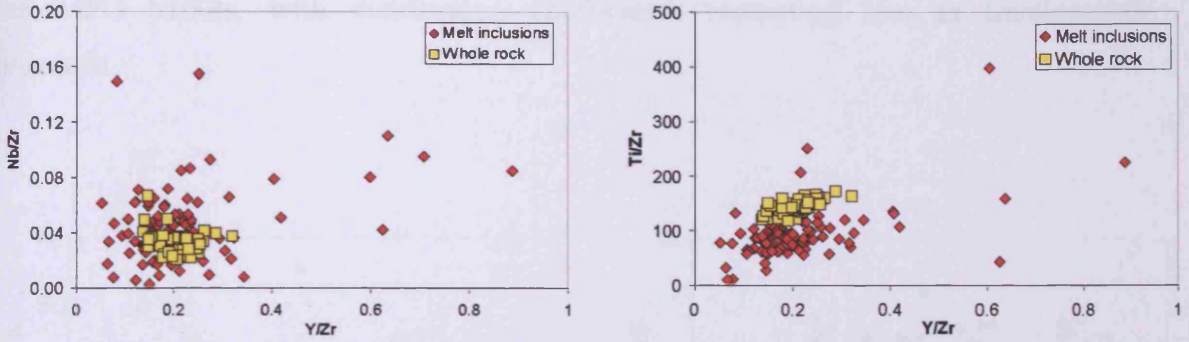

Fig. 6.2. Plots of selected HFSE ratios for MPG basalts, whole rock and olivine hosted melt inclusion data. The melt inclusions ratios show greater spread than the whole rock data, but probably represent primary igneous values.

6.2.2 Major elements (Si, Fe, Al, Ca, Mg, Mn)

Major elements, plotted in Fig. 6.3, show that SiO_2, Al_2O_3, Fe_2O_3, MnO, MgO and CaO appear to have experienced little or no post-emplacement modification. Therefore, it is unlikely that the olivine-hosted melt inclusions have experienced any modification since emplacement. However, it is difficult to assess whether there has been any modification of major elements in the olivine-hosted melt inclusions, because of possible fractionation of these elements during analysis (Chapter 5).

6.2.3 Transition metal elements (V, Zn, Ni, Cr, Cu)

Transition metal elements (TME) may be mobile in basalts, particularly at elevated temperatures (Seewald and Seyfried, 1990; Rollinson, 1993). In the MPG basalts, Ni and Cr show considerable compositional dispersion (Fig. 6.4), whereas Cu, V and Zn show far less spread; however, Ni, Cr and possibly Cu decrease with increasing Zr abundances, similar observations were made by Gibson *et al.* (1982) in the Icelandic basalts. Fractionation of olivine and augite is probably responsible for these trends, and possibly the large variations in concentrations seen for these elements in the MPG basalts (Fig. 6.4). Gibson *et al.* (1982) propose that the original variations

in Cr, Ni and Cu are difficult to estimate and hence secondary alteration effects are not easy to distinguish from original magmatic signatures. In contrast, Zn and V values increase as lavas become more evolved, indicating that Zn and V are incompatible in the MPG basalts, with distribution coefficients remaining low as fractionation proceeds.

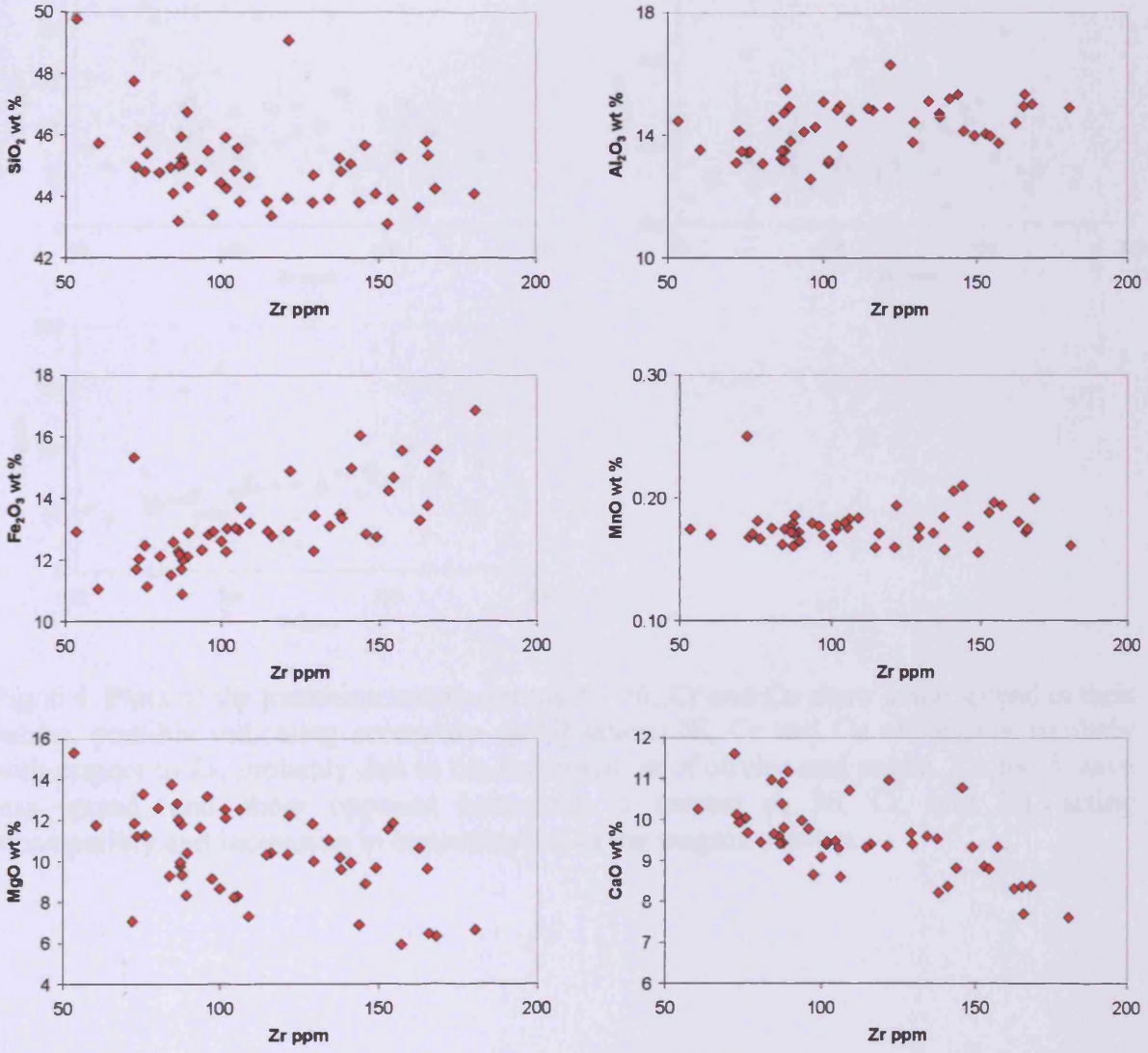

Fig. 6.3. Plots of major elements for the MPG basalts, indicating that they have undergone none or very little modification since emplacement.

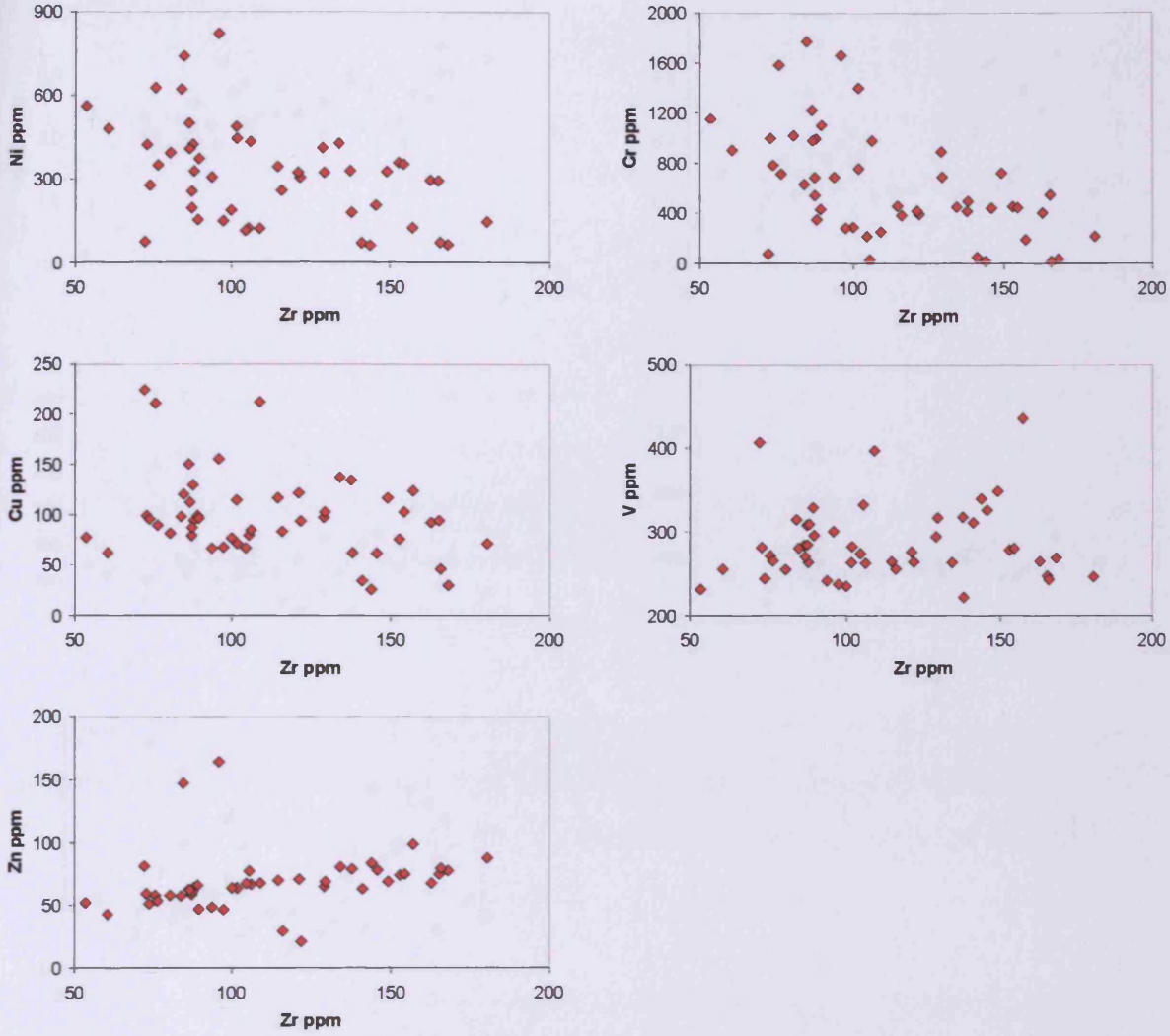

Fig. 6.4. Plots of the transition metals versus Zr. Ni, Cr and Cu show some spread in their values, possibly indicating secondary mobilisation. Ni, Cr and Cu all behave similarly with respect to Zr, probably due to the fractionation of olivine and augite. Zn and V have less spread, and show opposite behaviour in respect to Ni, Cr, and Cu, acting incompatibly and increasing in concentration as the magma evolves.

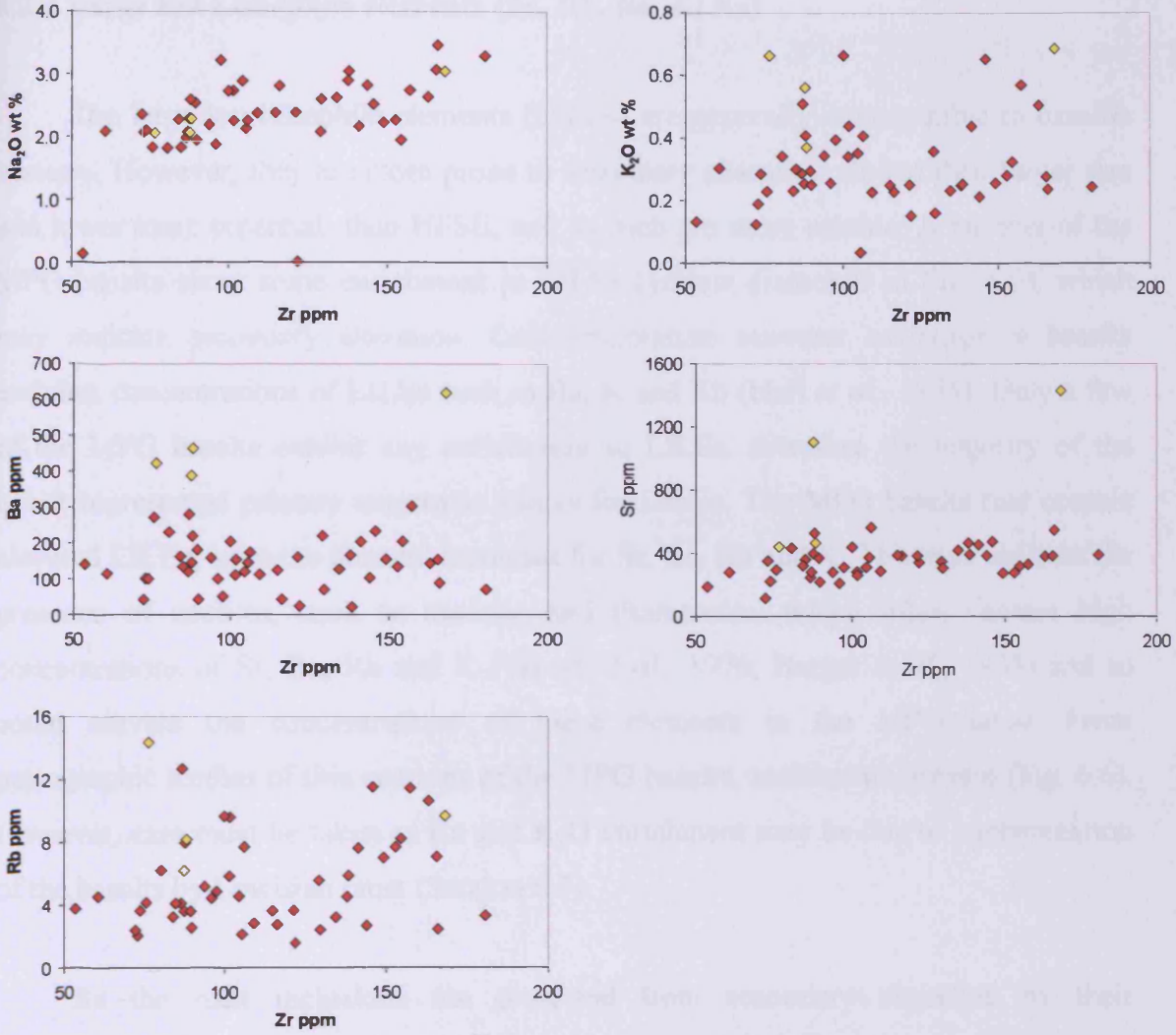

Fig. 6.5. Plots of the LILEs versus Zr for the MPG basalts. There is an indication that some of the lavas have elevated concentrations of Ba and Sr (yellow diamonds) implying that they may have been affected by alteration. However, these are limited, and most of the basalts probably represent primary compositions.

6.2.4 Large Ion Lithophile elements (Sr, Rb, Ba, K, Na)

The large ion lithophile elements (LILEs) are generally incompatible in basaltic systems. However, they are more prone to secondary alteration, due to their larger size and lower ionic potential, than HFSE, and as such are more soluble. A number of the MPG basalts show some enrichment in LILEs (yellow diamonds in Fig. 6.5), which may indicate secondary alteration. Low-temperature seawater exchange in basalts enriches concentrations of LILEs such as Ba, K and Rb (Hart *et al.*, 1974). Only a few of the MPG basalts exhibit any enrichment in LILEs, therefore the majority of the basalt represented primary magmatic values for LILEs. The MPG basalts that contain elevated LILEs, have the greatest increases for Sr, Ba, Rb and K. This may indicate the presence of zeolites, such as analcite and thomsonite, which often contain high concentrations of Sr, Ba, Rb and K (Wood *et al.*, 1976; Berger *et al.*, 1988) and so could elevate the concentrations of these elements in the MPG lavas. From petrographic studies of thin sections of the MPG basalts, zeolites are present (Fig. 6.6). However, care must be taken as Ba and K_2O enrichment may be due to contamination of the basalts by Lewisian crust (Section 6.3).

As the melt inclusions are protected from secondary alteration by their enveloping olivine crystals, they should have primary LILE/Zr ratios. Therefore, if the MPG basalts have been affected by secondary alteration, their LILE/Zr ratios should be considerably different to those of the melt inclusions. From Fig. 6.7, it is clear that this is not the case as the MPG basalts have LILE/Zr ratios that are very similar to the melt inclusions. In fact it is the inclusions that show the greatest range in values; therefore, these plots show is that there has been very little, if any, secondary alteration of the MPG basalts.

The MPG basalts have total loss on ignition (L.O.I.) values of between 1 and 6 percent. There is no significant positive correlation between increasing L.O.I. values and concentrations of LILEs (Fig. 6.8). In fact, the LILEs all show a similar range of values, for low L.O.I. to high L.O.I. values, indicating that there has been little alteration of LILE values, due to hydrothermal alteration.

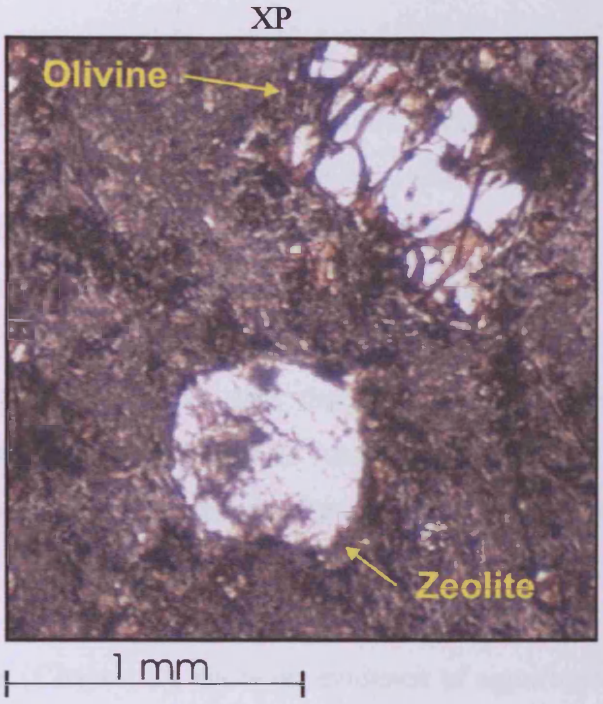

Fig. 6.6. Photomicrograph of sample BM2, showing olivine phenocryst and zeolite crystal. Zeolites are common throughout the MPG basalts.

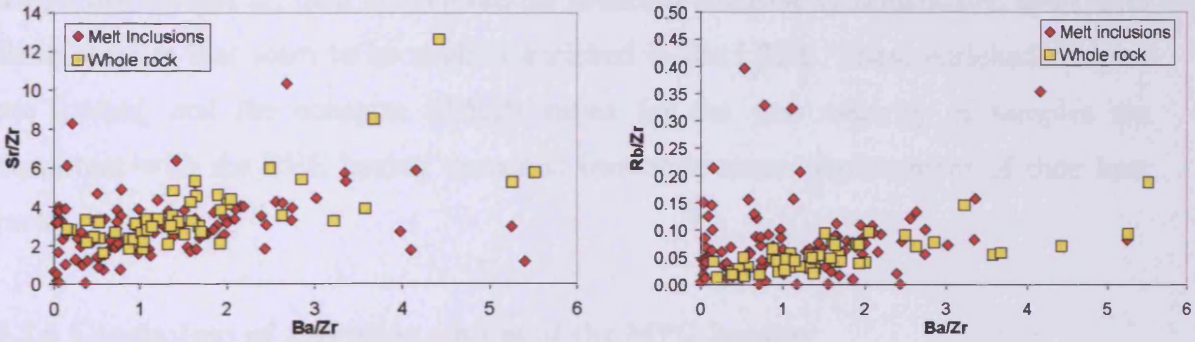

Fig. 6.7. Ratio/ratio plots of LIL elements, for both whole rock and melt inclusions. The ratios remain very similar, signifying little change to the LILE, due to secondary alteration.

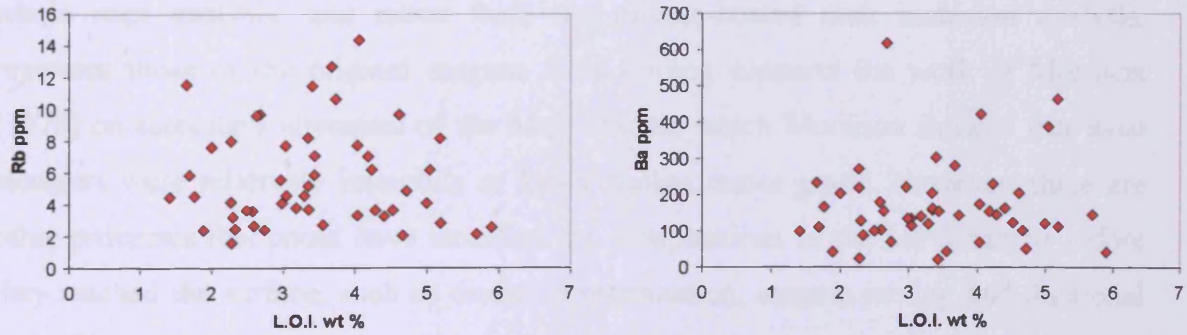

Fig. 6.8. Plots of LOI. versus selected LIL elements. There is no correlation between the LOI. values and LILE values, indicating little change to the LILEs, because of secondary alteration.

6.2.5 Rare-earth elements

Rare-earth element (REE) mobility in low-grade metamorphic rocks has been addressed by numerous workers (e.g. Morrison, 1978; Gibson *et al.*, 1982; Dostal and Strong, 1983; Bienvenu *et al.*, 1990; Marsh, 1991). The REE are highly-to-moderately incompatible, and are generally concentrated in the mesostasis, and thus have the potential to be altered (Humphris *et al.*, 1984). Therefore, mobility of the REE is more influenced by the crystallisation history of the rock, than the metamorphic grade reached. For example, a basalt that contains large amounts of interstitial glass would experience higher levels of modification of REE abundances than a highly crystalline basalt.

The highly crystalline MPG basalts (Chapter 3), show no evidence of significant secondary REE mobilisation. Fig. 6.9 shows that, when selected REE (light and heavy) are plotted against Zr, their concentrations generally increase systematically, apart from three samples that seem to be slightly enriched in the LREE. These enriched samples are limited, and the constant REE/Zr ratios for the vast majority of samples are consistent with the REE having remained immobile since emplacement of their host rocks.

6.2.6 Conclusions of alteration studies of the MPG basalts

The MPG basalts have only been affected by limited secondary alteration (zeolite facies). Therefore, it is reasonable to assume that the elemental concentrations in the whole rock analysis, and ratios from the olivine-hosted melt inclusion analysis, represent those of the original magma. This finding supports the work of Morrison (1978) on secondary alteration of the Mull basalts, which Morrison showed that most elements were relatively immobile at lower zeolite facies grade. However, there are other processes that could have modified the compositions of the MPG basalts before they reached the surface, such as crustal contamination, magma mixing and fractional crystallisation.

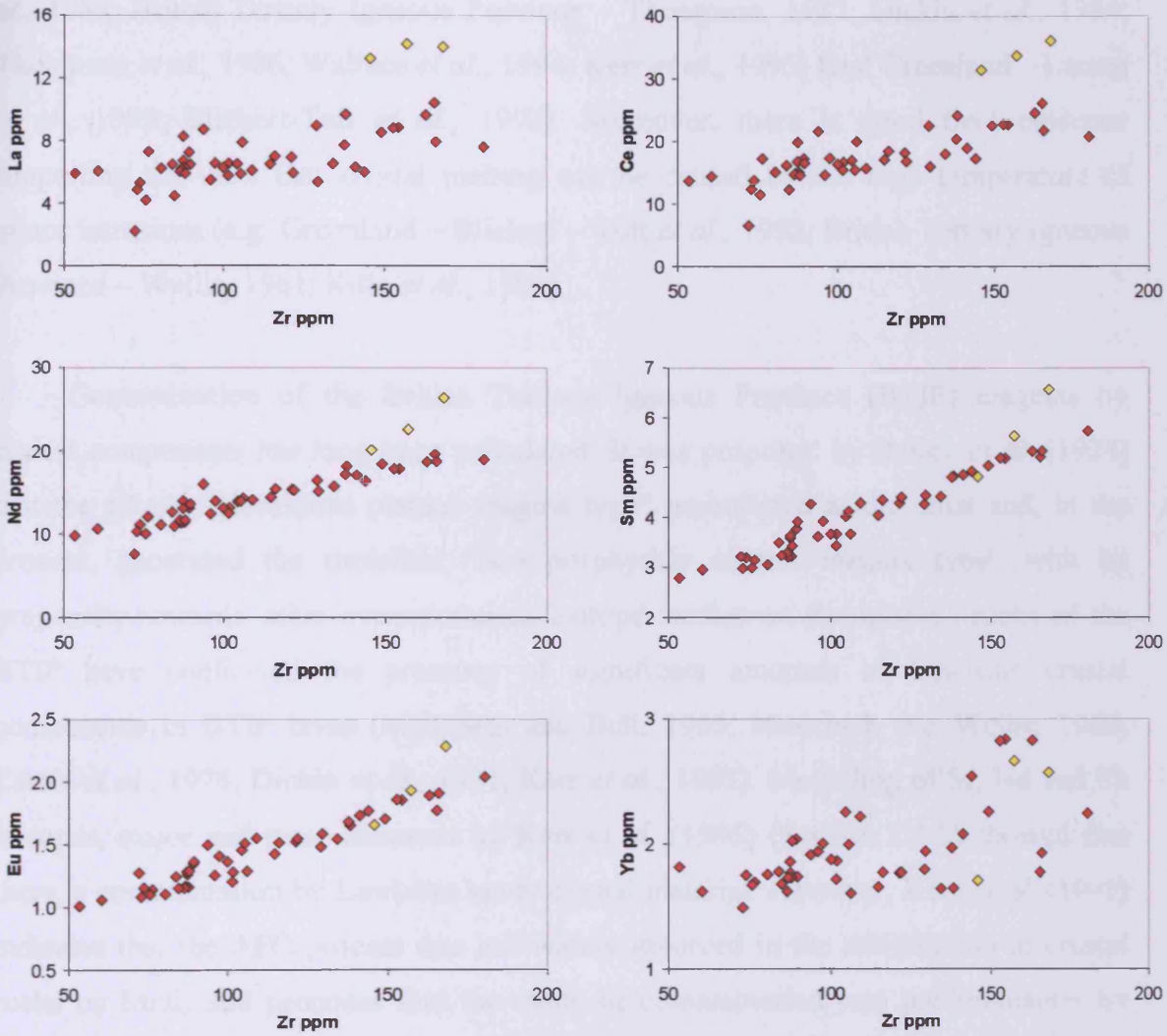

Fig. 6.9. Plots of REE/Zr ratios of the MPG basalts. The tight ratios are consistent with the incompatible nature of the REEs and their lack of secondary mobilisation.

6.3 Crustal contamination of the MPG basalts

Contamination of hot basaltic magmas by crustal components, while passing through thick continental crust, is a plausible and thermodynamically possible process. Two methods of contamination have been postulated: assimilation of crustal rocks with concomitant fractional crystallisation (AFC-DePaolo (1981) Section 1.4.3); and assimilation of crustal rock during turbulent assent (ATA-Moorbath and Thompson (1980) Section 1.4.3). Crustal contamination processes have been demonstrated geochemically in many different igneous provinces (e.g. Deccan Traps – Cox and Hawkesworth, 1985; Devey and Cox, 1987; Karoo – Cox, 1988; Parana – Mantovani *et*

al., 1985; British Tertiary Igneous Province – Thompson, 1982; Dickin *et al.*, 1984; Thompson *et al.*, 1986; Wallace *et al.*, 1994; Kerr *et al.*, 1995; East Greenland – Larsen *et al.*, 1989; Blichert-Toft *et al.*, 1992). Moreover, there is good field evidence supporting the view that crustal melting can be caused by the high temperature of minor intrusions (e.g. Greenland – Blichert – Toft *et al.*, 1992; British Tertiary Igneous Province – Wyllie, 1961; Kille *et al.*, 1986).

Contamination of the British Tertiary Igneous Province (BTIP) magmas by crustal components has long been postulated. It was proposed by Bailey *et al.* (1924) that the alkalic "Hebridean plateau magma type" assimilated acidic crust and, in the process, generated the tholeiitic "non porphyritic central magma type" with its propensity towards silica oversaturation. Isotope studies on the igneous rocks of the BTIP have confirmed the presence of significant amounts of Lewisian crustal components in BTIP lavas (Moorbath and Bell, 1965; Moorbath and Welke, 1969; Carter *et al.*, 1978; Dickin *et al.*, 1987; Kerr *et al.*, 1995). Modelling of Sr, Nd and Pb isotopes, major and trace elements by Kerr *et al.* (1995) (Section 2.4.2) showed that there is contamination by Lewisian lower crustal material. However, Kerr *et al.* (1995) indicates that the AFC process was not widely involved in the assimilation of crustal rocks on Mull, and proposes that the mode of contamination was predominantly by ATA. I.e. the hottest (most MgO-rich) magmas have assimilated small amounts <5% acidic partial melts of Lewisian lower crust during turbulent ascent through thin, poorly connected dyke and sill like magma chambers.

Although whole rock data from the MPG basalts indicates, the mode of crustal contamination of the MPG basalts was predominantly by ATA the process (Kerr *et al* (1995), the melt inclusion data presented below reveal that the processes that led to the contamination of the MPG basalts are much more complicated than previously thought. Geochemical evidence does support the view that the ATA process was the mode of contamination for many MPG lavas. However, there is evidence from other lava flows that AFC process was equally important, this has also been shown by Kerr, (1995). Furthermore, the timing of contamination differs from flow to flow, with some magmas exhibiting contamination at the same time as fractionation, and other magmas fractionating before or after crustal contamination.

6.3.1 Whole rock geochemistry

Kerr (1993a) has divided the lower half of the Mull lavas into chemically distinctive groups of flows, which are occasionally interleaved. These units are predominantly of two types: 1) a high-MgO basalt (>8 % MgO) relatively enriched in Ba and K; 2) a low-MgO basalt-hawaiite (< 8 % MgO) type, with lower levels of Ba and K. These differences can be seen on Primitive Mantle normalised (Sun and McDonough, 1989) diagrams (Fig. 6.10a and d). The Type-1 basalts (> 8 % MgO, $(Ba/Nb)_{mn} > 2$) are shown in Fig. 6.10a, and make up the bulk of the samples analysed in this study, most of which have a distinctive Nb trough. The Type-2 basalt-hawaiite (< 8 % MgO, $(Ba/Nb)_{pmn} < 2$) are shown in Fig. 6.10b and are quite limited in this study; unlike the type one basalts, these have no discernable Nb trough

Having separated the MPG lavas (this study) on the basis of their MgO and $(Ba/Nb)_{pmn}$ ratios, a number of samples do not fall into either of the defined groups, and have been ascribed their own groups as defined by Kerr, (1995). The Type-3 basalt-hawaiite, (< 8 % MgO, $(Ba/Nb)_{pmn} >2$ (Fig. 6.10c)) have similar Nb troughs to the Type-1 basalts, but lower MgO. In contrast, the Type-4 basalts (> 8 % MgO, $(Ba/Nb)_{mn}$ <2 (Fig.6.10d)) have no Nb troughs, akin to Type 1 basalts, but higher MgO. A plot of $(Ba/Nb)_{pmn}$ versus MgO for all the MPG samples (Fig. 6.11) show that although the correlation between $(Ba/Nb)_{pmn}$ and MgO is far from perfect, the trend is for the $(Ba/Nb)_{pmn}$ ratios to rise as the MgO concentrations increase. Thus, in general, the more basic lavas have the highest $(Ba/Nb)_{pmn}$ ratios (Type-1), with just two of the lavas having low $(Ba/Nb)_{pmn}$ ratios and MgO concentrations (Type-2).

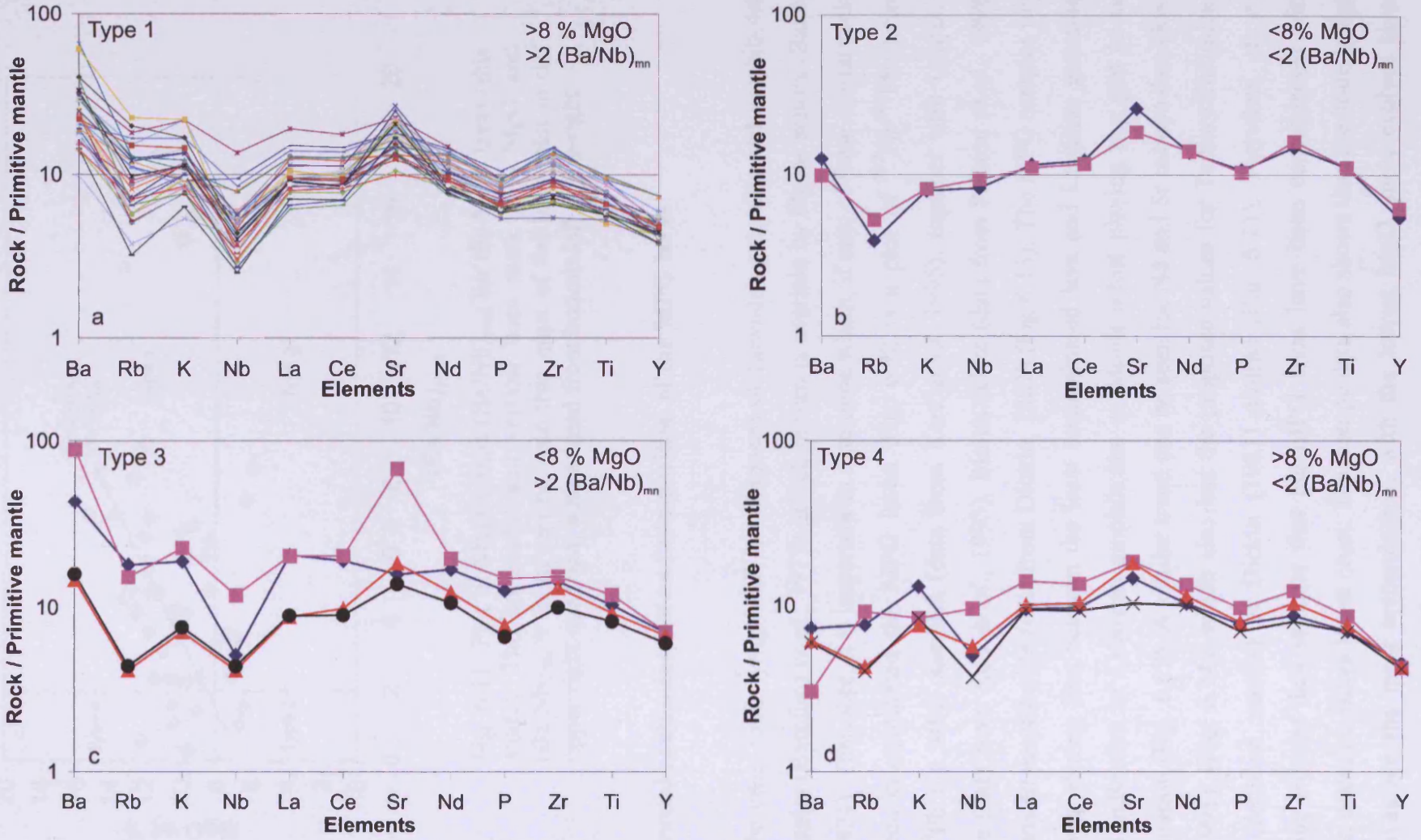

Fig. 6.10a-d. Primitive Mantle (Sun and McDonough, 1989) normalised diagrams showing analyses of the four chemically distinctive lava types found in the lower half of the MPG lavas

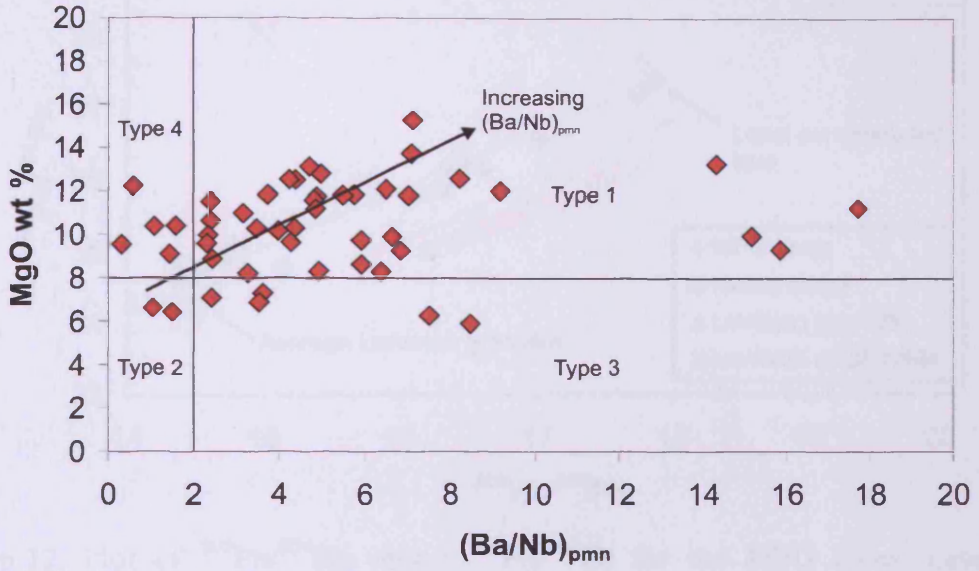

Fig. 6.11. Plot of MgO versus $(Ba/Nb)_{pmn}$ for the MPG lavas (this study). The horizontal and vertical lines mark 8 % MgO and $(Ba/Nb)_{mn} = 2$. In can be seen that most of the lavas plot in the upper right quadrant, with a trend from bottom-left to top-right.

6.3.2 Crustal contamination and composition of the MPG lavas

The crust underlying Mull is composed of Lewisian granulite and amphibolite facies gneiss (Bamford *et al.*, 1977), which in turn is overlain by Moine schists (Bailey *et al.*, 1924). Therefore, it is important to determine which, if any, of these crustal rocks have been contaminated the MPG lavas. Fig. 6.12 is a plot of $^{207}Pb/^{204}Pb$ versus $^{206}Pb/^{204}Pb$ for MPG samples (data from Kerr *et al.* 1995), together with Lewisian granulite (data from Kerr *et al.*, 1995), Moine schist (data from Preston *et al.*, 1998) and Lewisian amphibolite (data from Dickin, 1981) (Fig 6.13). The MPG samples plot on a direct mixing line between the least contaminated lava and Lewisian granulite, with no indication of Lewisian amphibolite or Moine schist playing any part in the contamination (Fig. 6.12). A similar trend can be seen for Nd and Sr isotope data (Kerr *et* al., 1995), (Fig. 6.14), which also has the proposed values for Tertiary Hebridean mantle (depleted mantle) of Dickin (1981) plotted (Fig. 6.13). Therefore, all the radiogenic isotope data indicate that the MPG lavas have been contaminated with Lewisian granulite facies lower crust. The isotope data also shows than the hottest, high MgO lavas are the most contaminated, with the lowest MgO, most evolved lavas having been least contamination (Fig. 6.15a).

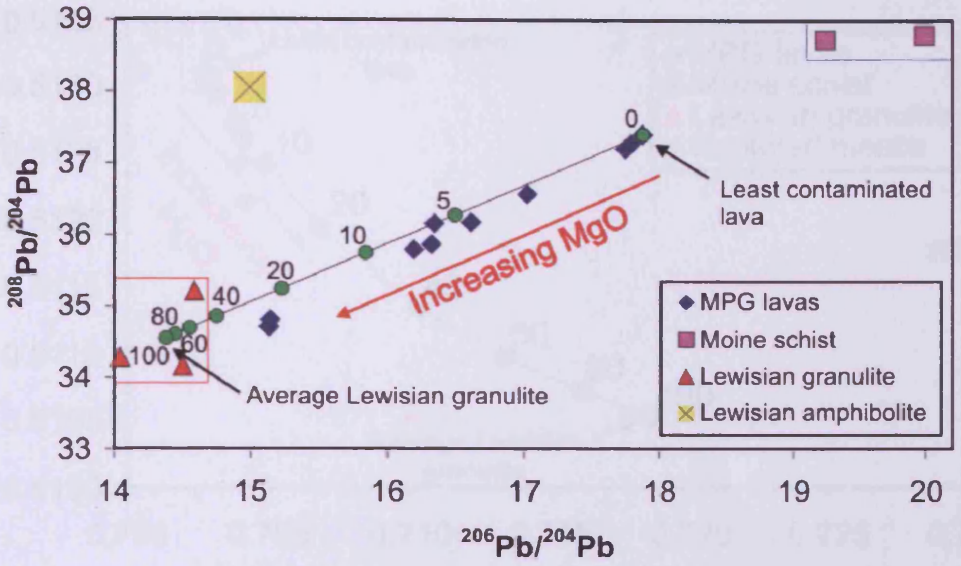

Fig. 6.12. Plot of $^{208}Pb/^{204}Pb$ versus $^{206}Pb/^{204}Pb$ for the MPG lavas, Lewisian granulite, Lewisian amphibolite and Moine schist. The Pb isotope trends indicate that the MPG lavas have been contaminated with lower crust Lewisian granulite. The numbers indicate the % of Lewisian crust on the mixing line between the least contaminated lava and average Lewisian crust

	$^{206}Pb/^{204}Pb$	$^{208}Pb/^{204}Pb$	Source
Least contaminated MPG	17.87	37.61	Kerr *et al.* 1995
Moine schist	19.99	38.99	Preston *et al.* 1998
Lewisian granulite ave	14.38	34.75	Kerr *et al.* 1995
Lewisian amphibolite	15.00	38.25	Dickin 1981
	$^{87}Sr/^{86}Sr$	$^{143}Nd/^{144}Nd$	
Least contaminated MPG	0.7029	0.5105	Kerr *et al.* 1995
Moine schist	0.7299	0.5122	Preston *et al.* 1998
Lewisian granulite ave	0.7186	0.5105	Kerr *et al.* 1995
Depleted mantle	0.7026	0.5130	Dickin 1981

Fig. 6.13. Table of the isotope ratios used in Figs. 6.13 and 6.14

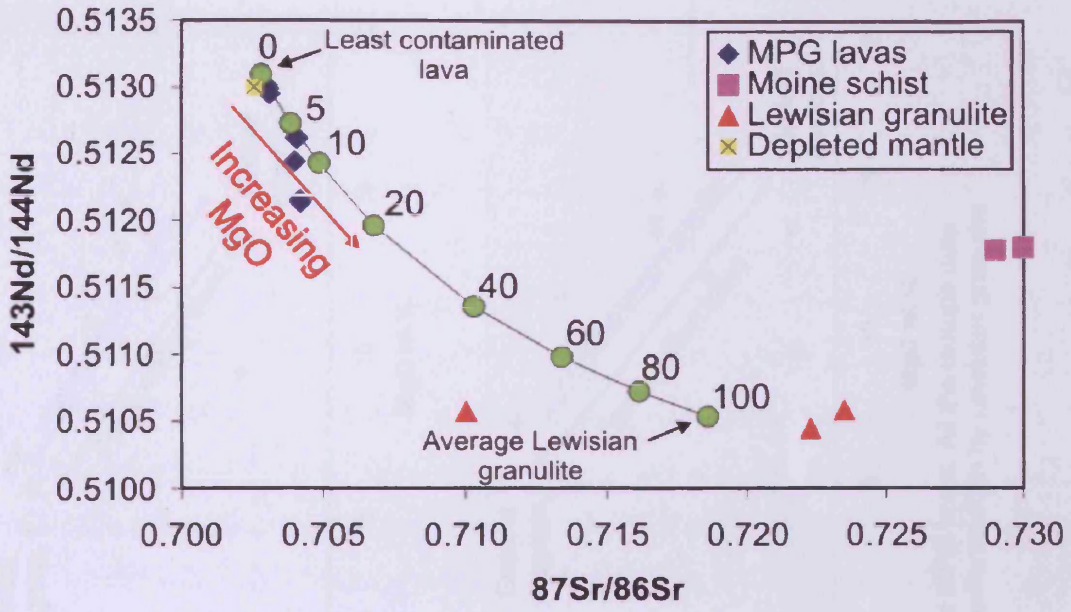

Fig. 6.14. Plot of $^{143}Nd/^{144}Nd$ versus $^{87}Sr/^{86}Sr$ for the MPG lavas, Lewisian granulite, Moine schist and proposed Tertiary Hebridean depleted mantle of Dickin (1981). The depleted mantle values are very close to that of the least contaminated lava, with the overall isotope trends indicating contamination with Lewisian crust. The number indicate the % of Lewisian crust on the mixing line, between the least contaminated lava and average Lewisian crust.

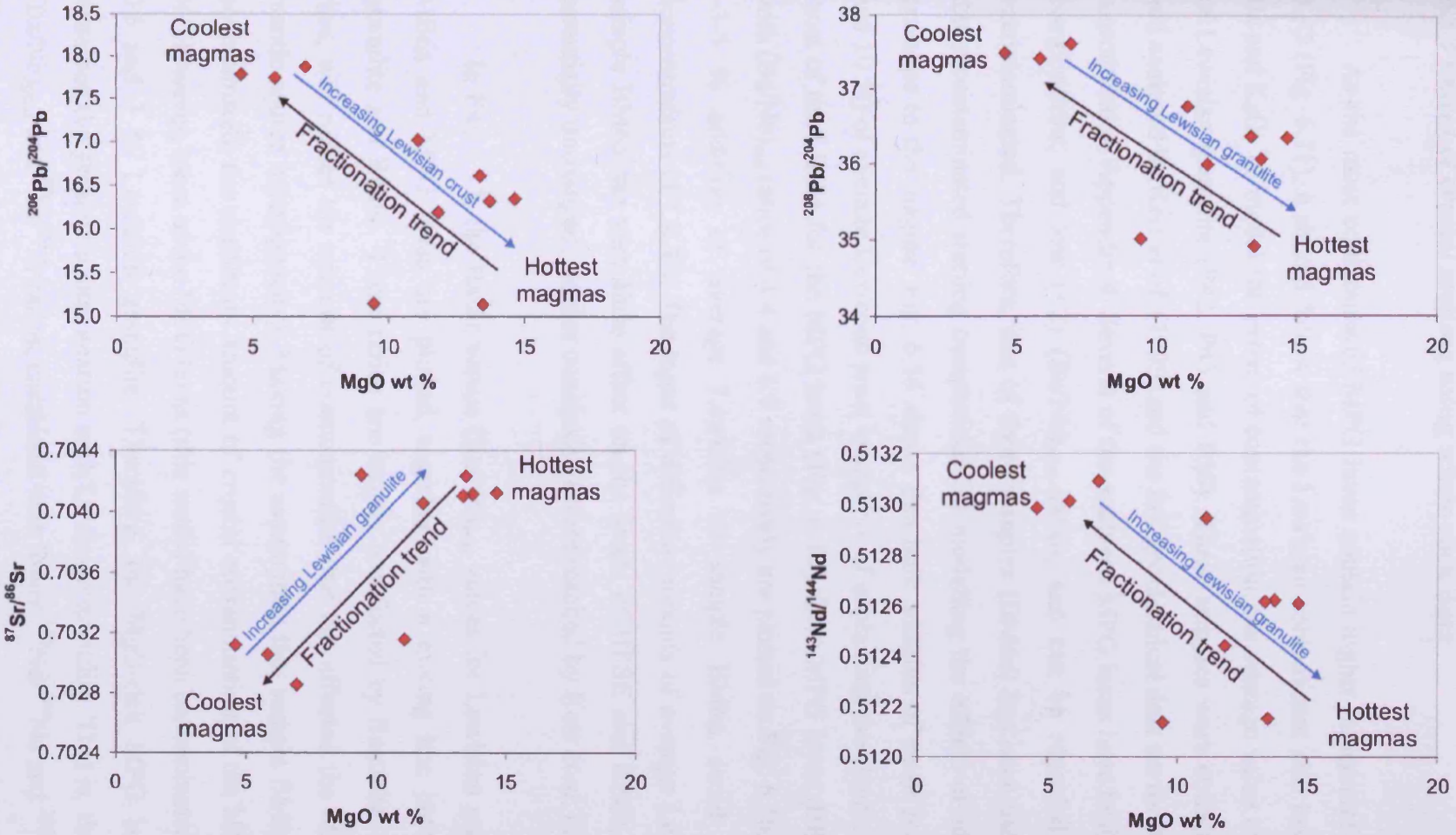

Fig. 6.15. Plots of MgO wt % versus radiogenic isotope ratios for selected MPG lavas. All the isotope data points to the hottest most primitive magmas having suffered the greatest contamination by Lewisian granulite

6.3.3 Extent of crustal melting using whole rock data

As the most contaminated MPG lavas contain higher concentrations of Ba and K_2O (Fig. 6.11), it should follow that the Lewisian contaminant also has high levels of Ba and K_2O. To model the extent of contamination, the average value of three samples of Lewisian granulite (P42, P43 and P50). These samples were collected from Tiree and analysed by Kerr *et al.* (1995) and the full geochemical data set for these samples is reproduced in Appendix 4. Several of the analysed MPG lavas have basic (>8 %) MgO compositions, and low (<2) $(Ba/Nb)_{pmn}$ ratios, and can be regarded as essentially uncontaminated. Therefore, one of these samples (BM6a) has been used to represent the uncontaminated starting composition, in modelling the effects of adding Lewisian granulite to the magma. Fig. 6.16 shows that bulk addition of small proportions (3, 5 and 10 %) of average Lewisian crust is capable of explaining the chemical variations in most of the LILEs for the MPG lavas (Fig. 6.10). Two MPG lavas, BB21 and BB22, with $(Ba/Nb)_{mn}$ ratios of 4.4 and 6.7 respectively are plotted on Fig. 6.16, and show that ~3-5 % addition of average Lewisian to sample BM6a could produce their concentrations of LILEs. The input of differing amounts of average Lewisian crust to sample BM6a has very little affect on the levels of HFSE and REEs, which remain essentially unchanged; similar conclusions were reached by Kerr *et al.* (1995).

In Fig. 6.17, the Ba/Zr versus $(Ba/Nb)_{pmn}$ values for Lewisian granulite, sample MB6a and MPG lavas are plotted, together with a mixing line between Lewisian granulite and BM6a. These ratios are largely unaffected by fractional crystallisation; thus, will reflect the amount of contamination that has affected the MPG basalts (or mantle source heterogeneity). Making the assumption that sample BM6a has not been contaminated; the maximum amount of crustal contamination of the MPG lavas is ~5 %. However, most of the MPG lavas (this study) have been contaminated with between 0.5 and 3 % Lewisian granulite. Therefore, the MgO-rich MPG lavas that have sustained the greatest contamination with Lewisian granulite. That is, they have higher $(Ba/Nb)_{pmn}$ and $^{87}Sr/^{86}Sr$ ratios, combined with lower $^{143}Nd/^{144}Nd$ and $^{206}Pb/^{204}Pb$ ratios (Figs. 6.11, 6.12, 6.14 and 6.17). In contrast, the more evolved lavas have lower $(Ba/Nb)_{pmn}$ and $^{87}Sr/^{86}Sr$ ratios and higher $^{143}Nd/^{144}Nd$ and $^{206}Pb/^{204}Pb$ ratios. Kerr *et al.* (1995) has shown that these trends are consistent with an origin for the more evolved lavas by fractional crystallisation, with very little contamination by Lewisian crust.

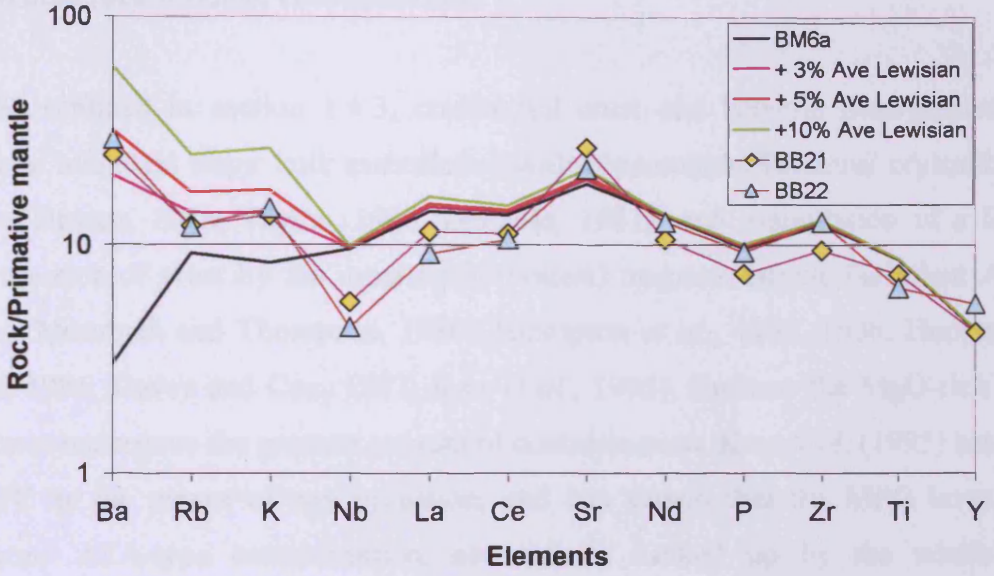

Fig. 6.16. Primitive Mantle (Sun and McDonough, 1989) normalised diagram showing the effects of adding 3, 5 and 10 % average Lewisian granulite to the relatively uncontaminated primitive MPG sample (BM6a). Two (BB21 and BB22) relatively contaminated MPG samples are plotted for comparison.

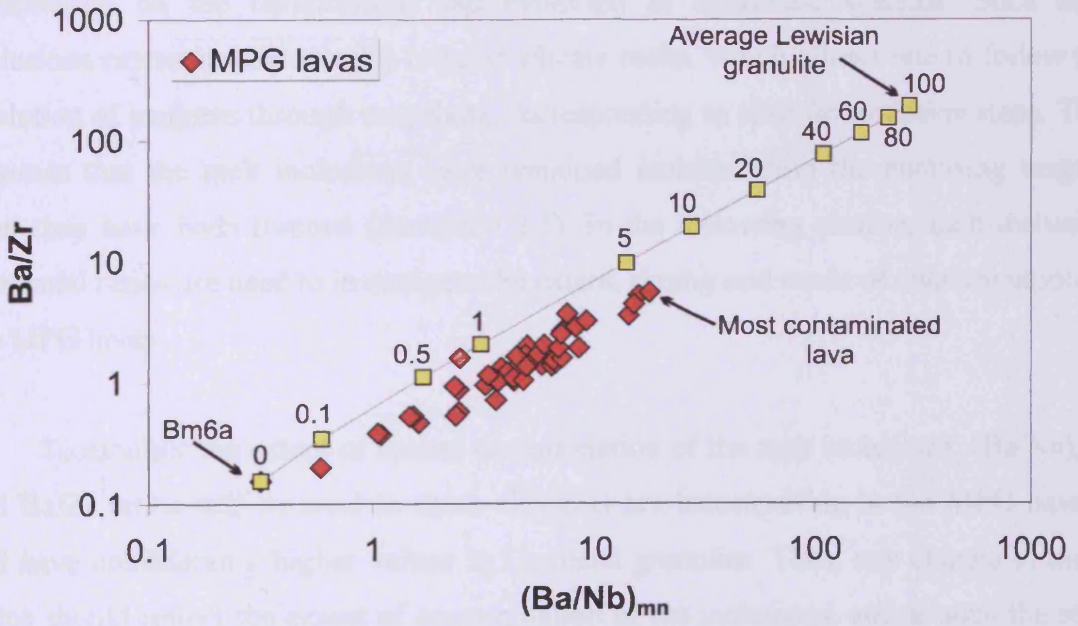

Fig. 6.17. Plot of Ba/Zr versus $(Ba/Nb)_{pmn}$ ratios for the MPG lavas, along with a mixing line between BM6a (least contaminated lava) and average Lewisian granulite. These data indicate that the maximum amount of contamination of the MPG lavas by Lewisian granulite was ~5%.

6.3.4 Whole rock mode of contamination

As outlined in section 1.4.3, continental crust can become incorporated into magma in two main ways: bulk assimilation with concomitant fractional crystallisation (AFC – Bowen, 1928; Taylor, 1980; DePaolo, 1981): and assimilation of a fusible acidic fraction of crust by the most basic (hottest) magmas during Turbulent Ascent (ATA – Moorbath and Thompson, 1980; Thompson *et al.*, 1982, 1986; Huppert and Sparks, 1985; Devey and Cox, 1987; Kerr *et al.*, 1995). Because the MgO-rich MPG lavas have undergone the greatest amount of contamination, Kerr *et al.* (1995) has ruled out AFC as the means of contamination, and has shown that the MPG lavas have undergone ATA-type contamination, and this is backed up by the whole rock geochemistry in this study.

6.3.5 Melt inclusion geochemistry

Olivine-hosted, silicate melt inclusions in igneous rocks can provide important information on the composition and evolution of magmatic systems. Such melt inclusions represent accidentally-trapped silicate melts, which allows one to follow the evolution of magmas through snapshots, corresponding to specific evolution steps. This assumes that the melt inclusions have remained isolated from the enclosing magma after they have been trapped (Section 4.2.5). In the following section, melt inclusion elemental ratios are used to investigate the extent, timing and mode of contamination of the MPG lavas.

To monitor the extent of crustal contamination of the melt inclusions, $(Ba/Nb)_{pmn}$ and Ba/Zr ratios will be used as these elements are incompatible in the MPG basalts and have considerably higher values in Lewisian granulite. Thus, any change in these ratios should reflect the extent of contamination of the inclusions, and as such the melt that the olivine is fractionating from. Fig. 6.18 shows the trends that would be observed with differing processes operating during the evolution of magma as it travels up through the crust. During the process of ATA contamination, the $(Ba/Nb)_{pmn}$ ratios will increase without any major change in the forsterite content of the olivine crystals, because the hot magma rises rapidly through the crust, with minimal fractionation.

However during AFC contamination the $(Ba/Nb)_{pmn}$ ratios will increase, and the forsterite content of the olivine crystals will fall, because the magmas pond and fractionate olivine at the same time as the magma is assimilating crustal components. A third possibility is fractionation without contamination (FWC), where the magma evolves without any assimilation of crustal components. This would occur if the magma ponds and equilibrates in the refractory lithosphere, where fractionation of olivine would proceed without contamination of the magma by the wall rocks, because of their high melting temperatures.

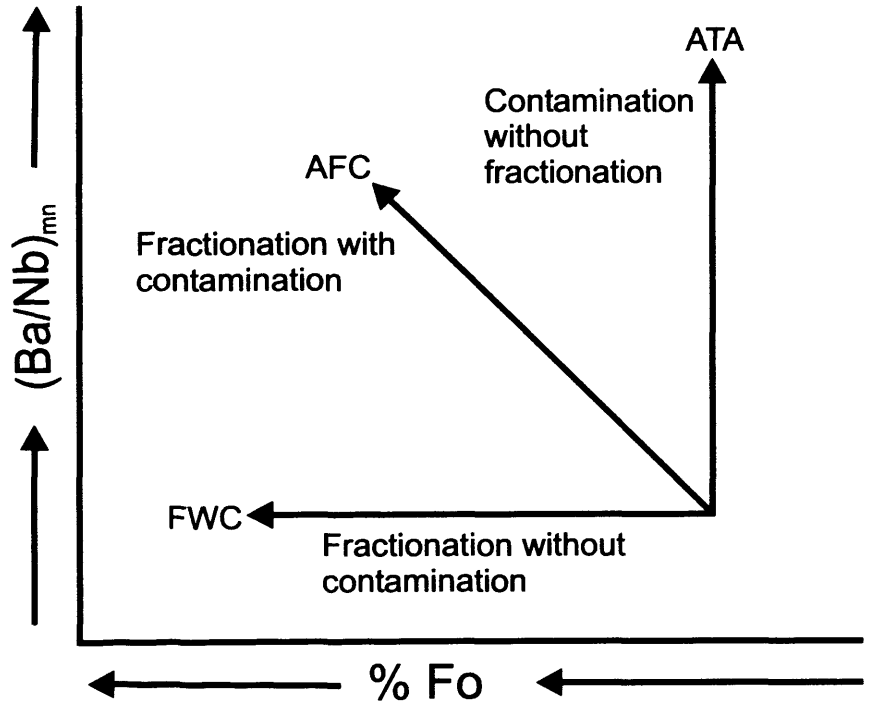

Fig. 6.18. Diagram showing the differing trends possible for the fractionation of olivine, and crustal contamination, during the ascent of MPG magmas through Lewisian granulite crust.

6.3.6 Melt inclusions mode of contamination

In Fig. 6.19 the melt inclusion $(Ba/Nb)_{pmn}$ ratios are plotted against the forsterite content of their host olivines for a series of MPG lavas. For individual MPG lavas, the forsterite content of the olivines never varies by more than three percent, indicating that fractionation in these lavas was limited. However, the highest forsterite contents of the olivines vary considerably between individual MPG lavas, from Fo 76-77 for samples BHI3 and MR9, to ~Fo86 for samples AM7b and MR10. The $(Ba/Nb)_{mn}$ ratios for all MPG lavas have low values of below 2 (shown to be uncontaminated by Kerr *et al.* 1995), and high values ranging from ~4 for sample BHI3 to ~13 for sample MR10. Therefore, these MPG lavas were considerably contaminated, while undergoing limited olivine fractionation. The best mode of contamination to explain these trends is the ATA process where the lavas have been contaminated by turbulent flow in thin dyke like conduits, while rising rapidly to the surface, as proposed by Kerr *et al.* (1995).

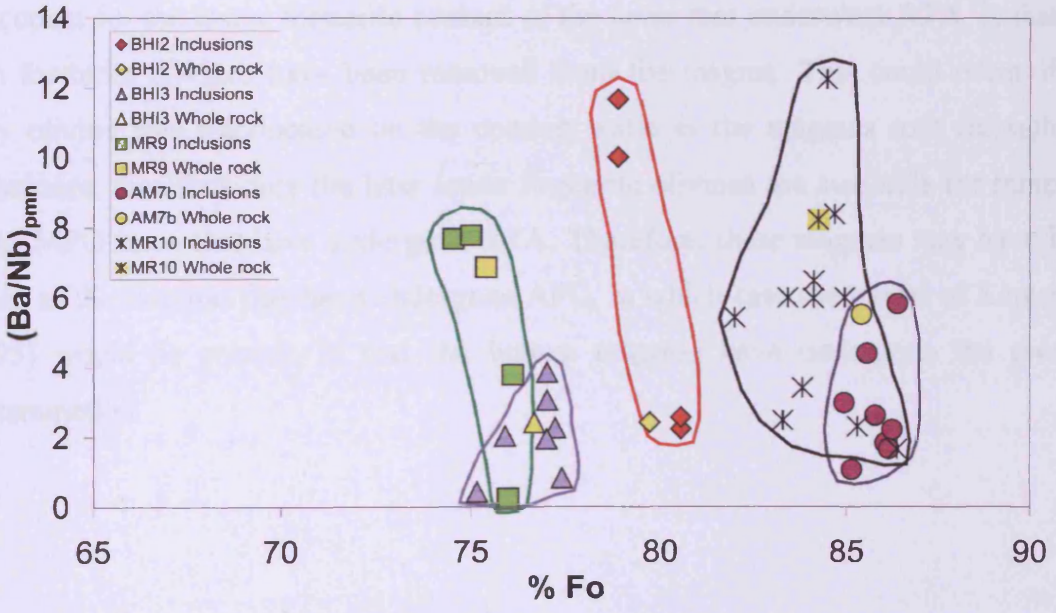

Fig. 6.19. Plot of the forsterite content of olivines for selected MPG lavas, versus the $(Ba/Nb)_{pmn}$ ratios of melt inclusions hosted in these olivine crystals. The forsterite content of the olivines very by <3%, whereas the $(Ba/Nb)_{pmn}$ ratios range from <2 to >13, all of which indicates contamination by the ATA process.

Fig. 6.20 shows forsterite content of olivines plotted against $(Ba/Nb)_{pmn}$ ratios for three MPG lavas (BM6, MR12a and AM7a). Unlike the MPG samples in Fig. 6.19, these samples show a significant range in their forsterite content. All the samples have a maximum of Fo 88, with lower values of Fo 81 for BM6 and AM7a and Fo 68 for MR12a. Although the forsterite content for these MPG samples differ for the samples in Fig. 6.19, the $(Ba/Nb)_{pmn}$ ratios are very similar, ranging from <2 for all samples to ~6 for BM6 and AM7a, and ~8 for MR12a. Thus, contamination of these MPG lavas was contemporaneous with the fractionation of olivine from the magma. This indicates that the mode of contamination of these lavas was AFC, that is, these MPG basalts possibly ponded in the lower Lewisian granulite crust where fractionation was accompanied by contamination. Interestingly, the maximum forsterite contents of these samples are all higher than that seen for the samples contaminated by ATA. As the forsterite content of the olivine is a good indicator of the temperature of the host magma, it indicates at least for the MPG samples analysed here, that the hottest magmas have undergone AFC. This is different to the findings of Kerr *et al.* (1995), who showed that the hottest magmas suffered contamination by ATA. One possibility to account for the lower forsterite content of the lavas that underwent ATA, is that the high forsterite olivines have been removed from the magma. This could occur if the early olivine was fractionated on the conduit walls as the magmas rose through the lithosphere, therefore only the later lower forsterite olivines are available for sampling in the MPG lavas that have undergone ATA. Therefore, these magmas may have been as hot as the magmas that have undergone AFC, in which case the model of Kerr *et al.* (1995) would be correct, in that the hottest magmas have undergone the greatest contamination.

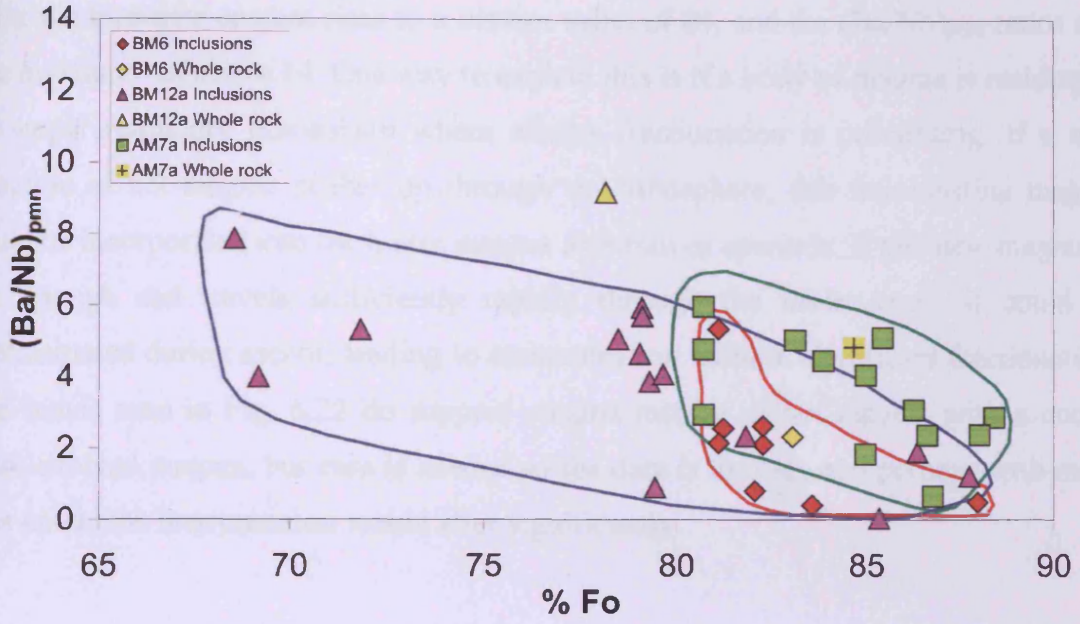

Fig. 6.20. Plot of the forsterite content of olivines for selected MPG lavas, versus the $(Ba/Nb)_{mn}$ ratios of melt inclusions hosted in these olivine crystals. The forsterite content of the olivines varies by between 7 and 20 %, whereas the $(Ba/Nb)_{mn}$ ratios very from <2 to >6, indicating that the mode of contamination was by the AFC process.

Fig. 6.21 is a plot of forsterite content versus $(Ba/Nb)_{pmn}$ for the olivine-hosted inclusions in sample AM10b. The forsterite contents of the olivines have a range between Fo77-84, indicating that a certain amount of fractionation has occurred. However, the $(Ba/Nb)_{pmn}$ ratios are all very low, having values between 0.1-0.6. These low $(Ba/Nb)_{pmn}$ ratios indicate that these inclusions have not been contaminated by Lewisian crust, possibly because the olivine fractionates from the melt before the magma has risen from the lithospheric mantle into the Lewisian crust. Thus, the melt trapped in these inclusions may represent the composition/s of uncontaminated mantle melt/s.

Not all the patterns of contamination recorded in the melt inclusions are as easy to interpret. In Fig. 6.22, the forsterite content of the olivines are plotted against the $(Ba/Nb)_{pmn}$ ratios of inclusions hosted in these olivines, for sample BM2. Even though the forsterite content and $(Ba/Nb)_{pmn}$ ratios are similar to the ranges seen in Figs. 6.19 and 6.20, the patterns seen in these values are quite different. There is a fractionation trend where the forsterite content drops from Fo 84 to Fo 77, with possibly a small Lewisian crustal input, causing $(Ba/Nb)_{pmn}$ values to reach ~3. However, from that

point the forsterite content rises to a maxim value of 84, and the $(Ba/Nb)_{pmn}$ ratios rise to a maximum of above 14. One way to explain this is if a body of magma is residing in the upper refractory lithosphere where olivine fractionation is proceeding. If a new injection of hot magma pushes up through the lithosphere, this fractionating magma could be incorporated into the hotter magma as it moves upwards. If this new magma is hot enough and travels sufficiently rapidly through the lower crust, it could be contaminated during ascent, leading to contamination without significant fractionation. The trends seen in Fig. 6.22 do support magma mixing of hot magma with a cooler more evolved magma, but care is needed as the data is limited, and perhaps with more data points the interpretation would alter significantly.

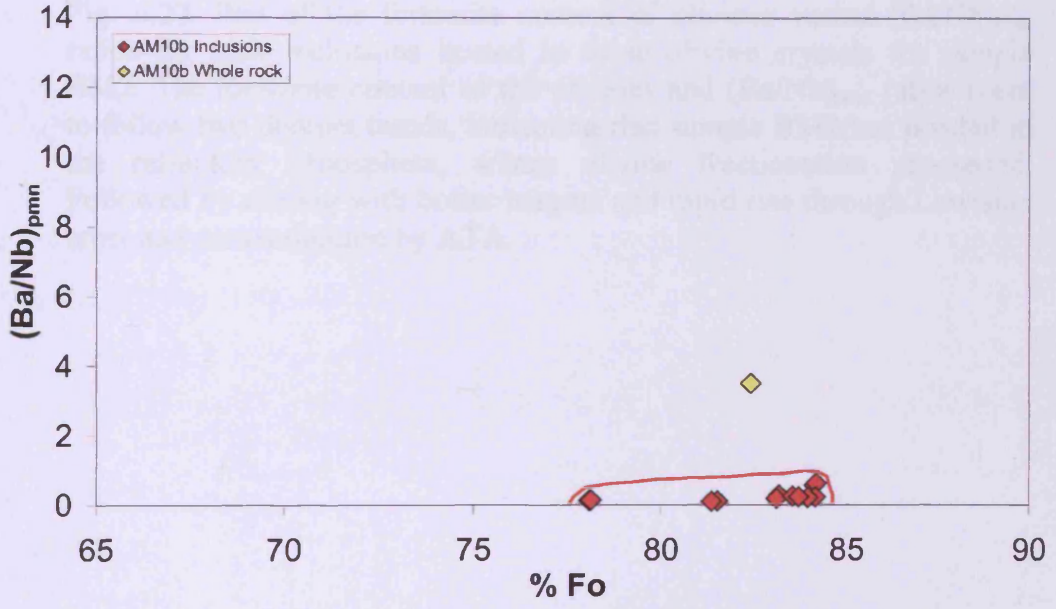

Fig. 6.21. Plot of the forsterite content of olivines versus $(Ba/Nb)_{mn}$ ratios for melt inclusions hosted in these olivine crystals. The forsterite content indicates a certain amount of fractionation, whereas the $(Ba/Nb)_{mn}$ ratios remain very low, with a maximum value of 0.6, thus these inclusions have not been contaminated by Lewisian crust.

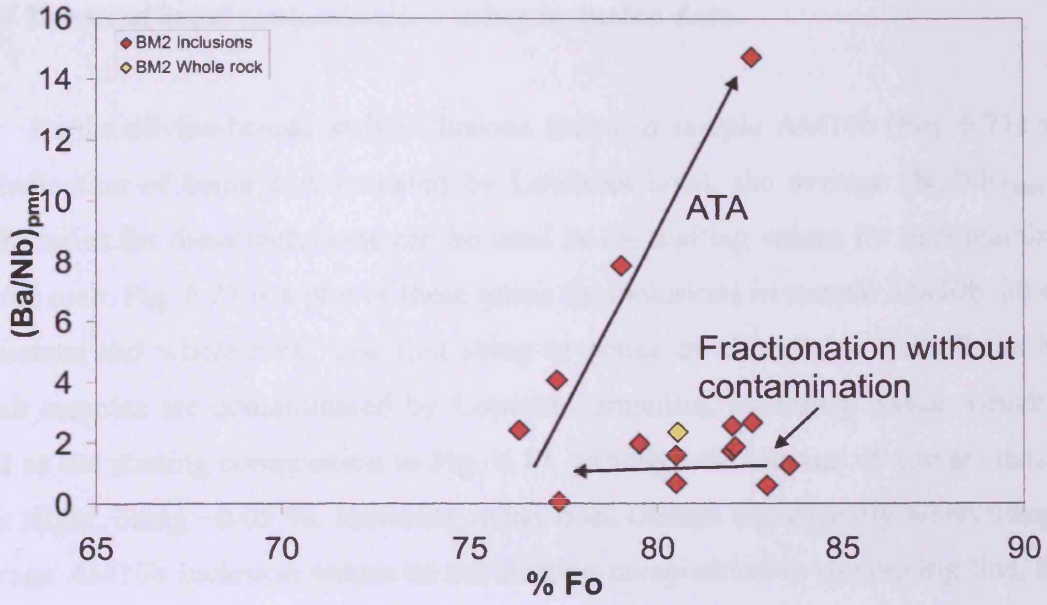

Fig. 6.22. Plot of the forsterite content of olivines versus $(Ba/Nb)_{pmn}$ ratios for melt inclusions hosted in these olivine crystals for sample BM2. The forsterite content of the olivines and $(Ba/Nb)_{pmn}$ ratios seem to follow two distinct trends, indicating that sample BM2 has ponded in the refractory lithosphere, where olivine fractionation proceeded. Followed by mixing with hotter magma and rapid rise through Lewisian crust and contamination by ATA.

6.3.7 Extent of crust contamination using inclusion data

As the olivine-hosted melt inclusions found in sample AM10b (Fig. 6.21) show no indication of being contaminated by Lewisian crust, the average $(Ba/Nb)_{pmn}$ and Ba/Zr ratios for these inclusions can be used as the starting values for uncontaminated mantle melt. Fig. 6.23 is a plot of these ratios for inclusions in sample AM10b, all other inclusions and whole rock. The first thing to notice on this plot is that all the MPG basalt samples are contaminated by Lewisian granulite, including BM6a, which was used as the starting composition in Fig. 6.17, although the amount of contamination is only slight, being ~0.05 %. However, what does change significantly when using the average AM10b inclusion values as the starting composition in the mixing line, is the maximum extent of contamination affecting the MPG lavas as modelled using the whole rock data. From Fig. 6.17, the maximum contamination affecting the MPG lavas is ~5 %, whereas from Fig 6.23 the maximum contamination would be ~7 %. Thus, it is possible that Kerr *et al.* (1995) have underestimated the extent of contamination affecting the MPG lavas by several percent, because all the MPG lavas are contaminated to some extent, and as such do not represent the composition of uncontaminated mantle melt.

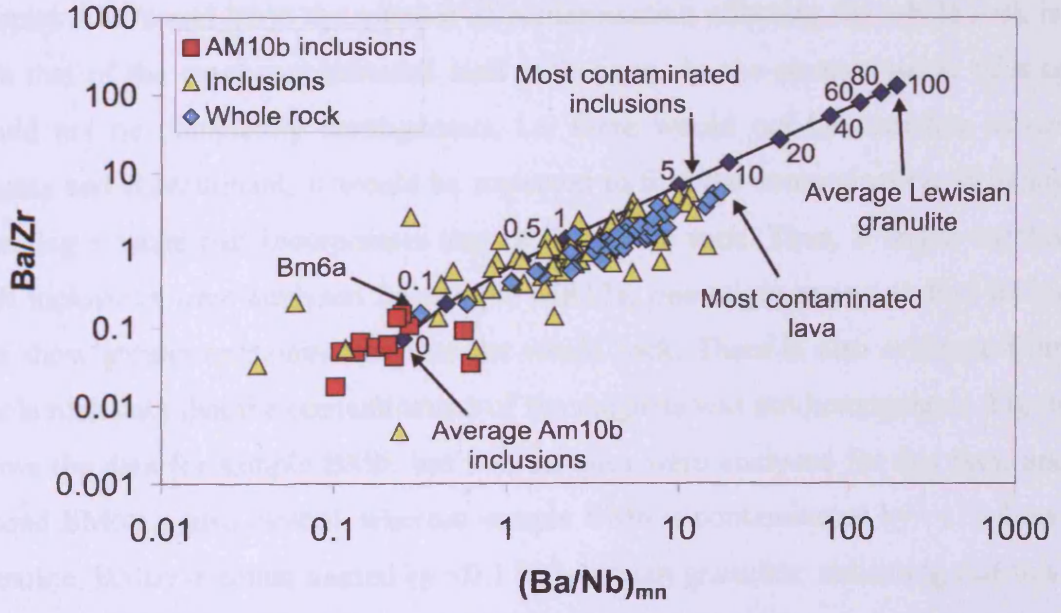

Fig. 6.23. Plot of Ba/Zr versus $(Ba/Nb)_{mn}$ ratios for inclusions, whole rock and mixing line between average AM10b inclusions value and average Lewisian granulite. These data suggest maximum contamination of ~7 % and ~5 % for the whole rock and melt inclusions respectively.

6.3.8 Timing of fractionation of olivine and contamination of magma

Fig. 6.24a-l are plots of olivine-hosted melt inclusions, and whole rock $(Ba/Nb)_{pmn}$ and Ba/Zr ratios for individual MPG lavas. From these graphs, it is obvious that there are a number of distinct patterns of fractionation of olivine and contamination of the inclusions and whole rock. Fig. 6.24a is the $(Ba/Nb)_{pmn}$ and Ba/Zr data for sample AM10b, which from Fig 6.21 hosts uncontaminated melt inclusions, and their average value has been used as the uncontaminated magma end-member in the mixing lines. Unlike the melt inclusions, the whole rock $(Ba/Nb)_{pmn}$ and Ba/Zr indicates that the magma has been contaminated by >1 % Lewisian granulite. Therefore, olivine fractionation must have preceded contamination, either due to olivine fractionation occurring before the magma had risen into the crust from the mantle lithosphere, or olivine fractionating in the crust, but before contamination.

The $(Ba/Nb)_{pmn}$ and Ba/Zr ratios for the three lavas (MR12a, AM7a, BM6) that have been contaminated by AFC processes are shown in Fig. 6.24b-d. The whole rock data suggests contamination by ~1-5 % Lewisian granulite, with a similar range for the most contaminated melt inclusions. However, for sample MR12a the whole rock has undergone greater contamination than the olivine-hosted inclusions, whereas for samples AM7a and BM6 the amount of contamination affecting the whole rock is less than that of the most contaminated melt inclusions. As the contamination of magmas would not be completely homogenous, i.e. there would not be complete mixing of magma and contaminant, it would be expected to find the contamination of inclusions spanning a range that incorporates that of the whole rock. Thus, if larger numbers of melt inclusions were analysed for sample MR12a, one might expect to find inclusions that show greater contamination that the whole rock. There is also evidence from the whole rock data that the contamination of the magmas was not homogenous. Fig. 6.24d shows the data for sample BM6, but two samples were analysed for this lava, and the second BM6a is also plotted, whereas sample BM6 is contaminated by ~1 % Lewisian granulite, BM6a is contaminated by <0.1 % Lewisian granulite, indicating that this lava at least is heterogeneous as far as crustal contamination is concerned. I.e. there was not complete mixing between the magma represented by samples BM6 and BM6a, and the Lewisian granulite contaminant.

All the three lavas (MR12a, AM7a, BM6) that show contamination by AFC, also have melt inclusions with $(Ba/Nb)_{pmn}$ and Ba/Zr ratios that plot within the field for the uncontaminated AM10b sample inclusions. This could indicate that fractionation started in the lithospheric mantle. However, if this were the case, it would be expected that the olivines that hosted these uncontaminated inclusions would have the highest forsterite content. This is not the case, as the uncontaminated inclusions were hosted in olivines with forsterite contents of 84-87, whereas the highest forsterite content for olivines in all three samples is ~88. Therefore, the olivines that host these uncontaminated inclusions probably fractionated in the crust, but without being contaminated.

The MPG lavas (BHI2, BHI3. MR9, AM7b, MR10, AM10c, BHI18) that have been contaminated by the ATA processes show trends similar to those for the lavas contaminated by AFC (Fig. 6.24e-i). However, there are a few subtle differences. Firstly some of the lavas (BHI2, AM10c, BHI18) have olivine-hosted inclusions that are considerably more contaminated that the whole rock; and second, only one inclusion (sample MR9) from all those analysed has $(Ba/Nb)_{pmn}$ and Ba/Zr ratios that plot within the uncontaminated AM10b inclusions field. Therefore, contamination of these lavas preceded the fractionation of olivine and, as contamination is dependant on turbulent flow, there would be considerable mixing of magma and Lewisian granulite melts resulting in the contamination of olivine-hosted inclusions. However, as outlined in Section 6.4.1, it is possible that olivine was fractionating out of the magma earlier than suggested here, but this olivine was crystallising on the conduit walls; thus it is not present in the MPG lavas that have been contaminated by ATA.

Melt inclusions in BM2 shows trends that indicate contamination by ATA (Fig. 6.22), having inclusions that are far more contaminated than the whole rock. However there are many inclusions with low $(Ba/Nb)_{pmn}$ and Ba/Zr ratios, which are indicative of fractionation without contamination. Thus, fractionation preceeded contamination, probably because of ponding in the refractory lithosphere, followed by mixing with hotter magma and rapid rise through the Lewisian crust, where the magma was contaminated by ATA proceeses.

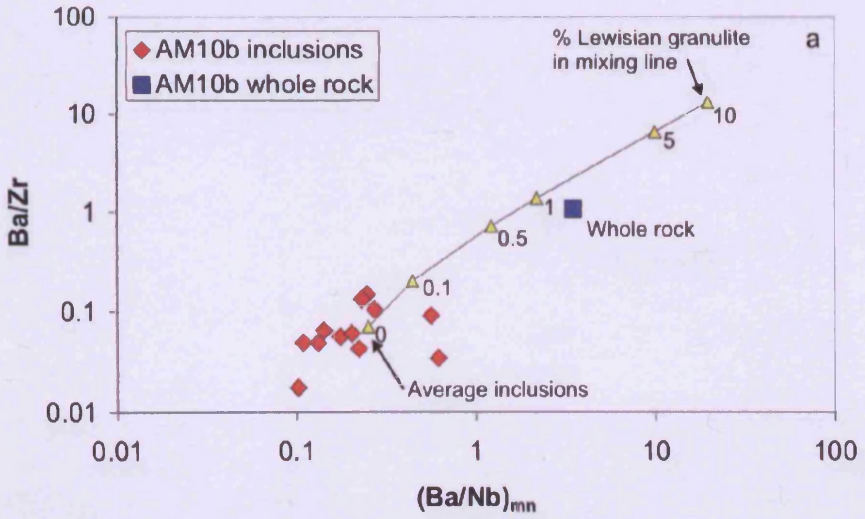

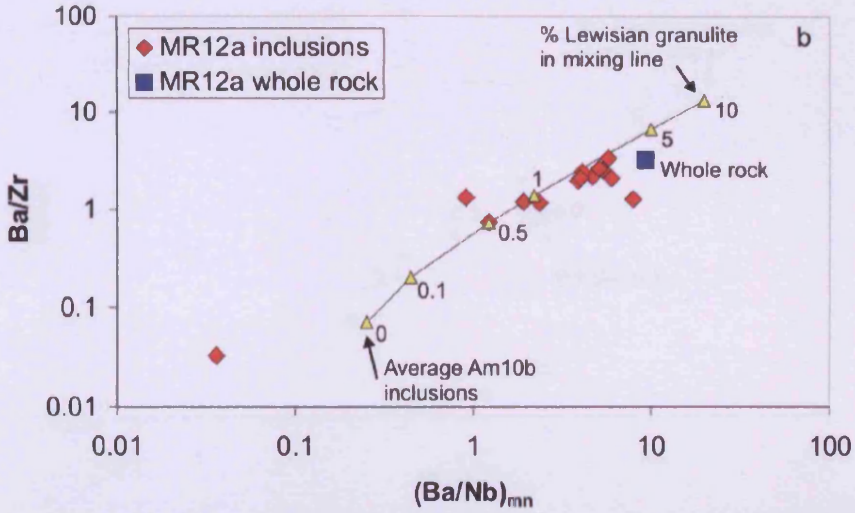

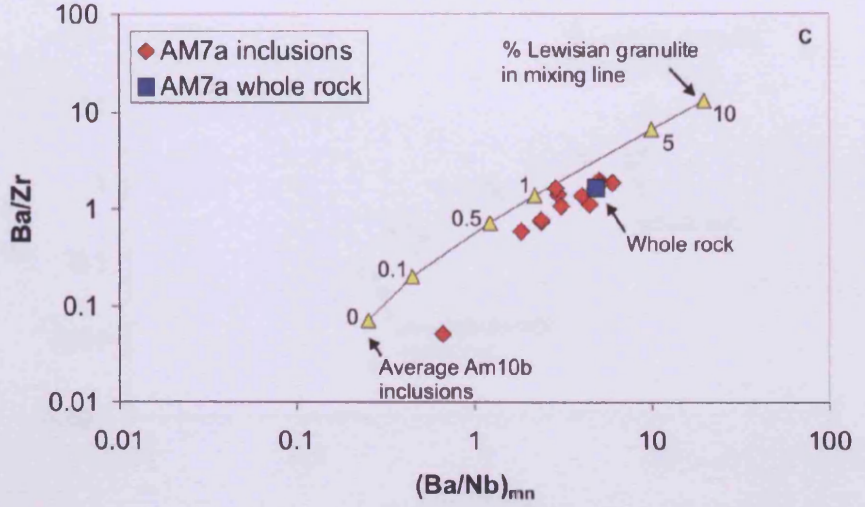

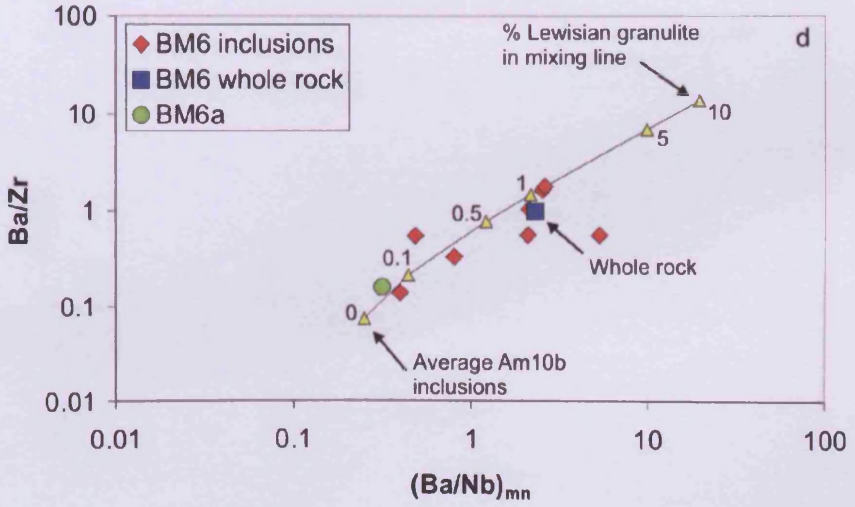

Fig.6.24a-d. Graphs of $(Ba/Nb)_{mn}$ versus Ba/Zr ratios for olivine hosted melt inclusions, and their respective whole rock ratios. All mixing lines are calculated from average Lewisian granulite, and average Am10b olivine-hosted melt inclusions.

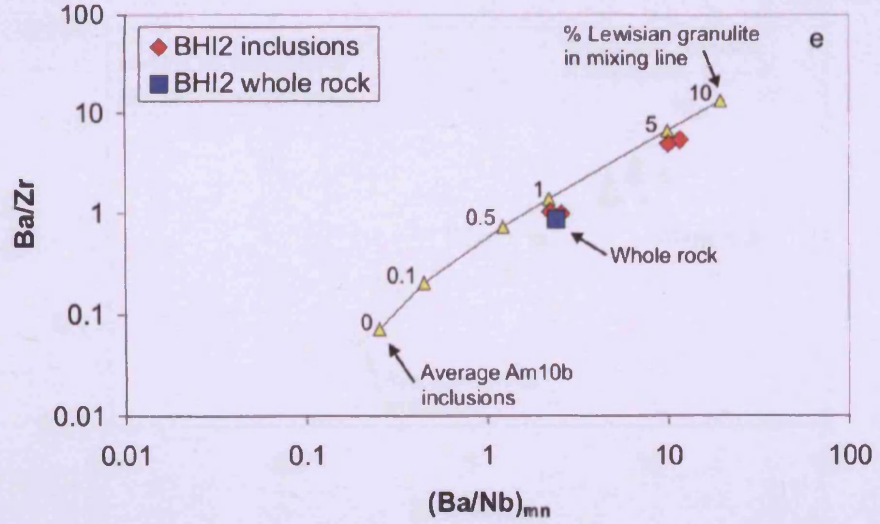

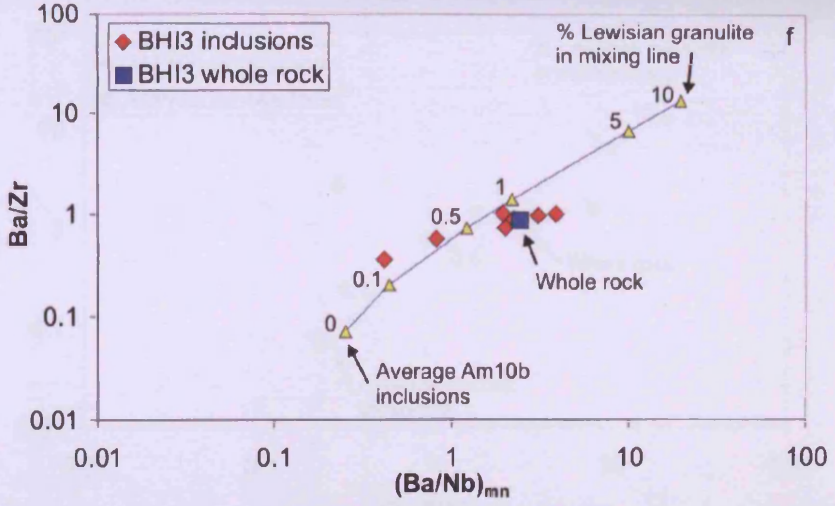

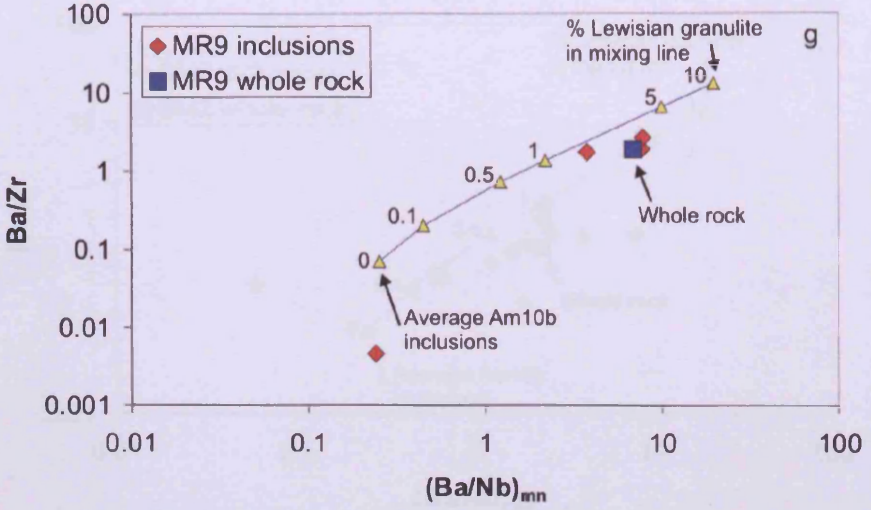

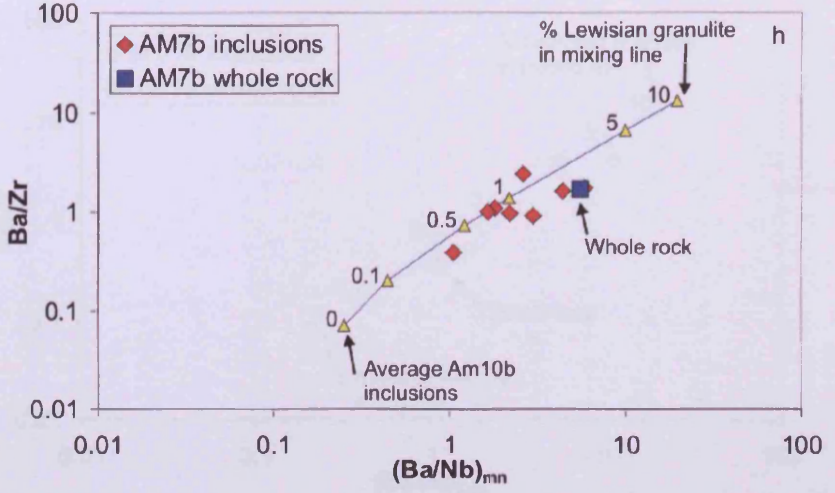

Fig.6.24e-h. Graphs of $(Ba/Nb)_{mn}$ versus Ba/Zr ratios for olivine hosted melt inclusions, and their respective whole rock ratios. All mixing lines are calculated from average Lewisian granulite, and average Am10b olivine-hosted melt inclusions.

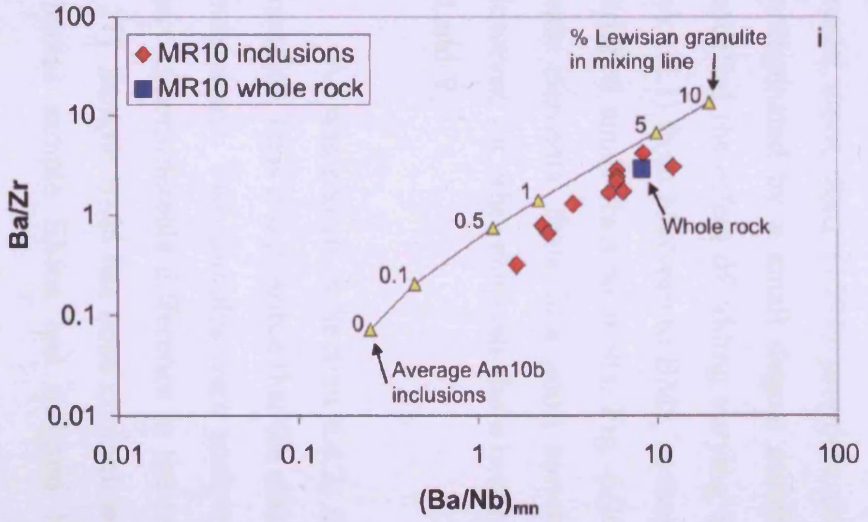

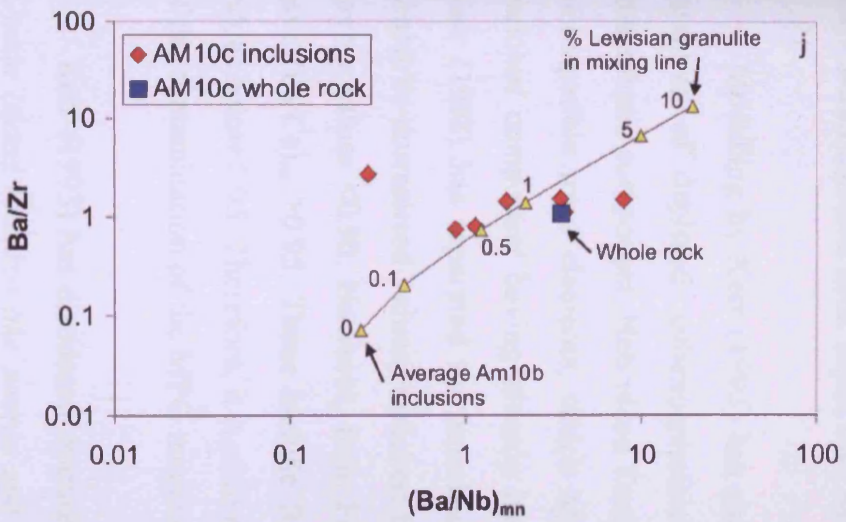

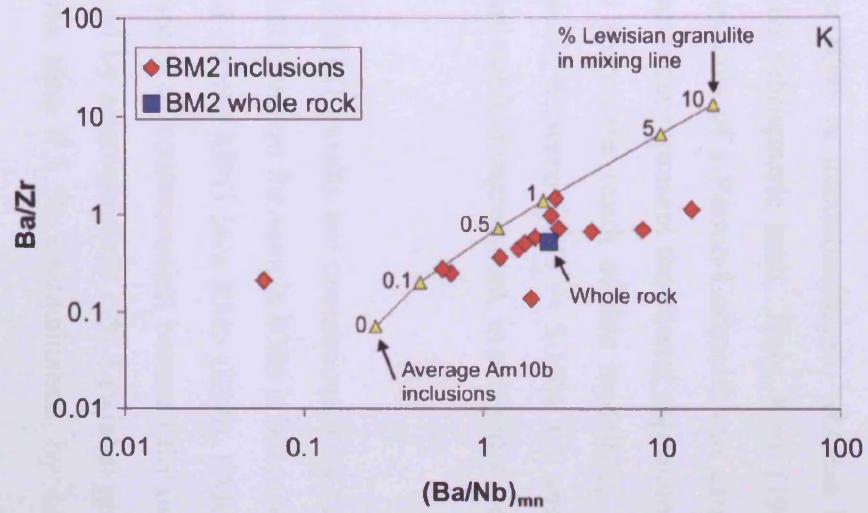

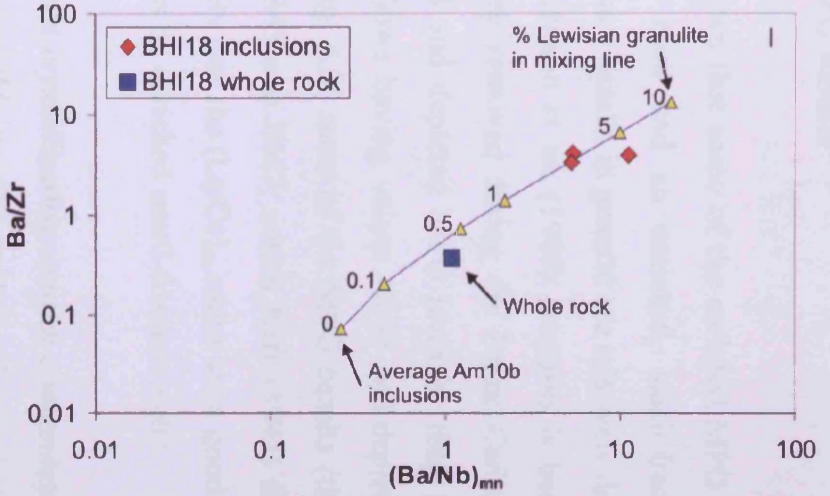

Fig.6.24i-l. Graphs of $(Ba/Nb)_{mn}$ versus Ba/Zr ratios for olivine hosted melt inclusions, and their respective whole rock ratios. All mixing lines are calculated from average Lewisian granulite, and average Am10b olivine-hosted melt inclusions.

6.3.9 Small fraction melt input into MPG basalts

Modelling by Kerr (1993) has shown that some of the enriched MPG lavas are mixtures of depleted asthenosphereic melt and an enriched, small-fraction-melt lithospheric component. Hebridean Tertiary basalts in general are relatively depleted in incompatible trace elements, which Morrison *et al.* (1980) proposes is because the enriched component having already been removed during the Permo-Carboniferous. Kerr (1993) has separated the enriched and depleted MPG lavas by their $(La/Ce)_{cn}$ chondrite-normalised values, enriched flows having values >0.95 and depleted flows having values <0.90. However, from Fig. 6.25 most of the MPG basalts (this study) have $(La/Ce)_{cn}$ >0.95. These include BM5 and BM7, which Kerr (1993) finds have values below 0.95. Therefore, it is unlikely that the $(La/Ce)_{cn}$ ratios are a good indicator of the contamination of the MPG magmas by enriched small-fraction melts.

Kerr (1993) has dismissed *fractional crystallisation, crustal contamination, OIB (Ocean Island Basalts)-like source* and *variable partial melting of the mantle*, as the source of this enrichment, in favour of *contamination by an enriched small-degree-melt fraction*. Assuming that the lava samples BM2-7 are relatively uncontaminated with a crustal input, Kerr (1993) proposes that BM5 is uncontaminated, whereas BM6 is contaminated by a small degree enriched lithospheric melt. Thus, Kerr (1993) has modelled the effect of adding varying amounts of a Permo-Carboniferous camptonite dyke (L1) from Morvern to BM5, as these dykes represent the closest approximation to enriched small fraction melts. Fig. 6.26 shows the result of this modelling, and for some elements, there is a good correlation between BM5 + 5-10% L1 and BM6. However, for other elements there is considerable disagreement, in particular Nd, P, Zr, Ti and Y.

As was shown in Section 6.4.2, all MPG basalts are contaminated by Lewisian granulite. Thus it is possible that the enriched pattern for sample BM6 is because of this contaminant. Two samples were analysed for the MPG lava BM6 (BM6, BM6a), and there is considerable difference in the amount of contamination between the two (Fig. 6.27). Sample BM6 has been contaminated by approximately 1 % Lewisian granulite, whereas sample BM6a has suffered less than 0.1 % contamination by Lewisian

granulite. Therefore, attempts will be made to model the enriched pattern in BM6, by adding variable amounts of Lewisian granulite to sample BM6a.

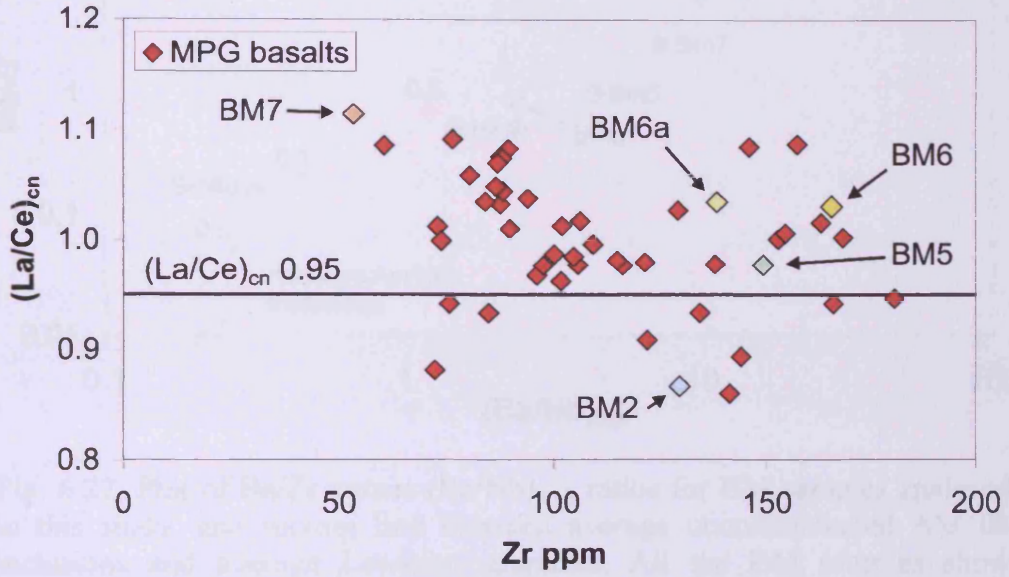

Fig. 6.25. Plot of $(La/Ce)_{cn}$ versus Zr for the MPG lavas analysed in this study. Modelling by Kerr (1993) proposes that lavas with $(La/Ce)_{cn}$ >0.95 have been contaminated by a enriched small fraction melt. However, using this criterion, most of the lavas sampled would be contaminated

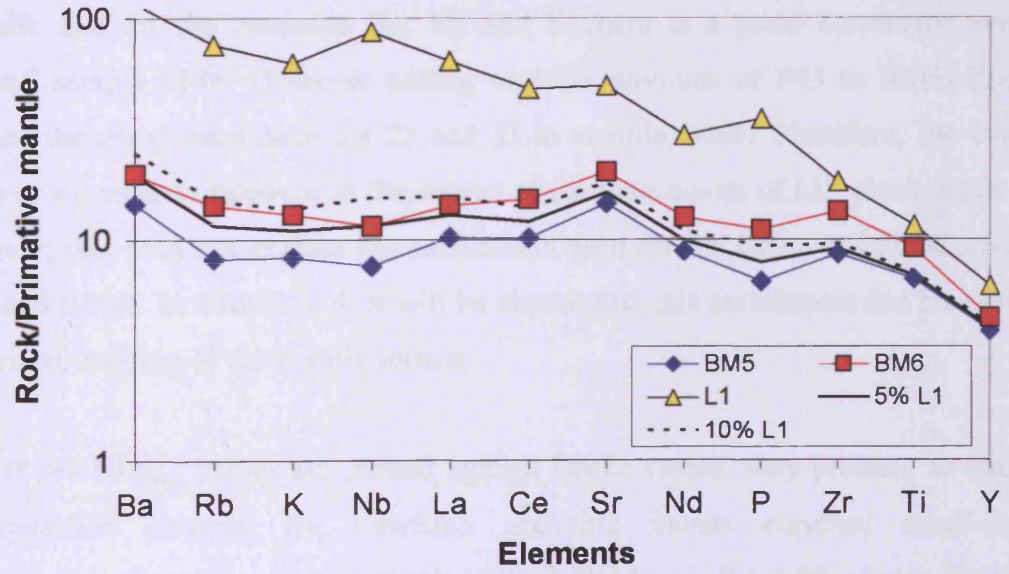

Fig. 6.26. Multi-element variation diagram showing the effects of adding 5-10% of an enriched component (L1) to sample BM5. The resultant patterns are similar to that seen for sample BM6, however there are conciderable differences in the values for many elements , in particular Nd, P, Zr, Ti and Y. Data from Kerr (1993)

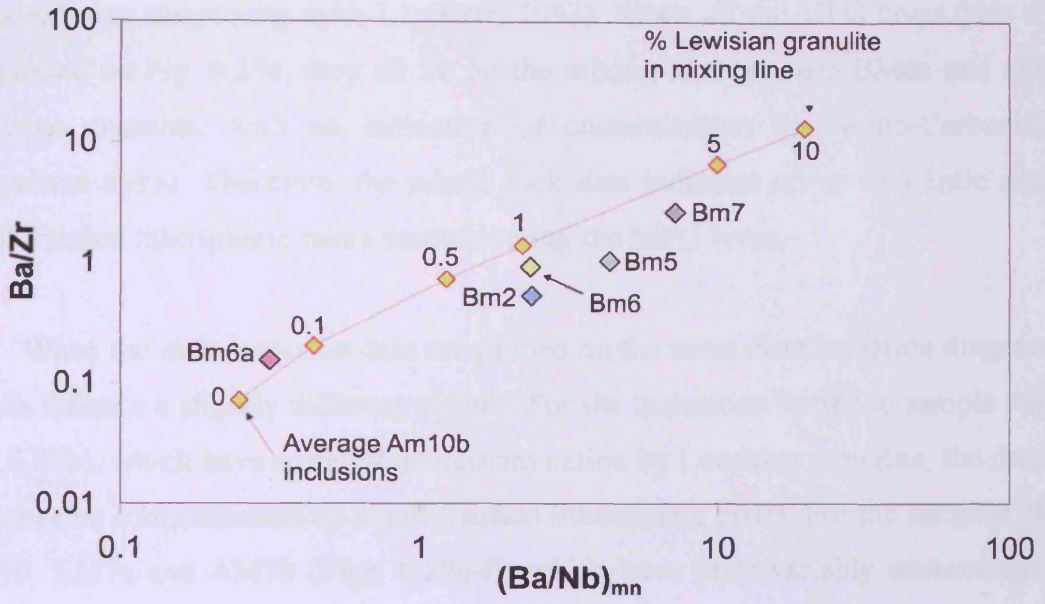

Fig. 6.27. Plot of Ba/Zr versus $(Ba/Nb)_{pmn}$ ratios for BM samples analysed in this study, and mixing line between average uncontaminated AM10b inclusions and average Lewisian granulite. All the BM samples show varying amounts of contamination by Lewisian crust.

When the average Lewisian granulite values are used to model enrichment of sample BM6a, the correlation is poor. However, when the Lewisian granulite sample P43 is used there is good correlation. Fig. 6.28 shows the results of adding 1-2 % P43 to BM6, and for the elements Ba, Rb and K there is a good correlation with the enriched sample BM6. However adding variable amounts of P43 to BM6a does not produce the enrichment seen for Zr and Ti in sample BM6. Therefore, the evidence points to a crustal component as the source of the enrichment of LIL elements in BM6. However, this does not explain the enrichment seen for the REEs and HFSEs for both MB6 and BM6a. In Section 6.4, it will be shown that this enrichment can be explained by variable melting of the mantle source.

If $(Ba/Nb)_{pmn}$ values are plotted against Nb/Zr values, they produce an excellent discrimination diagram for Lewisian granulite versus enriched small-fraction lithospheric melts as the contaminant/s in the MPG lavas. Fig 6.29a shows the mixing lines between the uncontaminated BM6a MPG lava and average Lewisian granulite, and between BM6a and P-average (P-ave, average of Permo-Carboniferous dykes in western Scotland (Morrison *et al.*, 1997; Baxter, 1987)). Also shown is the Permo-

Carboniferous camptonite dyke L1 (Kerr, 1993). When all the MPG lavas (this study) are plotted on Fig. 6.29a, they all lie on the mixing line between BM6a and average Lewisian granulite, with no indication of contamination by Permo-Carboniferous camptonite dykes. Therefore, the whole rock data indicates no or very little input of small fraction lithospheric melts contaminating the MPG lavas.

When the melt inclusion data are plotted on the same discrimination diagram, the results indicate a slightly different picture. For the inclusions hosted in sample AM10b (Fig.6.29b), which have suffered no contamination by Lewisian granulite, the data also indicates no contamination by small fraction lithospheric melts. For the samples, BHI2, MR10, AM7a and AM7b (Figs. 6.29c-f), which have been variably contaminated by Lewisian granulite, there is again no indication of contamination by small fraction lithospheric melts. However, for the samples BM2, MR9, MR12a, BM6, AM10c and BHI3 the data does support an enriched fraction within these MPG lavas. The amount of melt inclusions that show this enriched signature are limited, and have Nb/Zr values that indicate contamination by an enriched small fraction lithospheric melt by between 10 and 60 % P-Ave(Average Permo-Carboniferous dykes). It is impossible without radiogenic data to determine whether these inclusions are contaminated by small fraction melts. They could either be reflecting small scale heterogeneity within the magma, or small scale melting in the source region.

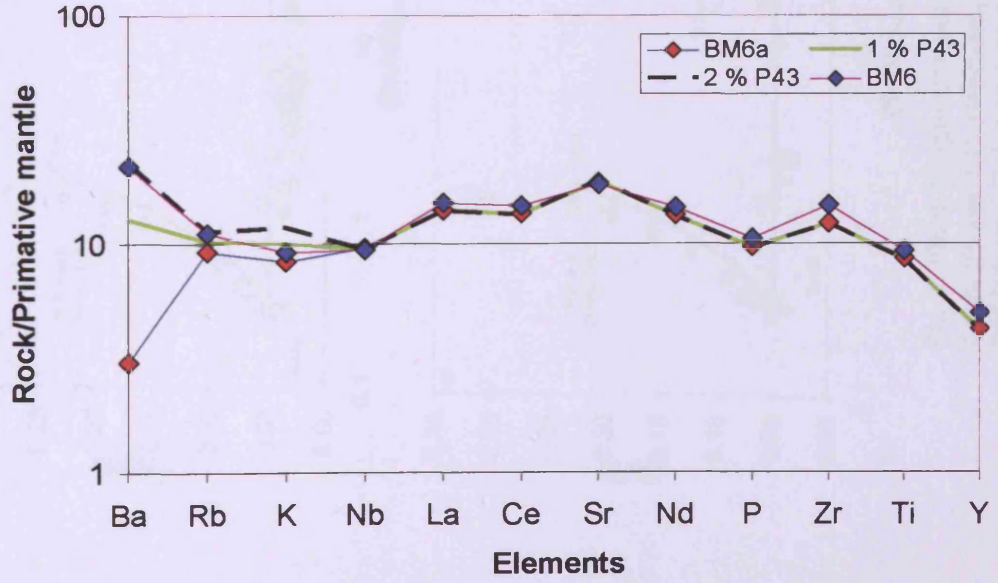

Fig. 6.28. Multi-element variation diagram showing the effects of adding 1-2 % Lewisian granulite (sample P43) to BM6a. The resultant pattern is very similar to BM6. This is particularly true for Ba, Rb and K, whereas the results of modelling are not so good for the elements Zr and Ti.

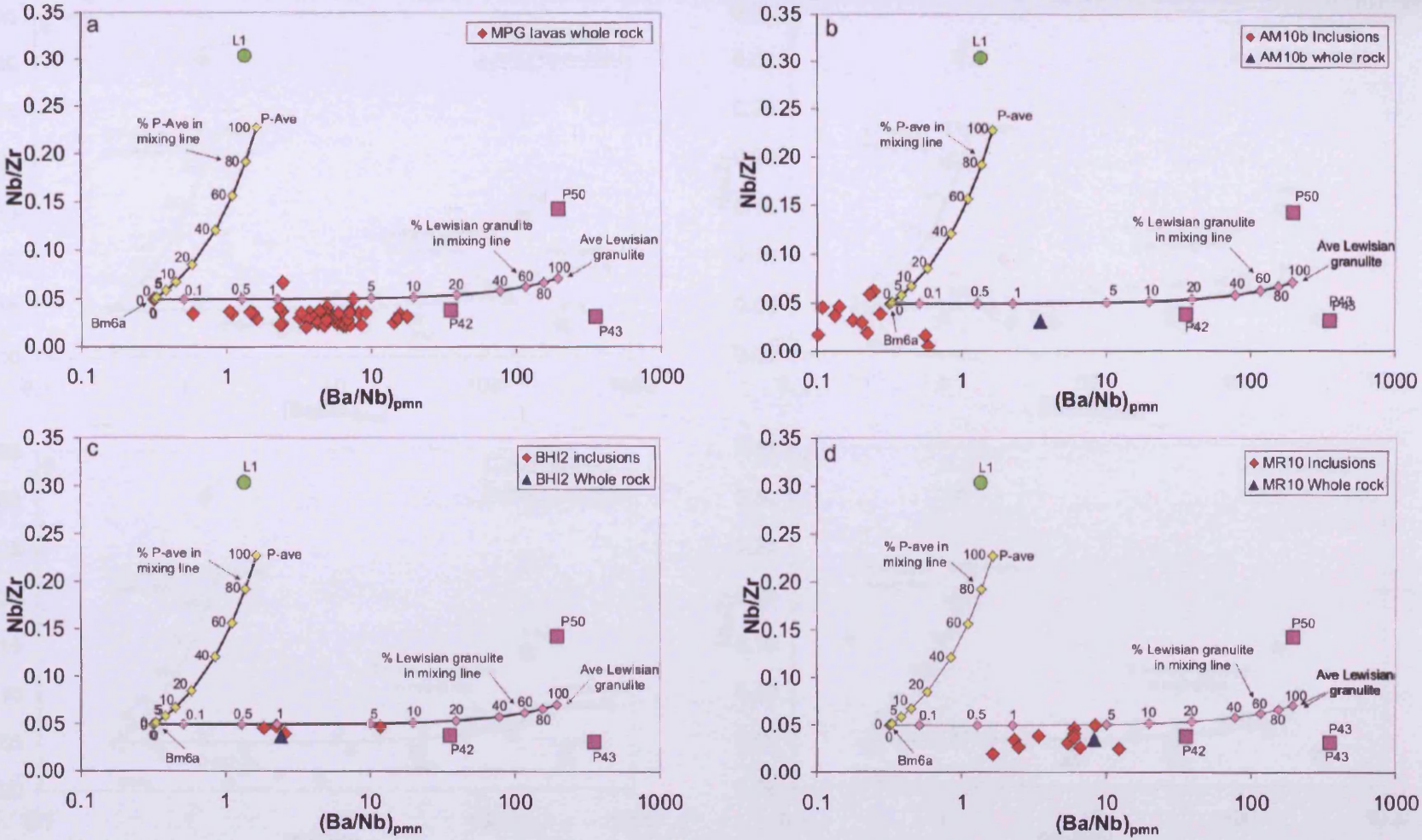

Fig. 6.29a-d. Graphs of $(Ba/Nb)_{pmn}$ versus Nb/Zr ratios for the least contaminated MPG lava (BM6a), Permo-Carboniferous dykes (P-ave, L1), Lewisian granulite (P42, P43, P50 and Ave Lewisian granulite) and mixing lines between BM6a and P-ave, and between BM6a and average Lewisian granulite. Plotted on these diagrams are the whole rock and melt inclusion data from this study.

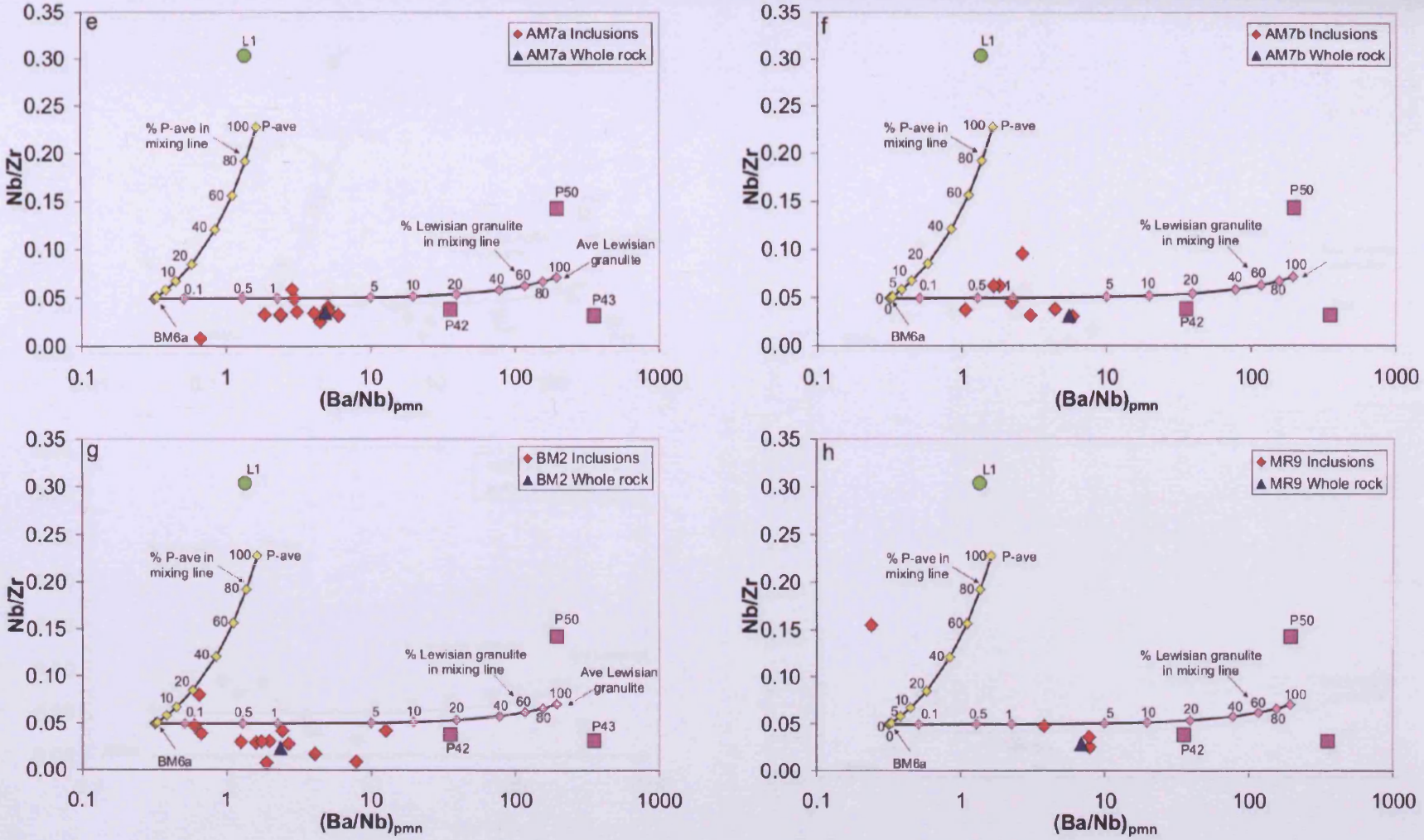

Fig. 6.29e-h. Graphs of $(Ba/Nb)_{pmn}$ versus Nb/Zr ratios for the least contaminated MPG lava (BM6a), Permo-Carboniferous dykes (P-ave, L1), Lewisian granulite (P42, P43, P50 and Ave Lewisian granulite) and mixing lines between BM6a and P-ave, and between BM6a and average Lewisian granulite. Plotted on these diagrams are the melt inclusion data from this study.

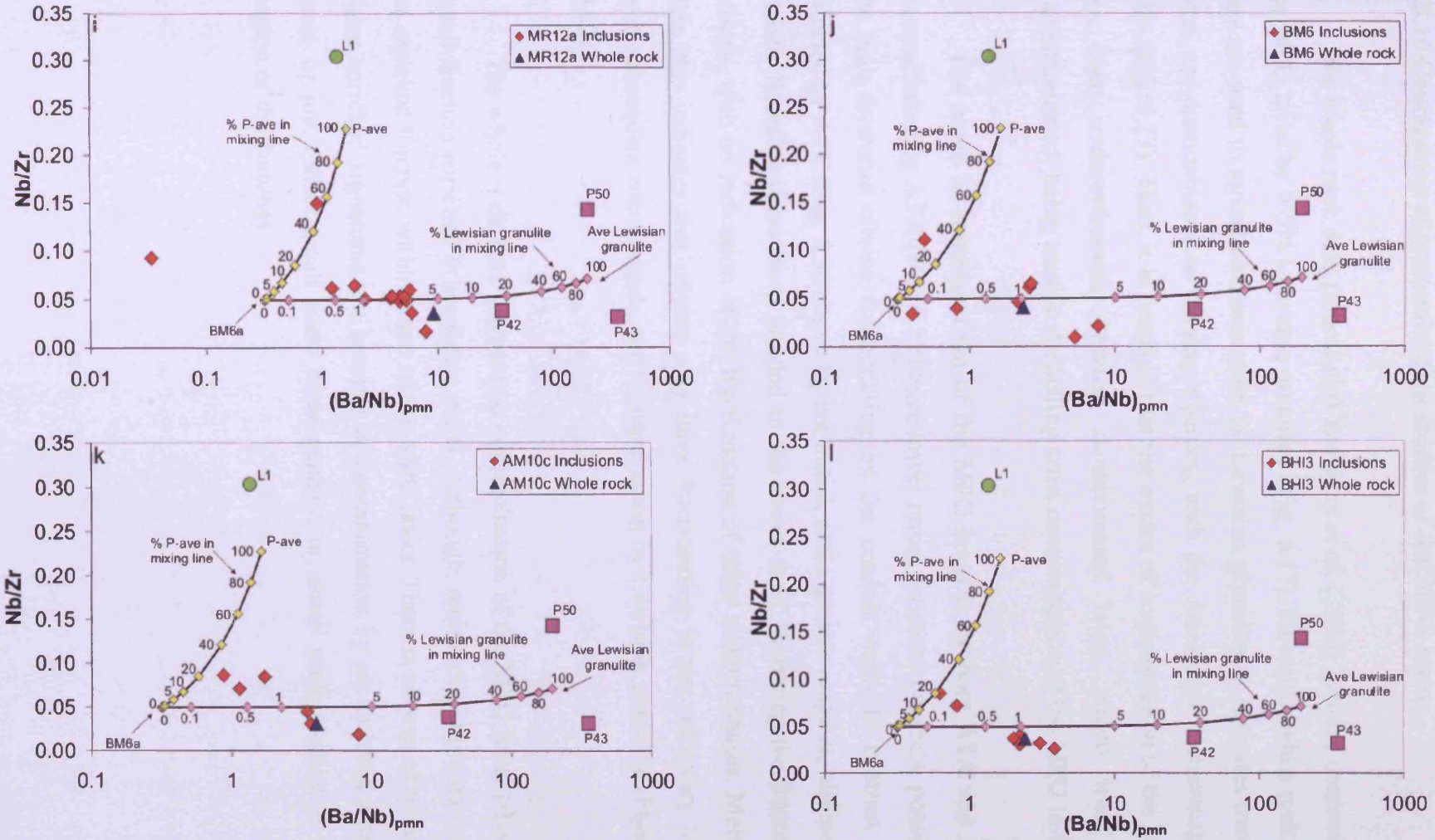

Fig. 6.29i-l. Graphs of $(Ba/Nb)_{pmn}$ versus Nb/Zr ratios for the least contaminated MPG lava (BM6a), Permo-Carboniferous dykes (P-ave, L1), Lewisian granulite (P42, P43, P50 and Ave Lewisian granulite) and mixing lines between BM6a and P-ave, and between BM6a and average Lewisian granulite. Plotted on these diagrams are the melt inclusion data from this study.

6.3.10 Conclusions of contamination studies of the MPG lavas

The whole rock data (this study) and Kerr *et al.* (1995) indicate contamination of the MPG lavas by 0-5% Lewisian granulite (Fig. 6.17). However, when melt inclusion data are used to model contamination by Lewisian granulite, it indicates that all MPG lavas are contaminated to varying degrees, with the maximum contamination being ~8% (Fig. 6.23). Thus, it is possible that the extent of contamination of the MPG lavas has been underestimated, because contaminated lavas, which were assumed uncontaminated, being used in modelling crust contamination of the MPG lavas.

The mode of contamination of the MPG lavas is by both ATA and AFC. The lavas affected by ATA (Fig. 6.19) have lower initial forsterite contents, possibly due to the high forsterite olivine fractionating on the conduit walls. In contrast, the lavas affected by AFC (Fig. 6.20) have higher initial, and a greater range in, olivine forsterite values, therefore these lavas ponded in the lower crust. Allowing the fractionation of olivine, with no indication of the fractionation of other mineral phases. Melt inclusion data also indicates that olivine may have fractionating in the refractory lithosphere, with subsequent rise through, and contamination by Lewisian granulite (Figs. 6.21 and 6.22).

The whole rock data indicate no contamination of the MPG lavas (this study) by small fraction enriched lithospheric melts. Although, melt inclusions data does support an enriched fraction within some of the MPG lavas. There is no way of telling whether these enriched signatures are because of contamination by an enriched small fraction melt, or just reflect small scale heterogeneity, or, small scale melting in the source region of the magmas.

6.4 Modelling of mantle melting processes

As outlined at the beginning of this Chapter, it is important that the effects of secondary alteration and lithospheric contamination (both crust and mantle) be taken into account, before any attempt is made to assess mantle melting processes and mantle source regions. The MPG lavas (this study) have undergone little or no secondary alteration, but have been variable contamination by Lewisian granulite, whereas olivine-hosted melt inclusions range from uncontaminated to 5% contamination by Lewisian granulite. Crustally-contaminated basalts can be used to elucidate mantle processes, but elements affected by contamination processes (generally LILEs) must first be excluded. Other incompatible elements, such as the REEs, Ti, P, Y and Zr, can yield important mantle petrogenetic information even in crustally-contaminated basalts, as can most of the major elements if used with care.

Klein and Langmuir (1987) and McKenzie and Bickle (1988) have established the melting systematics of major elements in response to changes in pressure, and these are outlined in Fig. 6.30. From Fig. 6.30, it is clear that the major element compositions of a suite of basaltic magmas may potentially be used to assess the pressure and extent of mantle melting, povided the magmas have not undergone significant subsequent fractional crystallisation involving minerals that contain the elements under consideration. Accepting the melting column model of McKenzie and Bickle (1988), (i.e. melting occurs through a vertical section of mantle, and that these melts are extracted and mixing simultaneously), there should be a positive correlation between Na_2O and FeO at constant MgO, whereas, for Na_2O and SiO_2 there would be a negative correlation at constant MgO. Relatively low Na_2O and FeO indicate the predominance of extensive melting at relatively low pressure (i.e. more of the pooled melt has come from the top of the melting column). However, high Na_2O and FeO indicates the predominance of less extensive melting at higher pressure (i.e. the pooled melt represents a deeper point and depth average).

Oxide	Major element melting systematices
SiO_2	At constant MgO, increases with X and decreases with increasing pressure
Al_2O_3	Decreases with X, perhaps decreases with increasing pressure
FeO	Constant or decreases slightly with X at constant pressure, increases with increasing pressure
MgO	Increases with X at constant pressure, increases with increasing pressure
Na_2O	Decreases with X, not pressure dependant
CaO	Increases with X, decreases with increasing pressure
TiO_2	Decreases with X, incompatible in mantle phases
K_2O	Decreases with X, incompatible in mantle phases

Fig. 6.30. Table of the major element melting systematics for anhydrous peridotites (Klein and Langmuir, 1987; McKenzie and Bickle, 1988). X is the melt fraction, and clinopyroxene is taken to be a residual phase at less than 22 % melting.

Also of importance in controlling the chemical composition/s of the magma/s produced is the metamorphic facies of the source region. The different metamorphic facies can be plagioclase-, spinel- or garnet-lherzolite, and the stability of each of these aluminous index minerals is critically dependant on pressure and therefore depth. Plagioclase lherzolite converts to spinel lherzolite at pressures greater than 10kb (~30km; Wyllie, 1988). Therefore, below continental regions, with thick refractory lithosphere (>50 km), there will be no melt produced in the plagioclase stability field. Below continents, melting in the spinel stability field is far more important, and this transforms gradually into garnet-bearing lherzolite between 60-80 km in depth (i.e. the 'spinel-garnet transition zone' Ellam, 1992).

The heavy rare earth elements (HREE) are much more compatible in garnet than in spinel (i.e. partition coefficient for Lu in garnet 5.5; for Lu in spinel 0.01 - McKenzie and O'Nions, 1991). Thus any fusion in the garnet stability field, or spinel-garnet transition zone will result in melt/s relatively depleted in the HREE (i.e. $(Sm/Yb)_{cn}$ >>1). In contrast, shallower melting within the spinel stability field will produce magmas with relatively flat chondrite-normalised REE patterns (i.e. $(Sm/Yb)_{cn}$ ~1).

6.4.1 Major element evidence for a melting column beneath Mull

Klein and Langmuir (1987, 1989) conducted a global study of mid-ocean ridge basalts, in which they made extensive use of major element compositional trends to assess the relative pressures and extents of melting. To achieve this, they first eliminated the effects of factional crystallisation by re-calculating FeO, SiO_2 and Na_2O values after the MgO content of the individual basalts was set at 8 % ($Fe_{8.0}$, $Si_{8.0}$ and $Na_{8.0}$ of Klein and Langmuir, 1987, 1989). Before the $Fe_{8.0}$, $Si_{8.0}$ and $Na_{8.0}$ values are calculated for the MPG basalts, the effect of crustal contamination on these major oxides needs to be taken into consideration. Fig. 6.31, shows the effects of adding 3, 5 and 10% average Lewisian granulite to sample BM6a, the least contaminated MPG basalt (this study). Addition of Lewisian granulite has very limited effect on Al_2O_3, Na_2O, TiO_2, MnO and P_2O_5, and only a limited effect on Fe_2O_3, MgO, CaO and SiO_2,. Similar findings were reported by Kerr (1993b). Also when calculating $Fe_{8.0}$, $Si_{8.0}$ and $Na_{8.0}$ values, only samples with MgO values between 6-9 % MgO are used, and it was shown in Section 6.3.2 that these low MgO basalts are the least contaminated with Lewisian granulite. Therefore, it is the least contaminated magmas that are used in calculating the $Fe_{8.0}$, $Si_{8.0}$ and $Na_{8.0}$ values.

	BM6a	Lew Ave	+ 3% crust	+ 5% crust	+ 10% crust
SiO_2	44.81	71.46	45.61	46.14	47.47
Al_2O_3	14.60	14.26	14.59	14.58	14.56
Fe_2O_3 (T)	13.34	1.56	12.99	12.76	12.17
MgO	9.57	0.73	9.30	9.12	8.68
CaO	8.22	1.23	8.01	7.87	7.52
Na_2O	3.04	3.68	3.06	3.08	3.11
K_2O	0.25	5.47	0.41	0.51	0.77
TiO_2	1.88	0.19	1.83	1.79	1.71
MnO	0.16	0.01	0.15	0.15	0.14
P_2O_5	0.21	0.09	0.21	0.20	0.20

Fig. 6.31. Table showing the effects on the major oxides of adding 3, 5 and 10 % Lewisian granulite to the relatively uncontaminated MPG sample BM6a.

The calculated $Fe_{8.0}$, $Si_{8.0}$ and $Na_{8.0}$ values are shown graphically in Figs. 6.32 and 6.33. There is considerable scatter of data points on these diagrams, but this could be due to crustal contamination by Lewisian crust, which produces contamination vectors at right angles to the pressure-melting trends, even so, overall trends are still visible. These trends approximate to the intra-column (local) trends of Klein and Langmuir (1989) with higher pressures of melting corresponding to lesser extents of melting, and lower pressures to greater extents of melting. The major element systematics indicates that the mantle melting which produced the MPG basalts was over a range of depths within a melting column. Thus, the magmas erupted at the surface must represent pooled melts (point and depth average composition) from different parts of the melting column, with the lavas that have a deeper melting signature having a great proportion of deeper melts, and the reverse being true for lavas with a shallower signature.

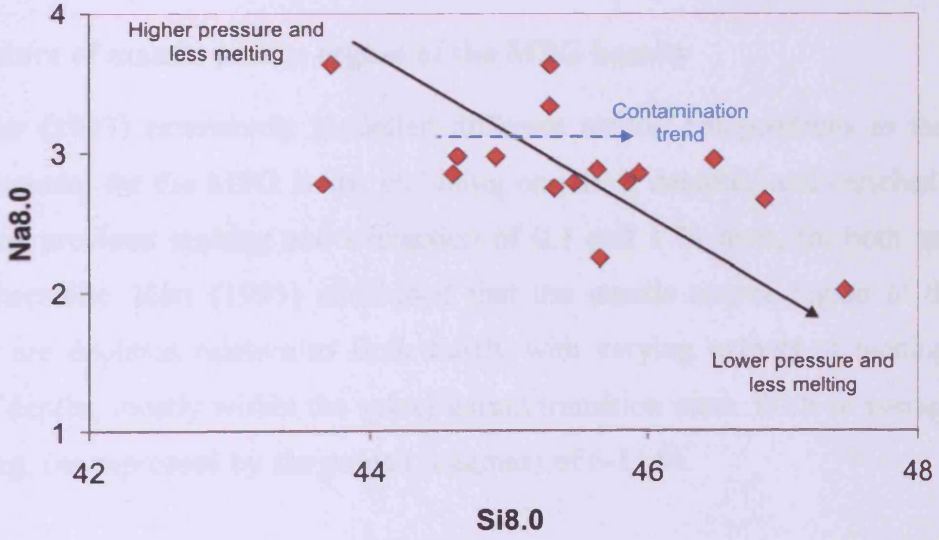

Fig. 6.32. Plot of $Na_{8.0}$ versus $Si_{8.0}$ for MPG lavas containing between 6 and 9 % MgO. The plot displays the intracolumn or local trend (Klein and Langmuir, 1989), with higher pressures of melting corresponding to lesser extents of melting, and lower pressures to greater extents of melting. Also shown is the trend for contamination by Lewisian granulite

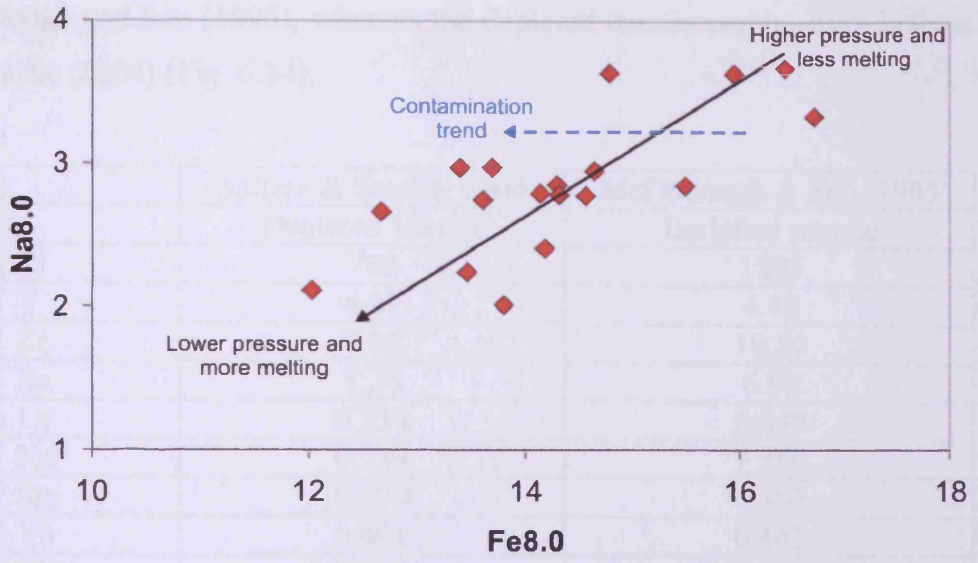

Fig. 6.33. Plot of $Na_{8.0}$ versus $Fe_{8.0}$ for MPG lavas containing between 6 and 9 % MgO. The plot displays the intracolumn or local trend (Klein and Langmuir, 1989), with higher pressures of melting corresponding to lesser extents of melting, and lower pressures to greater extents of melting. Also shown is the trend for contamination by Lewisian granulite

6.4.2 Nature of mantle source region of the MPG basalts

Kerr (1993) extensively modelled different mantle compositions as the mantle source material for the MPG lavas, including enriched, depleted and enriched that has undergone previous melting and extraction of 0.1 and 1 % melt, for both spinel and garnet lherzolite. Kerr (1993) concluded that the mantle source region of the MPG magmas are depleted relative to Bulk Earth, with varying extents of melting over a range of depths, mostly within the spinel/garnet transition zone. With an average extent of melting, (as expressed by the pooled magmas) of 6-11 %.

In order to reassess the nature of the source region, non-modal, equilibrium (batch) melting equations (taken from Kostopoulos and James, 1992) have been used to calculate trace element contents of the liquids produced during partial melting of depleted and enriched mantle for spinel lherzolite, garnet lherzolite and a 50-50 mixture between garnet and spinel lherzolite. The latter has been used to simulate melting in the spinel-garnet transition zone. The model mineralogy and the melting proportions of each of these sources are for Kostopoulos and James, (1992), the partition coefficients and the source composition for enriched mantle (Bulk Silicate Earth) are from

McDonough and Sun (1995), whereas the depleted mantle composition is from Salters and Stracke (2004) (Fig. 6.34).

	Salters & Stacke, 2004	McDonough & Sun, 1995
	Depleted Mantle	Enriched mantle
Ti	798	1205
Y	4.07	4.30
Zr	7.94	10.50
Ba	1.20	6.60
La	0.234	0.648
Nd	0.713	1.250
Sm	0.270	0.406
Yb	0.401	0.441
Ti/Y	196.07	280.23
Zr/Y	1.95	2.44
$(La/Nd)_{cn}$	0.65	1.02
$(Sm/Yb)_{cn}$	0.75	1.02
$(Ba/Nb)_{pmn}$	0.58	1.02

Fig. 6.34. Table of the starting compositions and elemental ratios used in this Section to model mantle melting

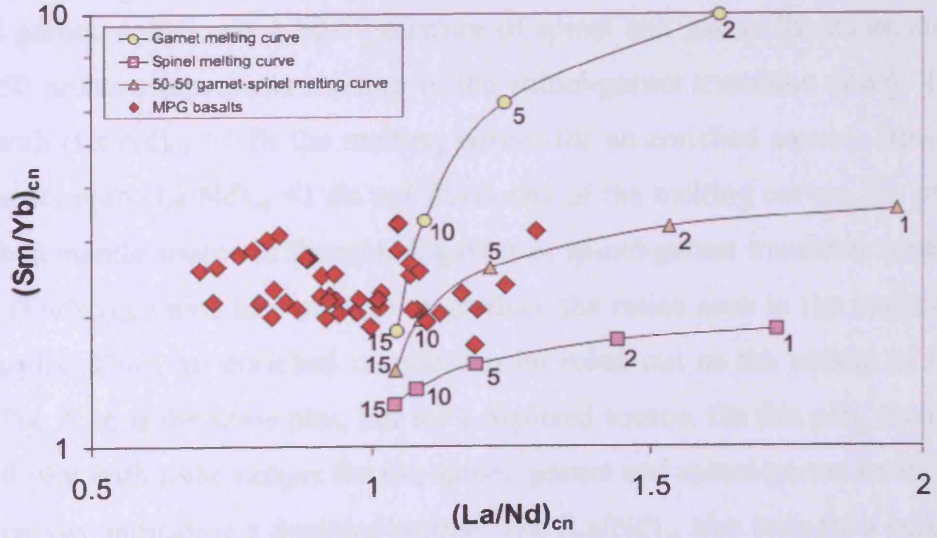

Fig. 6.35. Plot of $(Sm/Yb)_{cn}$ versus $(La/Nd)_{cn}$ (chondrite normalised Sun and McDonough, 1989) showing the composition of melts at differing melting proportions for **enriched** mantle in the spinel, garnet and spinel-garnet transition zone (numbers refer to percent of melting). Also shown are the MPG basalts analysed in this study.

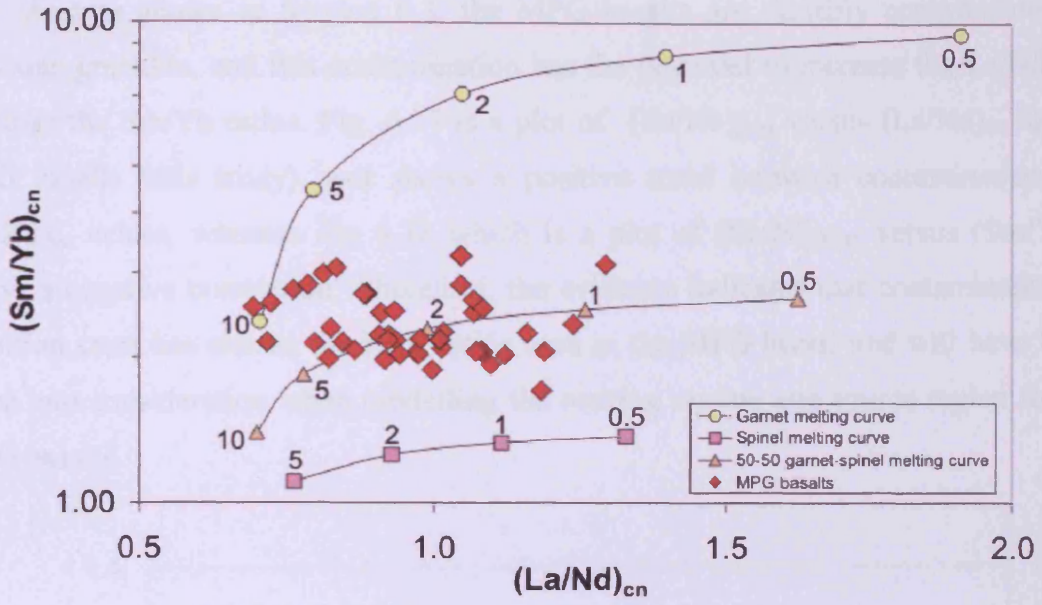

Fig. 6.36. Plot of $(Sm/Yb)_{cn}$ versus $(La/Nd)_{cn}$ (chondrite normalised Sun and McDonough, 1989) showing the composition of melts at differing melting proportions for **depleted** mantle in the spinel, garnet and spinel-garnet transition zone (numbers refer to percent of melting). Also shown are the values for the MPG basalts analysed in this study.

Figs. 6.35 and 6.36 are plots of $(La/Nd)_{cn}$ ratios, which may be used to assess the amount of melting and depletion in the source, versus $(Sm/Yb)_{cn}$ ratios, which can give a guide to the modal mineralogy of the source. In Fig. 6.35, the melting curves for enriched garnet, spinel and a 50-50 mixture of spinel and garnet lherzolite are shown, (the 50-50 mixture represents melting in the spinel-garnet transition zone). The MPG basalts with $(La/Nd)_{cn}$ >1 fit the melting curves for an enriched source. However, the MPG basalts with $(La/Nd)_{cn}$ <1 do not fit on any of the melting curves, i.e. melting of an enriched mantle source in the spinel, garnet or spinel-garnet transition zones, do not produce $(La/Nd)_{cn}$ ratios low enough to produce the ratios seen in the majority of the MPG basalts. Thus, an enriched mantle can be ruled out as the source of the MPG basalts, Fig. 6.36 is the same plot, but for a depleted source. On this plot, the $(La/Nd)_{cn}$ values all plot within the ranges for the spinel, garnet and spinel-garnet transition zone melting curves, indicating a depleted source. The $(La/Nd)_{cn}$ also indicate a maximum of ~10 % fusion in the source region, comparable to the findings of Kerr (1993), who proposed average melting of 6-11 %. The $(Sm/Yb)_{cn}$ ratios indicate that the model mineralogy of the source was a mixture of spinel and garnet, as most of the MPG basalts plot the spinel-garnet transition zone melting curve.

As was shown in Section 6.3, the MPG basalts are variably contaminated by Lewisian granulite, and this contamination has the potential to increase the La/Nd and decrease the Sm/Yb ratios. Fig. 6.37 is a plot of $(Ba/Nb)_{pmn}$ versus $(La/Nd)_{cn}$ for the MPG basalts (this study), and shows a positive trend between contamination and $(La/Nd)_{cn}$ values, whereas Fig 6.38 which is a plot of $(Ba/Nb)_{pmn}$ versus $(Sm/Yb)_{cn}$ shows a negative correlation. Therefore, the evidence indicates that contamination by Lewisian crust has altered the REE ratios seen in the MPG lavas, and will have to be taken into consideration when modelling the melting regime and source region for the MPG basalts.

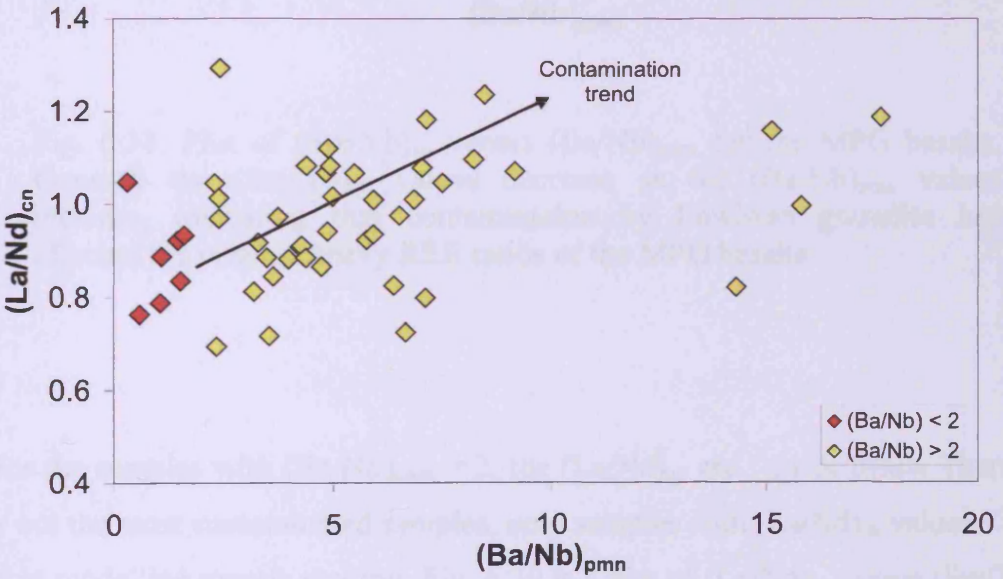

Fig. 6.37. Plot of $(La/Nd)_{cn}$ versus $(Ba/Nb)_{pmn}$ for the MPG basalts. Generally the $(La/Nd)_{cn}$ values rises as the $(Ba/Nb)_{pmn}$ values rise, indicating that contamination by Lewisian granulite has affected the origin light REE ratios of the MPG basalts.

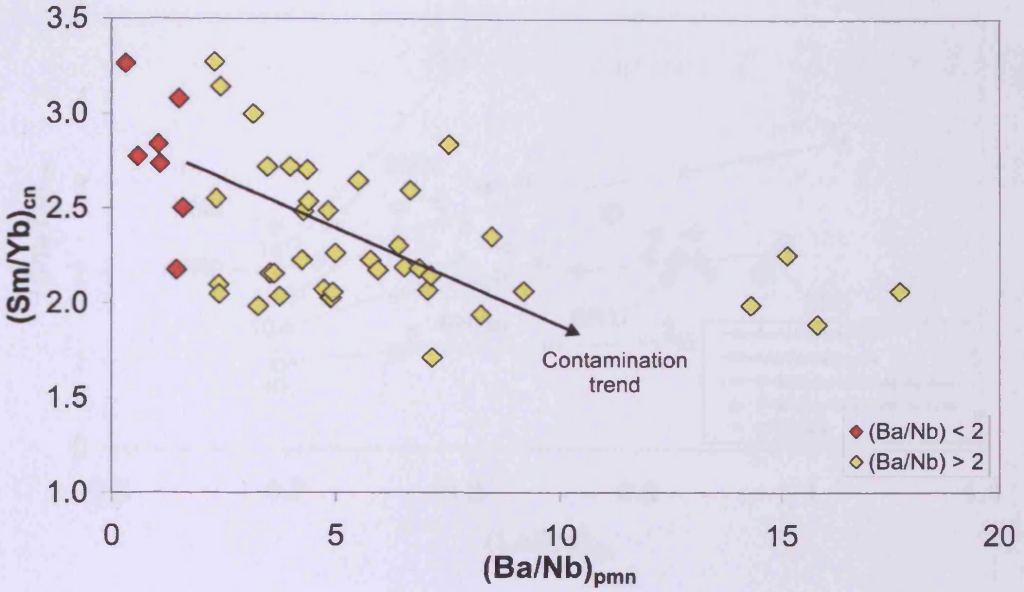

Fig. 6.38. Plot of $(Sm/Yb)_{cn}$ versus $(Ba/Nb)_{pmn}$ for the MPG basalts. Generall the $(Sm/Yb)_{cn}$ values decrease as the $(Ba/Nb)_{pmn}$ values increase, indicating that contamination by Lewisian granulite has affected the original heavy REE ratios of the MPG basalts.

For the samples with $(Ba/Nb)_{pmn}$ <2, the $(La/Nd)_{cn}$ are ≤ 1 or below Therefore, to filter out the most contaminated samples, only samples with $(La/Nd)_{cn}$ values <1 will be used in modelling mantle melting. Fig. 6.39 is a plot of $(La/Nd)_{cn}$ versus $(Sm/Yb)_{cn}$, with the melting curves for garnet, spinel, 50-50 mixture of garnet and spinel, and a 75-25% mixture of garnet and spinel respectively. Also plotted are the MPG basalts with $(La/Nd)_{cn}$ values below one. Most of the MPG basalts fall on the 50-50 garnet-spinel mixing line between 2 and 5 % melting, suggesting that the source region for these melts is in the spinel-garnet transition zone. However, there are a number of samples that do not fit this trend, and fall above the 75-25 garnet-spinel mixing line, which would suggest that these magmas have come from greater depths, where there is more garnet in the residue. When the samples (BM2, MR0, BB22) that show a greater garnet signature are plotted on a chondrite normalised diagram (Fig. 6.40a) along with 5 and 10 % garnet lherzolite melting, there is no correlation between the two. With the 5 and 10 % garnet lherzolite chondrite normalised values falling way below than seen for MPG basalt samples BM2, MR0 and BB22.

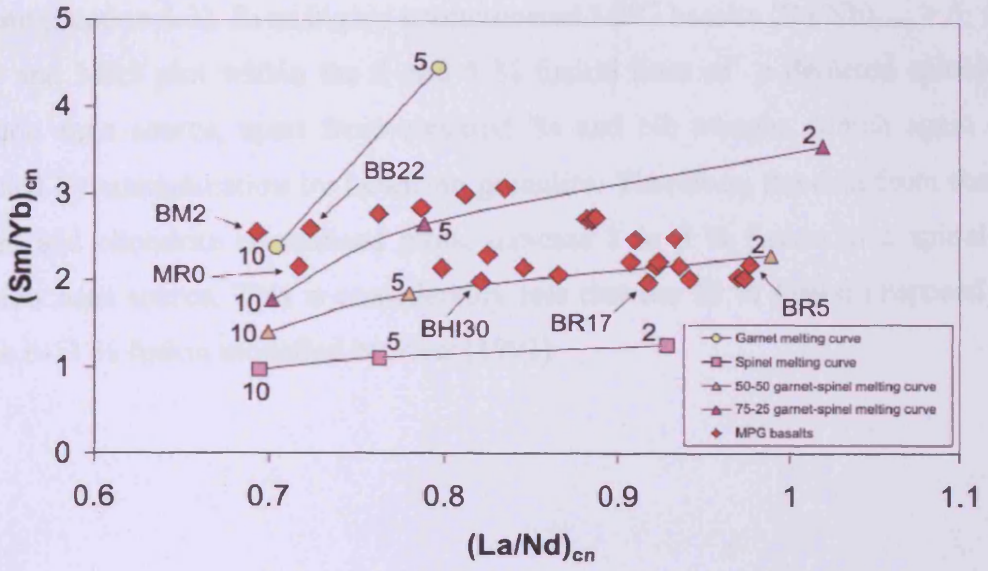

Fig. 6.39 Plot of $(Sm/Yb)_{cn}$ versus $(La/Nd)_{cn}$ for spinel lherzolite, garnet lherzolite, 50-50 % spinel-garnet, 25-75 % spinel-garnet and MPG basalts with $(La/Nd)_{cn}$ values below 1. Most of the MPG basalts fall on the 50-50 spinel-garnet melting line, however some do fall above the 25-75 spinel-garnet melting line.

However, when the chondrite-normalised values for BM2, MR0 and BB22 are plotted along with 2-5% melting of a 50-50 mixture of spinel and garnet lherzolite (Fig. 6.40b), there is a far better correlation, therefore these samples may have $(La/Nd)_{cn}$ values that are too low and their source melting region was in the spinel-garnet transition zone. Fig. 6.40c is a plot of three MPG basalts samples (BHI30, BR17, BR5) that plot on the 50-50 spinel-garnet lherzolite melting line, together with 2-5 % melting of a spinel-garnet transition zone melting source. Again, there is a correlation between the two, indicating a source region in the spinel-garnet transition zone.

Figs. 6.41a-c are multi element plots with 1, 2, 5 and 10 % fusion of a depleted 50-50 spinel-garnet lherzolite source. On Fig. 6.41a are plotted the relatively uncontaminated $(Ba/Nb)_{pmn} < 2$, MPG basalts BM6a and BHI18. Both of these samples plot between the 2 and 5 % fusion lines of a spinel-garnet transition zone source. It was proposed by Kerr (1993), and discussed in Section 6.3.9, that some of the MPG lavas had been contaminated by a small fraction enriched lithospheric melt, particularly the MPG basalt BM6. However, from Fig. 6.41b, it is obvious that the composition of BM6 can be produced by ~ 2 % fusion of a depleted spinel-garnet transition source. The exception is for Ba, which can be explained by contamination of BM6 by Lewisian

granulite (Section 6.3). Even highly contaminated MPG basalts $(Ba/Nb)_{pmn} > 5$, such as AM7b and MR9 plot within the 2 and 5 % fusion lines of a depleted spinel-garnet transition zone source, apart from elevated Ba and Nb troughs, which again can be explained by contamination by Lewisian granulite. Therefore, the data from the multi-element and chondrite normalised plots, indicate 2 to 5 % fusion of a spinel-garnet transition zone source. This is considerably less that the 10 % fusion proposed above, and the 6-11 % fusion modelled by Kerr (1993).

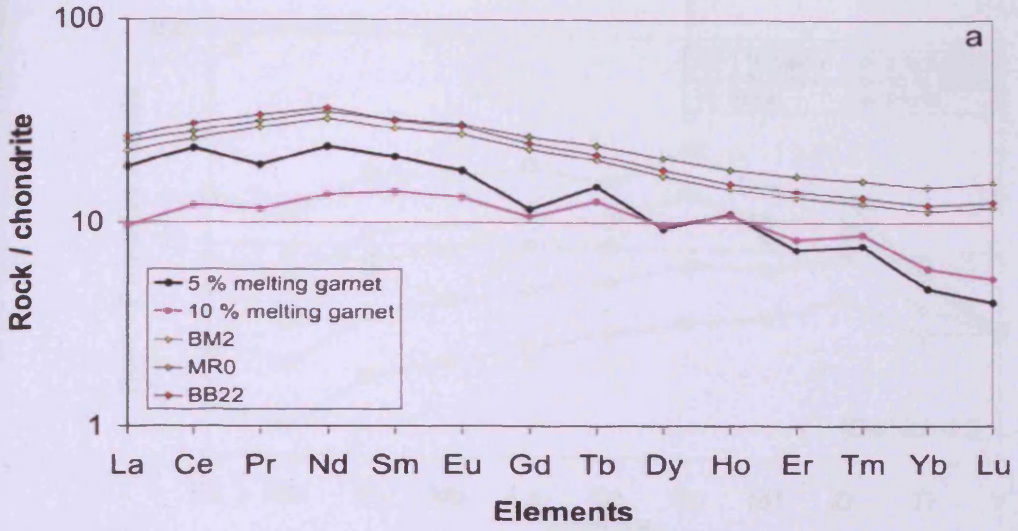

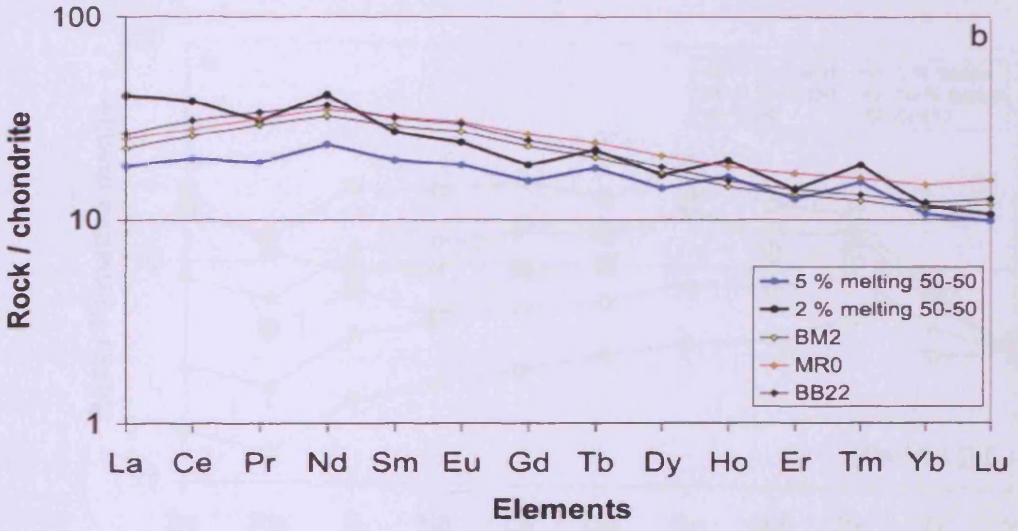

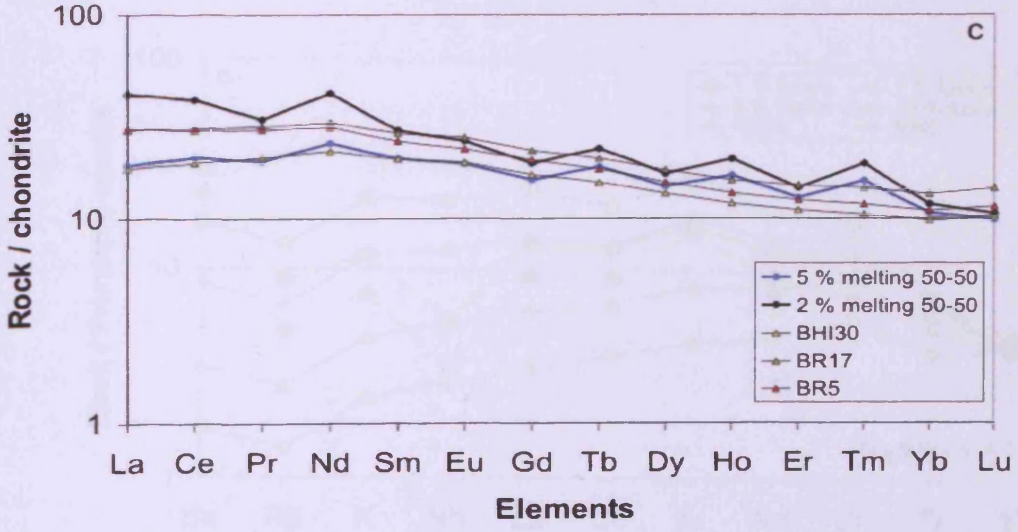

Figs. 6.40a-c. a) chondrite normalised (plot of 5 and 10 % melting of a depleted garnet source and MPG basalts BM2, MR0 and BB22. b) chondrite normalised plot of 2 and 5 melting of a 50-50 depleted spinel-garnet source and MPG basalts BM2, MR0 and BB22. c) chondrite-normalised plot of 2 and 5 % melting of a 50-50 depleted spinel-garnet source and MPG basalts BHI30, BR17 and BR5. (Sun and McDonough, 1989)

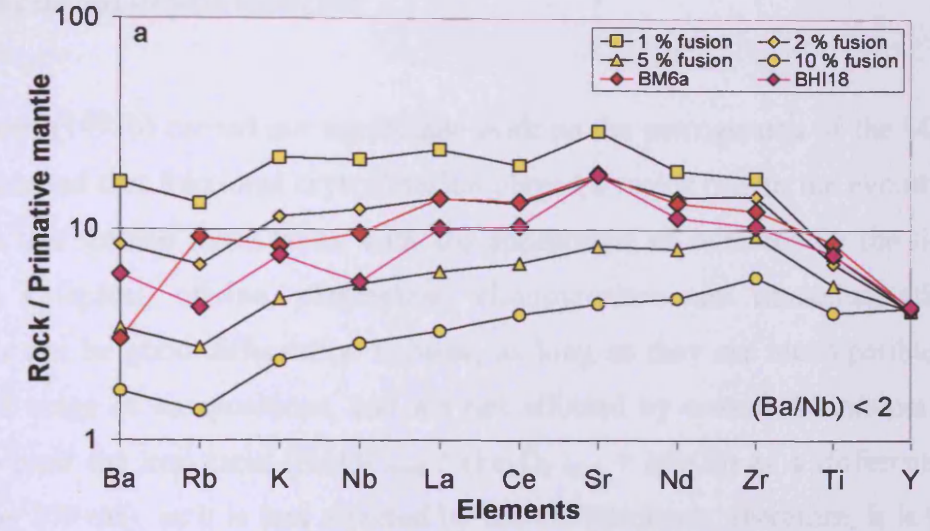

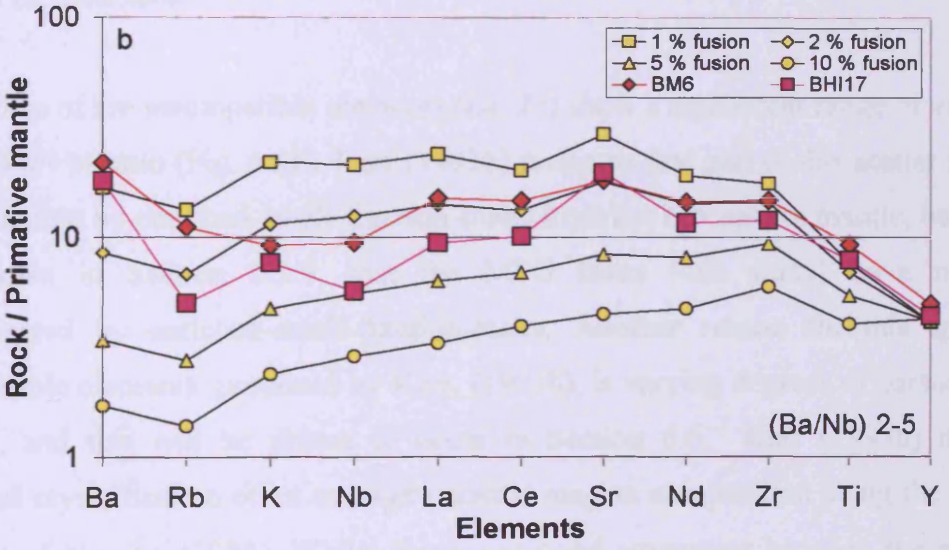

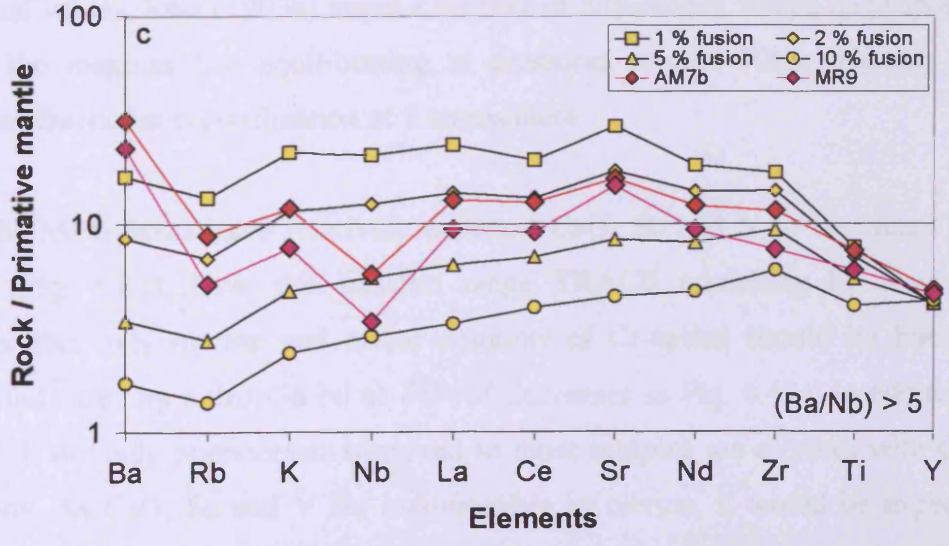

Figs. 6.41a-c. Multi-element plots with 1, 2, 5 and 10 % fusion of a depleted spinel-garnet transition zone plotted. a) Uncontaminated MPG basalts BM6a and BHI18 $(Ba/Nb)_{pmn} < 2$. b) Slightly contaminated MPG basalts BM6 and BHI17 $(Ba/Nb)_{pmn}$ 2-5. c) Highly contaminated MPG basalts AM7b and MR9 $(Ba/Nb)_{pmn} > 5$. (McDonough *et al.*, 1992)

6.5 Fractional crystallisation

Kerr, (1993b) carried out significant work on the petrogenesis of the MPG lavas, and concluded that fractional crystallisation played a major role in the evolution of the magmas that formed these lavas, with the appearance of minerals on the liquidus as follows; Cr-spinel, olivine, plagioclase, clinopyroxene and titanomagnetite. Trace elements can be good differention indexes, as long as they are incompatible over the observed range of compositions, and are not affected by crustal contamination. Kerr, (1993b) used the iron ratio ($Fe_2O_{3\ total}$ / ($Fe_2O_{3\ total}$ + MgO)) as a differention index (hereafter F/F+M), as it is less affected by mantle processes, therefore, it is this index that will be used here.

Some of the incompatible elements (La, Zr) show a significant range of values for a given F/F+M ratio (Fig. 6.42). Kerr (1993b) proposes that part of this scatter is due to contamination by enriched-small-fraction-melts from the lithosphere mantle, however it was shown in Section 6.3.9, that the MPG lavas (this study) have not been contaminated by enriched-small-fraction-melts. Another reason for this spread in incompatible elements, proposed by Kerr, (1993b), is varying degrees of partial mantle melting, and this will be shown to occur in Section 6.6. Kerr (1993b) modelled fractional crystallisation of an average parental magma composition using the TRACE program of Nielson (1988). Whilst there was good agreement between the modelled and actual values, Kerr (1993b) noted a number of differences, which he proposed were due to the magmas last equilibrating at pressures around 10kb, whereas TRACE calculates fractional crystallisation at 1 atmosphere.

The MPG lavas have relatively constant CaO, Sc and V in the range 0.45-0.6 F/F+M (Fig. 6.42). Over this basaltic range TRACE modelling by Kerr (1993b) indicates that only olivine and minor amounts of Cr-spinel should be fractionating phases, indicated by a drop in Ni as F/F+M decreases in Fig. 6.42c. In addition, from Chapter 3, the only phenocrysts observed in most samples are olivines with Cr-spinel inclusions. As CaO, Sc and V are incompatible in olivine, it would be expected that these elements would rise over the same F/F+M range as Ni decreases, but this is not the case, as they remain reasonable constant, indicating removal by another phase. Kerr

(1993b) suggests that clinopyroxene fractionation could account for this removal as CaO is a major constituent, and Sc and V are compatible in this phase (Ewart, 1989). Fractionation of clinopyroxene may also explain the decrease in Cr concentrations in the melt as fractionation proceeds (Fig. 6.42b) as Cr is highly compatible in clinopyroxene having a partition coefficient on 34 (Rollinson, 1993). Cr-spinel would also remove Cr from the melt, but is only found in small quantities in the MPG lava, therefore it is unlikely to remove Cr at the rates seen in Fig. 6.42b. However, no clinopyroxene phenocrysts have been found in the MPG lavas (this study), and only a few were found by Kerr (1993b) and Bailey *et al.* (1924).

The fractionation of unseen clinopyroxene is a common problem, not only in continental basalts, but also in Mid Ocean Ridge Basalts (MORB), (Larsen *et al.* 1989; Cox, 1979). It has also been noted in the Skye Main Lava Sequence (SMLS) by Thompson *et al.* (1972) and Thompson (1972). Atmospheric pressure melting experiments on the SMLS basalts by Thompson (1972) revealed that clinopyroxene crystallises well below the liquidus, i.e. the magmas are undersaturated with respect to clinopyroxene at atmospheric pressure. This was explained by postulating that the lava compositions were controlled by fractional crystallisation at pressures high enough for clinopyroxene to be a significant fractionating phase. Thompson (1974) carried out high-pressure melting experiments on basalts from Skye, in order to test this hypothesis. These experiments showed that, with increasing pressure, the clinopyroxene stability field moved closer to the liquidus, and so a fractionating phase at higher pressures.

Thompson *et al.* (1980) proposed that the SMLS magmas paused long enough during their assent from sub-crustal levels to dissolve their high-pressure phenocryst assemblages and crystallise low-pressure assemblages, without significant fractionation occurring. However, if this were the case, it would be expected that the concentrations of CaO, Sr and V would rise during olivine fractionation, as indicated by the drop in Ni as F/F+M increases (Fig. 6.42). Therefore, re-absorption of high pressure augite will not produce the flat patterns seen for CaO, Sr and V, whereas, removal of a mineral phase containing these elements will produce the observed patterns for these elements in Fig. 6.42. Kerr (1993b) proposes that in-situ or sidewall crystallisation (Langmuir 1989) can produce a situation where the geochemistry of the erupted magmas can be

explained by the removal of the observed phenocryst phases. That is, clinopyroxene and possibly olivine have been crystallised onto the walls of the magma chamber, and so would not be easily erupted. Such a situation would explain the major and trace element patterns (Fig. 6.42), and absence of augite phenocrysts in the MPG lavas.

The problem with in-situ or sidewall crystallisation is that ATA processes (Section 6.3.5) have contaminated the majority of MPG basalts. For ATA to work the hot basic magmas must be in contact with the conduit walls, so that assimilation can take place. If mineral phases such as clinopyroxene and olivine are crystallising onto the conduit walls they will form a shield, stopping assimilation of the crustal rocks. As was shown in Section 6.3.5, the ATA process was a mode of contamination affecting the MPG basalts, and that olivine was fractionating at the same time, because melt inclusions in these olivines are contaminated by Lewisian crust. Therefore, for in-situ or sidewall crystallisation to explain the removal of clinopyroxene, it must have been occurring at the same time as crustal assimilation by the ATA process.

Theoretically, it would be possible to assimilate crust at given points in a magma conduit, whilst fractionating mineral phases at another point. A good analogy would be a stream, where erosion (assimilation) takes place on the outside of a bend, and deposition (fractionation) takes place on the inside of the bend. Therefore, you would have Assimilation and Fractionation during Turbulent Assent (AFTA), which could explain the geochemistry of the MPG lavas. The effect that this fractionation would have on incompatible elements is to increase their concentrations in the magma, such as seen for La and more particularly Zr in Fig. 6.42. Therefore, when modelling incompatible elements such as the REE, Zr, Y and Ti, this rise in concentrations has to be taken into account. In Figs. 6.40 and 6.41, which are REE, and multi element plots the amount of fusion is indicated to be 2-5%, which due to this fractionation is too low. Therefore, elemental ratios that are not affected by fractional crystallisation will be used to model the amount of mantle fusion that led to the formation of the MPG lavas.

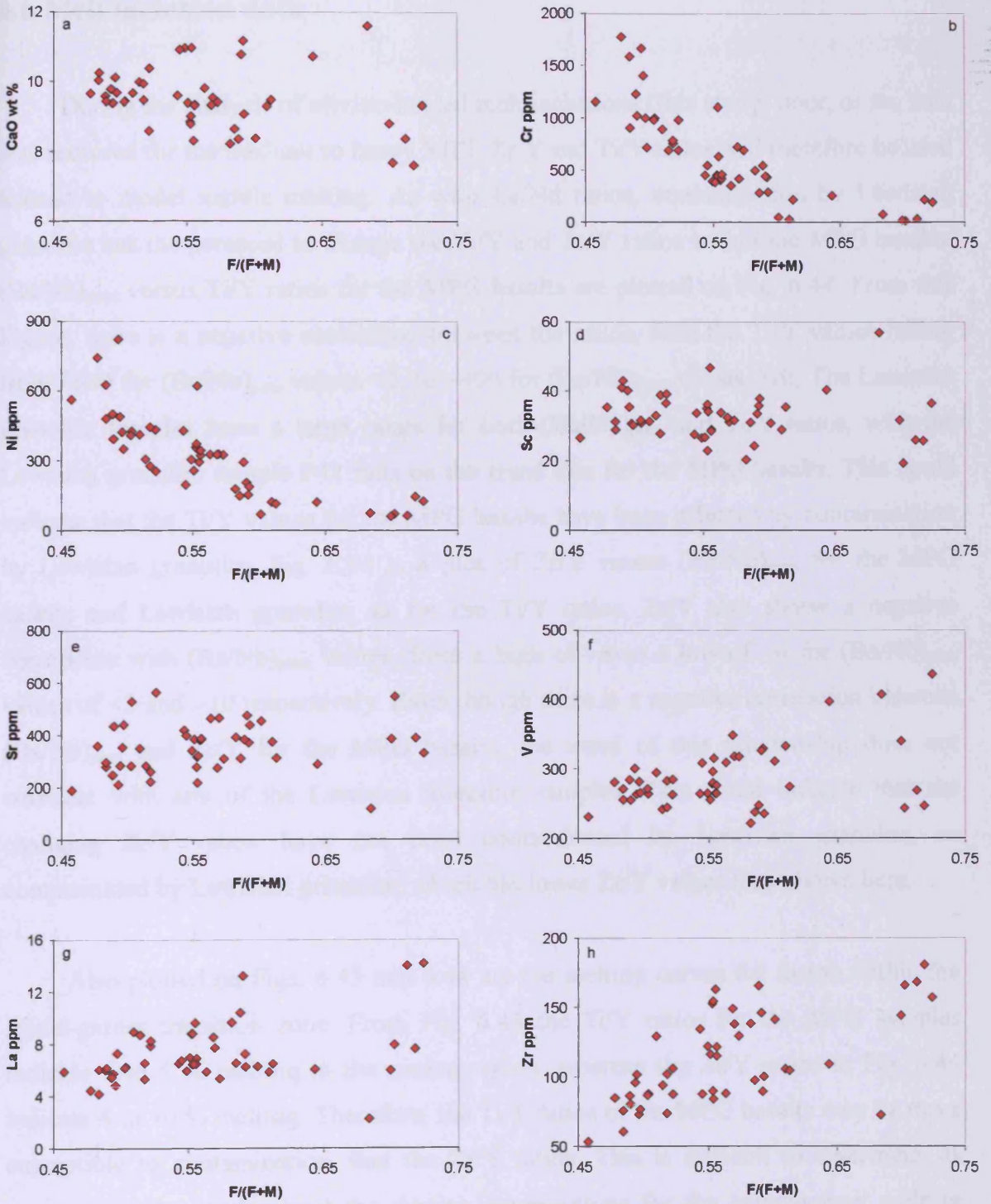

Fig. 6.42. Plots of major and trace elements versus $Fe_2O_3/(Fe_2O_3+MgO)$ for the MPG lavas.

6.6 Melt inclusion data

During the analysis of olivine-hosted melt inclusions (this study) poor, or no, data was acquired for the medium to heavy REE. Zr/Y and Ti/Y ratios will therefore be used instead to model mantle melting. As with La/Nd ratios, contamination by Lewisian granulite has the potential to change the Ti/Y and Zr/Y ratios within the MPG basalts. $(Ba/Nb)_{pmn}$ versus Ti/Y ratios for the MPG basalts are plotted on Fig. 6.44. From this Figure, there is a negative correlation between the ratios, with the Ti/Y values falling from ~600 for $(Ba/Nb)_{pmn}$ values <2, to ~400 for $(Ba/Nb)_{pmn}$ values >10. The Lewisian granulite samples have a large range for both $(Ba/Nb)_{pmn}$ and Ti/Y ratios, with the Lewisian granulite sample P42 falls on the trend line for the MPG basalts. This could indicate that the Ti/Y values for the MPG basalts have been affected by contamination by Lewisian granulite. Fig. 6.44 is a plot of Zr/Y versus $(Ba/Nb)_{pmn}$ for the MPG basalts and Lewisian granulite, as for the Ti/Y ratios, Zr/Y also shows a negative correlation with $(Ba/Nb)_{pmn}$ values, from a high of ~8 to a low of ~4 for $(Ba/Nb)_{pmn}$ values of <2 and >10 respectively. Even though there is a negative correlation between $(Ba/Nb)_{pmn}$ and Zr/Y for the MPG basalts, the trend of this relationship does not correlate with any of the Lewisian granulite samples. This could indicate that the changing Zr/Y ratios have not been contaminated by Lewisian granulite, or contaminated by Lewisian granulite, which has lower Zr/Y values than shown here.

Also plotted on Figs. 6.43 and 6.44 are the melting curves for fusion within the spinel-garnet transition zone. From Fig. 6.43 the Ti/Y ratios for the MPG samples indicate 1 to 5 % melting in the source region, whereas the Zr/Y ratios in Fig. 6.44 indicate 4 to 10 % melting. Therefore, the Ti/Y ratios of the MPG basalts may be more susceptible to contamination, that the Zr/Y ratios. This is difficult to determine, as assumptions are made about the starting compositions for the spinel-garnet melting curves, and changing the starting compositions change where the MPG basalts fall on the melting curve. What Figs 6.43 and 6.44 do show is that the more voluminous magmas are the most contaminated with Lewisian crust.

A melting curve for fusion within the garnet-spinel transition zone using Zr/Y and Ti/Y ratios is shown on Fig. 6.45, together with the MPG basalts (whole rock),

which have been separated on their $(Ba/Nb)_{pmn}$ ratios (Group 1 $(Ba/Nb)_{pmn}$ <2, Group 2 $(Ba/Nb)_{pmn}$ 2-8, Group 3 $(Ba/Nb)_{pmn}$ >8). From this Figure, it is obvious that there is a correlation between the amount of partial fusion and contamination by Lewisian granulite. Group 1 basalts $(Ba/Nb)_{pmn}$ <2 have undergone 4-9 % partial fusion, Group 2 $(Ba/Nb)_{pmn}$ 2-8, have undergone 4-13 % partial fusion, and Group 3 $(Ba/Nb)_{pmn}$ >8 have undergone 9-13 % partial fusion. As well as showing a correlation between amount of melting and contamination, the melting line for Zr/Y versus Ti/Y also indicates fusion in the garnet-spinel transition zone of between 4-13 %, and is close to the amount of fusion proposed by Kerr (1993) of between 6-11 %.

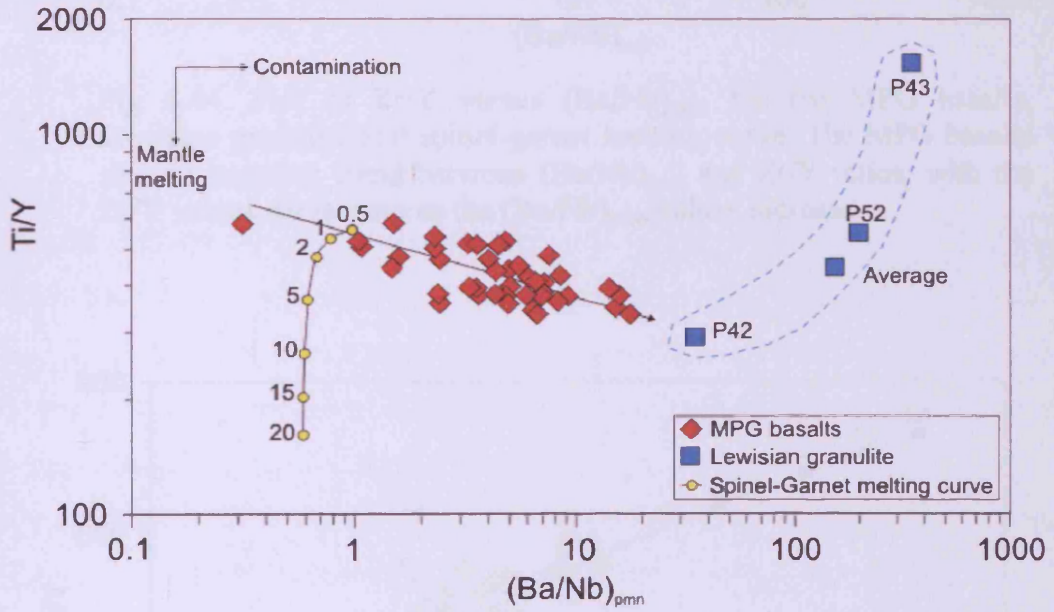

Fig 6.43. Plot of Ti/Y versus $(Ba/Nb)_{pmn}$ for the MPG basalts, Lewisian granulite and spinel-garnet melting curve. The MPG basalts show a negative trend between $(Ba/Nb)_{pmn}$ and Ti/Y ratios, with the Ti/Y values decreasing as the $(Ba/Nb)_{pmn}$ values increase.

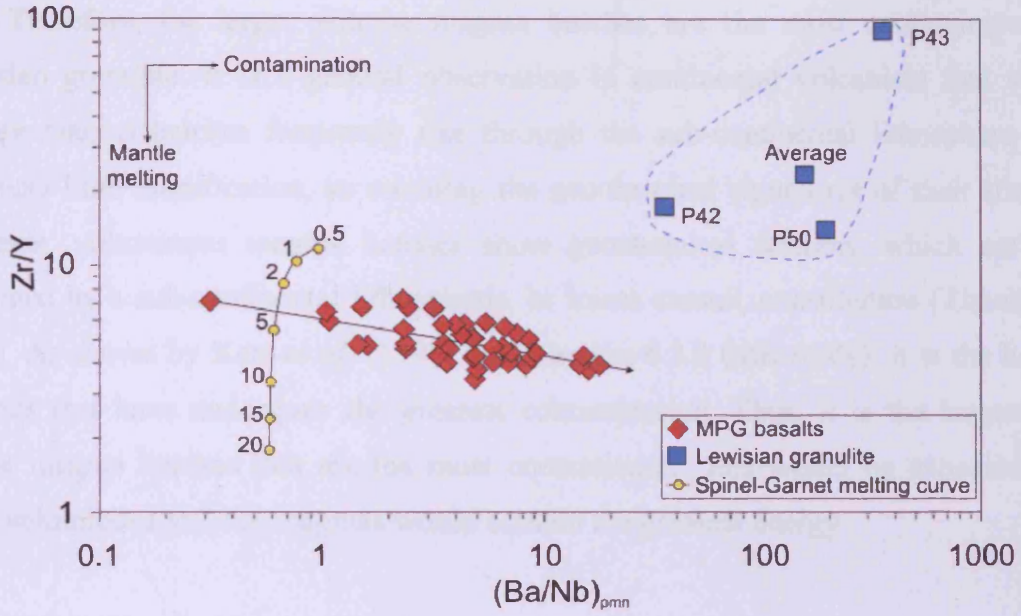

Fig 6.44. Plot of Zr/Y versus $(Ba/Nb)_{pmn}$ for the MPG basalts, Lewisian granulite and spinel-garnet melting curve. The MPG basalts show a negative trend between $(Ba/Nb)_{pmn}$ and Zr/Y ratios, with the Zr/Y values decreasing as the $(Ba/Nb)_{pmn}$ values increase.

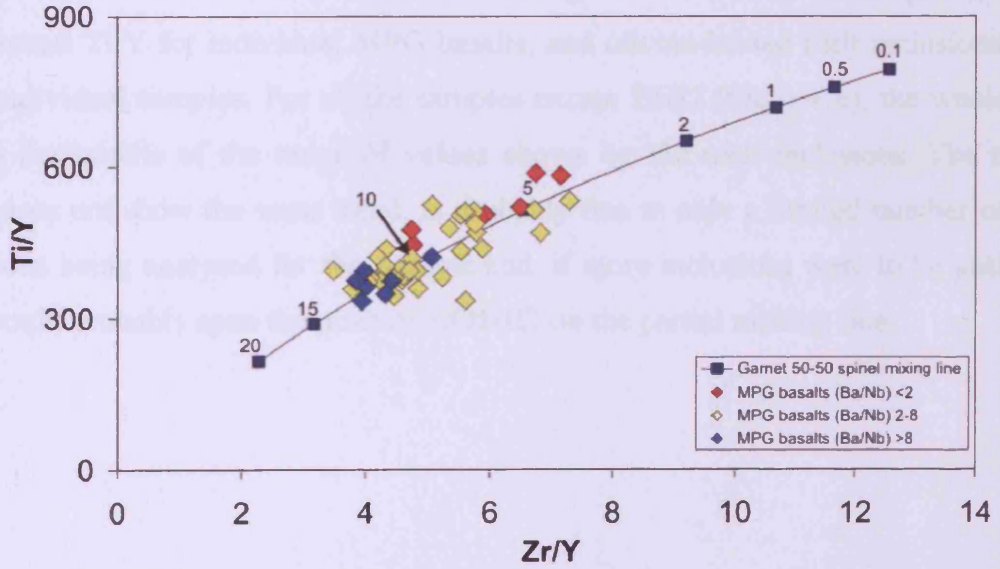

Fig. 6.45. Plot showing the melting curve for a source region within the garnet-spinel transition zone (number refer to amount of partial fusion). Also plotted are the MPG basalts (this study), as a function of their $(Ba/Nb)_{pmn}$ ratios. The trend indicates that as the Zr/Y and Ti/Y ratios fall, as the $(Ba/Nb)_{pmn}$ ratios increase.

Therefore, the larger volume magma batches are the most contaminated by Lewisian granulite. It is a general observation in continental volcanism that small-volume magma batches frequently rise through the sub-continental lithosphere with relatively little modification, so retaining the geochemical signatures of their sources. However, voluminous magma batches show geochemical features, which are best explained by a sub-continental lithospheric, or lower crustal, contribution (Thompson, 1986). As shown by Kerr *et al.* (1995), and Section 6.3.2 (this study), it is the hottest magmas that have undergone the greatest contamination. Thus, it is the largest and hottest magma batches that are the most contaminated, this would be expected, has these voluminous and hot magmas would contain the greatest energy .

The Zr/Y and Ti/Y ratios of the olivine-hosted melt inclusions are plotted on Fig. 6.46, with the MPG basalts whole rock values. The melt inclusions have a much larger range in ratios, than the whole rock, indicating that the melt inclusions represent aliquots of partial melts ranging from below ~2% fusion to 20% fusion. Therefore, the MPG basalts represent intermediate compositions of a range of partial melts, sampled by the melt inclusions. This is also shown in Figs. 6.47a-l, which are diagrams of the Zr/Y versus Ti/Y for individual MPG basalts, and olivine-hosted melt inclusions from these individual samples. For all the samples except BHI2 (Fig 6.47e), the whole rock plot in the middle of the range of values shown by the melt inclusions. The reason BHI2 does not show the same trend, is probably due to only a limited number of melt inclusions being analysed for this sample and, if more inclusions were to be analysed, they would probably span the position of BHI2 on the partial melting line.

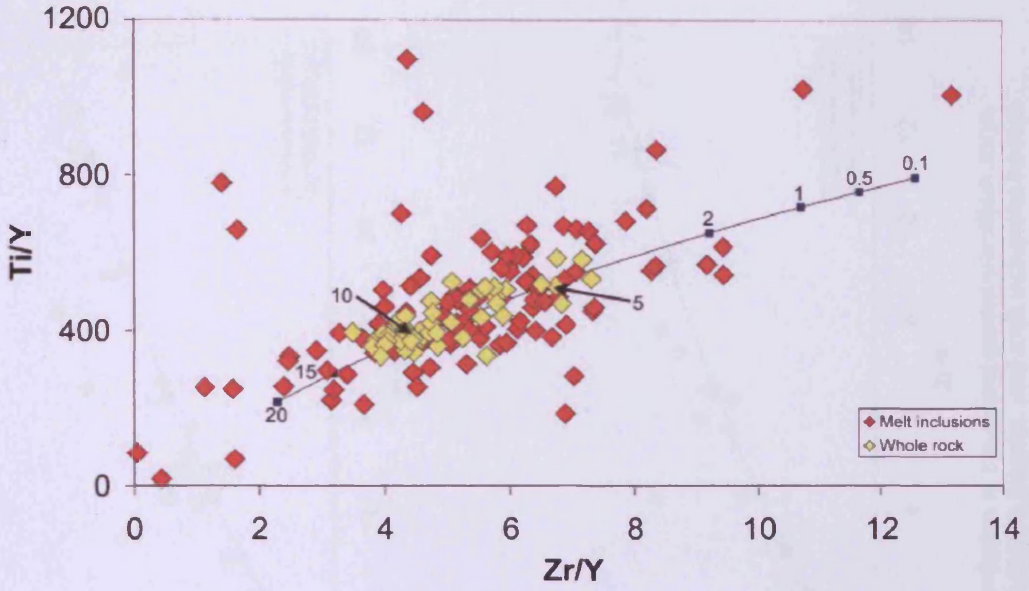

Fig. 6.46. Plot showing the melting curve for a source region within the garnet-spinel transition zone (number refer to amount of partial fusion). Also plotted are the MPG basalts whole rock, and olivine-hosted melt inclusion data (this study). The melt inclusions have a far greater spread than the whole rock data, indicating that the MPG basalts are a combination of differing melt fractions, which have their geochemical signatures preserved in the olivine-hosted melt inclusions.

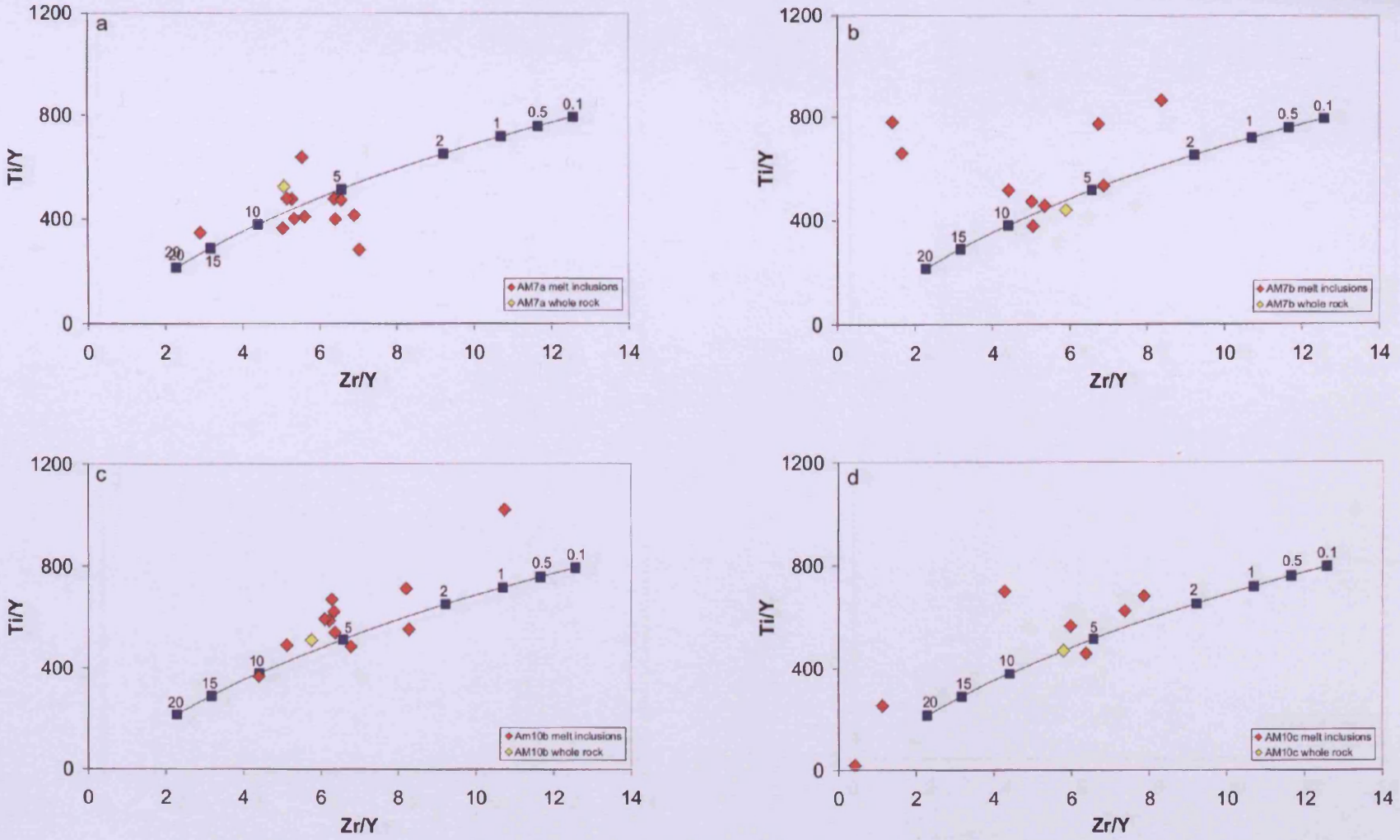

Figs. 6.47a-d. Trace element ratio diagrams, showing the partial melting curve for fusion in the spinel-garnet transition zone. Numbers next to symbols represent the amount of fusion. Also plotted are selected MPG basalts, and melt inclusions hosted in olivine crystals located in these MPG basalts.

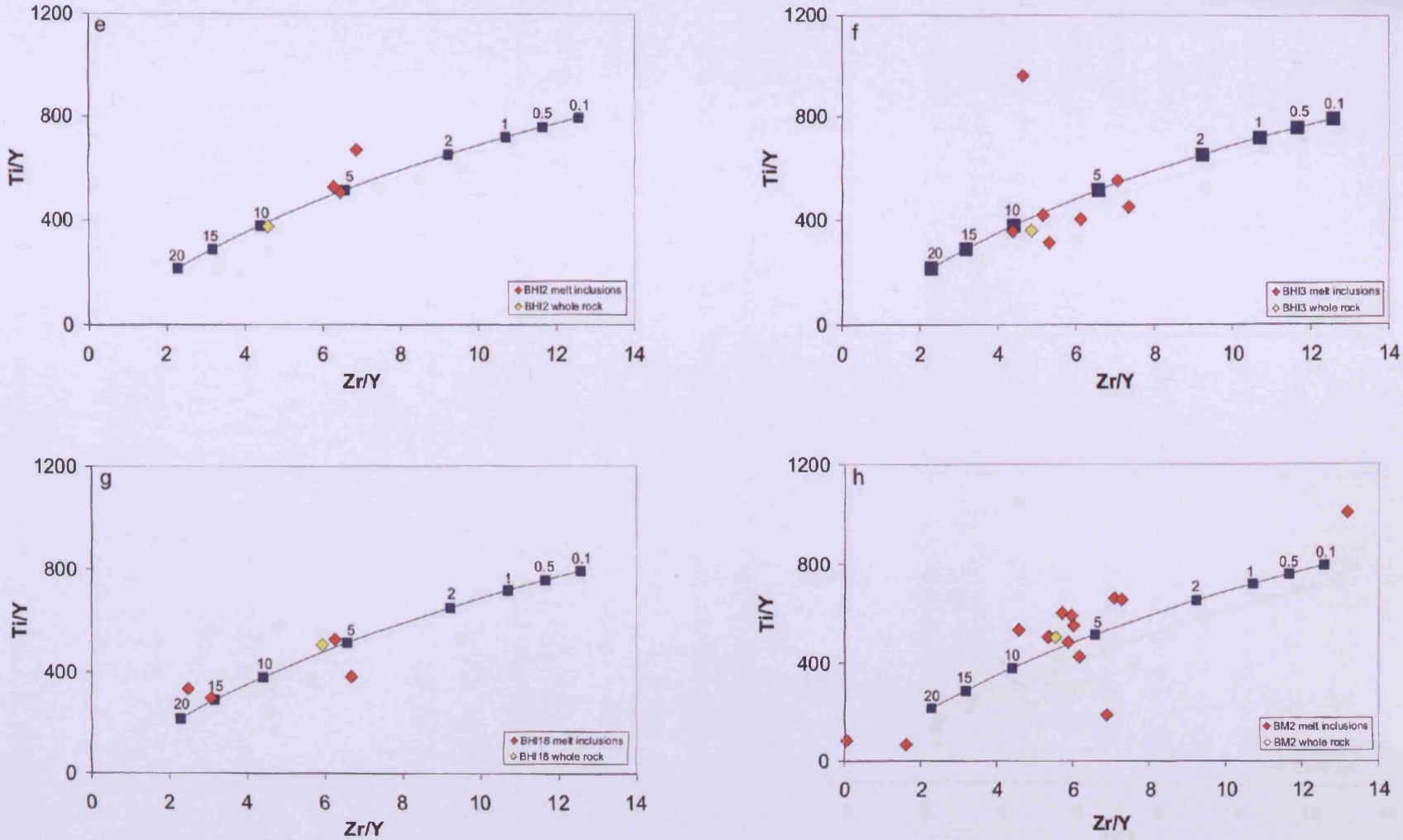

Figs. 6.47e-h. Trace element ratio diagrams, showing the partial melting curve for fusion in the spinel-garnet transition zone. Numbers next to symbols represent the amount of fusion. Also plotted are selected MPG basalts, and melt inclusions hosted in olivine crystals located in these MPG basalts.

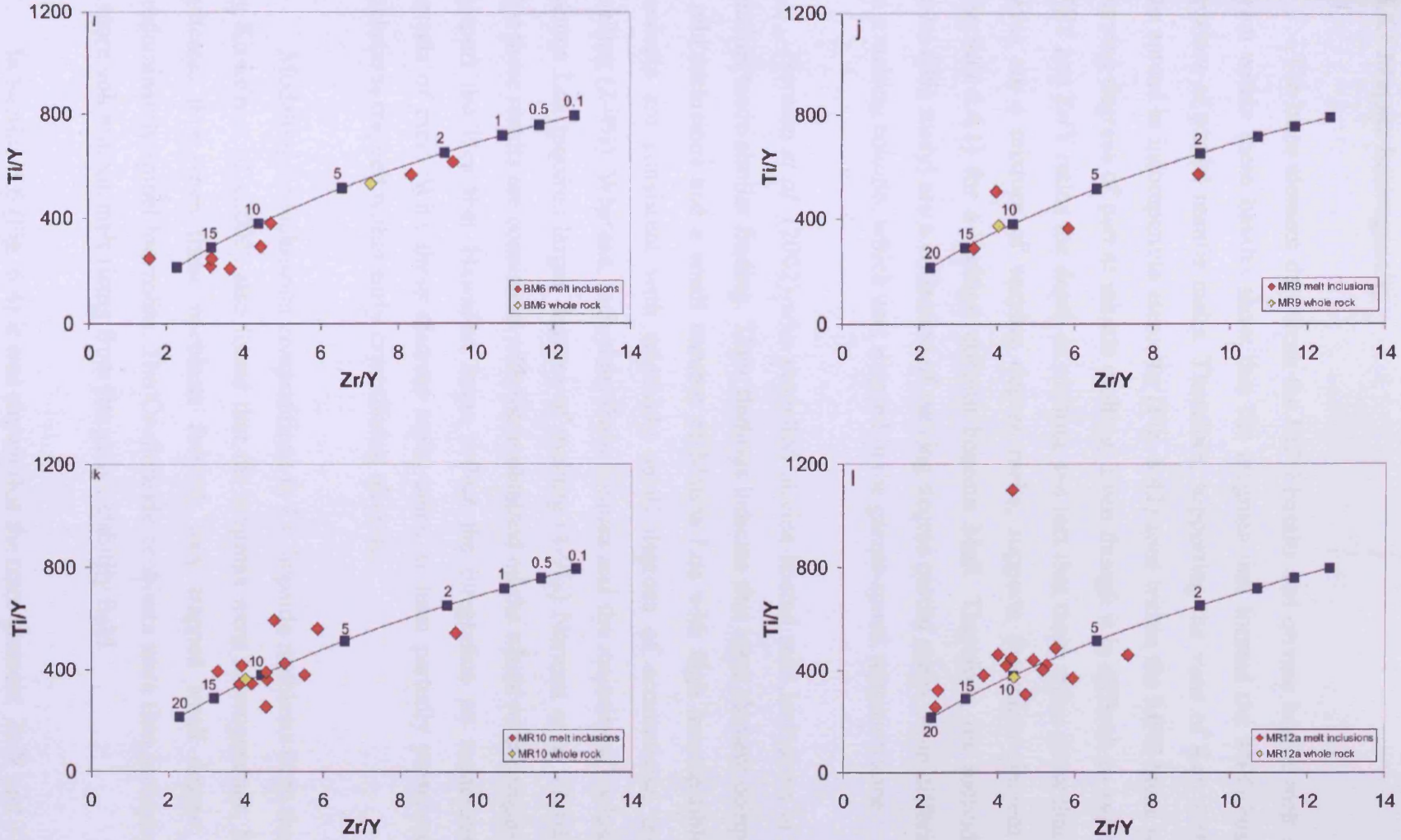

Figs. 6.47i-l. Trace element ratio diagrams, showing the partial melting curve for fusion in the spinel-garnet transition zone. Numbers next to symbols represent the amount of fusion. Also plotted are selected MPG basalts, and melt inclusions hosted in olivine crystals located in these MPG basalts.

6.6.1 Magma heterogeneity

The trace element data from the MPG basalts and olivine hosted melt inclusions from within these basalts show that the magmas that formed the MPG basalts are a mixture of partial mantle melts. Therefore, supporting the view of Kerr (1993b), that the spread in incompatible elements (Fig. 6.42) seen within the MPG lavas was due to varying degrees of partial mantle melting. Even though it is difficult to ascertain from Ti/Y and Zr/Y ratios the depth of melting, the fact that these ratios show that the MPG lavas are a mixture of varying degree melts, supports the major-element evidence (Section 6.4.1) for a melting column beneath Mull. Therefore, the individual MPG lavas (this study) are a collection of varying degree partial melts, from differing depths in a melting column, which was situated in the garnet-spinel transition zone.

Norman *et al.* (2002) who modelled olivine-hosted melt inclusions in Hawaiian picrites made similar finding. Their findings indicate that trace element composition of Loihi inclusions and a small number of Mauna Loa with high incompatible element contents are consistent with relatively small degrees of accumulated incremental melting (2-4%). Whereas, inclusions from Kilauea and the majority of inclusions from Mauna Loa required larger degrees of melting (4-9%) Norman *et al.* (2002) propose that these results are consistent with those obtained on the whole rock composition, and support the idea that Hawaiian lavas reflect the integration on numerous discrete parcels of melt. With these discrete melts being at least partially preserved as melt inclusions trapped within early crystallising olivines.

Modelling of inclusions compositions in Cr-diopside neoblasts from the Oslo rift by Kirstein *et al.* (2002) also found that the magmas were heterogeneous. Modelling indicates that when these neoblasts formed, they trapped small degree melts of predominantly spinel lherzolite. The Cr-diopside neoblasts were then incorporated into a more voluminous melt rising from the garnet stability field.

In Section 6.6 (Fig. 6.4) it was shown that the trace element Zr/Y and Ti/Y ratios for the inclusions have a range that spans that of the whole rock. Borisora *et al.* (2002) found similar trends for olivine-hosted melt inclusions in Kerguelen plume-derived picritic basalts. These inclusions had P_2O_5/Al_2O_3 and K_2O/P_2O_5 ratios that overlapped

the compositions of the host basalts. Borisora *et al.* (2002) propose that two-component mixing between different melts controlled the compositional characteristics of the picritic basalts.

6.7 Mantle melting regime

Calculations by McKenzie and Bickle (1988) showed that little basaltic magma can be produced in continental regions without either some extension (expressed in terms of the ß factor) and/or mantle potential temperatures (T_p) which are well in excess of 1280°C. In the Hebrides extension (calculated from aggregate dyke thicknesses) is generally around 5 % (ß = 1.05) and rarely exceeds 10 % (ß = 1.1) (Speight *et al.*, 1982). However, it has been proposed by Thompson and Gibson (1991) that the Palaeocene extension in the Hebridean region was superimposed on previous Mesozoic sedimentary basins, which may have resulted in lithospheric thin-spots, below which greater quantities of melt could have been generated.

Kerr (1995), using the equations and diagrams from McKenzie and Bickle (1988), obtained a crude estimate of T_p and extent of melting for a suite of magmas, For an average parental MPG magma with a MgO content of 13.5 wt %, the T_p is estimated to be within 1420°C and 1460°C. Depending on whether the entropy of melting (ΔS) is taken to be 250 J K^{-1} kg^{-1} (McKenzie and Bickle, 1991) or 400 J K^{-1} kg^{-1} (Watson and McKenzie, 1991). The calculations by Kerr (1995) indecated the mean extent of melting was in the order of 7-11 %, (very similar to the 4-13 % melting indicated by Zr/Y and Ti/Y modelling here) at pressures in the range of 2-2.5 GPa. Although Kerr (1995) indicates there could be considerable error in such calculations, the fact that considerable volumes of anhydrous melt have been produced below 70-80 km thick lithosphere (Ellam, 1992) also supports an elevated T_p below the Hebridean region. Both of these lines of evidence for elevated mantle potential temperature strongly support the view that melting of a plume, probably the North Atlantic (Icelandic) plume, was responsible for the generation of the Mull lava succession.

6.8 Model for the formation of the MPG basalts

This study has modelled the whole rock and olivine-hosted melt inclusions geochemistry for a suite of MPG lavas. The outcome of this modelling is a sequence of 11 major events (Fig. 6.48) that have led to the compositions and textures we now see in the MPG lavas.

1. Whole rock $(La/Nd)_{cn}$ and $(Sm/Yb)_{cn}$ ratios (Figs 6.35 and 6.36) indicate that melting occurred in the spinel-garnet transition zone. Modelling of these ratios also shows that the source composition must have been depleted relative to Bulk Earth.

2. Major element modelling (Section 6.4.1) indicates melting was over a range of depths within a melting column. Melt inclusions Zr/Y and Ti/Y ratios (Figs. 6.46 and 6.47a-l) show that the degree of partial melting within this column was in the range of 2-20%.

3. Whole rock and olivine-hosted melt inclusion Zr/Y and Ti/Y ratios (Fig. 6.47a-l) indicate that the individual MPG magmas, were a mixture of melts from the melting column. The mean extent of melting of the MPG magmas was between 4 and 13% (Fig. 6.41).

4. The extracted magmas rise through the lithosphere, with little interaction, probably due to the lithosphere having a refractory nature.

5. Some magma ponded in the upper lithosphere, where fractionation of olivine and possible clinopyroxene occurred. This is shown from Figs 6.21 and 6.22, where olivines in samples AM10 and BM2 have fractionated without contamination by Lewisian granulite. Modelling of fractional crystallisation (Section 6.5) shows that clinopyroxene must have been crystallising from the melts at the same time as olivine.

6. Modelling of crustal contamination (Section 6.36) using olivine forsterite content, and melt inclusion $(Ba/Nb)_{pmn}$ (Fig. 6.20) ratios indicate that some magma batches must have ponded in the lower crust, where they were contaminated by Lewisian crust by the AFC process.

7. Modelling as in (6) (Fig. 6.19) indicates that some magmas were contaminated by Lewisian crust by the ATA process.

8. As was shown in Section 6.36, contamination of magmas occurred at the same time that olivine was fractionating from the melt, that is olivine-hosted melt inclusions are contaminated by Lewisian crust. From Section 6.5 it is also shown that clinopyroxene was fractionating at the same time as olivine, with both phases being lost to the melt. Therefore, fractionation of olivine and clinopyroxene was occurring at the same time as the magmas were being contaminated by Lewisian crust, very often by the ATA process. Therefore, these phases must have been fractionating onto the conduit walls at the same time as the magmas were assimilating wall rock.

9. Whole rock Zr/Y and Ti/Y ratios in conjunction with $(Ba/Nb)_{pmn}$ (Section 6.6) and isotope data (Section 6.3.2) indicate that it was the hottest most voluminous magma that suffered the greatest contamination. With magmas of between 4-9% fusion have $(Ba/Nb)_{pmn}$ ratios below 2, magmas of between 4-13% fusions having $(Ba/Nb)_{pmn}$ ratios between 2-8, and magmas of between 9-13% fusion have $(Ba/Nb)_{pmn}$ ratios above 8.

10. The magmas rose from great depth extremely rapidly, without pausing in the upper crust. Evidence for this come from olivine-hosted decrepitated melt inclusions (Section 4.2.4), as melt inclusions only decrepitate when there is a rapid drop in pressure, without a corresponding drop in temperature

11. The MPG lavas have undergone post emplacement, secondary alteration to zeolite facies, due to the emplacement of the Mull Central Intrusive Complex (Section 6.2).

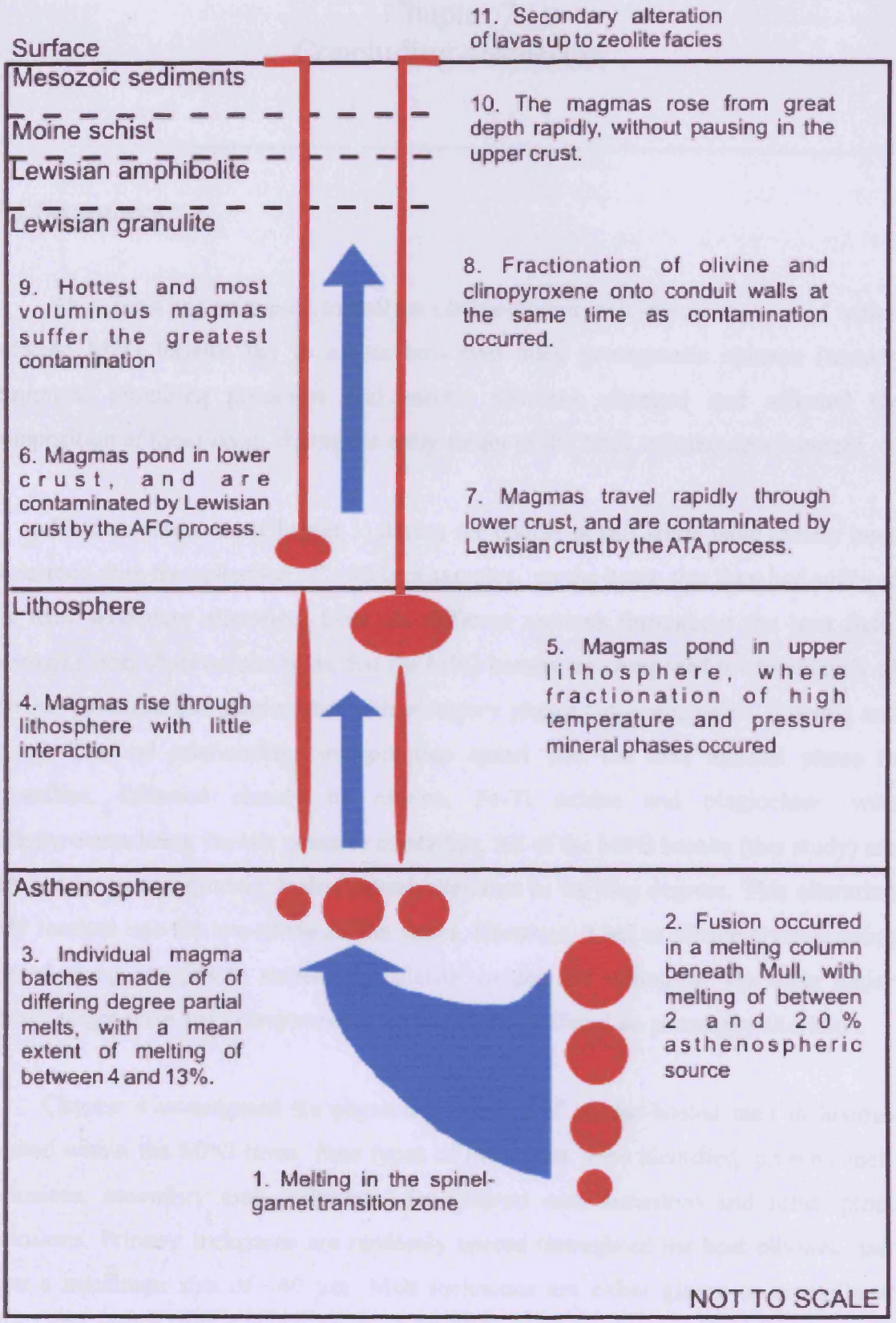

Fig. 6.48. Flow diagram showing the melting regime and extraction processes that have influenced the observed compositions of the MPG lavas.

Chapter 7
Concluding discussion

7.1 Summary

This thesis has attempted to analyse olivine-hosted melt inclusions located within selected MPG basalts and to assess how two main petrogenetic spheres (namely magmatic plumbing processes and mantle sources), changed and affected the composition of these lavas, during the early stages of the Mull volcano development.

Field investigation (Chapter 3) during the course of this study have chiefly been concerned with the collection of ~50 lava samples, on the basis, that they had suffered the least secondary alteration, from six different sections throughout the lava field. Petrographical observations show that the MPG basalts are composed predominantly of olivine, pyroxene and plagioclase, with accessory phases being magnetite, ilmenite and spinel. Textural relationships indicate that spinel was the first mineral phase to crystallise, followed closely by olivine, Fe-Ti oxides and plagioclase, with clinopyroxene being the last phase to crystallise. All of the MPG basalts (this study) are affected by post-magmatic, hydrothermal alteration to varying degrees. This alteration only reached into the low-grade zeolite facies. However, it led to olivine crystals being altered along margins to serpentine, chlorite, oxides and iddingsite, the other major phases plagioclase and clinopyroxene, seem to have suffered no secondary alteration.

Chapter 4 investigated the physical properties of olivine-hosted melt inclusions located within the MPG lavas. Four types of inclusions were identified, primary melt inclusions, secondary melt inclusions, decrepitated melt inclusions and solid spinel inclusions. Primary inclusions are randomly spaced throughout the host olivines, and have a maximum size of ~40 μm. Melt inclusions are either glassy or crystallised (Fig.4.10), glassy inclusions tend to be below 15 μm in diameter, whereas crystallised inclusions have a size range of 10-40 μm (Section 4.2.6). Secondary melt inclusions are derived from a younger (more evolved) melt than that from which the host phenocrysts crystallise. They are always small, being less than 10 μm in diameter, and are generally

located in fracture zones (Fig. 4.6). However, sometimes these fractures have healed, leaving a string of secondary inclusions as the only evidence that the fracture ever existed (Fig. 4.7).

Decrepitated inclusions are all over 40 μm in diameter (Fig. 4.9), indicating there is a maximum size to the melt inclusions that the host olivine can contain without decrepitation occurring. Inclusions decrepitate when dilatation stress caused by decompression exceeds a critical value. If this decompression is accompanied by temperature decrease along a typical geotherm (slow rise to the surface) then the pressure and temperature would cancel each other out. Therefore, it is possible to infer from the presence of these olivine-hosted decrepitated inclusions that the magmas that formed the MPG lavas (this study) decompressed rapidly with no corresponding drop in temperature (i.e. rapid rise to the surface).

Cr-spinels are only found enclosed, or partially enclosed within olivine phenocrysts in the MPG basalts. As indicated by Kerr (1998), it is highly likely that Cr-spinel was the first phase to crystallise, and provided sites for olivine nucleation. Generally the spinel inclusions are dark in colour, but there are a number of exceptions that have a lighter colour (Fig. 3.21).

7.2 Melt inclusion analysis

There are two main ways in which melt inclusions can be analysed. The glassy or crystalline melt inclusions can be reheated to homogenise their contents. The inclusions are then brought to the surface where they can be sampled. The main disadvantages with this approach, even if care is taken in the heating experiments, are melt inclusions may not be homogenised correctly (Fig. 4.16), and before an inclusion can be analysed, it has to be brought to the surface. Therefore, during this process many inclusions may be lost, just to glean information from one.

To overcome the problems associated with the homogenisation of inclusions, workers have been developing methods of analysing inclusions below the sample surface using LA-ICP-MS, (Gunther *et al.*, 1998; Audetat *et al.*, 1998; Ulrich *et al.*,

1999 and Halter *et al.*, 2002). The methods of analysis used in this study, were those of Halter *et al.* (2002), with modifications being made where necessary. Pits are ablated into the surface of the olivine, to a depth where the melt inclusion is completely ablated (Fig. 4.17). The interpretation of the analytical signal into quantitative elemental concentrations in the melt inclusions consist of a three-step process (Section 4.3).

1 Analytical signal is converted into element ratios through the use of an external standard.
2 The elemental concentrations are calculated by means of an internal standard, as no internal standard can be used in the mixed signal (olivine + inclusion – Fig.4.17) it is assumed that the major oxides sum to 100% of the analysis.
3 The host contribution (olivine) to the elemental concentration in the mixed host-inclusion signal (segment 3 in Figs 4.17 and 4.18) is subtracted.

This approach is not without its problems, not least, an independent internal standard for the melt inclusions is needed for the quantification of the melt inclusions. The main advantage is that many inclusions, even in the same crystal can be sampled, without prior homogenisation.

Chapter 5 investigates a number of ways of quantifying elemental concentrations in olivine-hosted melt inclusions, using different external standards (i.e. NIST glasses 610, 612, 614 and artificial glass rock standards BIR-1, BHVO-2 and BCR-2), and carrier gas (i.e. Ar, He). It is shown in Section 5.5 that He is a far better carrier gas than Ar. For elements with atomic masses up to phosphorus, the count rates for He are 3 to 8 fold that of Ar, whereas for elements with masses greater than phosphorus the increase in counts for He over Ar are 0.5 to 3 fold. The rock standards were chosen as the preferred external standards, as they have elemental concentration far closer to the MPG lavas than the NIST glasses (Section 5.3).

Determination of the mass factor x (i.e. mass of inclusion/mass of inclusion + host olivine), needed for the quantification of elements in the inclusions, proved to be very problematic (Section 5.8). Four different methods were used to calculate the mass factor: 1) constant internal standard for the melt inclusions (14 wt % Al_2O_3); 2) constant distribution coefficient of an element between mineral and melt (Dy =

0.0038); 3) constant internal standard for melt inclusions (48 wt % SiO_2); 4) variable SiO_2 concentrations. Using constant values for both Al_2O_3 and SiO_2 as an internal standard for the melt inclusions result in extreme values for other oxides such as -50 wt % to over 100 wt % for MgO. Whereas, using a constant distribution coefficient for Yttrium of 0.0038 (Zanetti *et al.*, 2004) resulted in mass factors that were too high (Fig, 5.30), being consistently above one, where a mass factor of one would indicate that only the inclusion had been ablated, with no host olivine, which is never the case. Using variable values for SiO_2, which result in no negative values for elements in the inclusions produced mass factors more accurate that the other methods, and major oxide values in the melt inclusions that are far closer to what would be expected for basaltic magmas (Fig. 5.33). Therefore, this method was used to calculate the mass factors for melt inclusions in this study.

The reasons for the difficulty with calculating the mass factors seem to be two fold, firstly fractionation trends develop that are different in the external standards and the unknowns (host olivine, host olivine + melt inclusion), resulting in ablated material being resampled as ablation continues (Section 5.9). This makes it very difficult to acquire accurate mass factors, and thus, quantitative values for elements in the inclusions. Secondly, removal of ablated aerosols for the ablation cell is too inefficient for determining accurately the signal for the host material (olivine) from that of the mixed signal (olivine + inclusion). Therefore, only elemental ratios are used in the interpretation of geochemical data acquired from melt inclusions.

7.3 Geochemical data interpretation

Chapter 6 examines the whole rock and melt inclusion geochemistry, in order to evaluate the processes that have influenced the composition of the MPG lavas. The effects of post-magmatic hydrothermal alteration on the primary mineral phases are obvious features of the lavas throughout the succession (Kerr, 1993b), including the MPG lavas sampled during this study. The lavas analysed during this study have only been affected by secondary alteration up to zeolite facies, leading to the alteration of olivine along margins and cracks to serpentine, chlorite, oxides and iddingsite (Section 3.2.1). Modelling of whole rock and melt inclusions geochemistry indicate that they

represent the compositions of the original magmas, supporting the work of Morrison (1978), who showed that most elements were relatively immobile at lower zeolite facies grade.

7.3.1 Crustal contamination of the MPG lavas

In Section 6.3, elemental and isotopic evidence has been presented which strongly favours contamination of the MPG magmas with acidic partial melts of Lewisian lower crust. Previous works on the MPG lavas have relied on whole rock data, which can indicate contamination trend, such as the more basic lavas being the most contaminated (Kerr, 1993b). Thus leading to the conclusion that the lavas have been contaminated by the ATA process (Assimilation during Turbulent Assent – Section 1.4.3). However, in Section 6.3.6 melt inclusion geochemical data allows the evolution of individual magmas to be monitored, indicating that the MPG magmas were not only contaminated by the ATA process, but also by the AFC process (Assimilation during Fractional Crystallisation – Section 1.4.3). Using uncontaminated melt inclusion data to model the amount of contamination, indicates that the maximum extent of contamination suffered by the MPG magmas was ~8% (Fig. 6.23). This is 3% higher than that indicated by whole rock modelling, due to all the MPG basalts being contaminated to varying degrees (Fig. 6.17). Kerr (1993a, 1993b) also proposed that some of the MPG magmas were contaminated by an enriched small-fraction-melt lithospheric component. However, data presented in Section 6.3.9, indicate that none of the MPG lavas (this study) have been contaminated by an enriched small-fraction-melt.

7.3.2 Fractional crystallisation

As was shown in Section 6.4 olivine hosted melt inclusions are contaminated by Lewisian granulite. Thus, olivine must have crystallising out of the melt whilst the magmas were travelling through the lower crust. Modelling of major and trace elements (Fig, 6.42) shows that Ni in the MPG lavas falls as F/(F+M) increases, therefore olivine is being lost to the magmas. For the same F/(F+M) range in valves, CaO, Sc and V concentrations remain relatively constant, indicating that a mineral phase is removing them from the magma. In has been proposed by Kerr (1993b) that the mineral phase removing these elements is clinopyroxene. Therefore, both olivine and clinopyroxene

are crystallising and being removed for the melts, at the same time that the magmas are being contaminated by Lewisian granulite. As the ATA process contaminated the majority of the MPG magmas, it makes sense that whilst the magmas were assimilating Lewisian crust by turbulent assent, olivine and clinopyroxene must have been crystallising onto the conduit walls to explain the lack of clinopyroxene phenocrysts and drop in Ni seen it the MPG lavas. Thus, Assimilation and Fractionation were occurring during Turbulent Assent (AFTA).

7.3.3 Source composition and melt regime

Major element systematics indicates that the mantle melting which produced the MPG lavas was over a range of depths within a melting column (Figs, 6.32 + 6.33). With trace element modelling indicating that melting occurred predominantly in the spinel-garnet transition zone, and had a depleted composition relative to Bulk Earth, supporting the finding of Kerr (1993b) who came to the same conclusions. Melt inclusion trace element data indicates that within the melting column, fusion of between 2-20% source rock occurred (Figs. 6.46 + 6.47a-l) and that these partial melts mixed to produce the parental magmas of the MPG lavas. The mean extent of these parental magmas was between 4-13% (Fig. 6.41).

7.4 Possible further work

During this study, only 49 MPG lavas were sampled. Of these lavas, only 13 contained olivine phenocrysts that hosted melt inclusions. Therefore, there exists significant scope for further analysis of olivine-hosted melt inclusions, including collecting several samples from each lava flow, which would increase the geochemical resolution of processes that have affected the MPG lavas.

To increase the accuracy of the analysis of olivine-hosted melt inclusions by LA-ICP-MS, a number of improvements could be made. Several olivine-hosted melt inclusions from each suite of lavas could be homogenised and analysed by methods that are more conventional. This would provide geochemical information on the compositions of the inclusions, making it easier to acquire independent internal

standards for the analysis of other melt inclusions from the same suite of lavas by LA-ICP-MS. Improvements could also be made to the laser ablation chamber, which at present, is to large for the efficient removal of ablated aerosols. A more direct method of supplying carrier gas to the ablation site may also help to cut down on the condensation of ablated material back onto the sample surface, and therefore reduce the fractionation of elements.

References cited in the text

Anderson, A.T. 1974. Evidence for a picritic, volatile-rich magma beneath Mt. Shasta, California. *Journal of Petrology*, **15,** 239-256.

Anderson, A.T. 1991. Hourglass inclusions: Theory and application to the Bishop rhyolitic tuff. *American Mineralogist*, **76,** 530-547.

Anderson, D.L. 1985. Hotspot magmas can form by fractionation and contamination of mid-ocean ridge basalts. *Nature*, **318,** 145-149.

Anderson, D.L. 1994. Lithosphere and flood basalts. *Nature*, **367,** 226.

Anderson, D.L., Tanimoto, T., & Zhang, Y. 1992. Plate tectonics and hotspots: the third dimension. *Science*, **256,** 1645-1651.

Anderson, F.W. & Dunham, K.C. 1966. The geology of northern Skye. *Memoirs Geological Survey. G.B., Scotland.*

Arndt, N.T., Kerr, A.C. & Tarney, J. 1997. Dynamic melting in plume heads: The formation of Gorgona komatiites and basalts. *Earth and Planetary Science Letters*, **146,** 289-301.

Audetat, A., Günther, D. & Heinrich, C.A. 1998. Formation of a magmatic-hydrothermal ore deposit: Insights with LA-ICP-MS analysis of fluid inclusions. *Science*, **279,** 2091-2094.

Audetat, A., Günther, D. & Heinrich, C.A. 2000. Magmatic-hydrothermal evolution in a fractionating granite: a microchemical study of the Sn-W-F-mineralized Mole Granite (Australia). *Geochimica et Cosmochimica Acta,* **64,** 3373-3393.

Bacon, C.R., Newman, S. & Stolper, E. 1992. Water, CO_2, Cl, and F in Melt Inclusions in Phenocrysts from 3 Holocene Explosive Eruptions, Crater Lake, Oregon. *American Mineralogist,* **77,** 1021-1030.

Baily, E.B., Clough, C.T., Wright, W.B., Richey, J.E. & Wilson, G.V. 1924. Tertiary and post-Tertiary geology of Mull, Loch Aline and Oban. *Memoirs Geological Survey. G.B., Scotland.*

Bamford, D., Nunn, K., Prodehl, C., & Jacob, B. 1977. LISP-III Upper crustal structure of northern Britain. *Journal of the Geological Society, London,* **133,** 481-488.

Baxter, A.N. 1987. Petrochemistry of late Palaeozoic alkali lamprophyre dykes from N Scotland. *Transactions of the Royal Society of Edinburgh: Earth Sciences,* **77,** 267-277.

Beddoe-Stephens, B., Aspden, J.A., & Shepherd, T.J. 1983. Glass inclusions and melt compositions of the Toba tuffs, northern Sumatra. *Contributions to Mineralogy and Petrology,* **83,** 278-287.

Beddoe-Stephens, B. & Mason, I. 1991. The volcanogenetic significance of garnet bearing minor intrusion within the Borrowdale Volcanic Group, Eskdale area, Cumbria. *Geological Magazine,* **128,** 505-516.

Berger, G., Schott, J. & Guy, C. 1988. Behavior of Li, Rb and Cs during basalt glass and olivine dissolution and chlorite, smectite and zeolite precipitation from seawater-experimental investigations and modelization between 50 and 300 degrees C. *Chemical Geology,* **71,** 297-312.

Best, M.G. & Christiansen, E.H. 1997. Origin of broken phenocrysts in ash-flow tuffs. *Geological Society of American Bulletin,* **109,** 63-73.

Bienvenu, P., Bougault, J.L., Treuil, M. & Dmitriev, L. 1990. MORB alteration: rare-earth element/non-rare-earth hygromagmaphile element fractionation. *Chemical Geology,* **82,** 1-14.

Bijwaard, H. & Spakman, W. 1998. Tomographic evidence for a narrow whole mantle plume below Iceland. *Earth and Planetary Science Letters,* **166,** 121-126.

Blichert-Toft, J., Lesher, C.E. & Rosing, M.T. 1992. Selectively contaminated magmas of the Tertiary East Greenland macrodyke complex. *Contributions to Mineralogy and Petrology,* **110,** 154-172.

Bor, L. 1951. The Glen More ring-dyke Mull [Unpublished PhD thesis], Cambridge University.

Borisova, A.Y., Nikogosian, I.K., Scoates, J.S., Weis, D., Damasceno, D., Shimizu, N. & Touret, J.L.R. 2002. Melt, fluid and crystal inclusions in olivine phenocrysts from Kerguelen plume-derived picritic basalts: evidence for interaction with the Kerguelen Plateau lithosphere. *Chemical Geology,* **183,** 195-220.

Bowen, N.L. 1928. *The evolution of the igneous rocks,* Princeton University Press.

Campbell, I.H. 1985. The difference between oceanic and continental tholeiites: a fluid dynamic explanation. *Contributions to Mineralogy and Petrology,* **91,** 37-43.

Campbell, I.H., Czamanske, G.K., Fedorenko, V.A., Hill, R.I. & Stepanov, V. 1992. Synchronism of the Siberian Traps and the Permian-Triassic boundary. *Science,* **258,** 1760-1763.

Campbell, I.H. & Griffiths, R.W. 1990. Implications of mantle plume structure for the evolution of flood basalts. *Earth and Planetary Science Letters,* **99,** 79-93.

Cann, J.R. 1970. Rb, Sr, Y, Zr and Nb in some ocean floor basaltic rocks. *Earth and Planetary Science Letters,* **10,** 7-11.

Carter, S.R., Evensen, N.M., Hamilton, P.J. & O'Nions, R.K. 1978. Neodymium and strontium isotope evidence for crustal contamination of continental volcanics. *Science,* **202,** 743-747.

Chambers, L.M. & Pringle, M.S. 2001. Age and duration of activity at the Isle of Mull Tertiary igneous centre, Scotland and confirmation of the existence of subchrons during Anomaly 26r. *Earth and Planetary Science Letters,* **193,** 333-345.

Chan, W.T., Leung, A.P.K., Mao, X.L. & Russo, R.E. 1998. Effects of gas environment on picosecond laser ablation. *Applied Surface Sciences,* **127-129,** 269-273.

Cloccchiatti, R. 1975. Glassy inclusions in crystals of quartz; optical thermo-optical and chemical studies, and geological applications. *Soc. Geol. de France., Mem., New Series,* **54,** 96.

Coffin, M.F. 1994. Large igneous provinces: crustal structure, dimensions, and external consequences, *Rev. Geophysics*, **32,** 1-36.

Coffin, M.F. & Eldholm, O. 1994. Exploring Large Subsea Igneous Provinces. *Oceanus*, **36,** 75-78.

Courtney, R. & White, R. 1986. Anomalous heat flow and geoid across the Cape verde Rise: evidence for dynamic support from a thermal plume in the mantle. *Journal of Geophysical Research,* **87,** 815-867.

Cox, K.G. 1979. A model for flood basalt volcanism. *Journal of Petrology,* **21,** 629-650.

Cox, K.G. 1988. The Karoo Province, *in* Macdougall, J.D., ed., *Continental Flood Basalts.* Dordrect, Netherlands, Kluwer Academic Publishers. 239-271.

Cox, K.G. & Hawkesworth, C.J. 1985. Geochemical stratigraphy of the Deccan Traps at Mahabaleshwar, western Ghats, India, with implications for open system magmatic processes. *Journal of Petrology,* **26,** 355-377.

Craig, G.Y. 1991. *Geology of Scotland.* London, The Geological Society. 612.

Danyushevsky, L.V., Della-Pasqua, F.N. & Sokolov, S. 2000. Re-equilibration of melt inclusions trapped by magnesium olivine phenocrysts from subduction related magmas: petrological implications. *Contributions to Mineralogy and Petrology,* **138,** 68-83.

Danyushevsky, L.V., McNeill, A.W. & Sobolev, A.V. 2002. Experimental and petrological studies of melt inclusions in phenocrysts from mantle-derived magmas; an overview of techniques, advantages and complications. *Chemical Geology,* **183,** 5-24.

DePaolo, D.J. 1981. Trace element and isotope effects of combined wallrock assimilation and fractional crystallization. *Earth and Planetary Science letters,* **53,** 189-202.

Devey, C.W. & Cox, K.G. 1987. Relationships between Crustal Contamination and Crystallization in Continental Flood-Basalt magmas with Special References to the Deccan Traps of the Western Ghats, India. *Earth and Planetary science Letters,* **84,** 59-68.

Dickin, A.P. 1981. Isotope geochemistry of Tertiary igneous rocks from the Isle of Skye, N.W. Scotland. *Journal of Petrology,* **22,** 155-189.

Dickin, A.P., Brown, J.L., Thompson, R.N., Halliday, A.N. & Morrison, M.A. 1984. Crustal contamination and the granite problem in the British Tertiary Volcanic Province. *Philosophical Transactions of the Royal Society London,* **A130,** 755-780.

Dickin, A.P., Jones, N.W., Thirlwall, M.F. & Thompson, R.N. 1987. A Ce/Nd isotope study of crustal contamination processes affecting Palaeocene magmas in Skye, Northwest Scotland. *Contributions to Mineralogy and Petrology,* **96,** 455-464.

Dickin, A.P., Moorbath, S. & Welke, H.J. 1981. Isotope trace element and major element geochemistry of Teriary igneous rocks, Isle of Arran, Scotland. *Transactions of the Royal Society of Edinburgh: Earth Sciences,* **72,** 159-170.

Dietrich, A., Lehmann, B. & Wallianos, A. 2000. Bulk rock and melt inclusion geochemistry of Bolivian tin porphyry systems. *Economic Geology,* **95,** 313-326.

Dostal, J. & Strong, D.F. 1983. Trace-element mobility during low-grade metamorphism and sisicification of basaltic rocks from Saint John, New Brunswick. *Canadian journal of Earth Sciences,* **20,** 431-435.

Dunbar, N.W. & Hervig, R.L. 1992. Petrogenesis and volatile stratigraphy of the Bishop Tuff: evidence from melt inclusions analysis. *Journal of Geophysical Research,* **97,** 15129-15150.

Eggins, S.M., Kinsley, L.P.J. & Shelley, J.M.G. 1998. Deposition and element fractionation processes during atmospheric pressure laser sampling for analysis by ICP-MS. *Applied Surface Sciences,* **127-129,** 278-286.

Eldholm, O. & Grue, K. 1994. North Atlantic volcanic margins: dimentions and production rates. *Journal of Geophysical Research,* **99,** 2955-2968.

Ellam, R.M. 1992. Lithospheric thickness as a control on basalt geochemistry. *Geology,* **20,** 153-156.

Emeleus, C.H. 1991. Tertiary igneous activity, *in* Craig, G.Y., ed. *Geology of Scotland.* Geological Society, London. 455-502.

Engdahl, E.R., Hilst, R.D.V.D. & Buland, R.P. 1998. Global Teleseismic earthquake relocation with improved travel times and procedures for depth determination. *Bulletin Seismological Society America,* **88,** 722-743.

Ewart, A. 1989. East Australian petrology and geochemistry. In, *Intraplate volcanism in Earstern Australia and New Zealand.* Ed. R.W. Johnson, Cambridge University Press, 189-256.

Faure, G. 2001. In, *Origin of Igneous Rocks, The Isotopic Evidence.* Springer, New York.

Fenner, C.N. 1937. A view of magmatic differentiation.

Fitton, j.G., Saunders, A.D., Norry, M.J., Hardarson, B.S. & Taylor, R.N. 1997. Thermal and chemical structure of the Iceland plume. *Earth and Planetary Science letters,* **153,** 197-208.

Floyd, P.A. & Tarney, J. 1978. First-order alteration chemistry of leg 49 basement rocks: Washington. US Government Printing Office.

Frezzotti, M.L. 2001. Silicate-melt inclusions in magmatic rocks: applications to petrology. *Lithos,* **55,** 273.299.

Gaetani, G.A. & Watson, E.B. 2000. Open system behaviour of olivine-hosted melt inclusions. *Earth and Planetary Science letters,* **183,** 27-41.

Geikie, A. 1881. On the Tertiary Volcanic Rocks of the British Islands. First Paper: Quarterly. *Journal Geological Society London,* **27,** 21-184.

Geohegan, D.B. & Puretzky, A.A. 1996. Laser ablation plume thermalization dynamics in background gases: combined imaging, optical absorption and emission spectroscopy, and ion probe measurements. *Applied Surface Sciences,* **96-98,** 131-138.

Gibson, I.L., Kirkpatrick, J., Emmerman, R., Schmincke, H., Pritchard, G., Oakley, P.J., Thorpe, R.S. & Marriner, G.F. 1982. The trace element compostion of lavas through the lavas and dykes from a 3 km vertical section through the lava pile of Eastern Greenland. *Journal of Geophysical Research,* **87,** 6532-6546.

Gillet, P., Ingrin, J. & Chopin, C. 1984. Coesite in subducted continental crust: P-T history deduced from an elastic model. *Earth and Planetary Science Letters,* **70,** 426-436

Govindaraju, K. 1994. 1994 compilation of working values and descriptions for 383 geostandards. *Geostandards Newsletter,* **118,** 1-158.

Gribble, C.D. & Hall, A.J. 1992. *Optical Mineralogy principles and Practice.* London, UCL Press Limited.

Griffiths, R.W. 1986. The differing effects of compositional and thermal buoyancies on the evolution of mantle diapers. *Physics of the Earth and Planetary Interiors,* **43,** 261-273.

Günther, D, Audetat, A., Frischknecht, R. & Heinrich, C.A. 1998. Quantitative analysis of major, minor and trace elements in fluid inclusions using laser ablation inductively coupled plasma mass spectrometry. *Journal of Analytical Atomic Spectrometry,* **13,** 263-270.

Halter, W.E., Pettke, T., Heinrich, C.A. & Rutishauser, B.R. 2002. Major to trace element analysis of melt inclusions by laser-ablation ICP-MS: methods of Quantification. *Chemical Geology,* **183,** 63-86.

Harker, A. 1904. The Tertiary igneous rocks of Skye. *Memoirs Geological Survey. G.B., Scotland.*

Hart, S.R., Erlank, A.J. & Kable, E.J.D. 1974. Seafloor basalt alteration: Some chemical and strontium isotope effects. *Contributions to Mineralogy and Petrology,* **44,** 707-725.

Hart, S.R., Hauri, E.H., Oschmann, L.A. & Whitehead, J.A. 1992. Mantle plumes and entrainment: isotope evidence. *Science,* **256,** 45-47.

Hauri, E. 2002. SIMS analysis of volatiles in silicate glasses, 2: isotope and abundances in Hawaiian melt inclusions. *Chemical Geology,* **183,** 115-141.

Holbrook, W.S., Larsen, H.C., Korenaga, J., Dahl-Jensen, T., Reid, I.D., Kelemen, P.B., Hopper, J.R., Kent, G.M., Lizarralde, D., Berstein, S. & Detrick, R.S. 2001. Mantle thermal structure and active upwelling during continental breakup in the North Atlantic. *Earth and Planetary Science Letters,* **190,** 251-262.

Holmes, A. 1931. The problem of the association of acid and basic rocks in central complexes. *Geological magazine,* **68,** 241-255.

Holmes, A. & Harwood, H.F. 1918. The basaltic rocks of the Arctic region. *Mineralogical Magazine,* **18,** 180-223.

Horn, I. & Günther, D. 2003. The influence of ablation carrier gasses Ar,He and Ne on the particle size distribution and transport efficiencies of laser ablation-induced aerosols: implications for LA-ICP-MS. *Applied Surface Sciences,* **207,** 144-157.

Humphris, S.E. 1984. The mobility of the rare earth elements in the crust, in *Rare Earth Element Geochemistry,* edited by P. Henderson, 315-341, Elsevier, Amsterdam.

Huppert, H.E. & Sparks, R.S.J. 1980. Restrictions on the compositions of mid-ocean ridge basalts: a fluid dynamical investigation. *Nature,* **286,** 46-48.

Huppert, H.E. & Sparks, R.S.J. 1985. Cooling and contamination of mafic and ultramafic magmas during ascent through continental crust. *Earth and Planetary Science Letters,* **74,** 371-386.

Judd, J.W. 1874. The secondary rocks of Scotland. Second paper. On the ancient volcanoes of the Highlands and the relations of their products to the Mesozoic strata. *Quarterly Journal Geological Society London,* **30,** 220-302.

Jurewicz, A.J.G. & Watson, E.B. 1988. Cations in olivine, Part 1: Calcium partitioning and calcium-magnesium distributions between olivines and coexisting melts, with petrological applications. *Contributions to Mineralogy and Petrology,* **99,** 176-185.

Kamenesky, V., Wolfe, R.C., Eggins, S.M., Mernagh, T.P. & Bastrakov, E. 1999. Volatile exsolution at the Dinkidi Cu-Au porphyry deposit, Philippines: a melt inclusion record of the initial ore-forming process. *Geology,* **27,** 691-694.

Kamenetsky, V.S., Davidson, P., Mernagh, T.P., Crawford, A.J., Gemmell, J.B., Portnyagin, M.V. & Shinjo, R. 2002. Fluid bubbles in melt inclusions and pillow-rim glasses: high-temperature precursors to hydrothermal fluids?. *Chemical Geology,* **183,** 349-364.

Kempton, P.D., Fitton, J.G., Saunders, A.D., Nowell, G.M., Taylor, R.N., Hardarson, B.S. & Pearson, G. 2000. The Iceland plume in space and time: a Sr-Nd-Pb-Hf study of the North Atlantic rifted margin. *Earth and Planetary Science letters,* **177,** 255-271.

Kennett, B.L.N., Engdahl, E.R. & Buland, R. 1995. Constraints on seismic velocities in the Earth from traveltimes. *Geophysical Journal International,* **122,** 108-124.

Kerr, A.C. 1993a. Elemental evidence for an enriched small-fraction melt input into Tertiary Mull basalts, Western Scotland. *Journal of the Geological Society, London,* **150,** 763-769.

Kerr, A.C. 1993b. The Geochemistry and Petrogenesis of the Mull and Morvern Tertiary Lava Succession, Argyll, Scotland [Unpublished PhD thesis]. Department of Geological Sciences, University of Durham.

Kerr, A.C. 1995. The geochemistry of the Mull-Morvern Tertiary lava succession, NW Scotland: An Assessment of mantle sources during plume related volcanism. *Chemical Geology,* **122,** 43-58.

Kerr, A.C. 1997. The geochemistry and significance of plugs intruding the Tertiary Mull-Morvern lava succession. *Scottish Journal of Geology,* **33,** 157-167.

Kerr, A.C. 1998. Mineral chemistry of the Mull-Morvern Tertiary lava succession, *Mineralogical Magazine,* **62,** 295-312.

Kerr, A.C., Kempton, P.D. & Thompson, R.N. 1995. Crustal assimilation during turbulent magma ascent (ATA); new isotopic evidence from the Mull Tertiary lava succession, N.W. Scotland. *Contributions to Mineralogy and Petrology,* **119,** 142-154

Kerr, A.C., Kent, R.W., Thompson, B.A., Seedhouse, J.K. & Donaldson, C.H. 1999. Geochemical evolution of the Tertiary Mull volcano, Western Scotland. *Journal of Petrology,* **40,** 873-908.

Kirstein, L.A., Dunworth, E.A., Nikogosian, I.K., Touret, J.L.R. & Lustenhouwer, W.J. 2002. Initiation of melting beneath the Oslo rift: a melt inclusion perspective. *Chemical Geology,* **183,** 221-236.

Klein, E.M. & Langmuir, C.H. 1987. Global correlations of ocean ridge basalt chemistry with axial depth and crustal thickness. *Journal of Geophysical Research,* **92,** 8089-8115.

Klein, E.M. & Langmuir, C.H. 1989. Local versus global variations in ocean ridge basalt composition: a reply. *Journal of Geophysical Research,* **94,** 4241-4252.

Kostopoulos, D.K. & James, S.D. 1992. Paramertarization of the melting regime of the shallow upper mantle and the effects of variable lithospheric stretching on mantle modal stratification and trace-element concentrations in magmas. *Journal of Petrology,* **33,** 665-691.

Lahaye, Y., Lambert, D. & Walters, S. 1997. Ultraviolet laser sampling and high resolution inductively coupled plasma mass spectrometry of NIST and BCR-2G glass reference materials. *Geostandards Newsletter – Journal of Geostandards and Geoanalysis.* **21,** 205-214.

Larsen, L.M., Watt, W.S. & Watt, M. 1989. Geology and petrology of the Lower Tertiary plateau basalts of the Scoresby Sund region, East Greenland. *Bulletin of the Geological Survey, Greenland,* **157,** 1-164.

Lodders, K. 2003. Solar System Abundances and Condensation Temperatures of the Elements. *The Astrophysical Journal,* **591,** 1220-1247.

Lofgren, G.E. & Donaldson, C.H. 1975. Curved branching crystals and differention in comb-layered rocks. *Contributions to Mineralogy and Petrology,* **49,** 309-319.

Loper, D.E. & Stacey, F.D. 1983. The dynamical and thermal structure of deep mantle plumes. *Physics of the Earth and Planetary Interiors,* **33,** 304-317.

Lowenstern, J.B. 1994. Chlorine, fluid immiscibility and degassing in peralkaline magmas from Pantelleria, Italy. *American Mineralogy,* **79,** 353-369.

Lowenstern, J.B. 1995. Applications of silicate-melt inclusions to the study of magmatic volatiles, in Magmas, Fluids and Ore Deposits. *Canada Short Courses,* **23,** 71-99.

Lowenstern, J.B., Clynne, M.A & Bullen, T.D. 1997. Comagmatic A-type granophere and rhyolite from the Alid volcanic centre, Eritrea, Northeast Africa. *Journal of Petrology,* **38,** 1707-1721.

Lowenstern, J.B., Mahood, G.A., Rivers, M.L. & Sutton, S.R. 1991. Evidence for extreme partitioning of copper into a magmatic vapour phase. *Science,* **252,** 105-110.

Ludden, J., Gelinas, L. & Trudel, P. 1982. Archean metavolcanics from the Rouyn-Noranda District, Abitibi Greenstone-belt, Quebec .2. Mobility of Trace Element and Petrogenetic Constraints. *Canadian Journal of Earth Sciences,* **19,** 2276-2287.

Ludden, J.N. & Thompson, G. 1979. An evaluation of the behaviour of the rare earth elements during the weathering of sea-floor basalts. *Earth and Planetary Science Letters,* **43,** 85-92.

Mahoney, J.J. 1988 Deccan Traps, *in* Macdougall, J.D. *Continental Flood Basalts.* Dordrecht, Netherlands, Kluwer Academic Publishers, 151-194.

Mainley, C.R. 1996. Morphology and maturation of melt inclusions in quartz phenocrysts from the Badlands rhyolite flow, southwestern Idaho. *American Mineralogy,* **81,** 158-168.

Mantovani, M.S.M., Cordani, U.G. & Roisenberg, A. 1985. Geoquimica isotopica em vulcanicas da bacia do Parana, e, implicacoes geneticas associadas. *Revista Brasiliera Geosciencas,* **15,** 61-65.

Mao, X.L., Ciocan, A.C., Borisov, O.V. & Russo, R.E. 1998. Laser ablation processes investigated using inductively coupled plasma-atomic emission spectroscopy (ICP-AES). *Applied Surface Sciences,* **127-129,** 262-268.

Marsh, J.S. 1991. REE fractionation and Ce anomalies in weathered Karoo dolerite. *Chemical Geology,* **90,** 189-194.

Marshall, L.A. 1984. Origin of mixed-magma and net-veined ring intrusions [Unpublished PhD thesis] Cambridge University.

Massare, D., Metrich, N. & Clocchiatti, R. 2002. High-temperature experiments on silicate melt inclusions in olivine at 1 atm: inference on temperatures of homogenization and H_2O concentrations. *Chemical Geology,* **183,** 87-98.

McDade, P., Wood, B.J. & Blundy, J.D. subjudice. Trace element partitioning at 3.0 GPa on the anhydrous garnet peridotites solidus. *Journal of Petrology.*

McKenzie, D.P. & Bickle, M.J. 1988a. Partial melt distributions from inversion of rare earth element concentrations. *Journal of petrology,* **32,** 1021-1091.

McKenzie, D.P. & Bickle, M.J. 1988b. The volume and composition of melt generated by extension of the lithosphere. *Journal of Petrology,* **29,** 625-679.

Mertz, D.F. & Haase, K.M. 1997. The radiogenic isotope composition of the high latitude North Atlantic mantle. *Geology,* **25,** 411-414.

Moorbath, S. & Bell, J.D. 1965. Strontium isotope abundance studies and Rb-Sr age determinations on Tertiary igneous rocks from the Isle of Skye, NW Scotland. *Journal of Petrology,* **6,** 37-66.

Moorbath, S. & Thompson, R.N. 1980 Strontium isotope geochemistry and petrogenesis of the early Tertiary lava pile of the Isle of Skye, Scotland, and other basic rocks of the British Tertiary Province: an example of magma-crust interaction. *Journal of Petrology,* **21,** 295-321.

Moorbath, S. & Welke, H. 1969. Lead isotope studies on the igneous rocks from the Isle of Skye, NW Scotland. *Earth and Planetary Science Letters,* **5,** 217-230.

Morgan, W.J. 1972. Deep mantle convective plumes and plate motions. *AAPG Bull,* **56,** 203-213.

Morgan, W.J. 1981. Hotspot tracks and the opening of the Atlantic and Indian Oceans, *in* Emiliani, C., ed., *The Oceanic lithosphere*, New York, Wiley-Interscience, 443-487.

Morrison, M.A. 1978. The use of immobile trace elements to distinguish Palaeotectonic affinities of metabasalts: applications to the Palaeocene basalts of Mull and Skye, NW Scotland. *Earth and Planetary Science Letters,* **39,** 407-416.

Morrison, M.A. 1979. Igneous and metamorphic geochemistry of Mull lavas [Unpublished PhD thesis] University of London.

Nielsen, R.L. 1988. A model for the simulation of combined major and trace element liquid lines of descent. *Geochimica et Cosmochimica Acta,* **52,** 27-38.

Norman, M.D., Garcia, M.O., Kamenetsky, V.S. & Nielsen, R.L. 2002. Olivine-hosted melt inclusions in Hawaiian picrites: equilibration melting, and plume source characteristics. *Chemical Geology,* **183,** 143-168.

Officer, C.B., Hallam, A., Drake, C.L. & Devine, J.D. 1987. Late Cretaceous and paroxysmal Cretaceous/Tertiary extinctions. *Nature,* **326,** 143-149.

Pankhurst, R.J., Walsh, J.N., Beckinsale, R.D. & Skelhorn, R.R. 1978. Isotopic and other geochemical evidence for the origin of the Loch Uisg granophyre, Isle of Mull, Scotland. *Earth and Planetary Science Letters,* **38,** 355-363.

Patchett, P.J. 1980. Thermal effects of basalt of continental crust and crustal contamination of magmas. *Nature,* **283,** 559-561.

Pearce, N.J.G., Perkins, W.T., Westgate, J.A., Gorton, M.P., Jackson, S.E., Neal, C.R. & Chernery, S.P. 1997. A compilation of new and published major and trace element data for NIST SRM 610 and NIST SRM 612 glass reference materials. *Geostandard newsletter – Journal of Geostandards and Geoanalysis,* **21,** 115-144.

Pettke, T., Halter, W.E., Webster, J.D., Aigner-Torres, M. & Heinrich, C.A. 2004. Accurate quantification of melt inclusions chemistry by LA-ICP-MS: a comparison with EMP and SIMS and advantages and possible limitations of these methods. *Lithos,* Article in press.

Preston, R.J. 1996. The Loch Scridain xenolithic sill complex, Isle of Mull, Scotland: Fractional crystallisation, assimilation, magma mixing and crustal anataxis in subvolcanic conduits. *Journal of Petrology,* **39,** 519-550.

Quin, Z., Lu, F. & Anderson, A.T. 1992. Diffusive re-equilibration of melt and fluid inclusions. *American Mineralogy,* **77,** 565-576.

Rampino, M.R. & Stothers, R.B. 1988. |Flood basalt volcanism during the past 250 million years. *Science,* **241,** 663-668.

Rea, D.K., Zachos, J.C., Owen, R.M. & Gingerich, P.D. 1990. Global change at the Paleocene-Eocene boundary: Climate and evolutionary consequences of tectonic events. *Palaeogeographical. Palaeoclimatology. Palaeoecology,* **79,** 117-128.

Rich, J.E., Johnson, G.I., Jones, J.E. & Campsie, J. 1986. A significant correlation between fluctuations in seafloor spreading rates and evolutionary pulsations. *Paleoceanography,* **1,** 85-95.

Richards, M.A., Duncan, R.A. & Courtillot, V.E. 1989. Flood basalts and hot spot tracks: plume heads and tails. *Science,* **246,** 103-107.

Richey, J.E. & Thomas, H.H. 1930. *The Geology of Ardnamurchan, Northwest Mull and Coll.* H.M.S.O. Edinburgh.

Roedder, E. 1979. Origin and significance of magmatic inclusions. *Bulletin of the Mineralogy Society,* **102,** 487-510.

Roedder, E. 1984. Fluid inclusions. *Rev Mineral,* **12,** 620.

Rollinson, H. 1993. *Using geochemical data: evaluation, presentation, interpretation,* Harlow, Longman.

Salters, V.J.M. & Stracke, A. 2004. Composition of depleted mantle. *Geochemistry, Geophysics, Geosystems* G^3, **5,** 1-27.

Saunders, A.D., Fitton, J., Kerr, A.C., Norry, M.J. & Kent, R.W. 1997. The North Atlantic Igneous Province, *American Geophysical Union Monograph,* **100,** 45-93.

Saunders, A.D., Storey, M., Kent, R.W. & Norry, M.J. 1992. Consequences of plume-lithosphere interactions. *in* Story, B.C., Alabaster, T. & Pankhurst, R.J., eds., Magmatism and the causes of Continental Breakup. *Geological Society of London Special Publication,* **68,** 41-60.

Schiano, P. 2003. Primitive mantle magmas recorded as silicate melt inclusions in igneous minerals. *Earth-Science Reviews,* **1290,** 1-24.

Schiano, P. & Bourdon, B. 1999. On the preservation of mantle information in ultramafic nodules: glass inclusions within minerals versus interstitial glasses. *Earth and Planetary Science Letters,* **169,** 173-188.

Seedhouse, J.K. 1994. Testing for compositional convection in silicate melts; crystal growth experiments and a petrographic study of a differentiated ring dyke [Unpublished PhD thesis], University of St Andrews.

Seewald, J.S. & Seyfried, W.S. 1990. The effect of temperature on metal mobility in seafloor hydrothermal systems: constraints from basalts alteration experiments. *Earth and Planetary Science Letters,* **101,** 388-403.

Sheth, H.C. 1999. Flood basalts and large igneous provinces from deep mantle plumes: fact, fiction, and fallacy. *Tectonophysics,* **311,** 1-29.

Simkin, T. & Smith, J.V. 1970. Minor-element distribution in olivine. *Journal of Geology,* **78,** 304-325.

Singer, B.S. & Pringle, M.S. 1996. Age and duration of the matuyama-Brunhes geomagmatic polarity reversal from $^{40}Ar/^{39}Ar$ incremental heating analysis of lavas. *Earth and Planetary Science Letters,* **139,** 47-61.

Sission, T.W. & Layne, G.D. 1993. H_2O in basaltic and basaltic andesite glass inclusions from four subduction-related volcanoes. *Earth and Planetary Science Letters,* **117,** 619-635.

Skelhorn, R.R., McDonald, J.D.S. & Longland, P.J.N. 1969. The Tertiary igneous geology of the Isle of Mull. *Geologists Association Guides,* **20,** 1-36.

Skirius, C.M., Peterson, J.W. & Anderson, A.T. 1990. Homogenizing rhyolitic glass inclusions from the Bishop Tuff, America. *Journal of Mineralogy,* **75,** 1381-1398.

Snyder, D., Crambes, C., Tait, S. & Wiebe, R.A. 1997. Magma mingling in dykes and sills. *Journal of Geology,* **105,** 75-86.

Sobolev, A.V. 1983. Origin of Siberian Meimechites in relation to the general problem of ultramafic magmas, [Unpublished Thesis] Moscow University, Moscow.

Sobolev, A.V., Barsukov, V.L., Nevsorov, V.N. & Slutsky, A.B. 1980. The formation conditions of the high-magnesian olivines from the monominerallic fraction of Luna 24 regolith. *Proceedings Lunar planet Science Conference,* **11,** 105-116.

Sobolev, A.V. & Danyushevsky, L.V. 1994. Petrology and geochemistry of boninites from the north terminal of the Tonga Trench: constraints on the generation conditions of primary high Ca bonitite magmas. *Journal of Petrology,* **35,** 1183-1211.

Sobolev, A.V. & Shimizu, N. 1993. Ultradepleted primary melt inclusions in olivine from the Mid-Atlantic Ridge. *Nature,* **363,** 151-154.

Sobolev, V.S. & Kostyuk, V.P.E. 1975. Magmatic Crystallization Based on Melt Inclusions. *Nauka Novosibirsk,* 184.

Sommer, M.A. 1977. Volatiles H_2O, CO_2 and CO in silicate melt inclusions in quartz phenocrysts from the rhyolitic bandolier air-fall and ash flow tuff, New Mexico. *Journal of Petrology,* **85,** 423-432.

Sparks R.S.J. 1988. Petrology and geochemistry of the Loch Ba ring-dyke, Mull (N.W. Scotland): an example of the extreme differentiation of tholeiitic magmas. *Contributions to Mineralogy and Petrology,* **100,** 446-461.

Sparks, R.S.J. & Huppert, H.E. 1984. Density changes during the fractional crystallization of basaltic magmas: fluid dynamic implications. *Contributions to Mineralogy and Petrology,* **85,** 300-309.

Speight, J.M., Skelhorn, R.R., Sloan, T. & Knapp, R.J. 1982. The dyke swarms of Scotland. In: *Igneous Rocks of the British Isles.* Sutherland, D.S., ed. Wiley pp. 449-459.

Steinberger, B. 2000. Plumes in a convecting mantle: Models and observations for individual hotspots. *Journal of Geophysical Research Solid Earth,* **105,** 11127-11152.

Student, J.J. & Bodnar, R.J. 1996. Melt inclusion microthermometry: petrologic constraints from the H_2O-saturated haplogranite system. *Petrology,* **4,** 291-306.

Sun, S. & McDonough, W.F. 1989. Chemical and isotope systematics of oceanic basalts: implications for mantle composition and processes, *in* Saunders, A.D. & Norry, M.J., eds., Magmatism in the Ocean Basins. *Geological Society of London, Special Publications,* **42,** 313-345.

Sylvester, P. 2001. *Laser-Ablation-ICPMS in Earth Sciences – Principles and Applications.* Mineralogical Association of Canada.

Tait, S. 1992. Selective preservation of melt inclusions in igneous phenocrysts. *American Mineralogy*, **77**, 146-155.

Taylor, H.P. 1980. The effects of assimilation of country rocks by magmas on $^{18}O/^{16}O$ and $^{87}Sr/^{86}Sr$ systematics in igneous rocks. *Earth and Planetary Science Letters*, **47**, 243-254.

Thirlwall, M.F. 1995. Generation of the Pb isotope characteristics of the Iceland plume. *Journal of the Geological Society London*, **152**, 991-996.

Thomas, E. 1990. Late-Cretaceous early-Eocene mass extinctions in the deep sea, *in* Sharpton, V.L. & Ward, P.D., eds., Global catastrophes in Earth History. *Geological Society of America, Special Publications*, **274**, 481-495.

Thompson, R.N. 1972. The one – atmosphere melting patterns of some basaltic volcanic series. *American Journal of Science*, **272**, 901-932.

Thompson, R.N. 1974. Primary basalts and magma genesis. *Contributions to mineralogy and Petrology*, **45**, 317-341.

Thompson, R.N. 1982. Magmatism of the British Tertiary Volcanic Province. *Scottish Journal of Geology*, **18**, 49-107.

Thompson, R.N., Dickin, A.P., Gibson, I.L. & Morrison, M.A. 1982. Elemental fingerprints of isotope contamination of Hebridean Palaeocene mantle derived magmas by Archean sial. *Contributions to Mineralogy and Petrology*, **79**, 159-168.

Thompson, R.N., Esson, J. & Dunham, A.C. 1972. Major element chemical variation in the Eocene lavas of the Isle of Skye. Scotland. *Journal of Petrology*, **21**, 265-293.

Thompson, R.N. & Gibson, S.A. 1991. Subcontinental mantle plumes, hotspots and pre-existing thinspots. *Journal of the Geological Society London*, **148**, 973-977.

Thompson, R.N., Gibson, I.L., Marriner, G.F., Mattey, D.P. & Morrison, M.A. 1980. Trace-element evidence of multistage mantle fusion and polybaric fractional crystallisation in the Palaeocene lavas of Skye, NW Scotland. *Journal of Petrology,* **21,** 265-293.

Thompson, R.N. & Morrison, M.A. 1988. Asthenosphereic and lower-lithospheric mantle contributions to continental extensional magmatism: an example from the British Tertiary Province. *Chemical Geology,* **68,** 1-15.

Thompson, R.N., Morrison, M.A., Dickin, A.P., Gibson, I.L. & Harmon, R.S. 1986. Two contrasting styles of interaction between basic magmas continental crust in British Tertiary Igneous Province. *Journal of geophysical Research,* **91,** 5985-5997.

Thomson, B.A. 1986. The petrology and geochemistry of the Tertiary cone-sheet complex, Isle of Mull, Scotland [Unpublished PhD thesis] Kings Collage London.

Tuttle, O.F. 1952. Origin of the contrasting mineralogy of extrusive and plutonic salic rocks. *Journal of Geology,* **60,** 107-124.

Tyrrell, G.W. 1928. The Geology of Arran. *Memoirs of the Geological Survey: Scotland.*

Ulrich, T. 1999. Genesis of the Bajo de la Alumbrera porthyry Cu-Au deposit, Argentina: Geological, fluid geochemical, and isotopic implications [Unpublished PhD thesis] ETHZ Zurich.

Ulrich, T., Gunther, D. & Heinrich, C.A. 1999. Gold concentrations of magmatic brines and the metal budget of porphyry copper deposits. *Nature,* **399,** 676-679.

Vervoort, J.D., Patchett, J., Blichert-Toft, J & Albarede, F. 1999. Relationships between Lu-Hf and Sm-Nd isotopic systems in the global sedimentary systems. *Earth and Planetary Science Letters,* **168,** 79-99.

Walker,G.P.L. 1970. The distribution of amygdale minerals in Mull and Morvern (Western Scotland). In Murty, T. V. V. G. R. K. and Rao, S.S. (Eds.) Studies in Earth Sciences, West Commemoration Volume. 181-194.

Wallace, J.M. 1998. Water partial melting in mantle plumes; interference from the dissolved H_2O concentrations of Hawaiian basaltic magmas. *Geophysical Research Letters,* **25,** 3639-3642.

Wallace, J.M., Ellam, R.M., Meighan, I.G., Lyle, P. & Rogers, N.W. 1994. Sr isotope data for the Tertiary lavas of Northern Ireland: Evidence for open system petrogenesis. *Journal of the Geological Society London,* **151,** 869-877.

Walsh, J.N., Beckinsale, R.D., Skelhorn, R.R. & Thorpe, R.S. 1979. Geochemistry and petrogenesis of the Tertiary granitic rocks from the Isle of Mull, Northwest Scotland. *Contributions to Mineralogy and Petrology,* **71,** 99-116.

Watson, E.B. 1976. Two-liquid partition coefficients: experimental data and geochemical implications. *Contributions to Mineralogy and Petrology,* **56,** 119-134.

Watson, S. & McKenzie, D.P. 1991. Melt generation by plumes a study of Hawaiian volcanism. *Journal of Petrology,* **32,** 501-537.

Webster, J.D. & Duffield, W.A. 1991. Volatiles and lithophile elements in Taylor Creek Rhyolite – constraints fron glass inclusion analysis. *American Mineralogist,* **76,** 1628-1645.

Webster, J.D. & Duffield, W.A. 1994. Extreme halogen abundances in tin-rich magma of the Taylor Creek Rhyolite, New-Mexico. *Economic Geology and the Bulletin of the Society of Economic Geologists,* **89,** 840-850.

White, R.S. 1988. A hot-spot model for the early Tertiary volcanism in the N Atlantic, *in* Morton, A.C. & Parson, L.M., eds., *Early Tertiary Volcanism and the Opening of the NE Atlantic.* Oxford Geological Society London Special Publications, **39,** 3-13.

White, R.S. & McKenzie, D.P. 1989. Magmatism at rift zones: the generation of volcanic continental margins and flood basalts. *Journal of Geophysical research,* **94,** 7685-7729.

White, R.S., Westbrook, G.K., Fowler, S.R., Spence, G.D., Barton, P.J., Joppen, M., Morgan, J., Bowen, A.N., Prestcott, C. & Bott, M.H.P. 1987. hatton Bank (northwest UK) continental margin structure. *Geophys. J. R. astr. Soc.* **89,** 265-272.

Whitehead, J.A. & Luther, D.S. 1975. Dynamics of laboratory diaper and plume models. *Journal of Geophysical Research,* **80,** 705-717.

Wilson, S.A. 1997. Data compilation for USGS reference material BHVO-2, Hawaiian Basalts, U.S. *Geological Survey Open File Report,* **98.**

Wilson, S.A. 1997. The collection preparation, and testing of USGS reference material BCR-2, Columbia River, Basalt, U.S. *Geological Survey Open File Report,* **98.**

Wood, D.A., Gibson, I.L. & Thompson, R.N. 1976. Elemental mobility during the zeolite facies metamorphism of the tertiary Basalts of Eastern Iceland. *Contributions to Mineralogy and Petrology,* **55,** 241-254.

Wyllie, P.J. 1988. Solidus curves mantle plumes and magma generation beneath Hawaii. *Journal of Geophysical Research,* **B93,** 4171-4181.

Yang, K. & Scott, S.D. 1996. Possible contributions of a metal-rich magmatic fluid to a sea-floor hydrothermal system. *Nature,* **383,** 52-54.

Zanetti, A., Tiepolo, M., Oberti, R. & Vannucci, R. 2004. Trace-element partitioning in olivine: modelling of a complete data set from a synthetic hydrous basanite melt. *Lithos,* **75,** 39-54.

Zhang, Y. 1998. Mechanical and phase equilibria in inclusion-host systems. *Earth and Planetary Science Letters,* **157,** 209-222.

Appendix 1
Analytical methods and data accuracy

A1.1 Inductively Coupled Plasma Optical Emission Spectrometry (ICP-OES)

The major elements (Si, Al, Fe, Mg, Ca, Na, K, Ti, Mn, P) of the 49 Mull plateau group lava samples were determined by ICP-OES on the Jobin Yvon Ultima 2 instrument, located at Cardiff University. The samples were analysed in one session (July 2003), three replicates were conducted per isotope, with the RF power set at 1000W.

A1.1.2 Sample Preparation

The samples were analysed in the form of aqueous solutions. For each sample 0.1 ± 0.005 g of dried powder was mixed with 0.4 ± 0.005 g of 100 % lithium tetraborate flux, and several drops of lithium iodide wetting agent. The samples were then fused in platinum crucibles, and poured in a molten state into a mixture of 30 ml 10 % HNO_3 + 20 ml de-ionised water (18.2MΩ), and stirred until fully dissolved. Finally, the samples were spiked with 1 ml of 100 ppm Rh, and diluted up to 100 ml with de-ionised water (18.2 MΩ).

A1.1.3 Calibration and data quality

A calibration line for each element was generated using the Certified Reference Materials (CRMS) PCC-1, DTS-1, BIR-1, W-2, MRG-1, JA2, JA3, STM-1 and a Total Procedural Blank (TPB): with the calibration lines being driven through the origin. Calibration lines were generated by the OES data reduction software, and improved where necessary by removal of standards, which lay considerably off the calibration line, and then re-calibrated. The samples runs were started with a TPB, followed by the MPG lavas in blocks of six unknowns, with each block preceded by an intra-session drift monitor, in this case the CRM BIR-1.

None of the elemental concentrations drifted for the drift monitor BIR-1, with the precision being within 5 %. Thus, no correction of the MPG lava samples was necessary. Elements in all the MPG lava sample values are above the typical limits of detection of the ICP-OES instrument (calculated by the software). The CRM (BIR-1) was analysed as a calibration independent standard. The acquired values for Si, Ti, Al, Fe, Mn, Mg and Ca display excellent correlation (± 5 %) with certified values of Govindaraju, (1994), (table A1.1).

Oxide	Certified values	Run-1	Run-2	Run-3	Run-4	Run-5	Run-6	Run-7	Run-8	Run-9	Run-10
SiO_2	47.96	47.49	47.42	47.84	47.32	47.14	47.19	47.15	47.33	46.03	46.92
TiO_2	0.96	0.98	1.00	0.98	0.99	0.95	0.99	0.97	1.00	0.95	0.94
Al_2O_3	15.50	15.56	15.66	15.21	15.08	14.55	14.74	14.81	14.76	14.60	14.61
Fe_2O_3	11.30	11.32	11.62	11.50	11.32	11.33	11.95	11.72	11.63	11.55	11.53
MnO	0.18	0.17	0.17	0.18	0.17	0.17	0.18	0.18	0.18	0.17	0.17
MgO	9.70	10.01	10.05	10.01	9.81	9.80	10.01	10.12	10.33	9.85	9.85
CaO	13.30	13.28	13.48	13.33	13.42	12.92	13.71	13.50	13.85	13.03	13.16
Na_2O	1.82	1.61	1.62	1.60	1.58	1.58	1.60	1.62	1.58	1.55	1.54
K_2O	0.03	0.01	0.02	0.01	0.01	0.04	0.03	0.04	0.03	0.03	0.03
P_2O_5	0.02	0.05	0.05	0.05	0.05	0.06	0.06	0.06	0.06	0.05	0.06
LOI		0.68	0.68	0.68	0.68	0.68	0.68	0.68	0.68	0.68	0.68
Total		101.15	101.78	101.38	100.41	99.20	101.14	100.84	101.45	98.51	99.49

Fig. A1.1. Table of acquired values for BIR-1, which was used as a calibration independent standard. All oxides are within 5 % of the certified value of reference material

A1.2 Inductively Coupled Plasma Mass Spectrometry (ICP-MS)

A Inductively-Coupled Plasma Mass Spectrometer (ICP-MS) instrument at Cardiff University was used to acquire the whole rock minor and trace element geochemical data presented in this work.. Fifty samples were analysed on the X7 series Thermo-Elemental spectrometer in 2003. The elemental concentrations are presented in Table A7.1 and the sample preparation techniques and instrument operating conditions presented below.

A1.2.1 Sample preparation

Powdered rock samples were dissolved into solution following the standard acid digestion method of Cardiff University Earth Sciences Department.

1. 0.100 ± 0.0005 g of each sample powder was weighed into a nalgene vial.
2. Several drops of concentrated HNO_3, and 3-4 ml Romil HF were added. Lids were placed on the vials, then heated on a hotplate for 48 hours at 125°C.
3. After cooling to room temperature, the container lids were tapped to prevent loss of any condensate, removed, and the samples evaporated on a hotplate to a white powder residue.
4. 3 ml of concentrated HNO_3 was added to each sample, vial lids replaced, and the samles heated on a hotplate overnight at 125°C.
5. After cooling a second time, the lids were tapped to prevent loss of any condensate then removed. The solutions were evaporated on the hotplate, until they had the consistency of wallpaper paste.
6. 5 ml of concentrated PRIMAR HNO_3 was added, the lids replaced, and the samples heated on a hotplate overnight at 125°C.
7. Cooled samples were spiced with 1 ml of 2500 ppb rhodium and 2500 ppb rhenium solution (naturally low abundance metals used as internal standards for each sample) and diluted up to exactly 50 ml with de-ionised water and stored in previously unused 60 ml nalgene bottles.
8. The day of analysis, 1 ml of sample was extracted, and diluted up to a volume of 10 ml with de-ionised water. Solutions of Certified Reference Materials (CRMs) and Total Procedural Blanks (TPBs) were prepared (CRMs from powder) simultaneously by the same method.

A1.2.2 Calibration and analysis

Before the MPG samples were run, solutions of eight CRMs (W2, BHVO-1, MGR-1, ENDV, JB1a, BCR-1, MRG-1, X108) and a TPB were analysed and a best fit calibration line (acquired count rate versus certified recommended concentrations (Govindaraju, 1994) and driven through the blank) was constructed for each element. CRM element concentrations that fell significantly off the calibration line were removed. All MPG sample element concentrations were then derived from the acquired number of counts using the calibration lines. The CRM, X108 and TPB were analysed

as unknown samples after every six MPG samples as calibration independent standards, permitting data accuracy to be checked after data reduction and drift correction checks.

The instrument parameters were:

Repetition time – 1200 ms
Dwell time – 240 ms
Number of sweeps per repetition – 5
Readings per repetition – 1
Number of repetitions – 4

A1.2.3 Drift correction

During the course of a sample run, concentrations of some elements 'drifted' typically to values lower than actual. A drift monitor, CRM X108 with well-certified elemental concentrations was analysed after every six MPG unknowns. The drift of each element in X108 was monitored at every X108 repetition, permitting a drift correction to be applied to the MPG samples following the procedure below.

1. X108 element concentrations were plotted against time (in the run) to determine whether the decay in concentrations was drift (constant decay curve through time) or precision (scatter of element concentrations with time).
2. Elements displaying fluctuating precision through time were not drift corrected.
3. Elements displaying drift through time were drift corrected. A correction factor for each X108 analysis was applied to correct drifted element values back to their values in the first run X108a ($element_i$ of X108 / $element_i$ of X108a + x). Correction factors for each set of six MPG samples (unknowns) between were determined by linear extrapolation of the correction factors of the bounding X108 runs and applied.

A1.2.4 Quality of data - limits of detection and quantification

Limits of Detection (LOD) and Limits of Quantification (LOQ) are defined as three times and ten times the standard deviation of the blanks respectively. Element values lower than the LOD are below detection and not used. Element values above the LOD, but below the LOQ are utilised but must be treated with caution.

A1.2.5 X7 series Thermo-Elemental ICP-MS

The LOD and LOQ for analyse carried out by ICP-MS, are calculated as follows.

1. Calculate the standard deviation of the sample intensities of the blanks (counts per second) for each element.
2. Multiply the standard deviation value by three and ten for LOD and LOQ respectively
3. Acquire the sensitivity value (gradient or 'm' of the calibration line) from the 'Reports' menu of the Plasmalab software for each element (as each element has a unique calibration line).
4. Rearrange $y = mx + c$ to $x = y/m$ (c is zero as the calibration lines were driven through the origin) to calculate x, that is the LOD and LOQ elemental concentration.

A1.2.6 Comparison of ICP-OES and ICP-MS data

Ti and Mn have been analysed by both ICP-OES and ICP-MS, and so a comparison can be made between the two analytical methods. In Figs. A1.2 and A1.3 the ICP-OES values are plotted against the ICP-MS values. In general, there is good correlation between the two methods, indicating that the calculated values for both analytical techniques are accurate.

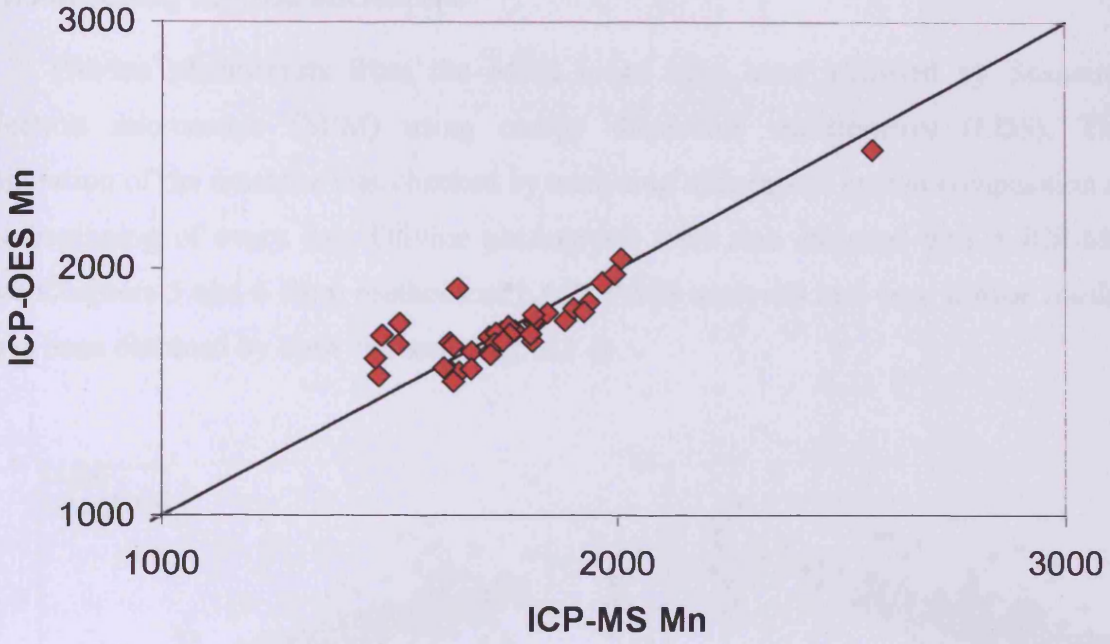

Fig. A1.2. Comparison of Mn concentrations (PPM) as calculated by ICP-OES and ICP-MS.

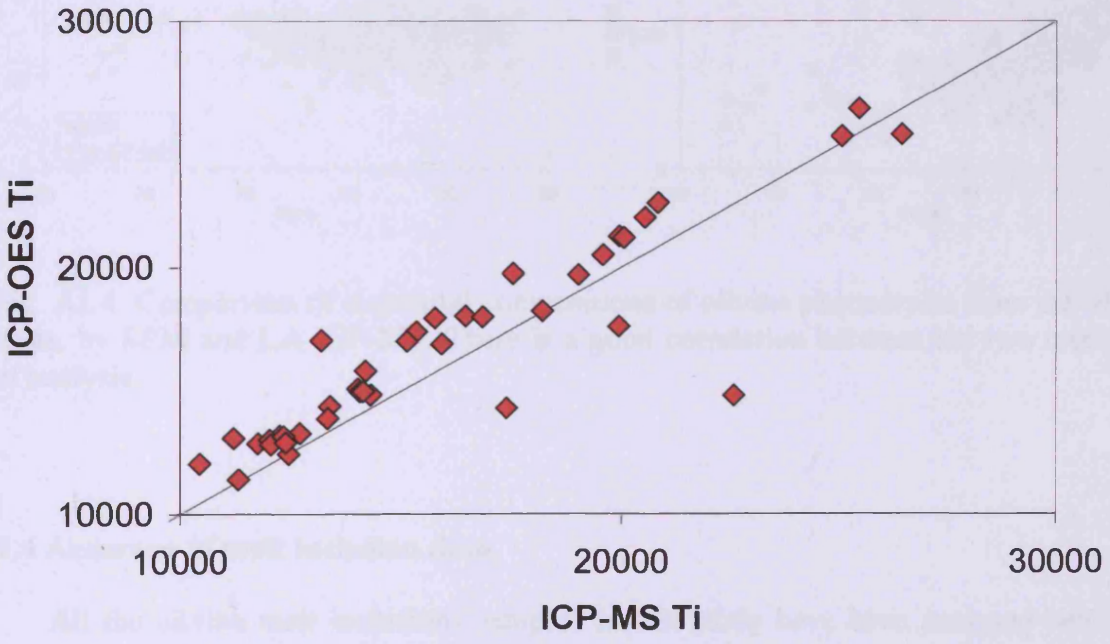

Fig. A1.3. Comparison of Mn concentrations (PPM) as calculated by ICP-OES and ICP-MS.

A1.3 Scanning electron microscope

Olivine phenocrysts from the MPG lavas have been analysed by Scanning Electron microscope (SEM) using energy dispersive spectrometry (EDS). The calibration of the machine was checked by analysing minerals of known composition at the beginning of every day. Olivine phenocrysts were also analysed by LA-ICP-MS (see Chapters 5 and 6 from methods of LA-ICP-MS analysis) and very similar results have been obtained by both methods (Fig. A1.4).

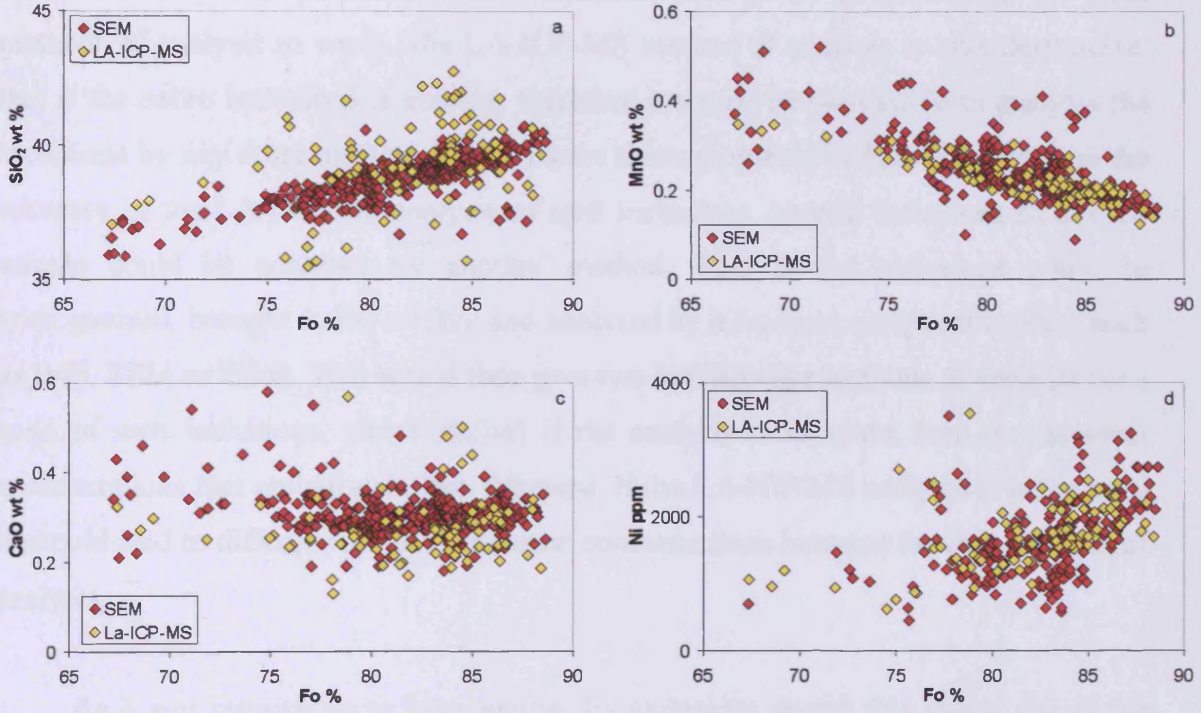

Fig. A1.4. Comparison of elemental compositions of olivine phenocrysts from the MPG lavas, by SEM and LA-ICP-MS. There is a good correlation between the two methods of analysis.

A1.4 Accuracy of melt inclusion data.

All the olivine melt inclusions sampled in this study have been analysed below the sample surface by LA-ICP-MS. To calculate the elemental concentrations in the inclusions a number of assumptions are made; 1) the concentration of an element in the inclusions is estimated from the whole rock concentration and this may not be accurate. 2) It is assumed that the fractionation trends of the external standards and unknowns

(i.e. melt inclusions) are the same, and it was shown in Chapter 5 that this may not be the case. 3) To determine accurately the concentrations in the inclusions, it is necessary to determine time slices in the analysis that incorporate host olivine and a mixed time slice that incorporates all the ablated melt inclusion material. It was shown in Chapter 5 that this is very problematic, and may not be completely possible.

To check the accuracy of this method of melt inclusion analysis, the inclusions could be analysed by another method of analysis such as IMP, SEM and PIXE. However, this is not possible, as the inclusions need to be at the surface for these methods of analysis to work. The LA-ICP-MS method of analysis is also destructive, that is the entire inclusions is ablated, therefore it would be impossible to analysis the inclusions by any other method. To overcome these problems in finding a check on the accuracy of the LA-ICP-MS analysis of melt inclusions, several inclusions from each sample could be analysed by another method. That is the inclusions could be homogenised, brought to the surface and analysed by a separate analytical method such as IMP, SEM or PIXE. This would then give two independent methods of analysis for a suite of melt inclusions, which should if the analysis is accurate, lead to elemental concentrations that are very similar. Whereas, if the LA-ICP-MS analysis is inaccurate, it should lead to difference in the elemental concentrations between the two methods of analysis.

As it was impossible to homogenise the inclusions during this study, due to the equipment not being available at Cardiff University, only elemental ratios were used in the interpretation of melt inclusions, as these should not be affected by inaccuracies in the methods of analysis.

Appendix 2
ICP-OES and ICP-MS data for MPG lavas

In the following tables, all iron is reported as Fe_2O_3. Major element values are given in wt%. Trace elements, LOD and LOQ values are given in PPM.

	BHI2	BHI3	BHI16	BHI17	BHI18	BHI19	LOD	LOQ
SiO_2	43.09	43.64	49.06	43.91	43.34	45.73		
TiO_2	2.09	2.02	0.02	1.71	1.65	1.14		
Al_2O_3	14.05	14.40	16.30	15.11	14.81	13.51		
Fe_2O_3	14.24	13.28	14.89	13.09	12.76	11.05		
MnO	0.19	0.18	0.19	0.17	0.17	0.17		
MgO	11.53	10.64	12.24	11.01	10.39	11.76		
CaO	8.85	8.31	10.95	9.59	9.39	10.25		
Na_2O	2.27	2.64	0.02	2.62	2.81	2.09		
K_2O	0.28	0.50	0.15	0.23	0.23	0.30		
P_2O_5	0.19	0.20	0.26	0.20	0.17	0.12		
Totals	99.81	99.55	106.36	99.94	99.28	99.16		
LOI	3.03	3.73	2.28	2.30	3.55	3.04		
Sc	35.09	46.77	26.58	27.57	26.72	28.89	0.405	1.352
Ti	20530.00	19940.00	15388.33	16430.00	15323.09	10441.87	0.330	1.101
V	278.20	264.90	264.33	263.60	255.63	255.53	0.073	0.242
Cr	452.80	403.20	392.85	451.90	382.02	905.08	134.339	447.797
Mn	1938.00	1884.00	1645.04	1726.00	1629.60	1635.98	1.021	3.403
Co	74.32	64.91	60.08	65.35	57.66	55.76	2.187	7.289
Ni	359.50	295.10	304.40	427.50	258.53	479.46	434.068	1446.894
Cu	75.83	92.27	93.85	137.32	83.50	61.90	16.127	53.755
Zn	73.62	67.25	20.76	80.23	29.26	42.68	31.479	104.928
Ga	16.94	17.50	17.12	19.06	15.41	14.51	0.073	0.242
Rb	7.68	10.63	1.56	3.19	2.72	4.53	0.182	0.606
Sr	277.20	382.10	340.38	417.80	384.30	279.12	0.012	0.042
Y	33.31	33.61	19.68	19.95	19.59	17.36	0.075	0.249
Zr	152.80	162.90	121.86	134.30	116.14	60.51	0.547	1.823
Nb	5.65	6.05	4.24	4.06	4.03	2.39	0.611	2.037
Cs	0.63	0.22	0.01	0.07	0.06	0.01	0.007	0.022
Ba	133.40	142.60	24.31	126.90	42.99	114.80	0.831	2.770
La	8.79	9.62	5.92	6.49	6.97	6.04	0.006	0.020
Ce	22.68	24.47	16.83	17.96	18.43	14.36	0.387	1.290
Pr	3.49	3.68	2.84	2.98	2.97	2.13	0.001	0.003
Nd	17.86	18.71	15.30	15.75	15.48	10.62	0.010	0.034
Sm	5.20	5.33	4.42	4.43	4.36	2.96	0.004	0.012
Eu	1.86	1.89	1.55	1.54	1.51	1.06	0.003	0.011
Gd	5.89	5.97	4.52	4.45	4.46	3.31	0.041	0.136
Tb	0.98	0.98	0.70	0.67	0.69	0.55	0.001	0.003
Dy	5.89	5.86	3.96	3.78	3.94	3.33	0.003	0.012
Ho	1.17	1.16	0.76	0.72	0.76	0.67	0.001	0.004
Er	3.16	3.15	2.01	1.88	2.00	1.81	0.003	0.009
Tm	0.47	0.47	0.30	0.27	0.29	0.27	0.001	0.002
Yb	2.82	2.83	1.77	1.64	1.77	1.62	0.002	0.007
Lu	0.43	0.44	0.27	0.25	0.27	0.25	0.001	0.003
Hf	4.04	4.18	3.30	3.29	3.18	1.87	0.019	0.065
Ta	0.39	0.43	0.25	0.26	0.24	0.13	0.001	0.003
Pb	0.18	0.37	-0.45	-0.21	-0.35	-0.28	4.066	13.554
Th	0.87	1.14	0.33	0.35	0.37	0.40	0.009	0.029
U	0.24	0.23	0.07	0.07	0.08	0.03	0.054	0.179

Appendix 2 MPG lava whole rock compositions

	BHI20	BHI26	BHI27	BHI28A	BHI28B	BHI30	LOD	LOQ
SiO_2	44.96	45.93	45.05	47.74	46.74	44.81		
TiO_2	1.22	1.36	1.43	1.42	1.41	1.25		
Al_2O_3	14.14	14.73	15.49	13.09	14.93	13.43		
Fe_2O_3	11.69	11.70	12.07	15.32	12.11	12.46		
MnO	0.17	0.18	0.19	0.25	0.17	0.18		
MgO	11.87	9.77	9.35	7.08	8.34	13.28		
CaO	10.11	10.90	9.80	11.60	11.16	10.03		
Na_2O	2.07	2.29	2.28	2.35	2.53	1.83		
K_2O	0.19	0.25	0.37	0.12	0.29	0.23		
P_2O_5	0.13	0.15	0.15	0.12	0.14	0.14		
Totals	101.20	101.55	101.36	101.00	100.41	99.92		
LOI	4.66	4.28	5.18	1.89	2.57	2.27		
Sc	30.71	33.73	33.87	56.89	35.84	31.28	0.405	1.352
Ti	11750.00	13360.00	14000.00	14050.00	14290.00	12240.00	0.330	1.101
V	281.40	308.30	309.10	407.20	329.00	271.20	0.073	0.242
Cr	999.80	544.70	353.50	76.40	434.10	1586.00	134.339	447.797
Mn	1677.00	1816.00	1903.00	2568.00	1812.00	1818.00	1.021	3.403
Co	65.56	54.14	57.09	57.08	53.65	77.02	2.187	7.289
Ni	422.70	195.50	327.30	74.13	154.00	626.90	434.068	1446.894
Cu	98.88	79.36	94.40	224.19	98.94	211.00	16.127	53.755
Zn	58.69	58.12	63.70	80.85	65.41	57.51	31.479	104.928
Ga	16.49	17.80	17.78	17.17	18.69	14.80	0.073	0.242
Rb	2.03	3.63	8.15	2.36	3.59	4.12	0.182	0.606
Sr	352.10	397.70	463.50	116.60	370.20	294.70	0.012	0.042
Y	17.37	21.46	22.93	39.86	23.54	19.05	0.075	0.249
Zr	72.92	87.43	88.09	72.24	89.34	75.68	0.547	1.823
Nb	1.79	2.48	2.99	1.74	3.70	1.93	0.611	2.037
Cs	0.01	0.03	0.03	0.03	0.02	0.01	0.007	0.022
Ba	101.00	144.30	463.10	41.42	179.20	270.80	0.831	2.770
La	4.84	6.72	5.88	2.23	7.23	4.19	0.006	0.020
Ce	12.35	16.81	14.55	6.52	17.25	11.49	0.387	1.290
Pr	1.98	2.60	2.25	1.23	2.60	1.90	0.001	0.003
Nd	10.33	13.12	11.63	7.62	13.17	10.05	0.010	0.034
Sm	2.98	3.63	3.44	3.22	3.77	2.99	0.004	0.012
Eu	1.08	1.28	1.29	1.28	1.35	1.10	0.003	0.011
Gd	3.27	3.96	3.96	4.76	4.24	3.39	0.041	0.136
Tb	0.54	0.64	0.66	0.92	0.70	0.56	0.001	0.003
Dy	3.16	3.82	3.98	6.21	4.18	3.38	0.003	0.012
Ho	0.62	0.76	0.81	1.36	0.83	0.68	0.001	0.004
Er	1.67	2.05	2.19	3.91	2.26	1.83	0.003	0.009
Tm	0.25	0.30	0.33	0.62	0.34	0.27	0.001	0.002
Yb	1.49	1.86	2.02	3.87	2.04	1.67	0.002	0.007
Lu	0.23	0.28	0.31	0.61	0.31	0.26	0.001	0.003
Hf	2.02	2.36	2.38	2.18	2.44	2.08	0.019	0.065
Ta	0.09	0.14	0.17	0.11	0.21	0.11	0.001	0.003
Pb	-0.13	-0.16	0.00	-0.52	0.08	-0.54	4.066	13.554
Th	0.21	0.24	0.32	0.21	0.31	0.18	0.009	0.029
U	0.00	0.02	0.02	0.03	0.05	0.02	0.054	0.179

Appendix 2 MPG lava whole rock compositions

	AM1	AM7	AM7B	AM10A	AM10B	AM10C	LOD	LOQ
SiO_2	43.88	44.83	43.79	43.92	43.83	45.23		
TiO_2	2.15	1.62	1.60	1.71	1.71	1.87		
Al_2O_3	13.97	14.11	13.77	14.90	14.87	14.71		
Fe_2O_3	14.66	12.32	12.27	12.94	12.91	13.48		
MnO	0.20	0.18	0.17	0.16	0.16	0.18		
MgO	11.84	11.62	11.81	10.32	10.30	10.17		
CaO	8.79	9.98	9.66	9.34	9.32	9.53		
Na_2O	1.95	2.19	2.08	2.38	2.38	2.90		
K_2O	0.32	0.34	0.36	0.25	0.25	0.25		
P_2O_5	0.21	0.17	0.18	0.18	0.18	0.20		
Totals	101.32	100.70	98.64	99.44	100.42	100.27		
LOI	3.34	3.35	2.96	3.35	4.52	1.76		
Sc	36.25	33.02	31.40	29.01	28.61	31.17	0.405	1.352
Ti	20830.00	13170.00	15900.00	16820.00	15740.00	19010.00	0.330	1.101
V	280.10	241.70	294.40	275.90	264.60	317.40	0.073	0.242
Cr	444.90	689.30	892.50	419.40	459.10	418.20	134.339	447.797
Mn	1967.00	1518.00	1716.00	1632.00	1649.00	1926.00	1.021	3.403
Co	72.13	51.68	63.04	62.11	62.90	63.57	2.187	7.289
Ni	352.90	306.30	411.50	324.20	343.80	328.80	434.068	1446.894
Cu	102.93	66.51	97.42	121.66	116.91	134.39	16.127	53.755
Zn	74.23	48.33	64.52	70.29	69.57	78.47	31.479	104.928
Ga	17.31	15.34	18.58	18.57	17.68	18.46	0.073	0.242
Rb	8.20	5.15	5.55	3.66	3.62	4.50	0.182	0.606
Sr	317.40	282.40	348.20	383.70	387.90	464.90	0.012	0.042
Y	33.50	18.48	21.93	21.02	19.97	23.83	0.075	0.249
Zr	154.40	93.81	129.10	121.30	114.80	137.80	0.547	1.823
Nb	5.55	3.33	4.07	3.76	3.61	4.26	0.611	2.037
Cs	0.94	0.08	0.03	0.04	0.14	0.13	0.007	0.022
Ba	204.20	157.70	219.80	161.20	123.40	166.60	0.831	2.770
La	8.81	8.69	8.93	6.90	6.49	7.69	0.006	0.020
Ce	22.62	21.62	22.46	18.20	17.07	20.32	0.387	1.290
Pr	3.49	3.26	3.36	2.94	2.77	3.29	0.001	0.003
Nd	17.85	16.04	16.49	15.37	14.44	17.19	0.010	0.034
Sm	5.19	4.28	4.28	4.30	4.05	4.82	0.004	0.012
Eu	1.85	1.50	1.48	1.52	1.43	1.68	0.003	0.011
Gd	5.86	4.55	4.45	4.45	4.17	4.97	0.041	0.136
Tb	0.98	0.73	0.70	0.69	0.65	0.78	0.001	0.003
Dy	5.87	4.24	4.05	3.92	3.66	4.37	0.003	0.012
Ho	1.17	0.83	0.78	0.75	0.71	0.84	0.001	0.004
Er	3.16	2.18	2.05	1.99	1.86	2.21	0.003	0.009
Tm	0.47	0.32	0.30	0.29	0.27	0.33	0.001	0.002
Yb	2.84	1.91	1.80	1.77	1.65	1.97	0.002	0.007
Lu	0.43	0.29	0.27	0.27	0.25	0.30	0.001	0.003
Hf	4.01	3.10	3.16	3.16	2.98	3.56	0.019	0.065
Ta	0.39	0.27	0.27	0.24	0.22	0.27	0.001	0.003
Pb	0.78	0.29	0.46	0.17	0.09	0.40	4.066	13.554
Th	0.84	0.45	0.48	0.37	0.34	0.41	0.009	0.029
U	0.23	0.10	0.11	0.08	0.07	0.09	0.054	0.179

Appendix 2 MPG lava whole rock compositions

	BM5	BM6	BM6A	BM7	BM8	BM12	LOD	LOQ
SiO_2	44.08	45.79	44.81	49.75	45.56	44.60		
TiO_2	1.95	2.01	1.88	0.33	1.36	1.73		
Al_2O_3	13.98	14.94	14.60	14.45	14.96	14.48		
Fe_2O_3	12.73	13.75	13.34	12.91	12.97	13.19		
MnO	0.16	0.17	0.16	0.17	0.18	0.18		
MgO	9.66	9.61	9.57	15.30	8.30	7.31		
CaO	9.32	8.36	8.22	1.76	9.29	10.71		
Na_2O	2.23	3.07	3.04	0.14	2.13	2.37		
K_2O	0.26	0.28	0.25	0.13	0.03	0.23		
P_2O_5	0.19	0.23	0.21	0.17	0.16	0.14		
Totals	98.73	101.65	99.50	98.31	100.61	100.13		
LOI	4.18	3.44	3.43	3.18	5.69	5.19		
Sc	32.45	24.26	20.32	26.57	28.92	40.40	0.405	1.352
Ti	19570.00	20040.00	17520.20	8726.00	17370.00	18180.00	0.330	1.101
V	348.50	247.60	221.49	231.10	332.70	397.10	0.073	0.242
Cr	722.30	546.90	496.82	1150.00	30.48	252.10	134.339	447.797
Mn	1637.00	1738.00	1473.02	1480.00	1744.00	1844.00	1.021	3.403
Co	60.63	62.17	56.91	65.42	61.31	53.10	2.187	7.289
Ni	326.20	293.70	179.28	561.80	122.40	121.90	434.068	1446.894
Cu	116.83	94.35	62.17	77.50	79.59	212.24	16.127	53.755
Zn	68.54	74.46	-2.28	51.53	76.97	67.07	31.479	104.928
Ga	18.28	18.61	14.96	13.41	20.74	20.81	0.073	0.242
Rb	7.00	7.06	5.84	3.76	2.12	2.80	0.182	0.606
Sr	274.70	384.00	391.43	188.40	374.10	287.70	0.012	0.042
Y	26.92	22.64	19.30	17.11	23.65	26.94	0.075	0.249
Zr	149.10	165.40	138.20	53.38	105.50	109.10	0.547	1.823
Nb	3.66	6.74	6.84	2.00	2.31	3.12	0.611	2.037
Cs	0.30	2.47	1.28	0.15	0.16	0.09	0.007	0.022
Ba	153.80	153.00	21.23	140.30	144.50	111.30	0.831	2.770
La	8.52	10.39	9.66	5.89	5.86	6.06	0.006	0.020
Ce	22.51	26.04	24.10	13.65	15.49	15.72	0.387	1.290
Pr	3.58	3.93	3.64	2.00	2.60	2.62	0.001	0.003
Nd	18.44	19.59	18.17	9.81	14.00	14.13	0.010	0.034
Sm	5.04	5.22	4.83	2.79	4.13	4.30	0.004	0.012
Eu	1.70	1.77	1.65	1.01	1.51	1.55	0.003	0.011
Gd	5.28	5.21	4.85	3.28	4.51	4.88	0.041	0.136
Tb	0.84	0.79	0.73	0.56	0.73	0.80	0.001	0.003
Dy	4.84	4.32	4.00	3.44	4.27	4.75	0.003	0.012
Ho	0.95	0.80	0.75	0.71	0.84	0.94	0.001	0.004
Er	2.52	2.07	1.92	1.95	2.24	2.50	0.003	0.009
Tm	0.37	0.30	0.28	0.30	0.33	0.37	0.001	0.002
Yb	2.26	1.77	1.65	1.81	1.99	2.22	0.002	0.007
Lu	0.35	0.27	0.25	0.28	0.31	0.34	0.001	0.003
Hf	3.68	3.95	3.66	1.76	2.86	2.98	0.019	0.065
Ta	0.23	0.45	0.41	0.13	0.14	0.17	0.001	0.003
Pb	0.64	0.83	1.57	0.41	0.32	0.35	4.066	13.554
Th	0.52	1.04	0.96	0.42	0.23	0.34	0.009	0.029
U	0.12	0.29	0.27	0.06	0.03	0.04	0.054	0.179

Appendix 2 MPG lava whole rock compositions

	BM14	BM15	BB19	BB20	BB21	BB22	LOD	LOQ
SiO_2	44.30	43.19	44.24	45.66	43.83	45.04		
TiO_2	1.50	1.26	2.51	1.67	1.62	1.41		
Al_2O_3	13.80	13.23	15.01	14.14	13.64	15.19		
Fe_2O_3	12.89	12.27	15.54	12.83	13.70	14.97		
MnO	0.16	0.18	0.20	0.18	0.18	0.21		
MgO	10.41	12.82	6.29	8.88	12.53	9.92		
CaO	9.02	9.58	8.38	10.77	8.59	8.37		
Na_2O	1.94	1.98	3.04	2.52	2.26	2.16		
K_2O	0.25	0.29	0.69	0.65	0.41	0.44		
P_2O_5	0.15	0.13	0.32	0.21	0.16	0.20		
Totals	100.33	99.91	98.90	99.16	100.95	99.90		
LOI	5.90	4.99	2.67	1.65	4.03	2.00		
Sc	22.96	41.05	26.02	33.54	36.65	30.94	0.405	1.352
Ti	14168.53	12700.00	25440.00	19930.00	15100.00	22560.00	0.330	1.101
V	295.73	284.20	268.80	325.90	262.50	311.00	0.073	0.242
Cr	1104.95	1226.00	34.71	441.90	980.60	49.08	134.339	447.797
Mn	1465.95	1755.00	1994.00	1773.00	1814.00	2008.00	1.021	3.403
Co	64.17	68.44	50.73	53.12	70.59	57.28	2.187	7.289
Ni	371.97	500.10	64.00	206.30	433.90	69.60	434.068	1446.894
Cu	96.42	150.67	29.83	61.84	84.76	34.46	16.127	53.755
Zn	46.70	61.99	77.24	77.72	66.22	62.66	31.479	104.928
Ga	16.84	16.11	17.57	19.60	18.06	19.15	0.073	0.242
Rb	2.55	4.08	9.66	11.52	7.70	7.59	0.182	0.606
Sr	217.99	247.40	1430.00	475.20	563.40	453.20	0.012	0.042
Y	18.93	18.97	31.44	21.35	18.93	25.14	0.075	0.249
Zr	89.64	86.45	168.20	145.80	106.10	141.24	0.547	1.823
Nb	2.64	2.44	8.39	9.71	4.02	3.11	0.611	2.037
Cs	0.04	0.04	0.04	0.11	0.07	0.05	0.007	0.022
Ba	41.54	119.60	618.10	232.90	173.30	203.40	0.831	2.770
La	6.46	6.00	13.98	13.20	7.87	6.28	0.006	0.020
Ce	16.52	14.78	36.02	31.43	19.97	18.86	0.387	1.290
Pr	2.62	2.28	5.36	4.32	2.96	3.21	0.001	0.003
Nd	13.65	11.63	26.34	20.11	14.31	17.10	0.010	0.034
Sm	3.91	3.30	6.56	4.83	3.66	4.86	0.004	0.012
Eu	1.36	1.15	2.28	1.66	1.29	1.73	0.003	0.011
Gd	4.21	3.61	6.66	4.81	3.81	5.08	0.041	0.136
Tb	0.67	0.58	1.01	0.73	0.60	0.80	0.001	0.003
Dy	3.90	3.43	5.72	4.01	3.44	4.62	0.003	0.012
Ho	0.76	0.68	1.10	0.76	0.67	0.89	0.001	0.004
Er	1.99	1.81	2.90	1.97	1.78	2.36	0.003	0.009
Tm	0.29	0.27	0.42	0.29	0.27	0.35	0.001	0.002
Yb	1.74	1.62	2.57	1.71	1.60	2.08	0.002	0.007
Lu	0.26	0.25	0.40	0.26	0.25	0.32	0.001	0.003
Hf	2.70	2.29	4.14	3.54	2.73	3.53	0.019	0.065
Ta	0.15	0.13	0.52	0.63	0.24	0.20	0.001	0.003
Pb	0.65	0.16	0.37	0.58	1.00	-1.41	4.066	13.554
Th	0.29	0.30	0.63	0.89	0.44	0.22	0.009	0.029
U	0.05	0.05	0.14	0.22	0.09	0.01	0.054	0.179

Appendix 2 MPG lava whole rock compositions

	BR1	BR4	BR5	BR6	BR8	BR12	LOD	LOQ
SiO_2	44.09	45.90	44.26	45.33	45.24	44.10		
TiO_2	2.41	1.24	1.42	2.41	1.18	1.32		
Al_2O_3	14.89	13.08	13.16	15.33	13.18	11.92		
Fe_2O_3	16.85	12.26	13.01	15.19	10.88	12.58		
MnO	0.16	0.17	0.18	0.17	0.16	0.17		
MgO	6.62	12.53	12.11	6.44	9.96	13.75		
CaO	7.61	9.38	9.46	7.69	10.37	9.65		
Na_2O	3.29	2.73	2.25	3.46	2.06	1.83		
K_2O	0.24	0.34	0.44	0.24	0.56	0.30		
P_2O_5	0.23	0.15	0.14	0.23	0.15	0.13		
Totals	100.43	99.49	99.06	98.83	98.79	98.73		
LOI	4.03	1.69	2.63	2.33	5.04	2.98		
Sc	25.72	35.49	38.90	19.33	39.25	35.41	0.405	1.352
Ti	26430.00	12020.00	14120.00	25040.00	12450.00	13320.00	0.330	1.101
V	246.70	263.20	282.30	243.20	284.70	280.50	0.073	0.242
Cr	216.50	1402.00	755.80	16.54	689.80	1775.00	134.339	447.797
Mn	1616.00	1715.00	1759.00	1762.00	1676.00	1808.00	1.021	3.403
Co	58.90	63.37	67.66	53.86	52.80	71.04	2.187	7.289
Ni	146.10	488.40	445.50	71.83	255.80	741.30	434.068	1446.894
Cu	71.36	114.51	71.58	46.10	87.31	120.58	16.127	53.755
Zn	86.97	63.48	63.41	79.16	61.87	146.90	31.479	104.928
Ga	19.39	15.70	16.07	19.68	15.47	14.18	0.073	0.242
Rb	3.31	5.84	9.58	2.45	6.17	4.09	0.182	0.606
Sr	388.90	283.70	261.20	546.90	1104.00	358.30	0.012	0.042
Y	27.79	19.39	21.62	24.57	20.25	19.58	0.075	0.249
Zr	180.50	101.60	101.80	165.90	87.49	84.75	0.547	1.823
Nb	6.66	2.65	2.40	5.88	2.61	1.92	0.611	2.037
Cs	0.03	0.07	0.03	0.02	0.02	0.26	0.007	0.022
Ba	68.83	110.30	153.60	87.46	387.10	133.90	0.831	2.770
La	7.59	5.75	6.53	7.92	8.25	4.43	0.006	0.020
Ce	20.71	15.44	16.65	21.72	19.81	12.27	0.387	1.290
Pr	3.48	2.46	2.60	3.53	2.90	2.05	0.001	0.003
Nd	19.00	12.49	13.18	18.70	14.03	10.94	0.010	0.034
Sm	5.73	3.44	3.67	5.34	3.59	3.24	0.004	0.012
Eu	2.04	1.20	1.28	1.91	1.26	1.15	0.003	0.011
Gd	6.02	3.67	4.00	5.48	3.76	3.61	0.041	0.136
Tb	0.93	0.59	0.65	0.84	0.60	0.59	0.001	0.003
Dy	5.16	3.49	3.84	4.63	3.58	3.53	0.003	0.012
Ho	0.98	0.69	0.76	0.87	0.72	0.70	0.001	0.004
Er	2.53	1.87	2.05	2.23	1.94	1.87	0.003	0.009
Tm	0.37	0.28	0.31	0.32	0.29	0.28	0.001	0.002
Yb	2.24	1.72	1.86	1.93	1.77	1.68	0.002	0.007
Lu	0.35	0.26	0.29	0.29	0.27	0.26	0.001	0.003
Hf	4.43	2.63	2.69	4.00	2.33	2.32	0.019	0.065
Ta	0.41	0.16	0.14	0.37	0.15	0.11	0.001	0.003
Pb	0.54	0.69	0.00	-0.06	0.72	1.42	4.066	13.554
Th	0.57	0.28	0.38	0.55	0.22	0.20	0.009	0.029
U	0.12	0.05	0.08	0.11	0.01	0.03	0.054	0.179

Appendix 2 MPG lava whole rock compositions

	MR10	MR11	MR12	MR12A	MR13	LOD	LOQ
SiO_2	44.76	45.11	45.39	44.99	45.90		
TiO_2	1.22	1.25	1.08	1.22	1.24		
Al_2O_3	13.07	13.49	13.45	13.50	13.47		
Fe_2O_3	12.10	11.98	11.14	12.18	12.04		
MnO	0.18	0.17	0.17	0.17	0.17		
MgO	12.61	11.81	11.26	12.03	11.21		
CaO	9.44	9.43	9.67	9.41	9.93		
Na_2O	1.82	2.59	2.06	2.08	2.10		
K_2O	0.34	0.41	0.66	0.51	0.29		
P_2O_5	0.13	0.13	0.13	0.13	0.13		
Totals	99.89	98.64	99.06	99.89	98.98		
LOI	4.23	2.27	4.05	3.67	2.49		
Sc	43.05	30.89	30.27	31.68	27.85	0.405	1.352
Ti	12040.00	12330.00	11320.00	12380.00	11210.00	0.330	1.101
V	255.00	263.60	265.40	270.90	244.40	0.073	0.242
Cr	1023.00	999.20	715.50	982.10	784.10	134.339	447.797
Mn	1731.00	1728.00	1718.00	1746.00	1516.00	1.021	3.403
Co	61.60	63.24	56.24	62.75	51.94	2.187	7.289
Ni	393.50	424.20	349.20	408.50	278.10	434.068	1446.894
Cu	81.42	129.42	89.39	112.54	95.64	16.127	53.755
Zn	57.42	60.67	53.27	61.80	50.97	31.479	104.928
Ga	15.43	14.68	15.91	15.99	14.51	0.073	0.242
Rb	6.19	7.95	14.34	12.66	3.64	0.182	0.606
Sr	434.20	526.30	439.90	282.40	222.50	0.012	0.042
Y	20.13	19.69	19.43	19.64	17.02	0.075	0.249
Zr	80.42	87.80	76.42	86.78	73.80	0.547	1.823
Nb	2.85	3.17	2.43	3.11	2.09	0.611	2.037
Cs	0.02	0.11	0.04	0.05	0.02	0.007	0.022
Ba	229.60	218.90	421.60	279.40	99.66	0.831	2.770
La	6.18	6.26	7.28	6.17	5.31	0.006	0.020
Ce	15.07	15.05	17.22	14.90	13.73	0.387	1.290
Pr	2.26	2.29	2.51	2.26	2.17	0.001	0.003
Nd	11.10	11.43	12.07	11.35	11.12	0.010	0.034
Sm	3.06	3.22	3.15	3.21	3.20	0.004	0.012
Eu	1.10	1.16	1.14	1.17	1.16	0.003	0.011
Gd	3.45	3.57	3.48	3.56	3.57	0.041	0.136
Tb	0.57	0.58	0.56	0.58	0.58	0.001	0.003
Dy	3.46	3.48	3.39	3.47	3.49	0.003	0.012
Ho	0.70	0.70	0.68	0.70	0.70	0.001	0.004
Er	1.90	1.89	1.86	1.87	1.90	0.003	0.009
Tm	0.29	0.28	0.28	0.28	0.29	0.001	0.002
Yb	1.75	1.73	1.69	1.73	1.75	0.002	0.007
Lu	0.27	0.27	0.26	0.27	0.27	0.001	0.003
Hf	2.14	2.37	2.07	2.35	2.34	0.019	0.065
Ta	0.16	0.18	0.13	0.18	0.15	0.001	0.003
Pb	0.00	0.60	0.52	0.51	0.21	4.066	13.554
Th	0.30	0.51	0.29	0.50	0.37	0.009	0.029
U	0.02	0.12	0.05	0.12	0.06	0.054	0.179

Appendix 2 MPG lava whole rock compositions

Appendix 3
SEM analysis of olivine phenocrysts from the MPG lavas

	BM2 Ph1	BM2 Ph2	BM2 Ph3	BM2 Ph4	BM2 Ph5	BM2 Ph6	BM2 Ph7	BM2 Ph8
MgO	39.77	38.76	45.02	44.69	41.02	38.92	42.78	44.30
SiO_2	37.98	37.32	39.29	38.72	38.11	37.88	38.65	38.93
CaO	0.30	0.30	0.31	0.24	0.27	0.30	0.23	0.26
MnO	0.32	0.28	0.23	0.18	0.27	0.30	0.22	b-d
Fe_2O_3	21.49	21.88	15.84	15.38	19.42	22.33	17.89	15.50
CoO	0.16	0.15	b-d	0.20	0.21	b-d	b-d	b-d
NiO	b-d	b-d	0.23	0.31	0.26	b-d	0.23	b-d
Total	100.02	98.69	100.92	99.72	99.56	99.73	100.00	98.99
Fo content	76.74	75.95	83.51	83.82	79.01	75.65	81.00	83.59

	BM2 Ph9	BM2 Ph10	BM2 Ph11	BM2 Ph12	BM2 Ph13	BM6 Ph1	BM6 Ph2	BM6 Ph3
MgO	45.21	41.91	40.19	40.74	44.71	32.82	34.20	30.53
SiO_2	39.23	38.08	38.15	38.00	39.24	36.55	37.24	36.28
CaO	0.25	0.29	0.27	0.28	0.25	0.38	0.39	0.45
MnO	0.17	0.30	0.32	0.30	b-d	0.44	0.45	0.53
Fe_2O_3	15.32	18.06	21.60	19.73	15.38	29.07	28.83	32.67
CoO	b-d	b-d	b-d	0.11	b-d	0.21	0.28	0.39
NiO	0.19	b-d	b-d	b-d	0.29	0.16	b-d	0.04
Total	100.37	98.64	100.53	99.16	99.87	99.63	101.39	100.89
Fo content	84.03	80.53	76.83	78.63	83.82	66.80	67.89	62.49

	BM6 Ph4	BM6 Ph5	BM6 Ph6	BM6 Ph7	BM6 Ph8	BM6 Ph9	BM6 Ph10	BM6 Ph11
MgO	36.79	37.41	36.04	32.87	31.62	29.74	29.75	28.41
SiO_2	38.08	38.46	37.25	36.56	36.40	36.11	35.98	35.73
CaO	0.32	0.33	0.33	0.43	0.44	0.45	0.45	0.41
MnO	0.36	0.33	0.38	0.45	0.52	0.55	0.54	0.63
Fe_2O_3	25.62	25.18	24.07	28.40	30.50	32.23	32.14	33.96
CoO	0.28	0.24	0.31	0.24	0.21	0.29	0.29	0.30
NiO	0.23	0.19	0.17	0.11	0.03	0.03	0.11	b-d
Total	101.68	102.14	98.55	99.06	99.72	99.40	99.26	99.44
Fo content	71.91	72.59	72.74	67.35	64.89	62.19	62.26	59.86

	BM6 Ph12	BM7 Ph1	BM7 Ph2	BM7 Ph3	BM7 Ph4	BM7 Ph5	BM7 Ph6	BM7 Ph7
MgO	29.23	47.39	47.44	46.30	46.59	47.63	46.54	45.71
SiO_2	35.85	40.04	40.11	39.70	40.01	40.13	39.82	39.34
CaO	0.44	0.30	0.32	0.35	0.30	0.25	0.31	0.36
MnO	0.55	0.15	0.15	0.18	0.16	0.16	0.18	0.18
Fe_2O_3	32.91	11.26	11.46	12.98	12.36	10.90	11.97	12.76
CoO	0.33	b-d	b-d	0.08	0.06	b-d	b-d	b-d
NiO	0.08	0.36	0.34	0.27	0.31	0.43	0.35	0.30
Total	99.39	99.50	99.82	99.86	99.79	99.50	99.17	98.65
Fo content	61.29	88.24	88.06	86.41	87.04	88.62	87.39	86.46

	BM7 Ph8	BM7 Ph9	BM7 Ph10	BM7 Ph11	BM15 Ph1	BM15 Ph2	BM15 Ph3	BM15 Ph4
MgO	46.16	46.80	46.51	46.58	46.86	46.86	47.62	44.60
SiO_2	39.50	40.23	40.05	39.84	39.74	39.74	40.38	39.04
CaO	0.31	0.30	0.28	0.31	0.34	0.34	0.32	0.33
MnO	0.20	0.17	0.18	0.18	0.17	0.17	0.17	0.19
Fe_2O_3	12.51	12.84	12.89	12.65	11.77	11.77	11.46	13.84
CoO	b-d	b-d	b-d	b-d	0.04	0.04	0.12	0.10
NiO	0.30	0.37	0.26	0.32	0.34	0.34	0.43	0.30
Total	98.98	100.71	100.17	99.88	99.26	99.26	100.50	98.40
Fo content	86.80	86.66	86.54	86.78	87.65	87.65	88.10	85.17

Appendix 3, results of SEM-EDS analysis of the cores of olivine phenocrysts. (b-d below detection)

	BM15 Ph5	BM15 Ph6	BM15 Ph7	BM15 Ph8	BM15 Ph9	BM15 Ph10	BM15 Ph11	BM15 Ph12
MgO	47.51	46.26	46.63	47.74	44.79	44.79	44.79	44.57
SiO_2	40.43	39.58	39.96	40.71	39.46	39.46	39.46	39.53
CaO	0.31	0.31	0.29	0.31	0.31	0.31	0.31	0.29
MnO	0.15	0.18	0.16	0.16	0.20	0.20	0.20	0.20
Fe_2O_3	11.35	12.67	12.50	12.05	14.44	14.44	14.44	14.87
CoO	0.10	0.04	0.09	0.08	0.15	0.15	0.15	0.15
NiO	0.39	0.36	0.40	0.43	0.36	0.36	0.36	0.35
Total	100.24	99.40	100.03	101.48	99.71	99.71	99.71	99.96
Fo content	88.18	86.68	86.93	87.60	84.68	84.68	84.68	84.23

	BHI3 Ph1	BHI3 Ph2	BHI3 Ph3	BHI3 Ph4	BHI3 Ph5	BHI3 Ph6	BHI3 Ph7	BHI3 Ph8
MgO	41.95	41.70	40.70	40.72	40.36	40.97	41.54	41.03
SiO_2	38.81	38.69	38.50	38.32	38.19	38.88	38.84	38.62
CaO	0.27	0.30	0.28	0.29	0.30	0.28	0.29	0.32
MnO	0.22	0.23	0.26	0.25	0.24	0.27	0.25	0.25
Fe_2O_3	18.46	18.32	19.71	19.30	19.44	19.91	18.69	19.10
CoO	0.16	0.17	0.29	0.19	0.19	0.11	0.18	0.10
NiO	0.22	0.23	0.18	0.25	b-d	0.21	b-d	b-d
Total	100.09	99.64	99.92	99.32	98.72	100.63	99.79	99.42
Fo content	80.20	80.23	78.64	78.99	78.73	78.58	79.85	79.29

	BHI3 Ph9	BHI3 Ph10	BHI3 Ph11	BHI3 Ph12	BHI3 Ph13	BHI3 Ph14	BHI3 Ph15	BHI3 Ph16
MgO	40.94	41.84	41.97	41.79	42.06	42.07	41.20	41.52
SiO_2	38.40	38.69	39.01	39.09	39.12	39.11	38.48	38.66
CaO	0.27	0.32	0.29	0.28	0.29	0.26	0.28	0.31
MnO	0.25	0.22	0.22	0.24	0.23	0.24	0.24	0.23
Fe_2O_3	19.01	18.24	18.84	19.10	18.60	18.94	18.96	18.63
CoO	0.17	0.21	0.08	0.12	0.17	0.21	0.15	0.18
NiO	0.21	0.18	b-d	b-d	b-d	0.24	0.26	0.26
Total	99.25	99.70	100.41	100.62	100.47	101.07	99.57	99.79
Fo content	79.33	80.35	79.88	79.59	80.12	79.84	79.48	79.89

	BHI19 Ph1	BHI19 Ph2	BHI19 Ph3	BHI19 Ph4	BHI19 Ph5	BHI19 Ph6	BHI19 Ph7	BHI19 Ph8
MgO	45.92	45.05	45.38	45.67	46.26	45.85	46.15	45.88
SiO_2	39.63	39.65	39.53	39.42	39.87	39.76	39.65	39.87
CaO	0.33	0.31	0.30	0.36	0.32	0.34	0.33	0.33
MnO	0.18	0.19	0.21	0.20	0.20	0.20	0.18	0.19
Fe_2O_3	13.15	14.04	13.82	13.37	13.04	13.12	12.71	13.57
CoO	b-d	b-d	0.03	b-d	b-d	b-d	b-d	b-d
NiO	0.24	0.29	0.25	0.30	0.29	0.25	0.29	0.27
Total	99.45	99.53	99.52	99.32	99.98	99.52	99.31	100.11
Fo content	86.16	85.12	85.41	85.89	86.34	86.17	86.62	85.77

	BHI19 Ph9	BHI19 Ph10	BHI19 Ph11	BHI30 Ph1	BHI30 Ph2	BHI30 Ph3	BHI30 Ph4	BHI30 Ph5
MgO	44.75	45.29	46.16	43.66	46.17	41.21	43.14	47.09
SiO_2	39.58	39.74	39.93	39.59	39.75	38.59	39.00	39.99
CaO	0.36	0.31	0.36	0.32	0.33	0.33	0.24	0.34
MnO	0.19	0.20	0.17	0.23	0.17	0.27	0.22	0.18
Fe_2O_3	14.54	13.91	12.86	16.42	12.76	18.33	16.02	11.78
CoO	b-d	b-d	b-d	0.15	0.07	0.18	0.15	0.18
NiO	b-d	0.31	0.28	0.26	0.31	0.30	0.20	0.33
Total	99.42	99.76	99.76	100.63	99.56	99.21	98.97	99.89
Fo content	84.58	85.30	86.48	82.58	86.58	80.03	82.76	87.69

Appendix 3, results of SEM-EDS analysis of the cores of olivine phenocrysts. (b-d below detection)

	BHI30 Ph6	BHI30 Ph7	BHI30 Ph8	BHI30 Ph9	BHI16 Ph1	BHI16 Ph2	BHI16 Ph3	BHI16 Ph4
MgO	46.41	46.59	44.65	47.96	44.04	43.58	44.59	44.50
SiO_2	39.93	40.23	39.70	40.46	39.30	39.46	39.15	39.53
CaO	0.35	0.34	0.33	0.35	0.32	0.31	0.27	0.35
MnO	0.15	0.17	0.19	0.14	0.24	0.24	0.19	0.25
Fe_2O_3	12.65	12.78	15.18	11.11	16.12	16.56	14.32	15.88
CoO	0.16	0.15	0.13	0.10	0.15	0.14	0.08	0.08
NiO	0.32	0.33	0.26	0.33	0.15	0.15	0.23	0.19
Total	99.97	100.59	100.44	100.45	100.32	100.44	98.83	100.78
Fo content	86.74	86.66	83.98	88.50	82.96	82.43	84.73	83.32

	BHI16 Ph5	BHI16 Ph6	BHI16 Ph7	BHI16 Ph8	BHI16 Ph9	BHI16 Ph10	BHI16 Ph11	BHI16 Ph12
MgO	43.29	43.80	44.66	45.07	44.55	45.35	44.01	44.11
SiO_2	38.78	39.18	39.21	39.47	39.95	39.83	39.53	39.71
CaO	0.34	0.35	0.30	0.29	0.34	0.32	0.33	0.31
MnO	0.22	0.25	0.18	0.20	0.24	0.21	0.24	0.22
Fe_2O_3	15.41	15.62	14.17	14.56	15.61	14.56	16.11	15.69
CoO	0.08	0.05	0.13	0.20	0.15	0.11	0.12	0.10
NiO	0.14	0.16	0.16	0.19	0.19	0.19	0.13	0.13
Total	98.26	99.41	98.81	99.98	101.03	100.57	100.47	100.27
Fo content	83.35	83.33	84.89	84.66	83.57	84.74	82.96	83.36

	BHI17 Ph1	BHI17 Ph2	BHI17 Ph3	BHI17 Ph4	BHI17 Ph5	BHI17 Ph6	BHI17 Ph7	BHI17 Ph8
MgO	41.86	42.52	39.93	41.75	39.81	40.22	37.16	40.66
SiO_2	39.04	39.31	38.27	38.90	38.55	38.18	37.32	38.51
CaO	0.27	0.31	0.55	0.34	0.29	0.35	0.44	0.28
MnO	0.27	0.26	0.29	0.29	0.27	0.25	0.36	0.27
Fe_2O_3	18.98	17.87	21.12	18.81	21.23	20.68	23.73	19.88
CoO	0.22	0.15	0.28	0.10	0.10	0.20	0.25	0.12
NiO	0.24	0.25	0.26	0.17	0.20	0.19	0.16	0.24
Total	100.88	100.67	100.70	100.36	100.45	100.07	99.42	99.96
Fo content	79.72	80.92	77.12	79.82	76.97	77.61	73.62	78.47

	BHI17 Ph9	BHI17 Ph10	BHI17 Ph11	BHI17 Ph12	BHI17 Ph13	BHI17 Ph14	BHI17 Ph15	BHI17 Ph16
MgO	42.92	41.84	40.52	42.57	43.28	42.63	42.90	44.14
SiO_2	39.16	38.91	38.84	38.84	39.14	39.23	39.27	39.23
CaO	0.27	0.26	0.29	0.28	0.27	0.27	0.32	0.31
MnO	0.17	0.25	0.24	0.20	0.23	0.21	0.18	0.15
Fe_2O_3	17.42	18.62	20.47	17.71	16.84	17.53	16.89	15.39
CoO	0.23	0.14	0.09	0.16	0.12	0.04	0.03	0.19
NiO	0.32	0.25	0.12	0.25	0.25	0.25	0.25	0.34
Total	100.49	100.27	100.57	100.01	100.13	100.16	99.84	99.75
Fo content	81.45	80.02	77.92	81.08	82.08	81.25	81.91	83.64

	BHI17 Ph17	BHI18 Ph1	BHI18 Ph2	BHI18 Ph3	BHI18 Ph4	BHI18 Ph5	BHI18 Ph6	BHI18 Ph7
MgO	38.48	44.39	44.66	44.77	44.79	42.58	42.89	44.14
SiO_2	37.92	39.47	39.24	39.74	39.67	39.02	39.28	39.49
CaO	0.35	0.28	0.27	0.26	0.27	0.32	0.28	0.29
MnO	0.29	0.19	0.20	0.17	0.24	0.22	0.23	0.17
Fe_2O_3	22.11	15.56	15.32	15.64	15.45	17.89	17.50	16.00
CoO	0.21	0.27	0.09	0.11	0.12	0.07	0.06	0.21
NiO	0.10	0.26	0.28	0.29	0.33	0.27	0.23	0.26
Total	99.46	100.42	100.06	100.98	100.87	100.37	100.47	100.56
Fo content	75.62	83.57	83.86	83.61	83.79	80.92	81.37	83.10

Appendix 3, results of SEM-EDS analysis of the cores of olivine phenocrysts.
(b-d below detection)

	BHI18 Ph8	BHI18 Ph9	BHI18 Ph10	BHI18 Ph11	BHI18 Ph12	BHI18 Ph13	BHI18 Ph14	BHI18 Ph15
MgO	42.92	43.76	42.47	44.29	44.12	44.17	43.41	40.17
SiO_2	39.10	39.19	39.04	39.41	39.15	39.18	39.15	38.33
CaO	0.31	0.30	0.28	0.30	0.30	0.27	0.28	0.29
MnO	0.22	0.19	0.21	0.20	0.19	0.24	0.17	0.26
Fe_2O_3	17.55	16.06	17.59	15.46	15.63	15.55	16.20	20.31
CoO	0.14	0.16	0.11	0.09	0.15	0.14	0.12	0.16
NiO	0.28	0.31	0.30	0.30	0.26	0.29	0.24	0.21
Total	100.52	99.97	100.00	100.05	99.80	99.84	99.57	99.73
Fo content	81.34	82.93	81.14	83.62	83.42	83.51	82.69	77.90

	BHI18 Ph16	BHI18 Ph17	BHI18 Ph18	BHI18 Ph19	BHI18 Ph20	BHI18 Ph21	AM10c Ph1	AM10c Ph2
MgO	43.20	41.91	43.85	41.76	43.83	43.55	42.67	38.79
SiO_2	39.22	39.03	39.18	38.68	39.00	39.21	38.29	37.74
CaO	0.28	0.34	0.31	0.25	0.30	0.27	0.27	0.28
MnO	0.22	0.24	0.18	0.23	0.20	0.21	0.23	0.31
Fe_2O_3	17.07	18.54	16.04	18.37	15.25	16.20	17.09	21.22
CoO	0.18	0.19	0.17	0.11	0.14	0.19	0.15	0.19
NiO	0.26	0.22	0.28	0.23	0.26	0.35	0.30	0.26
Total	100.43	100.47	100.01	99.63	98.98	99.98	99.00	98.79
Fo content	81.85	80.12	82.97	80.21	83.67	82.73	81.65	76.52

	AM10c Ph3	AM10c Ph4	AM10c Ph5	AM10c Ph6	AM10c Ph7	AM10c Ph8	AM10c Ph9	AM10c Ph10
MgO	41.09	43.38	43.37	44.52	42.00	43.59	43.92	41.14
SiO_2	38.16	39.16	39.20	39.46	38.82	39.06	38.79	38.25
CaO	0.27	0.32	0.25	0.30	0.25	0.28	0.30	0.27
MnO	0.30	0.24	0.22	0.26	0.29	0.20	0.22	0.32
Fe_2O_3	18.12	17.22	16.98	15.44	18.12	15.88	15.25	18.36
CoO	0.21	0.13	0.08	0.09	0.15	0.15	0.18	0.21
NiO	0.13	0.24	0.13	0.27	0.21	0.18	0.26	0.18
Total	98.28	100.69	100.23	100.34	99.84	99.34	98.92	98.73
Fo content	80.17	81.79	81.99	83.71	80.51	83.03	83.70	79.98

	AM10c Ph11	AM10c Ph12	AM10c Ph13	AM10c Ph14	AM10b Ph1	AM10b Ph2	AM10b Ph3	AM10b Ph4
MgO	40.60	44.57	39.35	42.36	44.16	43.65	44.41	40.43
SiO_2	38.01	39.56	38.33	38.76	38.89	39.00	39.36	38.52
CaO	0.28	0.25	0.27	0.26	0.30	0.33	0.26	0.29
MnO	0.27	0.21	0.28	0.26	0.20	0.20	0.18	0.28
Fe_2O_3	19.17	15.41	21.58	17.84	14.61	15.98	15.15	19.86
CoO	0.23	0.09	0.21	0.09	0.12	0.16	0.13	0.23
NiO	0.17	0.28	0.23	0.28	0.35	0.32	0.21	0.17
Total	98.73	100.37	100.25	99.85	98.63	99.64	99.70	99.78
Fo content	79.06	83.75	76.47	80.89	84.34	82.96	83.94	78.40

	AM10b Ph5	AM10b Ph6	AM10b Ph7	AM10b Ph8	AM10b Ph9	AM10b Ph10	AM10b Ph11	AM10b Ph12
MgO	44.93	42.98	43.12	43.10	42.99	43.39	43.82	44.60
SiO_2	39.30	38.71	38.96	38.72	38.84	38.65	38.93	38.95
CaO	0.27	0.29	0.27	0.27	0.28	0.30	0.26	0.19
MnO	0.17	0.23	0.26	0.24	0.21	0.23	0.24	0.16
Fe_2O_3	14.87	15.98	16.19	15.57	16.10	15.55	14.80	14.34
CoO	0.14	0.07	0.09	0.14	0.18	0.03	0.09	0.16
NiO	0.31	0.26	0.22	0.23	0.26	0.28	0.29	0.17
Total	99.99	98.52	99.11	98.27	98.86	98.43	98.43	98.57
Fo content	84.34	82.74	82.60	83.15	82.64	83.26	84.07	84.72

Appendix 3, results of SEM-EDS analysis of the cores of olivine phenocrysts.
(b-d below detection)

	AM10b Ph13	BHI2 Ph1	BHI2 Ph2	BHI2 Ph3	BHI2 Ph4	BHI2 Ph5	BHI2 Ph6	BHI2 Ph7
MgO	44.09	41.79	40.59	42.17	42.74	42.54	39.36	41.30
SiO_2	38.97	38.93	38.73	39.01	39.43	39.26	38.42	38.83
CaO	0.28	0.35	0.27	0.27	0.28	0.31	0.28	0.29
MnO	0.21	0.22	0.29	0.24	0.21	0.25	0.33	0.30
Fe_2O_3	14.76	18.98	20.18	18.73	18.32	18.23	22.31	19.67
CoO	0.09	0.14	0.17	0.05	0.11	0.20	0.08	0.20
NiO	0.25	0.15	0.19	0.16	0.17	0.20	0.15	0.13
Total	98.65	100.56	100.42	100.63	101.26	100.99	100.93	100.72
Fo content	84.19	79.69	78.19	80.05	80.61	80.62	75.87	78.91

	BHI2 Ph8	BHI2 Ph9	BHI2 Ph10	BHI2 Ph11	BHI2 Ph12	BHI20 Ph1	BHI20 Ph2	BHI20 Ph3
MgO	38.85	42.66	41.32	41.88	41.74	44.71	43.12	42.21
SiO_2	38.18	38.84	38.31	39.22	38.61	39.33	38.78	38.50
CaO	0.31	0.30	0.27	0.36	0.25	0.28	0.32	0.34
MnO	0.31	0.24	0.21	0.25	0.30	0.18	0.25	0.22
Fe_2O_3	22.25	17.29	18.70	19.00	18.76	14.19	16.18	16.42
CoO	0.26	0.14	0.13	0.12	0.23	0.10	0.07	0.14
NiO	0.07	0.11	0.19	0.16	0.21	0.33	0.24	0.20
Total	100.23	99.58	99.13	100.99	100.10	99.12	98.96	98.03
Fo content	75.68	81.47	79.75	79.71	79.86	84.89	82.61	82.09

	BHI20 Ph4	BHI20 Ph5	BHI20 Ph6	BHI20 Ph7	BHI20 Ph8	BHI20 Ph9	BHI20 Ph10	BHI20 Ph11
MgO	43.40	44.86	44.44	44.35	47.70	45.97	45.09	45.60
SiO_2	38.93	39.50	39.40	39.29	40.63	40.17	40.19	39.88
CaO	0.37	0.32	0.32	0.31	0.29	0.29	0.29	0.30
MnO	0.26	0.16	0.26	0.18	0.19	0.24	0.24	0.17
Fe_2O_3	16.75	14.46	15.70	14.71	12.13	14.72	15.80	15.00
CoO	0.15	0.15	0.20	0.13	0.15	0.16	0.08	0.22
NiO	0.23	0.25	0.26	0.35	0.43	0.31	0.25	0.16
Total	100.09	99.70	100.58	99.32	101.52	101.86	101.94	101.33
Fo content	82.20	84.69	83.46	84.31	87.51	84.77	83.57	84.42

	BHI27 Ph1	BHI27 Ph2	BHI27 Ph3	BHI27 Ph4	BHI27 Ph5	BHI27 Ph6	BHI27 Ph7	BHI27 Ph8
MgO	43.17	43.70	42.57	42.05	42.75	43.74	43.64	44.14
SiO_2	38.81	39.20	38.92	38.26	38.13	39.03	39.18	39.18
CaO	0.30	0.28	0.31	0.37	0.31	0.33	0.33	0.31
MnO	0.28	0.29	0.24	0.29	0.30	0.24	0.24	0.28
Fe_2O_3	16.40	16.24	17.10	17.60	16.94	15.89	16.37	15.44
CoO	0.19	0.12	0.19	0.24	0.11	0.12	0.15	0.16
NiO	0.22	0.10	0.18	0.18	0.19	0.17	0.15	0.10
Total	99.37	99.93	99.51	98.99	98.73	99.52	100.06	99.61
Fo content	82.43	82.75	81.61	80.98	81.81	83.07	82.61	83.59

	BHI26 Ph1	BHI26 Ph2	BHI26 Ph3	BHI26 Ph4	BHI26 Ph5	BHI26 Ph6	BHI26 Ph7	BHI26 Ph8
MgO	43.71	43.82	44.30	44.76	44.10	44.68	44.29	44.34
SiO_2	38.82	38.73	39.33	39.49	39.44	39.33	39.56	39.28
CaO	0.33	0.32	0.33	0.28	0.33	0.30	0.35	0.32
MnO	0.25	0.23	0.26	0.20	0.28	0.26	0.20	0.22
Fe_2O_3	15.67	15.38	15.89	15.18	16.01	15.40	15.96	15.35
CoO	0.03	0.05	0.18	0.15	0.13	0.09	0.20	0.18
NiO	0.22	0.19	0.14	0.18	0.12	0.22	0.17	0.23
Total	99.03	98.72	100.43	100.24	100.41	100.28	100.73	99.92
Fo content	83.26	83.55	83.25	84.01	83.08	83.80	83.18	83.74

Appendix 3, results of SEM-EDS analysis of the cores of olivine phenocrysts. (b-d below detection)

	BHI26 Ph9	BHI26 Ph10	MR9 Ph1	MR9 Ph2	MR9 Ph3	MR9 Ph4	MR9 Ph5	MR9 Ph6
MgO	44.44	44.44	40.44	40.73	40.54	39.36	40.86	40.07
SiO_2	39.72	39.24	38.02	38.01	38.31	37.65	38.28	37.76
CaO	0.32	0.30	0.34	0.33	0.24	0.28	0.42	0.35
MnO	0.23	0.19	b-d	b-d	b-d	b-d	b-d	0.31
Fe_2O_3	15.59	15.47	21.65	20.18	20.91	21.67	20.41	21.58
CoO	0.12	0.10	b-d	b-d	b-d	b-d	b-d	b-d
NiO	0.09	0.20	b-d	b-d	b-d	b-d	b-d	b-d
Total	100.51	99.94	100.45	99.25	100.00	98.97	99.97	100.07
Fo content	83.56	83.66	76.90	78.25	77.56	76.40	78.11	76.80

	MR9 Ph7	MR9 Ph8	MR9 Ph9	MR10 Ph1	MR10 Ph2	MR10 Ph3	MR10 Ph4	MR10 Ph5
MgO	39.96	39.89	40.29	46.98	44.53	43.35	46.09	43.15
SiO_2	38.08	37.50	38.31	39.45	38.66	38.67	39.31	39.03
CaO	0.41	0.35	0.34	0.32	0.36	0.36	0.28	0.30
MnO	b-d	b-d	b-d	b-d	0.32	0.39	b-d	b-d
Fe_2O_3	20.67	21.33	20.87	12.31	16.29	17.61	13.83	16.84
CoO	b-d	b-d	b-d	b-d	b-d	b-d	b-d	b-d
NiO	b-d	b-d	b-d	0.51	b-d	b-d	b-d	b-d
Total	99.12	99.08	99.81	99.57	100.18	100.38	99.51	99.33
Fo content	77.51	76.92	77.48	87.18	82.97	81.44	85.59	82.04

	MR10 Ph6	MR10 Ph7	MR10 Ph8	MR10 Ph9	MR10 Ph10	MR10 Ph11	MR10 Ph12	MR10 Ph13
MgO	45.16	46.68	46.40	44.67	45.92	47.07	45.80	44.45
SiO_2	38.84	39.39	39.33	39.51	38.59	39.25	39.54	38.86
CaO	0.30	0.39	0.31	0.21	0.30	0.35	0.26	0.34
MnO	0.37	b-d	b-d	b-d	b-d	b-d	b-d	b-d
Fe_2O_3	15.10	14.04	14.15	15.55	14.80	13.08	15.26	15.29
CoO	b-d	b-d	b-d	b-d	b-d	b-d	b-d	b-d
NiO	b-d	b-d	b-d	b-d	0.46	0.49	b-d	b-d
Total	99.77	100.50	100.19	99.95	100.07	100.24	100.85	98.94
Fo content	84.20	85.56	85.39	83.66	84.69	86.51	84.25	83.82

	MR10 Ph14	MR12 Ph1	MR12 Ph2	MR12 Ph3	MR12 Ph4	MR12 Ph5	MR12 Ph6	MR12 Ph7
MgO	45.61	45.51	44.76	44.28	43.78	47.58	46.52	46.79
SiO_2	38.66	39.09	39.38	39.12	38.48	39.65	39.45	39.17
CaO	0.31	0.29	0.30	0.37	0.29	0.23	0.28	0.30
MnO	b-d	0.34	b-d	0.41	b-d	b-d	b-d	b-d
Fe_2O_3	14.04	15.04	16.25	16.42	18.19	13.14	13.46	13.52
CoO	b-d	b-d	b-d	b-d	b-d	b-d	b-d	b-d
NiO	b-d	b-d	b-d	b-d	b-d	b-d	b-d	b-d
Total	98.61	100.27	100.70	100.60	100.74	100.59	99.70	99.77
Fo content	85.27	84.36	83.08	82.78	81.10	86.58	86.03	86.05

	MR12 Ph8	MR12 Ph9	MR12 Ph10	MR12 Ph11	MR12a Ph1	MR12a Ph2	MR12a Ph3	MR12a Ph4
MgO	46.09	46.53	47.10	46.63	41.56	43.12	39.41	39.41
SiO_2	39.42	39.49	39.95	40.11	38.29	38.89	37.74	37.74
CaO	0.21	0.28	0.26	0.30	0.26	0.48	0.34	0.34
MnO	b-d	b-d	b-d	b-d	b-d	b-d	0.44	0.44
Fe_2O_3	14.38	12.97	13.29	13.37	19.24	17.57	22.50	22.50
CoO	b-d	b-d	b-d	b-d	b-d	b-d	b-d	b-d
NiO	b-d	b-d	b-d	b-d	b-d	b-d	b-d	b-d
Total	100.10	99.27	100.59	100.42	99.35	100.06	100.42	100.42
Fo content	85.10	86.48	86.33	86.14	79.38	81.39	75.74	75.74

Appendix 3, results of SEM-EDS analysis of the cores of olivine phenocrysts. (b-d below detection)

	MR12a Ph5	MR12a Ph6	MR12a Ph7	MR12a Ph8	MR12a Ph9	MR12a Ph10	MR12a Ph11	MR12a Ph12
MgO	38.72	38.91	34.58	32.01	36.27	36.38	40.09	44.63
SiO_2	38.14	37.65	36.97	35.89	37.24	37.47	38.54	39.18
CaO	0.58	0.46	0.46	0.60	0.54	0.41	0.33	0.18
MnO	b-d	0.31	0.51	0.47	b-d	b-d	b-d	b-d
Fe_2O_3	23.17	23.21	28.13	31.24	26.29	25.34	22.16	15.64
CoO	b-d	b-d	b-d	b-d	b-d	b-d	b-d	b-d
NiO	b-d	b-d	b-d	b-d	b-d	b-d	b-d	b-d
Total	100.60	100.54	100.64	100.20	100.33	99.59	101.12	99.62
Fo content	74.87	74.93	68.66	64.62	71.09	71.90	76.33	83.57

	MR12a Ph13	BR1 Ph1	BR1 Ph2	BR1 Ph3	BR1 Ph4	BR1 Ph5	BR1 Ph6	BR1 Ph7
MgO	44.47	33.99	44.52	41.63	43.17	35.05	45.59	44.09
SiO_2	38.89	35.97	38.16	36.68	36.69	37.12	39.54	38.56
CaO	0.41	0.21	0.30	0.37	0.23	0.26	0.24	0.31
MnO	b-d	0.42	b-d	0.22	0.21	0.26	0.21	0.23
Fe_2O_3	16.32	29.21	14.89	16.91	14.10	29.54	14.95	17.75
CoO	b-d	b-d	b-d	b-d	b-d	b-d	b-d	b-d
NiO	b-d	b-d	b-d	b-d	0.40	b-d	b-d	b-d
Total	100.08	99.79	97.87	95.80	94.80	102.23	100.51	100.95
Fo content	82.93	67.47	84.20	81.44	84.51	67.90	84.46	81.58

	BR1 Ph8	BR1 Ph9	BR1 Ph10	BR1 Ph11	BR1 Ph12	BR2 Ph1	BR2 Ph2	BR2 Ph3
MgO	45.58	35.56	45.47	45.04	34.48	42.64	38.73	46.42
SiO_2	39.18	36.88	39.33	39.15	36.95	38.56	37.58	39.41
CaO	0.26	0.22	0.26	0.39	0.24	0.30	0.34	0.28
MnO	0.20	0.29	0.20	0.18	0.39	0.29	0.31	0.28
Fe_2O_3	14.90	29.31	15.98	15.99	30.75	17.85	23.60	13.39
CoO	b-d	b-d	b-d	b-d	b-d	b-d	b-d	b-d
NiO	0.43	b-d	b-d	b-d	b-d	b-d	b-d	0.36
Total	100.13	102.27	101.24	100.76	102.81	99.56	100.56	100.00
Fo content	84.50	68.38	83.53	83.39	66.65	80.99	74.52	86.08

	BR2 Ph4	BR2 Ph5	BR2 Ph6	BR2 Ph7	BR2 Ph8	BR2 Ph9	BR2 Ph10	BR2 Ph11
MgO	39.50	39.57	41.39	45.23	48.32	46.05	45.83	44.52
SiO_2	38.02	38.01	38.41	39.73	40.15	39.81	39.58	39.25
CaO	0.30	0.34	0.31	0.25	0.24	0.32	0.30	0.28
MnO	0.35	0.34	0.18	0.29	0.16	0.09	0.18	0.25
Fe_2O_3	23.10	23.32	21.04	16.30	11.66	15.14	15.39	17.49
CoO	b-d	b-d	b-d	b-d	b-d	b-d	b-d	b-d
NiO	b-d	b-d	b-d	0.36	0.43	0.50	0.35	0.39
Total	101.27	101.40	101.34	102.15	100.97	101.91	101.63	102.18
Fo content	75.30	75.15	77.81	83.18	88.08	84.43	84.15	81.94

	BR2 Ph12	BR2 Ph13	BR2 Ph14	BR2 Ph15	BR2 Ph16	BR2 Ph17	BR2 Ph18	BR2 Ph19
MgO	32.51	46.17	41.98	35.83	35.83	44.20	40.87	42.19
SiO_2	36.15	39.16	38.06	36.88	36.88	38.23	37.55	40.48
CaO	0.34	0.31	0.35	0.34	0.34	0.33	0.34	0.38
MnO	0.44	0.19	0.29	0.42	0.42	0.21	0.31	b-d
Fe_2O_3	31.36	14.34	18.34	26.16	26.16	15.79	19.79	22.75
CoO	b-d	b-d	b-d	b-d	b-d	0.13	b-d	b-d
NiO	b-d	b-d	b-d	b-d	b-d	0.28	b-d	b-d
Total	100.80	100.18	99.03	99.62	99.62	99.16	98.86	105.80
Fo content	64.89	85.16	80.31	70.94	70.94	83.30	78.64	41.55

Appendix 3, results of SEM-EDS analysis of the cores of olivine phenocrysts. (b-d below detection)

	BR2 Ph20	BR2 Ph21	BR2 Ph22	BR2 Ph23	BR2 Ph24	BR6 Ph1	BR6 Ph2	BR6 Ph3
MgO	45.01	45.21	45.39	41.12	40.70	28.04	27.68	24.91
SiO_2	40.56	39.59	39.62	38.41	37.93	34.87	34.88	34.37
CaO	0.34	0.40	0.33	0.28	0.30	0.33	0.36	0.49
MnO	0.31	0.26	0.26	0.22	b-d	0.50	0.41	0.62
Fe_2O_3	20.32	15.32	16.09	21.58	21.24	37.76	39.42	41.64
CoO	b-d	b-d	b-d	b-d	b-d	b-d	b-d	b-d
NiO	b-d	b-d	0.36	b-d	b-d	b-d	b-d	b-d
Total	106.54	100.77	102.05	101.62	100.17	101.51	102.74	102.04
Fo content	79.79	84.03	83.41	77.25	77.35	56.96	55.59	51.60

	BR6 Ph4	BR6 Ph5	BR6 Ph6	BR6 Ph7	BR6 Ph8	BR12 Ph1	BR12 Ph2	BR12 Ph3
MgO	25.51	26.55	23.11	26.95	25.02	39.87	40.68	39.36
SiO_2	34.94	34.55	33.84	34.90	34.26	38.07	38.25	37.73
CaO	0.45	0.43	0.52	0.37	0.48	0.40	0.33	0.29
MnO	0.63	0.52	0.53	0.44	0.68	0.44	0.39	0.00
Fe_2O_3	40.62	39.40	43.80	39.32	41.84	22.28	21.72	21.29
CoO	b-d	b-d	b-d	b-d	b-d	b-d	b-d	b-d
NiO	b-d	b-d	b-d	b-d	b-d	b-d	0.39	b-d
Total	102.15	101.46	101.80	101.99	102.28	101.05	101.76	98.67
Fo content	52.82	54.57	48.47	54.99	51.59	76.13	76.95	76.72

	BR12 Ph4	BR12 Ph5	BR12 Ph6	BR12 Ph7	BR12 Ph8	BR12 Ph9	BR12 Ph10	BR12 Ph11
MgO	43.11	44.71	40.87	45.65	46.59	46.76	41.49	45.90
SiO_2	38.91	38.74	37.87	39.12	39.29	39.57	38.35	39.03
CaO	0.28	0.29	0.35	0.28	0.31	0.29	0.24	0.30
MnO	0.22	0.19	0.42	0.24	0.18	0.22	0.24	0.17
Fe_2O_3	18.45	15.86	20.86	14.39	13.79	13.32	20.18	14.56
CoO	b-d	b-d	b-d	b-d	b-d	b-d	b-d	b-d
NiO	0.34	0.55	b-d	0.38	b-d	0.39	b-d	0.33
Total	101.31	100.33	100.37	100.05	100.15	100.57	100.49	100.29
Fo content	80.64	83.40	77.74	84.97	85.76	86.22	78.56	84.89

	BR12 Ph12	BR12 Ph13	BR12 Ph14	BR12 Ph15	BR12 Ph16	BR12 Ph17	BR12 Ph18	BR12 Ph19
MgO	40.66	39.10	36.42	42.43	47.17	46.87	46.61	46.61
SiO_2	37.72	37.77	36.78	38.39	39.34	39.10	39.26	39.90
CaO	0.30	0.33	0.31	0.21	0.32	0.27	0.26	0.33
MnO	0.31	0.29	0.52	0.22	0.21	0.19	0.18	0.14
Fe_2O_3	21.25	23.35	25.86	18.44	12.67	13.10	12.86	13.09
CoO	b-d	b-d	b-d	b-d	b-d	b-d	b-d	b-d
NiO	b-d	b-d	b-d	b-d	0.42	0.45	b-d	b-d
Total	100.24	100.83	99.89	99.69	100.12	99.99	99.16	100.07
Fo content	77.33	74.90	71.51	80.40	86.90	86.44	86.60	86.39

	BR12 Ph20	BR12 Ph21	BR12 Ph22	BR13 Ph1	BR13 Ph2	BR13 Ph3	BR13 Ph4	BR13 Ph5
MgO	46.40	46.39	46.66	43.21	43.52	43.52	42.95	43.03
SiO_2	39.31	39.25	38.90	37.51	37.68	37.68	37.21	37.16
CaO	0.35	0.23	0.30	0.28	0.24	0.24	0.35	0.28
MnO	0.16	0.16	0.21	0.19	0.20	0.20	b-d	b-d
Fe_2O_3	12.85	13.17	12.11	11.69	11.89	11.89	12.09	10.77
CoO	b-d	b-d	b-d	b-d	b-d	b-d	b-d	b-d
NiO	b-d	0.38	0.36	b-d	b-d	b-d	b-d	b-d
Total	99.06	99.58	98.54	92.88	93.53	93.53	92.58	91.24
Fo content	86.55	86.26	87.29	86.82	86.71	86.71	86.36	87.69

Appendix 3, results of SEM-EDS analysis of the cores of olivine phenocrysts. (b-d below detection)

	BR16 Ph1	BR16 Ph2	BR16 Ph3	BR16 Ph4	BR16 Ph5	BR16 Ph6	BR16 Ph7	BR16 Ph8
MgO	42.31	41.22	41.89	39.63	39.84	42.44	42.33	39.95
SiO_2	37.94	37.59	37.64	37.29	37.30	37.56	37.83	37.28
CaO	0.33	0.31	0.28	0.35	0.19	0.30	0.26	0.30
MnO	0.31	0.10	0.26	0.23	0.34	0.26	0.26	0.20
Fe_2O_3	18.45	19.71	18.30	21.02	21.16	17.77	18.25	20.14
CoO	b-d	b-d	b-d	b-d	b-d	b-d	b-d	b-d
NiO	b-d	b-d	0.38	b-d	b-d	b-d	b-d	b-d
Total	99.35	98.93	98.75	98.52	98.82	98.33	98.94	97.88
Fo content	80.34	78.85	80.32	77.07	77.04	80.98	80.52	77.95

	BR16 Ph9	BR16a Ph1	BR16a Ph2	BR16a Ph3	BR16a Ph4	BR16a Ph5	BR16a Ph6	BR16a Ph7
MgO	33.50	41.55	41.37	42.00	41.80	41.96	41.92	41.14
SiO_2	35.92	37.66	38.06	37.59	37.95	37.72	37.84	37.53
CaO	0.34	0.24	0.19	0.19	0.30	0.21	0.32	0.22
MnO	0.37	0.24	0.19	0.15	0.27	0.19	0.34	0.28
Fe_2O_3	29.14	18.47	19.90	18.29	18.74	17.62	18.08	19.29
CoO	b-d	b-d	b-d	b-d	b-d	b-d	b-d	b-d
NiO	b-d	b-d	b-d	b-d	b-d	b-d	b-d	b-d
Total	99.26	98.14	99.71	98.22	99.06	97.70	98.50	98.47
Fo content	67.20	80.04	78.75	80.37	79.90	80.93	80.52	79.17

	BR16a Ph8	BR16a Ph9	BR16a Ph10	BR16a Ph11	BR16a Ph12	BR16a Ph13	BR16a Ph14	BR16a Ph15
MgO	42.10	41.88	42.02	41.29	39.78	40.11	41.84	41.47
SiO_2	38.39	38.06	38.00	37.77	37.94	37.19	37.92	37.68
CaO	0.32	0.27	0.26	0.28	0.30	0.33	0.32	0.25
MnO	0.14	0.17	0.35	0.21	0.21	0.21	0.14	0.29
Fe_2O_3	18.73	18.44	18.38	18.77	20.46	20.73	18.55	18.19
CoO	b-d	b-d	b-d	b-d	b-d	b-d	b-d	b-d
NiO	b-d	b-d	b-d	b-d	b-d	b-d	b-d	b-d
Total	99.68	98.82	99.02	98.32	98.70	98.56	98.78	97.89
Fo content	80.03	80.19	80.30	79.68	77.61	77.52	80.08	80.25

	BR17 Ph1	BR17 Ph2	BR17 Ph3	BR17 Ph4	BR17 Ph5	BR17 Ph6	BR17 Ph7	BR17 Ph8
MgO	33.78	35.32	30.93	23.45	33.30	29.22	32.95	24.29
SiO_2	35.96	36.31	34.98	33.53	36.02	35.26	35.58	33.39
CaO	0.35	0.39	0.37	0.44	0.41	0.46	0.40	0.43
MnO	0.39	0.39	0.47	0.68	0.35	0.48	0.38	0.67
Fe_2O_3	30.08	27.33	33.20	43.15	29.33	35.44	30.59	41.36
CoO	b-d	b-d	b-d	b-d	b-d	b-d	b-d	b-d
NiO	b-d	b-d	b-d	b-d	b-d	b-d	b-d	b-d
Total	100.55	99.73	99.95	101.25	99.41	100.86	99.90	100.14
Fo content	66.69	69.73	62.41	49.20	66.93	59.51	65.75	51.14

	BR17 Ph9	BR17 Ph10
MgO	34.49	31.63
SiO_2	35.87	35.33
CaO	0.35	0.47
MnO	0.33	0.44
Fe_2O_3	28.88	31.69
CoO	b-d	b-d
NiO	b-d	b-d
Total	99.92	99.56
Fo content	68.04	64.02

Appendix 3, results of SEM-EDS analysis of the cores of olivine phenocrysts. (b-d below detection)

Appendix 4
LA-ICP-MS data for olivine phenocrysts from the MPG lavas

From methods of analysis, see Chapter 4 and Chapter 5

		Am10b Ph12 In1 Olivine	Am10b Ph12 In2 Olivine	Am10b Ph11 In2 Olivine	Am10b PH11 In1 Olivine	Am10b Ph10 In1 Olivine	Am10b Ph8 In1 Olivine	Am10b Ph7 In1 Olivine	Am10b Ph7 In2 Olivine
Na_2O	%	0.02	0.01	b-d	b-d	0.01	0.04	b-d	b-d
MgO	%	45.84	42.96	40.47	40.58	42.29	43.79	43.82	44.56
Al_2O_3	%	0.05	0.04	0.01	b-d	0.05	0.07	0.05	0.06
SiO_2	%	37.07	39.18	38.75	38.70	39.67	40.79	39.71	39.87
P_2O_5	%	0.05	0.04	0.04	0.03	0.08	0.09	0.02	0.02
K_2O	%	b-d	b-d	b-d	b-d	b-d	b-d	b-d	b-d
CaO	%	0.22	0.20	0.16	0.13	0.31	0.21	0.28	0.28
TiO_2	%	0.01	0.01	0.01	0.01	0.01	0.01	0.01	0.01
MnO	%	0.21	0.19	0.29	0.29	0.30	0.28	0.22	0.25
Fe_2O_3	%	16.55	17.37	20.27	20.27	17.28	14.72	15.89	14.94
Forsterite	%	83.16	81.51	78.07	78.11	81.35	84.13	83.10	84.17
Cr	ppm	149.44	132.68	70.21	57.07	148.95	199.90	207.87	207.66
Co	ppm	185.88	161.70	196.66	200.96	216.66	209.25	195.33	199.25
Ni	ppm	1435.41	1482.89	1365.89	1373.78	1671.81	1968.89	2116.30	2297.75
Cu	ppm	1.05	3.74	b-d	b-d	b-d	b-d	1.87	4.09
Zn	ppm	121.70	81.32	160.75	165.67	140.31	138.98	115.06	135.20
Rb	ppm	b-d	b-d	b-d	b-d	b-d	0.01	b-d	0.10
Sr	ppm	0.03	0.13	0.05	0.00	b-d	b-d	0.14	0.18
Y	ppm	0.12	0.14	0.42	0.50	0.21	0.08	0.14	0.21
Zr	ppm	0.11	0.19	b-d	b-d	0.39	0.93	b-d	0.06
Nb	ppm	0.04	0.02	b-d	b-d	b-d	b-d	0.04	b-d
Cs	ppm	0.20	0.20	b-d	b-d	0.43	b-d	0.07	0.37
Ba	ppm	b-d	0.02	b-d	b-d	b-d	b-d	b-d	0.01
La	ppm	0.01	0.02	b-d	0.01	0.01	0.01	0.04	0.04
Ce	ppm	b-d	b-d	b-d	b-d	b-d	b-d	b-d	b-d
Nd	ppm	0.06	0.06	b-d	b-d	b-d	b-d	b-d	b-d

		Am10b Ph12 In1 Olivine	Am10b Ph12 In2 Olivine	Am10b Ph11 In2 Olivine	Am10b PH11 In1 Olivine	Am10b Ph10 In1 Olivine	Am10b Ph8 In1 Olivine	Am10b Ph7 In1 Olivine	Am10b Ph7 In2 Olivine
Na_2O	%	0.02	0.01	b-d	b-d	0.01	0.04	b-d	b-d
MgO	%	45.84	42.96	40.47	40.58	42.29	43.79	43.82	44.56
Al_2O_3	%	0.05	0.04	0.01	b-d	0.05	0.07	0.05	0.06
SiO_2	%	37.07	39.18	38.75	38.70	39.67	40.79	39.71	39.87
P_2O_5	%	0.05	0.04	0.04	0.03	0.08	0.09	0.02	0.02
K_2O	%	b-d	b-d	b-d	b-d	b-d	b-d	b-d	b-d
CaO	%	0.22	0.20	0.16	0.13	0.31	0.21	0.28	0.28
TiO_2	%	0.01	0.01	0.01	0.01	0.01	0.01	0.01	0.01
MnO	%	0.21	0.19	0.29	0.29	0.30	0.28	0.22	0.25
Fe_2O_3	%	16.55	17.37	20.27	20.27	17.28	14.72	15.89	14.94
Forsterite	%	83.16	81.51	78.07	78.11	81.35	84.13	83.10	84.17
Cr	ppm	149.44	132.68	70.21	57.07	148.95	199.90	207.87	207.66
Co	ppm	185.88	161.70	196.66	200.96	216.66	209.25	195.33	199.25
Ni	ppm	1435.41	1482.89	1365.89	1373.78	1671.81	1968.89	2116.30	2297.75
Cu	ppm	1.05	3.74	b-d	b-d	b-d	b-d	1.87	4.09
Zn	ppm	121.70	81.32	160.75	165.67	140.31	138.98	115.06	135.20
Rb	ppm	b-d	b-d	b-d	b-d	b-d	0.01	b-d	0.10
Sr	ppm	0.03	0.13	0.05	0.00	b-d	b-d	0.14	0.18
Y	ppm	0.12	0.14	0.42	0.50	0.21	0.08	0.14	0.21
Zr	ppm	0.11	0.19	b-d	b-d	0.39	0.93	b-d	0.06
Nb	ppm	0.04	0.02	b-d	b-d	b-d	b-d	0.04	b-d
Cs	ppm	0.20	0.20	b-d	b-d	0.43	b-d	0.07	0.37
Ba	ppm	b-d	0.02	b-d	b-d	b-d	b-d	b-d	0.01
La	ppm	0.01	0.02	b-d	0.01	0.01	0.01	0.04	0.04
Ce	ppm	b-d	b-d	b-d	b-d	b-d	b-d	b-d	b-d
Nd	ppm	0.06	0.06	b-d	b-d	b-d	b-d	b-d	b-d

Appendix 4, results of LA-ICP-MS analysis of the cores of olivine phenocrysts. (b-d below detection).

		AM10c Ph3 In1 Olivine	AM10c Ph4 In1 Olivine	AM10c Ph5 In1 Olivine	BHI2 Ph5 In1 Olivine	BHI2 Ph5 In2 Olivine	BHI2 Ph7 In1 Olivine	BHI2 Ph4 In1 Olivine	BHI3 Ph6 In1 Olivine
Na_2O	%	0.02	0.11	0.03	0.02	0.02	1.36	1.36	0.09
MgO	%	44.87	44.50	43.50	42.49	42.49	38.35	38.35	40.85
Al_2O_3	%	0.05	0.05	0.03	0.02	0.02	0.31	0.31	0.68
SiO_2	%	39.62	39.71	38.29	38.72	38.72	36.17	36.17	35.69
P_2O_5	%	0.03	0.04	0.03	0.01	0.01	0.14	0.14	b-d
K_2O	%	b-d	b-d	b-d	b-d	b-d	0.26	0.26	b-d
CaO	%	0.22	0.24	0.19	0.19	0.19	4.70	4.70	0.98
TiO_2	%	0.01	0.01	0.01	0.01	0.01	0.14	0.14	0.18
MnO	%	0.18	0.17	0.19	0.24	0.24	0.24	0.24	0.26
Fe_2O_3	%	14.99	15.17	17.72	18.29	18.29	18.32	18.32	21.28
Forsterite	%	84.21	83.95	81.40	80.55	80.55	78.87	78.87	77.38
Cr	ppm	200.83	175.10	105.30	87.81	87.81	1392.42	1392.42	68.06
Co	ppm	164.64	155.57	149.50	159.27	159.27	1832.97	1832.97	b-d
Ni	ppm	2009.50	1818.53	1200.40	1281.66	1281.66	1237.81	1237.81	b-d
Cu	ppm	0.62	1.61	b-d	1.17	1.17	37.22	37.22	38.68
Zn	ppm	77.87	88.82	100.28	105.86	105.86	92.15	92.15	31.94
Rb	ppm	b-d	b-d	b-d	b-d	b-d	1.37	1.37	0.87
Sr	ppm	0.10	0.35	0.05	b-d	b-d	0.31	0.31	17.21
Y	ppm	0.25	0.01	0.03	0.27	0.27	0.21	0.21	3.08
Zr	ppm	0.25	0.57	0.14	b-d	b-d	0.55	0.55	16.78
Nb	ppm	b-d	0.10	b-d	b-d	b-d	0.03	0.03	1.19
Cs	ppm	b-d	b-d	b-d	0.08	0.08	2.38	2.38	b-d
Ba	ppm	0.09	1.35	0.23	0.09	0.09	5.64	5.64	11.57
La	ppm	b-d	0.03	b-d	b-d	b-d	0.14	0.14	0.56
Ce	ppm	b-d	0.26	b-d	b-d	b-d	0.11	0.11	2.09
Nd	ppm	0.03	0.12	b-d	0.03	0.03	0.03	0.03	3.54

		BHI3 PH6 In2 Olivine	BHI3 Ph8a In1 Olivine	BHI3 Ph8b In1 Olivine	BHI3 Ph3 In3 Olivine	BHI3 Ph11 in2 Olivine	BHI3 Ph11 in 3 Olivine	BHI16 Ph3 in2 Olivine	BHI18 Ph7 In3 Olivine
Na_2O	%	1.14	0.11	0.04	0.00	0.01	0.01	b-d	0.05
MgO	%	39.82	39.88	42.03	40.71	41.70	41.70	29.31	41.04
Al_2O_3	%	0.38	0.50	0.04	0.04	0.04	0.04	0.09	0.20
SiO_2	%	36.72	35.81	34.95	34.67	35.48	35.48	60.37	36.21
P_2O_5	%	b-d	b-d	b-d	b-d	b-d	b-d	b-d	b-d
K_2O	%	b-d	b-d	b-d	b-d	0.02	0.02	b-d	b-d
CaO	%	0.70	0.71	0.25	0.26	0.25	0.25	0.50	0.30
TiO_2	%	0.04	0.12	0.02	0.02	0.02	0.02	0.01	0.01
MnO	%	0.24	0.27	0.27	0.31	0.26	0.26	0.14	0.28
Fe_2O_3	%	20.95	22.60	22.40	23.99	22.22	22.22	9.58	21.92
Forsterite	%	77.21	75.88	76.98	75.15	76.98	76.98	84.51	76.94
Cr	ppm	279.41	121.96	158.83	189.97	190.29	190.29	608.26	179.24
Co	ppm	b-d	b-d	b-d	b-d	215.34	215.34	b-d	b-d
Ni	ppm	4833.59	10907.63	2500.00	2698.05	1522.33	1522.33	1685.76	2240.42
Cu	ppm	42.49	52.81	b-d	4.67	6.85	6.85	b-d	5.85
Zn	ppm	122.60	111.06	111.99	144.16	136.98	136.98	139.64	175.85
Rb	ppm	0.60	0.63	0.23	0.07	0.05	0.05	b-d	0.11
Sr	ppm	1.07	9.56	b-d	0.43	0.04	0.04	b-d	1.74
Y	ppm	0.42	1.97	0.15	0.32	0.24	0.24	0.23	0.20
Zr	ppm	1.04	6.79	0.20	0.22	0.09	0.09	b-d	0.26
Nb	ppm	0.09	0.38	0.17	b-d	b-d	b-d	0.04	0.03
Cs	ppm	2.08	0.68	b-d	0.12	0.20	0.20	b-d	0.03
Ba	ppm	6.27	0.50	2.71	1.06	1.17	1.17	2.25	1.30
La	ppm	0.18	0.32	0.03	0.01	0.08	0.08	b-d	0.02
Ce	ppm	0.20	1.25	0.02	0.04	b-d	b-d	0.11	0.05
Nd	ppm	0.19	0.63	0.21	0.04	0.04	0.04	b-d	0.02

Appendix 4, results of LA-ICP-MS analysis of the cores of olivine phenocrysts. (b-d below detection).

		BHI18 PH7 In1 Olivine	BHI18 Ph7 In2 Olivine	BHI18 Ph1 In1 Olivine	BM2 Ph2 In1 Olivine	BM2 Ph2 In2 Olivine	BM2 Ph2 In3 Olivine	BM2 Ph3 In1 Olivine	BM2 PH3 In2 Olivine
Na_2O	%	0.05	0.05	0.05	0.03	0.03	0.03	0.13	0.13
MgO	%	41.04	41.04	41.04	41.23	41.23	41.23	41.39	41.39
Al_2O_3	%	0.20	0.20	0.20	0.06	0.06	0.06	0.10	0.10
SiO_2	%	36.21	36.21	36.21	40.15	40.15	40.15	42.18	42.18
P_2O_5	%	b-d	b-d	b-d	0.10	0.10	0.10	0.06	0.06
K_2O	%	b-d	b-d	b-d	0.00	0.00	0.00	0.01	0.01
CaO	%	0.30	0.30	0.30	0.37	0.37	0.37	0.31	0.31
TiO_2	%	0.01	0.01	0.01	0.02	0.02	0.02	0.02	0.02
MnO	%	0.28	0.28	0.28	0.25	0.25	0.25	0.22	0.22
Fe_2O_3	%	21.92	21.92	21.92	17.79	17.79	17.79	15.59	15.59
Forsterite	%	76.94	76.94	76.94	80.51	80.51	80.51	82.56	82.56
Cr	ppm	179.24	179.24	179.24	253.59	253.59	253.59	503.56	503.56
Co	ppm	b-d	b-d	b-d	210.73	210.73	210.73	209.60	209.60
Ni	ppm	2240.42	2240.42	2240.42	2053.92	2053.92	2053.92	2421.98	2421.98
Cu	ppm	5.85	5.85	5.85	3.59	3.59	3.59	10.12	10.12
Zn	ppm	175.85	175.85	175.85	140.15	140.15	140.15	113.90	113.90
Rb	ppm	0.11	0.11	0.11	0.45	0.45	0.45	0.81	0.81
Sr	ppm	1.74	1.74	1.74	0.12	0.12	0.12	0.99	0.99
Y	ppm	0.20	0.20	0.20	b-d	b-d	b-d	0.11	0.11
Zr	ppm	0.26	0.26	0.26	0.32	0.32	0.32	0.20	0.20
Nb	ppm	0.03	0.03	0.03	b-d	b-d	b-d	b-d	b-d
Cs	ppm	0.03	0.03	0.03	0.25	0.25	0.25	0.07	0.07
Ba	ppm	1.30	1.30	1.30	b-d	b-d	b-d	0.24	0.24
La	ppm	0.02	0.02	0.02	0.03	0.03	0.03	0.11	0.11
Ce	ppm	0.05	0.05	0.05	b-d	b-d	b-d	0.26	0.26
Nd	ppm	0.02	0.02	0.02	b-d	b-d	b-d	b-d	b-d

		BM2 Ph3 In3 Olivine	BM2 Ph3 In4 Olivine	BM2 Ph3 In5 Olivine	BM2 Ph5 In1 Olivine	BM2 Ph5 In2 Olivine	BM2 Ph12 In1 Olivine	BM2 Ph11 In1 Olivine	BM2 Ph10 In1 Olivine
Na_2O	%	0.13	0.13	0.13	0.07	0.07	0.08	b-d	b-d
MgO	%	41.39	41.39	41.39	39.16	39.16	39.86	38.80	38.61
Al_2O_3	%	0.10	0.10	0.10	0.05	0.05	0.01	0.06	0.05
SiO_2	%	42.18	42.18	42.18	39.44	39.44	40.05	41.66	39.89
P_2O_5	%	0.06	0.06	0.06	0.13	0.13	0.04	0.04	0.09
K_2O	%	0.01	0.01	0.01	0.00	0.00	b-d	b-d	b-d
CaO	%	0.31	0.31	0.31	0.34	0.34	0.85	0.57	0.88
TiO_2	%	0.02	0.02	0.02	0.01	0.01	b-d	b-d	0.04
MnO	%	0.22	0.22	0.22	0.30	0.30	0.26	0.29	0.30
Fe_2O_3	%	15.59	15.59	15.59	20.49	20.49	18.84	18.58	20.15
Forsterite	%	82.56	82.56	82.56	77.31	77.31	79.04	78.82	77.35
Cr	ppm	503.56	503.56	503.56	206.94	206.94	145.49	199.00	176.37
Co	ppm	209.60	209.60	209.60	213.35	213.35	113.45	204.65	169.49
Ni	ppm	2421.98	2421.98	2421.98	1542.81	1542.81	933.40	3539.28	4879.98
Cu	ppm	10.12	10.12	10.12	b-d	b-d	48.98	b-d	b-d
Zn	ppm	113.90	113.90	113.90	153.05	153.05	92.43	211.43	162.62
Rb	ppm	0.81	0.81	0.81	0.53	0.53	b-d	4.40	5.22
Sr	ppm	0.99	0.99	0.99	0.37	0.37	b-d	b-d	b-d
Y	ppm	0.11	0.11	0.11	0.08	0.08	b-d	5.58	0.37
Zr	ppm	0.20	0.20	0.20	b-d	b-d	b-d	0.17	1.13
Nb	ppm	b-d	b-d	b-d	b-d	b-d	b-d	b-d	b-d
Cs	ppm	0.07	0.07	0.07	0.25	0.25	1.71	7.44	1.09
Ba	ppm	0.24	0.24	0.24	0.26	0.26	4.15	9.99	0.20
La	ppm	0.11	0.11	0.11	b-d	b-d	4.48	b-d	b-d
Ce	ppm	0.26	0.26	0.26	0.18	0.18	b-d	0.69	b-d
Nd	ppm	b-d	b-d	b-d	b-d	b-d	b-d	b-d	b-d

Appendix 4, results of LA-ICP-MS analysis of the cores of olivine phenocrysts. (b-d below detection).

		BM2 Ph8 In1 Olivine	BM2 Ph8 in2 Olivine	BM6a Ph1 In1 Olivine	BM6a Ph4 In1 Olivine	BM6a Ph4 In2 Olivine	BM6a Ph6 In1 Olivine	BM6a Ph6 In2 Olivine	BM6a Ph7 In3 Olivine
Na_2O	%	b-d	b-d	0.01	0.03	0.03	0.00	0.00	0.07
MgO	%	42.51	42.89	44.38	43.47	43.87	43.98	43.98	45.30
Al_2O_3	%	0.07	0.08	0.05	0.04	0.04	0.06	0.06	0.08
SiO_2	%	39.75	39.08	39.50	39.00	37.46	38.59	38.59	40.76
P_2O_5	%	0.09	0.12	0.05	0.06	0.06	0.04	0.04	0.03
K_2O	%	0.01	0.01	b-d	b-d	b-d	0.00	0.00	b-d
CaO	%	0.75	0.91	0.27	0.23	0.26	0.24	0.24	0.30
TiO_2	%	b-d	b-d	0.01	0.01	0.01	0.01	0.01	0.01
MnO	%	0.20	0.24	0.17	0.19	0.20	0.18	0.18	0.17
Fe_2O_3	%	16.61	16.68	15.57	16.96	18.08	16.90	16.90	13.28
Forsterite	%	82.02	82.09	83.56	82.04	81.22	82.26	82.26	85.87
Cr	ppm	195.91	228.31	247.92	232.61	237.60	221.08	221.08	408.90
Co	ppm	183.80	207.05	141.86	144.57	138.18	166.12	166.12	147.62
Ni	ppm	995.71	6343.21	1783.60	1590.05	1838.92	1765.53	1765.53	2075.76
Cu	ppm	14.41	47.17	2.41	6.10	6.26	5.81	5.81	b-d
Zn	ppm	37.19	82.06	88.65	104.50	97.66	99.35	99.35	98.66
Rb	ppm	b-d	b-d	0.36	b-d	b-d	b-d	b-d	0.23
Sr	ppm	3.33	4.27	0.23	0.06	b-d	0.69	0.69	b-d
Y	ppm	2.09	2.88	0.02	0.01	0.01	0.51	0.51	0.17
Zr	ppm	1.03	1.33	0.39	b-d	b-d	0.53	0.53	b-d
Nb	ppm	b-d	b-d	0.06	0.06	0.23	b-d	b-d	b-d
Cs	ppm	b-d	b-d	b-d	b-d	0.26	0.12	0.12	b-d
Ba	ppm	15.47	18.15	0.20	b-d	b-d	3.79	3.79	b-d
La	ppm	b-d	b-d	b-d	0.08	0.08	b-d	b-d	0.12
Ce	ppm	b-d	b-d	0.01	0.07	0.06	b-d	b-d	b-d
Nd	ppm	b-d	b-d	b-d	b-d	0.21	b-d	b-d	b-d

		BM6a Ph8 In4 Olivine	BM6a Ph9 In1 Olivine	BM6a Ph9 In2 Olivine	MR9 Ph1 In1 Olivine	MR9 Ph2 In3 Olivine	MR9 Ph3 In1 Olivine	MR9 Ph5 In1 Olivine	MR10 Ph1 In1 Olivine
Na_2O	%	0.04	0.06	0.06	0.01	0.03	0.00	0.01	b-d
MgO	%	47.21	42.53	42.53	37.63	37.34	37.39	37.34	42.27
Al_2O_3	%	0.08	0.05	0.05	0.02	0.02	0.02	0.03	0.03
SiO_2	%	40.63	39.16	39.16	40.69	39.19	39.79	41.01	40.63
P_2O_5	%	0.04	0.09	0.09	0.04	0.02	0.02	0.04	0.05
K_2O	%	b-d	b-d	b-d	b-d	b-d	0.00	b-d	b-d
CaO	%	0.32	0.22	0.22	0.24	0.33	0.25	0.23	0.23
TiO_2	%	0.01	0.01	0.01	0.01	0.01	0.01	0.01	0.00
MnO	%	0.16	0.22	0.22	0.27	0.29	0.27	0.25	0.23
Fe_2O_3	%	11.52	17.66	17.66	21.09	22.77	22.23	21.06	16.56
Forsterite	%	87.96	81.10	81.10	76.08	74.51	74.98	75.96	81.98
Cr	ppm	507.39	171.49	171.49	118.91	139.60	65.92	131.23	202.62
Co	ppm	139.00	188.02	188.02	173.98	152.99	173.32	158.72	166.40
Ni	ppm	1895.94	1348.49	1348.49	860.86	613.40	756.48	873.60	1323.09
Cu	ppm	9.13	b-d	b-d	2.67	4.08	2.98	3.16	1.21
Zn	ppm	75.55	133.65	133.65	115.60	136.22	99.56	100.15	118.00
Rb	ppm	0.80	b-d	b-d	b-d	b-d	b-d	b-d	0.01
Sr	ppm	0.31	0.37	0.37	b-d	b-d	0.05	b-d	0.01
Y	ppm	b-d	0.03	0.03	0.15	0.16	0.23	0.10	0.31
Zr	ppm	0.47	b-d	b-d	b-d	b-d	0.54	0.72	0.13
Nb	ppm	0.34	b-d	b-d	b-d	0.07	b-d	b-d	b-d
Cs	ppm	b-d	0.11	0.11	b-d	b-d	b-d	b-d	b-d
Ba	ppm	2.84	2.62	2.62	0.25	b-d	b-d	b-d	b-d
La	ppm	0.00	0.06	0.06	b-d	b-d	0.02	b-d	0.01
Ce	ppm	0.02	b-d	b-d	b-d	b-d	b-d	b-d	0.01
Nd	ppm	b-d	b-d	b-d	b-d	b-d	b-d	b-d	0.03

Appendix 4, results of LA-ICP-MS analysis of the cores of olivine phenocrysts. (b-d below detection).

		MR10 Ph1 In2 Olivine	MR10 Ph2 In1 Olivine	MR10 Ph3 In1 Olivine	MR10 Ph4 In1 Olivine	MR10 Ph4 In2 Olivine	MR10 Ph5 In1 Olivine	MR10 Ph5 In2 Olivine	MR10 Ph7 In1 Olivine
Na_2O	%	0.02	0.05	0.03	0.01	1.02	0.04	0.02	0.03
MgO	%	42.95	42.86	44.88	44.23	42.26	44.22	42.08	44.98
Al_2O_3	%	0.04	0.04	0.05	0.04	0.09	0.04	0.05	0.07
SiO_2	%	41.22	41.81	40.73	41.10	41.97	40.97	42.30	41.73
P_2O_5	%	0.07	0.05	0.03	0.11	0.17	0.03	0.04	0.03
K_2O	%	b-d	b-d	b-d	b-d	0.02	b-d	b-d	b-d
CaO	%	0.27	0.23	0.27	0.31	0.42	0.22	0.25	0.31
TiO_2	%	0.01	0.01	0.00	0.01	0.01	0.01	0.01	0.01
MnO	%	0.21	0.21	0.20	0.20	0.19	0.19	0.20	0.17
Fe_2O_3	%	15.22	14.76	13.80	13.98	13.85	14.28	15.06	12.67
Forsterite	%	83.41	83.81	85.29	84.94	84.47	84.67	83.28	86.36
Cr	ppm	261.16	297.57	363.83	247.54	301.14	283.87	264.69	400.56
Co	ppm	160.85	159.93	154.34	157.79	143.55	140.00	150.01	145.48
Ni	ppm	1538.83	1794.44	2062.85	1577.93	1571.65	1737.66	1626.03	2190.93
Cu	ppm	4.65	4.44	3.36	b-d	4.52	27.34	6.37	b-d
Zn	ppm	105.11	103.26	99.29	100.77	79.18	96.01	114.21	103.74
Rb	ppm	b-d	b-d	0.05	0.18	0.18	0.08	b-d	0.43
Sr	ppm	0.03	b-d	0.22	b-d	0.27	b-d	0.08	0.09
Y	ppm	0.17	0.07	0.32	0.15	0.00	0.06	0.00	0.12
Zr	ppm	0.21	b-d	b-d	0.25	0.45	b-d	b-d	b-d
Nb	ppm	b-d	b-d	0.05	0.04	b-d	b-d	b-d	b-d
Cs	ppm	b-d	b-d	b-d	b-d	b-d	b-d	b-d	b-d
Ba	ppm	b-d	b-d	0.00	0.24	0.70	b-d	b-d	b-d
La	ppm	b-d	0.00	0.01	b-d	b-d	b-d	b-d	0.04
Ce	ppm	0.00	0.00	0.01	0.01	0.03	b-d	b-d	0.02
Nd	ppm	b-d	b-d	b-d	b-d	b-d	b-d	b-d	b-d

		MR10 Ph8 In1 Olivine	MR10 Ph11 In1 Olivine	MR10 Ph11 In2 Olivine	MR12a Ph1 In1 Olivine	MR12a Ph1 In2 Olivine	MR12a Ph1 In3 Olivine	MR12a Ph2 In1 Olivine	MR12a Ph4 In1 Olivine
Na_2O	%	0.03	0.03	0.04	0.02	0.01	0.02	0.01	0.02
MgO	%	42.37	43.14	43.17	41.08	41.23	41.08	46.50	33.37
Al_2O_3	%	0.05	0.04	0.04	0.03	0.04	0.04	0.05	0.03
SiO_2	%	42.75	41.89	41.75	38.89	38.98	39.62	39.95	37.05
P_2O_5	%	0.05	0.04	0.03	0.04	0.05	0.05	0.04	0.05
K_2O	%	b-d	b-d	b-d	b-d	b-d	b-d	b-d	b-d
CaO	%	0.26	0.25	0.21	0.27	0.26	0.25	0.20	0.32
TiO_2	%	0.01	0.01	0.01	0.01	0.01	0.01	0.00	0.01
MnO	%	0.21	0.21	0.21	0.23	0.22	0.23	0.15	0.35
Fe_2O_3	%	14.28	14.40	14.54	19.43	19.20	18.71	13.10	28.80
Forsterite	%	84.10	84.23	84.11	79.03	79.28	79.64	86.35	67.37
Cr	ppm	272.27	240.26	245.49	193.91	188.28	194.51	338.06	91.16
Co	ppm	158.35	152.38	155.55	139.53	134.67	178.10	129.25	171.61
Ni	ppm	1676.23	1513.94	1567.82	1425.27	1380.38	1686.19	2043.16	1059.41
Cu	ppm	3.89	5.32	5.23	6.32	5.08	3.30	3.37	1.04
Zn	ppm	91.38	104.02	110.47	118.43	129.62	110.62	70.13	202.23
Rb	ppm	b-d	0.12	0.36	b-d	b-d	b-d	0.18	b-d
Sr	ppm	0.04	b-d	b-d	0.03	0.03	0.07	0.07	b-d
Y	ppm	0.05	0.00	b-d	0.32	0.30	0.17	0.13	0.36
Zr	ppm	b-d	0.28	b-d	0.16	b-d	0.15	b-d	b-d
Nb	ppm	b-d	b-d	0.07	b-d	b-d	0.17	b-d	b-d
Cs	ppm	b-d	b-d	b-d	b-d	b-d	b-d	b-d	b-d
Ba	ppm	0.33	0.12	0.15	b-d	b-d	0.29	b-d	b-d
La	ppm	b-d	0.02	b-d	b-d	0.01	0.01	b-d	b-d
Ce	ppm	0.04	0.02	0.04	0.01	0.01	0.01	b-d	b-d
Nd	ppm	b-d	b-d	b-d	b-d	b-d	0.07	b-d	b-d

Appendix 4, results of LA-ICP-MS analysis of the cores of olivine phenocrysts. (b-d below detection).

		MR12a Ph4 In2 Olivine	MR12a Ph6 In1 Olivine	MR12a Ph7 In1 Olivine	MR12a Ph8 In1 Olivine	MR12a Ph9 In1 Olivine	MR12a Ph9 In2 Olivine	MR12a Ph12 In1 Olivine	MR12a Ph11 In1 Olivine
Na_2O	%	0.03	0.02	0.05	0.04	0.02	0.03	0.04	0.03
MgO	%	33.86	34.18	35.72	46.62	41.22	43.05	40.57	40.41
Al_2O_3	%	0.03	0.03	0.04	0.08	0.05	0.03	0.05	0.04
SiO_2	%	37.78	37.92	38.61	38.54	39.16	39.46	38.94	39.83
P_2O_5	%	0.05	0.06	0.05	0.02	0.04	0.02	0.04	0.12
K_2O	%	b-d	b-d	b-d	b-d	0.00	b-d	0.00	0.00
CaO	%	0.27	0.30	0.25	0.23	0.23	0.17	0.24	0.27
TiO_2	%	0.01	0.01	0.01	0.01	b-d	b-d	0.01	0.01
MnO	%	0.33	0.35	0.32	0.18	0.25	0.19	0.26	0.25
Fe_2O_3	%	27.65	27.13	24.95	14.29	19.03	17.06	19.85	19.05
Forsterite	%	68.58	69.19	71.84	85.33	79.43	81.81	78.47	79.09
Cr	ppm	83.96	116.22	96.85	288.77	253.38	208.96	214.78	183.13
Co	ppm	158.78	169.28	140.96	142.45	149.93	132.54	151.22	154.60
Ni	ppm	954.38	1191.65	937.52	1695.10	1346.77	1332.31	1229.81	1571.66
Cu	ppm	b-d	3.08	1.06	8.37	2.03	4.67	2.58	5.65
Zn	ppm	210.03	178.75	202.98	99.18	128.00	124.26	144.79	108.89
Rb	ppm	b-d	b-d	b-d	b-d	0.23	b-d	0.01	b-d
Sr	ppm	b-d	b-d	0.21	b-d	b-d	b-d	0.32	0.41
Y	ppm	0.30	0.36	0.47	0.08	0.22	0.30	0.20	0.30
Zr	ppm	0.20	0.07	0.40	b-d	0.12	0.09	0.23	b-d
Nb	ppm	b-d	0.07	b-d	b-d	b-d	0.09	b-d	b-d
Cs	ppm	b-d	b-d	b-d	b-d	b-d	b-d	b-d	b-d
Ba	ppm	b-d	b-d	0.14	0.21	0.30	b-d	0.29	b-d
La	ppm	b-d	0.01	0.00	0.01	0.01	b-d	0.03	b-d
Ce	ppm	b-d	0.06	0.02	0.00	0.01	b-d	0.06	0.02
Nd	ppm	b-d	b-d	b-d	b-d	b-d	b-d	0.03	b-d

		MR12a Ph11 In2 Olivine	MR12a Ph14 In1 Olivine	AM7a Ph1 In1 Olivine	AM7a Ph1 In3 Olivine	AM7a Ph1 In4 Olivine	AM7a Ph2 In1 Olivine	AM7a Ph3 In1 Olivine	AM7a Ph3 In2 Olivine
Na_2O	%	0.03	0.02	b-d	b-d	b-d	0.01	0.03	0.04
MgO	%	40.63	48.89	43.61	43.61	43.61	48.57	47.91	49.19
Al_2O_3	%	0.04	0.03	0.04	0.04	0.04	0.04	0.05	0.07
SiO_2	%	39.54	38.50	37.16	37.16	37.16	39.65	38.40	38.15
P_2O_5	%	0.12	0.04	0.05	0.05	0.05	0.04	0.07	0.07
K_2O	%	b-d	b-d	b-d	b-d	b-d	b-d	b-d	b-d
CaO	%	0.26	0.21	0.29	0.29	0.29	0.18	0.31	0.34
TiO_2	%	0.01	0.00	0.01	0.01	0.01	0.01	0.01	0.01
MnO	%	0.25	0.13	0.26	0.26	0.26	0.14	0.19	0.19
Fe_2O_3	%	19.13	12.18	18.58	18.58	18.58	11.35	13.03	11.94
Forsterite	%	79.10	87.74	80.70	80.70	80.70	88.41	86.77	88.01
Cr	ppm	188.47	189.97	265.20	265.20	265.20	236.77	230.31	255.75
Co	ppm	154.06	117.34	195.24	195.24	195.24	131.25	170.67	188.41
Ni	ppm	1580.80	1778.96	1892.71	1892.71	1892.71	1696.24	1936.11	2204.69
Cu	ppm	6.40	10.79	4.24	4.24	4.24	3.06	4.01	4.18
Zn	ppm	105.37	65.60	144.08	144.08	144.08	78.07	147.30	135.33
Rb	ppm	b-d	0.01	0.07	0.07	0.07	b-d	0.02	0.02
Sr	ppm	0.39	b-d	0.01	0.01	0.01	0.05	0.18	0.08
Y	ppm	0.19	0.08	0.19	0.19	0.19	0.05	0.21	0.24
Zr	ppm	b-d	0.11	0.08	0.08	0.08	0.01	0.12	b-d
Nb	ppm	b-d	b-d	0.02	0.02	0.02	b-d	0.02	b-d
Cs	ppm	b-d	b-d	0.02	0.02	0.02	b-d	b-d	b-d
Ba	ppm	b-d	0.53	b-d	b-d	b-d	0.06	b-d	0.03
La	ppm	b-d	0.00	b-d	b-d	b-d	b-d	b-d	0.01
Ce	ppm	b-d	b-d	b-d	b-d	b-d	0.01	0.02	0.04
Nd	ppm	0.07	b-d	0.00	0.00	0.00	b-d	0.03	b-d

Appendix 4, results of LA-ICP-MS analysis of the cores of olivine phenocrysts. (b-d below detection).

		AM7a Ph4 In1 Olivine	AM7a Ph4 In2 Olivine	AM7a Ph5 In1 Olivine	AM7a Ph5 In2 Olivine	AM7a Ph6 In1 Olivine	AM7a Ph7 In1 Olivine	AM7a Ph8 In1 Olivine	AM7b Ph3 In1 Olivine
Na_2O	%	0.00	0.01	0.04	0.02	b-d	0.02	0.12	0.03
MgO	%	47.09	47.04	44.66	45.69	46.14	46.92	44.59	45.97
Al_2O_3	%	0.05	0.06	0.06	0.04	0.04	0.05	0.06	0.06
SiO_2	%	39.03	39.47	38.42	37.99	39.16	37.55	40.39	40.58
P_2O_5	%	0.05	0.05	0.13	0.11	0.10	0.16	0.09	0.04
K_2O	%	b-d	b-d	b-d	b-d	b-d	b-d	b-d	0.00
CaO	%	0.24	0.24	0.27	0.26	0.33	0.31	0.44	0.29
TiO_2	%	0.01	0.01	0.01	0.01	0.01	0.01	0.02	0.01
MnO	%	0.17	0.17	0.23	0.21	0.19	0.20	0.22	0.20
Fe_2O_3	%	13.37	12.96	16.18	15.68	14.03	14.78	14.07	12.81
Forsterite	%	86.26	86.61	83.11	83.86	85.43	84.98	84.96	86.48
Cr	ppm	223.69	250.20	214.27	221.04	196.91	211.99	340.33	364.88
Co	ppm	146.16	155.53	182.06	157.77	165.48	165.71	214.54	185.60
Ni	ppm	1707.88	1871.94	1752.84	1580.43	1802.31	1708.33	2548.18	2491.37
Cu	ppm	3.24	4.87	7.64	5.04	10.49	7.81	15.60	0.16
Zn	ppm	113.57	112.26	180.62	144.49	122.47	123.70	136.64	80.58
Rb	ppm	b-d	0.07	0.04	b-d	b-d	0.30	b-d	b-d
Sr	ppm	b-d	b-d	0.13	b-d	b-d	0.72	1.64	0.22
Y	ppm	0.29	0.01	0.36	0.16	0.32	0.40	0.54	0.09
Zr	ppm	0.09	b-d	b-d	0.12	b-d	b-d	0.48	0.07
Nb	ppm	b-d	b-d	0.06	b-d	0.11	0.26	b-d	b-d
Cs	ppm	b-d	b-d	b-d	b-d	0.18	0.12	b-d	b-d
Ba	ppm	0.17	b-d	0.18	b-d	0.85	b-d	2.09	0.12
La	ppm	0.01	b-d	b-d	b-d	0.05	0.01	0.30	b-d
Ce	ppm	0.01	b-d	b-d	b-d	b-d	b-d	0.01	b-d
Nd	ppm	b-d	b-d	b-d	0.02	0.23	0.05	0.20	b-d

		AM7b Ph4 In1 Olivine	AM7b Ph5 In1 Olivine	AM7b Ph6 In1 Olivine	AM7b Ph6 In2 Olivine	AM7b Ph6 In3 Olivine	AM7b Ph7 In1 Olivine	AM7b Ph7 In2 Olivine	AM7b Ph7 In3 Olivine	AM7b Ph10 In1 Olivine
Na_2O	%	b-d	0.02	0.02	0.02	0.03	b-d	b-d	b-d	0.02
MgO	%	46.01	45.61	46.29	46.40	46.05	45.82	47.09	47.14	43.09
Al_2O_3	%	0.06	0.07	0.08	0.08	0.07	0.10	0.08	0.08	0.05
SiO_2	%	39.85	40.01	39.61	39.71	40.06	39.00	39.01	37.53	38.56
P_2O_5	%	0.04	0.05	0.06	0.06	0.06	0.08	0.07	0.08	0.05
K_2O	%	b-d	b-d	b-d	b-d	b-d	0.00	b-d	b-d	b-d
CaO	%	0.23	0.29	0.32	0.30	0.29	0.29	0.29	0.29	0.29
TiO_2	%	0.01	0.01	0.01	0.01	0.01	0.01	0.01	0.01	0.01
MnO	%	0.19	0.21	0.21	0.21	0.21	0.20	0.19	0.19	0.26
Fe_2O_3	%	13.61	13.74	13.38	13.21	13.21	14.50	13.25	14.67	17.68
Forsterite	%	85.77	85.55	86.05	86.22	86.13	84.92	86.37	85.13	81.29
Cr	ppm	245.05	368.89	347.14	339.43	337.66	390.49	313.30	321.70	274.55
Co	ppm	182.47	193.81	199.90	193.08	187.06	185.95	185.31	187.53	208.24
Ni	ppm	2120.04	2412.68	2327.64	2300.38	2116.78	2259.33	2300.15	2350.49	1781.76
Cu	ppm	2.18	4.84	4.89	2.41	13.52	9.51	6.02	5.86	3.69
Zn	ppm	97.38	80.26	87.78	89.33	89.00	95.28	91.09	93.17	103.71
Rb	ppm	b-d	b-d	b-d	b-d	b-d	b-d	b-d	b-d	b-d
Sr	ppm	0.12	0.05	0.83	0.43	0.15	0.73	0.20	0.33	b-d
Y	ppm	0.19	0.10	0.26	0.23	0.14	0.23	0.17	0.17	0.27
Zr	ppm	0.06	b-d	0.30	0.27	0.09	0.07	b-d	b-d	0.45
Nb	ppm	b-d	0.02	b-d	b-d	b-d	b-d	b-d	b-d	b-d
Cs	ppm	b-d	b-d	b-d	b-d	b-d	b-d	b-d	b-d	b-d
Ba	ppm	0.65	b-d	0.32	0.15	b-d	0.81	0.48	0.47	0.08
La	ppm	b-d	0.02	b-d	b-d	b-d	0.02	0.03	0.02	b-d
Ce	ppm	b-d	0.01	0.05	0.02	b-d	0.06	0.06	0.06	b-d
Nd	ppm	0.04	b-d	b-d	b-d	b-d	0.12	0.14	0.11	b-d

Appendix 4, results of LA-ICP-MS analysis of the cores of olivine phenocrysts. (b-d below detection).

Appendix 5
LA-ICP-MS data for olivine-hosted melt inclusions from the MPG lavas

From methods of analysis, see Chapter 4 and Chapter 5

Sample		Am10b	Am10b	Am10b	Am10b	Am10b	Am10b	Am10b	Am10b
Inclusion		Ph12 In1	Ph12 In2	Ph11 In2	PH11 In1	Ph10 In1	Ph8 In1	Ph7 In1	Ph7 In2
Na_2O	%	1.63	2.67	3.82	2.58	3.96	12.85	2.91	1.32
MgO	%	28.33	17.50	5.14	24.65	34.52	28.02	20.35	35.10
Al_2O_3	%	4.78	8.47	11.51	7.01	9.69	3.79	10.08	7.96
SiO_2	%	48.00	48.00	48.00	43.90	42.10	42.90	48.00	39.00
P_2O_5	%	0.15	0.20	0.38	0.18	0.04	0.39	0.15	0.08
K_2O	%	0.17	0.34	0.43	0.30	0.45	0.29	0.26	0.10
CaO	%	3.67	5.63	10.14	4.73	5.04	4.40	7.22	3.71
TiO_2	%	0.73	1.08	1.85	1.05	0.59	0.43	1.25	0.57
MnO	%	0.16	0.19	0.30	0.07	0.09	0.11	0.16	0.18
Fe_2O_3	%	12.38	15.92	18.43	15.54	3.52	6.81	9.61	11.98
Forsterite	%	83.16	81.51	78.07	78.11	81.35	84.13	83.10	84.17
Cr	ppm	17.08	5.68	524.24	134.17	12.27	1056.68	575.35	7299.39
Co	ppm	121.31	110.49	61.22	3.29	14.04	144.69	145.25	163.45
Ni	ppm	411.98	779.66	1828.01	442.50	1038.14	2600.72	1905.01	1834.73
Cu	ppm	86.78	1055.59	2006.11	721.11	23.01	1158.55	1218.49	9.09
Zn	ppm	130.46	135.14	264.84	72.69	159.65	5.88	91.44	270.95
Rb	ppm	2.70	5.63	5.59	4.97	4.94	3.39	3.24	0.71
Sr	ppm	121.60	251.08	438.67	246.73	339.68	86.24	280.35	6.85
Y	ppm	11.88	10.39	10.85	11.58	6.82	5.27	11.19	4.82
Zr	ppm	52.16	65.75	116.51	73.62	107.41	26.92	70.20	39.53
Nb	ppm	2.05	3.02	4.39	3.43	1.89	0.45	2.28	0.23
Cs	ppm	70.85	121.09	203.16	131.31	124.79	36.80	108.40	15.48
Ba	ppm	5.49	3.22	5.69	4.78	1.89	2.47	3.95	1.33
La	ppm	14.56	12.75	19.06	13.89	6.79	3.67	15.84	4.69
Ce	ppm	12.16	9.26	15.02	9.69	4.39	6.10	9.76	4.09
Nd	ppm	4.22	3.65	2.69	4.56	3.47	2.62	2.20	0.87
Sm	ppm	b-d	b-d	b-d	b-d	b-d	b-d	b-d	b-d
Pb	ppm	b-d	b-d	b-d	b-d	b-d	b-d	b-d	b-d
Th	ppm	0.08	0.65	0.64	0.87	1.02	0.83	0.56	b-d
U	ppm	0.15	b-d	0.68	0.36	b-d	b-d	0.28	0.06

Sample		Am10b	Am10b	Am10b	Am10b	AM10c	AM10c	AM10c	AM10c
Inclusion		Ph7 In3	Ph7 In4	Ph6 In1	Ph6 In2	Ph1 In1	Ph1 In2	Ph2 In1	Ph2 In2
Na_2O	%	3.45	3.50	2.96	5.36	0.06	2.36	1.98	1.73
MgO	%	2.12	13.91	25.24	15.15	44.06	23.11	23.71	29.09
Al_2O_3	%	23.17	12.10	8.21	12.86	0.38	8.94	5.99	5.66
SiO_2	%	41.10	48.00	48.00	48.00	39.90	48.00	48.00	48.00
P_2O_5	%	0.27	0.24	0.29	0.49	0.05	0.15	0.14	0.06
K_2O	%	0.27	0.39	0.77	1.06	0.00	0.26	0.21	0.14
CaO	%	12.31	9.09	4.26	8.65	0.30	4.56	5.56	4.08
TiO_2	%	1.93	1.58	0.69	1.66	0.03	0.69	1.11	0.85
MnO	%	0.24	0.19	0.13	0.09	0.18	0.11	0.15	0.11
Fe_2O_3	%	15.13	11.02	9.45	6.69	15.05	11.81	13.16	10.28
Forsterite	%	84.15	83.95	83.54	83.70	83.97	83.95	84.75	80.24
Cr	ppm	16919.64	156.24	175.76	146.89	584.05	3255.99	34.48	115.58
Co	ppm	93.61	77.51	108.18	83.94	160.73	122.72	92.26	86.43
Ni	ppm	2355.49	465.55	1110.44	1280.97	1942.40	3700.39	692.81	1908.31
Cu	ppm	1769.67	220.69	26.02	289.33	11.93	1293.01	167.67	705.35
Zn	ppm	658.71	110.93	64.23	97.97	98.14	213.87	82.15	52.05
Rb	ppm	4.30	3.95	13.23	20.08	0.03	3.80	2.29	2.20
Sr	ppm	392.26	369.50	378.43	538.93	4.05	174.46	269.85	194.10
Y	ppm	19.72	15.95	7.49	20.39	0.25	9.02	11.83	8.20
Zr	ppm	122.40	97.21	61.94	138.09	1.05	57.36	70.68	60.49
Nb	ppm	2.40	2.96	3.86	8.18	0.09	1.08	3.16	1.87
Cs	ppm	106.12	173.09	358.43	494.03	b-d	b-d	b-d	b-d
Ba	ppm	5.23	5.91	9.34	18.52	0.78	84.64	106.82	67.00
La	ppm	20.82	19.78	21.44	42.82	0.04	3.20	4.40	3.30
Ce	ppm	15.75	15.13	9.66	23.22	0.20	8.82	14.14	10.92
Nd	ppm	4.57	4.68	1.79	6.35	0.16	6.58	11.03	7.20
Sm	ppm	b-d	b-d	b-d	b-d	0.04	1.78	2.35	2.39
Pb	ppm	b-d	b-d	b-d	b-d	0.04	1.25	0.81	b-d
Th	ppm	1.00	1.02	3.24	2.85	b-d	b-d	b-d	b-d
U	ppm	0.53	0.20	0.91	1.42	b-d	b-d	b-d	b-d

Appendix 5, results of LA-ICP-MS analysis of olivine-hosted melt inclusions. (b-d below detection).

Sample		AM10c	AM10c	AM10c	BHI2	BHI2	BHI2	BHI2	BHI3
Inclusion		Ph3 In1	Ph4 In1	Ph5 In1	Ph5 In1	Ph5 In2	Ph7 In1	Ph4 In1	Ph6 In1
Na_2O	%	0.73	2.66	0.02	2.04	1.80	1.49	1.39	4.12
MgO	%	42.39	28.61	29.97	25.21	27.75	37.82	38.15	2.80
Al_2O_3	%	0.68	4.82	3.30	7.72	6.04	2.25	0.53	22.62
SiO_2	%	40.00	48.00	48.00	48.00	48.00	33.00	36.00	46.00
P_2O_5	%	0.09	0.20	0.25	0.31	0.41	0.10	0.14	0.29
K_2O	%	0.03	0.20	0.10	0.25	0.24	0.27	0.26	0.14
CaO	%	0.38	2.89	1.33	5.77	4.91	3.49	4.68	14.77
TiO_2	%	0.01	0.69	0.02	1.35	1.19	0.55	0.16	3.14
MnO	%	0.17	0.11	0.02	0.12	0.14	0.28	0.24	0.10
Fe_2O_3	%	15.53	11.81	16.98	9.21	9.51	20.76	18.44	6.45
Forsterite	%	84.21	83.95	81.40	80.55	80.55	78.87	78.87	77.38
Cr	ppm	248.22	22.02	37.99	624.59	393.29	1345.39	1803.75	7107.15
Co	ppm	169.94	146.06	163.80	134.04	160.22	2075.21	1849.65	b-d
Ni	ppm	2040.00	2887.35	2699.21	900.33	1371.56	893.49	1232.35	6020.38
Cu	ppm	25.60	1444.87	17.98	1173.68	1332.01	611.60	37.32	358.44
Zn	ppm	77.90	72.78	290.67	66.72	102.60	110.55	97.84	271.17
Rb	ppm	1.06	0.33	5.47	5.34	5.45	3.10	1.46	49.72
Sr	ppm	2.45	233.57	27.51	269.96	215.07	76.11	1.25	237.83
Y	ppm	0.34	6.07	6.32	15.94	13.57	4.92	0.26	59.97
Zr	ppm	0.38	47.74	2.66	102.77	85.12	33.72	1.09	317.78
Nb	ppm	0.03	3.39	2.66	4.88	3.37	1.54	0.05	22.84
Cs	ppm	b-d	b-d	b-d	0.33	0.40	1.18	2.37	b-d
Ba	ppm	0.54	37.49	7.15	106.36	84.67	27.70	5.88	183.07
La	ppm	0.03	2.61	0.24	7.08	4.60	1.83	0.17	28.93
Ce	ppm	0.11	9.60	0.20	18.59	15.09	5.17	0.19	87.92
Nd	ppm	0.00	5.40	b-d	13.80	10.55	3.86	0.10	64.40
Sm	ppm	0.04	2.27	b-d	4.21	3.93	1.09	0.18	19.32
Pb	ppm	0.39	0.45	2.71	b-d	0.14	0.45	0.90	b-d
Th	ppm	b-d	b-d	b-d	0.50	0.36	0.20	0.00	4.54
U	ppm	b-d	b-d	b-d	0.13	0.06	0.04	0.00	1.06

Sample		BHI3	BHI3	BHI3	BHI3	BHI3	BHI3	BHI16	BHI18
Inclusion		PH6 In2	Ph8a In1	Ph8b In1	Ph3 In3	Ph11 in2	Ph11 in 3	Ph3 in2	Ph7 In3
Na_2O	%	5.70	0.87	0.16	0.01	0.19	1.27	0.07	0.11
MgO	%	14.52	33.01	40.22	40.37	39.90	31.24	28.60	40.99
Al_2O_3	%	8.90	5.72	0.45	0.29	0.46	6.47	6.62	0.24
SiO_2	%	48.00	36.50	34.00	34.60	37.00	39.00	48.00	36.21
P_2O_5	%	0.49	0.05	0.15	0.08	0.01	0.16	0.09	0.11
K_2O	%	0.03	0.20	0.13	0.02	0.01	0.24	0.15	0.10
CaO	%	6.62	3.34	0.47	0.36	0.42	4.24	3.27	0.34
TiO_2	%	1.18	0.72	0.10	0.12	0.09	0.91	0.55	0.01
MnO	%	0.22	0.24	0.26	0.32	0.26	0.22	0.15	0.28
Fe_2O_3	%	14.87	19.60	24.33	23.93	21.67	16.25	12.74	21.82
Forsterite	%	77.21	75.88	76.98	75.15	76.98	76.98	84.51	76.94
Cr	ppm	1029.81	158.39	129.30	188.71	165.10	41.08	894.69	181.51
Co	ppm	b-d	b-d	b-d	b-d	212.86	158.21	b-d	b-d
Ni	ppm	78448.29	3994.43	12307.52	2376.59	2793.36	1668.53	2081.35	2256.89
Cu	ppm	609.61	116.81	1696.49	51.98	7.55	281.73	1027.24	5.54
Zn	ppm	182.53	97.02	130.30	142.24	115.82	10.94	167.24	174.34
Rb	ppm	8.03	3.83	0.69	0.16	0.80	2.43	3.43	0.22
Sr	ppm	208.74	104.42	15.38	3.21	13.00	215.39	35.06	3.72
Y	ppm	15.66	12.12	1.12	0.77	1.30	13.02	23.16	0.26
Zr	ppm	114.73	53.00	7.89	3.56	7.92	66.97	298.26	0.63
Nb	ppm	4.62	1.97	0.24	0.30	0.26	1.77	13.95	0.05
Cs	ppm	24.81	0.74	0.06	0.13	0.31	2.74	b-d	0.03
Ba	ppm	101.14	38.94	5.30	1.85	7.67	66.85	16.22	2.63
La	ppm	6.86	2.69	0.33	0.17	0.41	3.86	8.12	0.06
Ce	ppm	18.21	8.29	1.27	0.46	0.85	10.08	27.14	0.23
Nd	ppm	11.39	6.62	0.69	0.35	0.54	8.34	11.36	0.10
Sm	ppm	3.02	2.32	b-d	0.13	b-d	4.04	4.55	0.01
Pb	ppm	2.99	b-d	b-d	0.11	b-d	b-d	86.14	0.31
Th	ppm	0.72	0.23	0.03	0.01	0.05	0.71	b-d	b-d
U	ppm	0.21	0.09	0.01	0.01	b-d	0.17	b-d	0.06

Appendix 5, results of LA-ICP-MS analysis of olivine-hosted melt inclusions. (b-d below detection).

Sample		BHI18	BHI18	BHI18	BM2	BM2	BM2	BM2	BM2
Inclusion		PH7 In1	Ph7 In2	Ph1 In1	Ph2 In1	Ph2 In2	Ph2 In3	Ph3 In1	PH3 In2
Na_2O	%	6.36	1.12	0.25	1.26	2.50	0.31	0.33	3.55
MgO	%	24.39	39.18	41.06	32.40	17.58	38.12	40.48	13.54
Al_2O_3	%	4.59	1.05	0.25	4.66	9.79	0.83	2.12	19.95
SiO_2	%	45.00	37.00	36.00	42.00	47.00	41.00	40.00	44.00
P_2O_5	%	0.14	0.07	0.07	0.10	0.16	0.08	0.08	0.16
K_2O	%	0.00	0.01	0.04	0.07	0.13	0.02	0.01	0.23
CaO	%	7.55	1.33	0.31	3.47	11.32	1.07	0.33	10.13
TiO_2	%	0.91	0.12	0.01	0.65	2.01	0.19	0.05	2.20
MnO	%	0.16	0.27	0.27	0.22	0.15	0.25	0.22	0.09
Fe_2O_3	%	11.03	19.94	21.85	15.16	9.37	18.12	16.39	6.15
Forsterite	%	76.94	76.94	76.94	80.51	80.51	80.51	82.56	82.56
Cr	ppm	1.33	177.19	410.85	1637.70	2756.79	180.05	7560.53	520.84
Co	ppm	b-d	b-d	b-d	169.94	119.33	210.47	216.18	72.14
Ni	ppm	2157.20	2318.38	2366.50	1631.86	616.34	1865.72	2399.31	1131.34
Cu	ppm	469.75	38.23	9.09	47.36	210.67	25.91	5.20	866.23
Zn	ppm	65.93	141.51	179.90	226.63	128.37	136.99	197.37	140.91
Rb	ppm	0.92	0.71	0.58	2.50	2.04	1.02	2.63	4.38
Sr	ppm	353.52	49.23	1.55	140.59	253.44	21.16	1.16	426.55
Y	ppm	14.23	1.38	0.19	5.91	20.01	2.72	0.15	22.28
Zr	ppm	94.87	8.60	0.57	41.77	114.21	16.77	0.25	132.73
Nb	ppm	0.28	0.56	0.02	1.27	3.30	0.65	0.02	4.02
Cs	ppm	0.22	0.02	0.03	0.02	b-d	0.05	0.04	0.56
Ba	ppm	175.50	28.76	2.28	24.55	51.39	4.23	0.13	68.18
La	ppm	8.40	0.96	0.06	1.88	5.11	0.82	0.09	4.25
Ce	ppm	19.65	3.32	0.15	7.41	16.45	2.83	0.16	22.02
Nd	ppm	12.87	1.51	0.04	5.27	16.28	1.52	b-d	16.88
Sm	ppm	4.32	0.45	0.00	1.72	5.22	0.62	0.15	0.18
Pb	ppm	b-d	b-d	0.12	0.58	1.62	0.69	5.43	5.58
Th	ppm	0.22	0.02	0.01	0.05	0.23	0.11	0.02	b-d
U	ppm	0.00	0.04	0.05	0.11	0.23	b-d	1.79	0.17

Sample		BM2	BM2	BM2	BM2	BM2	BM2	BM2	BM2
Inclusion		Ph3 In5	Ph5 In1	Ph5 In2	Ph12 In1	Ph11 In1	Ph10 In1	Ph8 In1	Ph8 in2
Na_2O	%	0.44	0.71	0.22	0.47	0.67	0.71	0.07	1.38
MgO	%	38.01	33.38	38.17	36.95	36.61	35.49	42.12	32.05
Al_2O_3	%	2.16	2.34	0.39	1.62	1.38	1.93	0.21	4.99
SiO_2	%	42.00	41.00	40.00	41.00	42.00	42.00	40.00	44.00
P_2O_5	%	0.09	0.12	0.11	0.11	0.08	0.09	0.09	0.11
K_2O	%	0.03	0.05	0.01	0.01	0.02	0.05	0.01	0.11
CaO	%	0.95	1.98	0.72	2.32	1.53	1.95	0.88	4.11
TiO_2	%	0.18	0.39	0.09	0.40	0.20	0.38	0.02	0.79
MnO	%	0.22	0.30	0.30	0.24	0.26	0.26	0.20	0.18
Fe_2O_3	%	15.91	19.73	19.97	16.89	17.26	17.14	16.39	12.29
Forsterite	%	82.56	77.31	77.31	79.04	78.82	77.35	82.02	82.09
Cr	ppm	3443.64	167.47	200.44	283.93	210.52	183.31	266.46	1019.35
Co	ppm	209.69	188.19	202.39	119.73	170.23	2948.24	183.61	169.77
Ni	ppm	2287.02	1442.82	1621.81	1289.50	3346.16	1942.06	967.06	6596.14
Cu	ppm	192.87	38.41	66.40	120.29	350.53	80.84	36.16	653.14
Zn	ppm	181.31	170.56	162.52	137.41	207.68	48.10	37.24	141.04
Rb	ppm	1.05	1.06	0.75	b-d	1.28	63.03	0.24	6.21
Sr	ppm	34.60	96.66	15.59	54.90	43.95	8.60	8.75	160.91
Y	ppm	1.67	4.69	1.02	4.91	6.41	27.20	1.85	4.70
Zr	ppm	12.11	24.99	6.12	28.79	44.09	1.04	2.96	61.90
Nb	ppm	0.34	1.04	0.10	0.26	b-d	0.37	0.13	0.47
Cs	ppm	0.05	0.09	0.14	0.38	0.64	26.44	0.07	1.01
Ba	ppm	8.80	24.62	4.15	20.37	14.64	0.22	15.53	8.64
La	ppm	0.56	1.36	0.35	1.00	1.16	5.62	b-d	1.89
Ce	ppm	2.10	4.08	0.97	3.49	2.37	6.67	0.42	9.72
Nd	ppm	1.56	2.70	1.20	1.96	10.46	1.74	0.26	12.06
Sm	ppm	0.51	0.91	0.29	2.81	2.32	b-d	b-d	1.94
Pb	ppm	0.40	0.42	0.28	1.80	3.89	1.22	0.94	0.08
Th	ppm	0.03	0.06	0.02	b-d	b-d	b-d	b-d	0.40
U	ppm	0.01	0.07	0.02	b-d	b-d	b-d	b-d	b-d

Appendix 5, results of LA-ICP-MS analysis of olivine-hosted melt inclusions. (b-d below detection).

Sample		BM6a	BM6a	BM6a	BM6a	BM6a	BM6a	BM6a	BM6a
Inclusion		Ph1 In1	Ph4 In1	Ph4 In2	Ph6 In1	Ph6 In2	Ph7 In3	Ph8 In4	Ph9 In1
Na_2O	%	0.42	0.16	0.07	0.04	0.08	0.05	0.12	1.83
MgO	%	24.65	42.66	43.35	43.68	43.50	41.54	44.04	17.02
Al_2O_3	%	7.28	0.32	0.17	0.20	0.23	0.72	0.66	6.32
SiO_2	%	48.00	40.00	38.00	38.58	39.00	40.80	41.00	48.00
P_2O_5	%	0.14	0.07	0.07	0.04	0.04	0.05	0.04	0.08
K_2O	%	0.18	0.01	0.00	0.01	0.01	0.03	0.00	0.14
CaO	%	5.22	0.41	0.32	0.34	0.35	0.71	1.06	12.07
TiO_2	%	1.22	0.05	0.03	0.03	0.04	0.14	0.08	1.84
MnO	%	0.10	0.18	0.19	0.18	0.18	0.19	0.16	0.21
Fe_2O_3	%	12.79	16.13	17.79	16.89	16.57	15.79	12.82	12.49
Forsterite	%	83.56	82.04	81.22	82.26	82.26	85.87	87.96	81.10
Cr	ppm	1872.70	221.02	298.96	239.08	215.49	565.60	485.61	135.89
Co	ppm	86.32	131.96	138.20	161.79	154.16	164.34	142.44	68.85
Ni	ppm	1364.98	1562.01	1848.75	1743.86	1715.15	1694.25	1762.90	379.10
Cu	ppm	434.56	23.78	10.72	5.71	13.36	292.76	11.70	2.94
Zn	ppm	86.12	107.89	96.88	101.12	101.33	131.19	92.94	130.03
Rb	ppm	6.74	0.20	b-d	0.07	0.04	0.05	1.18	2.50
Sr	ppm	107.99	9.70	4.27	4.72	6.70	6.86	4.04	267.83
Y	ppm	12.93	0.53	0.12	0.89	0.88	2.22	1.89	52.57
Zr	ppm	107.93	5.03	2.24	2.79	2.79	10.47	2.98	192.29
Nb	ppm	3.65	0.20	0.14	0.06	0.18	0.13	0.33	1.86
Cs	ppm	0.86	0.07	0.13	0.11	0.21	b-d	b-d	0.23
Ba	ppm	14.35	1.58	3.46	4.42	4.71	b-d	1.57	96.30
La	ppm	3.88	0.50	0.16	0.05	0.33	0.63	b-d	8.62
Ce	ppm	14.89	1.14	0.28	0.43	0.64	1.30	0.82	31.37
Nd	ppm	8.74	0.38	0.37	0.30	0.51	b-d	1.75	39.33
Sm	ppm	2.88	0.05	b-d	0.20	b-d	1.98	0.48	16.12
Pb	ppm	5.69	0.14	0.24	0.45	0.27	0.24	1.51	3.58
Th	ppm	0.89	b-d	b-d	0.01	0.02	b-d	0.08	0.36
U	ppm	0.08	b-d	b-d	b-d	b-d	b-d	b-d	0.05

Sample		BM6a	MR9	MR9	MR9	MR9	MR10	MR10	MR10
Inclusion		Ph9 In2	Ph1 In1	Ph2 In3	Ph3 In1	Ph5 In1	Ph1 In1	Ph1 In2	Ph2 In1
Na_2O	%	0.33	1.09	1.04	1.04	0.03	0.11	0.28	1.75
MgO	%	39.77	31.56	23.98	28.06	37.27	41.70	40.61	26.07
Al_2O_3	%	0.74	2.69	2.52	2.37	0.21	0.34	0.90	6.28
SiO_2	%	40.00	45.00	48.00	48.00	40.05	41.00	42.00	48.00
P_2O_5	%	0.09	0.04	0.23	0.10	0.03	0.06	0.08	0.14
K_2O	%	0.03	0.15	0.15	0.10	0.00	0.01	0.04	0.19
CaO	%	0.97	2.22	2.08	2.40	0.25	0.53	0.95	5.37
TiO_2	%	0.13	0.36	0.40	0.36	0.01	0.04	0.11	0.71
MnO	%	0.23	0.20	0.28	0.23	0.25	0.23	0.21	0.15
Fe_2O_3	%	17.72	16.68	21.33	17.34	21.89	15.98	14.83	11.34
Forsterite	%	81.10	76.08	74.51	74.98	75.96	81.98	83.41	83.81
Cr	ppm	122.92	2.59	48.51	74.49	871.16	216.32	236.75	990.61
Co	ppm	177.19	128.72	184.67	135.78	161.71	162.53	158.50	105.43
Ni	ppm	1156.23	775.40	663.66	738.77	889.20	1350.58	1536.20	1304.65
Cu	ppm	12.33	428.99	12.40	658.83	4.74	1.92	134.13	113.62
Zn	ppm	132.12	112.46	127.55	92.18	109.66	113.09	104.96	128.57
Rb	ppm	0.99	2.77	4.18	2.59	0.05	0.26	0.43	1.75
Sr	ppm	33.36	91.30	93.58	100.64	0.04	9.52	25.55	135.12
Y	ppm	2.58	5.97	4.18	7.54	0.17	0.65	1.55	7.61
Zr	ppm	11.50	34.77	38.27	25.61	0.69	2.97	7.73	44.61
Nb	ppm	0.53	1.67	0.97	0.92	0.11	0.09	0.36	1.72
Cs	ppm	0.00	b-d	b-d	b-d	b-d	b-d	b-d	b-d
Ba	ppm	11.19	61.88	74.31	70.27	0.25	4.92	21.17	57.32
La	ppm	0.60	2.90	1.79	2.62	0.02	0.21	0.68	2.63
Ce	ppm	2.93	8.76	8.28	10.01	0.03	0.72	2.11	9.31
Nd	ppm	2.60	5.34	4.80	6.43	0.02	0.45	1.32	6.33
Sm	ppm	b-d	1.68	1.28	0.87	0.03	0.06	0.40	1.83
Pb	ppm	0.46	0.28	0.19	1.70	0.48	10.74	0.11	0.68
Th	ppm	b-d	b-d	b-d	b-d	b-d	b-d	b-d	b-d
U	ppm	b-d	b-d	b-d	b-d	b-d	b-d	b-d	b-d

Appendix 5, results of LA-ICP-MS analysis of olivine-hosted melt inclusions. (b-d below detection).

Sample		MR10	MR10	MR10	MR10	MR10	MR10	MR10	MR10
Inclusion		Ph3 In1	Ph4 In1	Ph4 In2	Ph5 In1	Ph5 In2	Ph7 In1	Ph8 In1	Ph11 In1
Na_2O	%	1.85	2.18	1.82	0.50	0.30	2.17	1.54	1.89
MgO	%	25.21	23.73	26.33	39.86	38.74	23.74	27.34	30.38
Al_2O_3	%	8.43	8.40	7.42	1.10	0.92	9.09	5.88	6.96
SiO_2	%	48.00	47.00	48.00	44.00	42.00	48.00	48.00	47.00
P_2O_5	%	0.10	0.07	0.16	0.04	0.06	0.09	0.10	0.26
K_2O	%	0.11	0.28	0.26	0.35	0.02	0.09	0.18	0.28
CaO	%	6.30	7.44	5.18	0.72	0.95	6.91	4.87	6.26
TiO_2	%	0.84	0.89	0.73	0.14	0.11	0.87	0.63	0.78
MnO	%	0.13	0.15	0.14	0.16	0.23	0.12	0.15	0.14
Fe_2O_3	%	9.04	9.85	9.96	13.13	16.67	8.92	11.31	6.04
Forsterite	%	85.29	84.94	84.47	84.67	83.28	86.36	84.10	84.23
Cr	ppm	1033.39	17.20	104.01	260.66	389.56	3780.85	170.06	95.27
Co	ppm	87.79	73.57	118.87	139.91	139.52	91.06	129.46	205.36
Ni	ppm	1025.77	548.98	2092.23	3282.22	1268.11	1678.56	2050.08	43.55
Cu	ppm	91.50	1.37	397.88	1149.99	12.62	312.40	530.79	626.92
Zn	ppm	76.61	91.08	56.27	88.44	171.40	96.28	96.29	380.60
Rb	ppm	1.56	1.25	3.67	17.17	0.74	0.72	2.11	7.14
Sr	ppm	141.84	225.04	225.65	24.81	12.96	158.10	142.46	213.87
Y	ppm	8.47	15.45	11.26	1.51	1.74	15.30	9.13	18.42
Zr	ppm	40.17	64.09	50.95	14.29	5.69	58.67	35.54	83.24
Nb	ppm	1.38	2.60	1.28	0.71	0.15	1.15	1.31	b-d
Cs	ppm	b-d	b-d	b-d	b-d	b-d	b-d	b-d	b-d
Ba	ppm	31.50	153.24	153.75	58.53	3.72	18.54	76.65	164.04
La	ppm	1.97	4.70	4.95	0.85	0.31	2.25	2.59	3.83
Ce	ppm	7.79	15.64	11.83	1.75	1.03	8.16	9.37	15.29
Nd	ppm	6.48	10.25	7.82	0.49	0.85	7.37	5.02	7.40
Sm	ppm	1.27	1.87	2.37	0.14	0.30	1.53	1.82	4.30
Pb	ppm	b-d	0.84	0.84	0.02	0.16	0.50	0.97	1.36
Th	ppm	b-d	b-d	b-d	b-d	b-d	b-d	b-d	b-d
U	ppm	b-d	b-d	b-d	b-d	b-d	b-d	b-d	b-d

Sample		MR10	MR12a	MR12a	MR12a	MR12a	MR12a	MR12a	MR12a
Inclusion		Ph11 In2	Ph1 In1	Ph1 In2	Ph1 In3	Ph2 In1	Ph4 In1	Ph4 In2	Ph6 In1
Na_2O	%	1.94	2.29	1.92	2.11	0.06	0.41	0.74	1.81
MgO	%	22.72	19.95	25.93	23.82	45.64	42.07	31.12	19.26
Al_2O_3	%	7.21	8.72	5.37	5.38	1.33	1.37	1.90	6.46
SiO_2	%	48.00	48.00	46.00	39.10	39.00	45.00	48.00	48.00
P_2O_5	%	0.15	0.13	0.10	0.11	0.04	0.11	0.04	0.16
K_2O	%	0.29	0.32	0.23	0.33	0.00	0.23	0.11	0.27
CaO	%	6.60	6.95	4.45	5.41	0.29	1.61	1.96	6.40
TiO_2	%	0.92	0.96	0.67	0.72	0.04	0.23	0.29	0.94
MnO	%	0.15	0.18	0.18	0.32	0.15	0.03	0.13	0.20
Fe_2O_3	%	12.01	12.50	15.17	22.69	13.45	9.15	15.71	16.50
Forsterite	%	84.11	79.03	79.28	79.64	86.35	67.37	68.58	69.19
Cr	ppm	128.55	106.36	12.49	15.33	6104.62	424.10	198.39	6359.08
Co	ppm	81.34	92.51	122.78	86.96	135.88	282.82	137.55	104.56
Ni	ppm	511.09	717.70	558.10	358.78	2062.23	1388.78	1545.09	638.82
Cu	ppm	281.47	627.87	738.26	122.37	30.51	30.16	1888.31	479.49
Zn	ppm	146.47	66.32	99.41	215.52	100.70	301.66	131.11	253.08
Rb	ppm	4.64	6.60	3.58	5.32	0.19	3.45	1.70	6.78
Sr	ppm	199.84	287.35	224.14	205.81	3.95	19.40	83.20	210.58
Y	ppm	14.55	13.65	10.90	14.24	0.21	4.35	3.79	12.75
Zr	ppm	80.30	71.81	64.71	67.21	0.91	10.69	27.89	62.72
Nb	ppm	2.13	3.46	3.36	3.59	0.06	b-d	0.46	3.35
Cs	ppm	b-d	b-d	b-d	b-d	b-d	b-d	b-d	b-d
Ba	ppm	137.38	157.39	127.25	164.67	1.09	11.81	35.74	131.01
La	ppm	4.37	5.82	4.00	3.87	0.06	1.20	1.55	4.69
Ce	ppm	15.62	15.18	10.50	13.18	0.22	3.49	4.62	15.02
Nd	ppm	9.59	10.60	8.34	7.53	0.12	1.87	3.19	7.92
Sm	ppm	3.17	2.62	2.15	2.46	0.03	0.38	1.12	2.20
Pb	ppm	1.37	1.82	1.05	3.87	0.05	1.37	1.40	1.34
Th	ppm	b-d	b-d	b-d	b-d	b-d	b-d	b-d	b-d
U	ppm	b-d	b-d	b-d	b-d	b-d	b-d	b-d	b-d

Appendix 5, results of LA-ICP-MS analysis of olivine-hosted melt inclusions. (b-d below detection).

Sample		MR12a	MR12a	MR12a	MR12a	MR12a	MR12a	MR12a	MR12a
Inclusion		Ph7 In1	Ph8 In1	Ph9 In1	Ph9 In2	Ph12 In1	Ph11 In1	Ph11 In2	Ph14 In1
Na_2O	%	1.98	0.20	1.50	0.06	1.84	1.85	1.85	1.66
MgO	%	21.63	27.25	43.65	43.79	21.70	25.53	26.87	25.40
Al_2O_3	%	5.83	5.44	4.08	0.15	4.89	6.73	5.04	5.03
SiO_2	%	48.00	48.00	43.00	40.00	48.00	48.00	48.00	48.00
P_2O_5	%	0.14	0.21	0.36	0.05	0.13	0.12	0.14	0.16
K_2O	%	0.25	0.02	0.15	0.00	0.23	0.21	0.25	0.09
CaO	%	5.05	3.91	3.05	0.26	4.14	4.29	3.31	4.92
TiO_2	%	0.65	0.46	0.57	0.02	0.64	0.50	0.45	0.54
MnO	%	0.21	0.07	0.05	0.17	0.23	0.10	0.17	0.14
Fe_2O_3	%	16.26	14.44	3.60	15.51	18.19	12.68	13.91	14.06
Forsterite	%	71.84	85.33	79.43	81.81	78.47	79.09	79.10	87.74
Cr	ppm	66.64	3417.04	4328.92	186.76	2701.19	8828.72	168.43	129.98
Co	ppm	89.77	103.75	134.81	128.13	92.60	73.36	98.19	103.70
Ni	ppm	558.92	2515.57	3529.32	1455.48	846.05	76.38	948.76	2022.24
Cu	ppm	190.87	2233.13	78.05	3.43	11.84	56.53	95.34	3996.60
Zn	ppm	149.63	155.37	86.31	111.22	146.27	208.92	95.88	126.14
Rb	ppm	4.73	3.94	1.66	b-d	5.02	3.68	4.80	0.94
Sr	ppm	166.19	13.67	96.97	2.36	157.50	150.50	162.10	91.56
Y	ppm	9.25	7.17	2.13	0.37	8.64	7.50	5.54	7.06
Zr	ppm	39.08	26.05	25.66	0.88	37.59	38.78	30.45	28.27
Nb	ppm	1.93	2.42	3.84	0.04	2.00	1.40	1.83	1.75
Cs	ppm	b-d	b-d	b-d	b-d	b-d	b-d	b-d	b-d
Ba	ppm	100.01	0.80	33.98	1.02	98.97	81.41	102.21	20.74
La	ppm	3.24	1.23	1.56	0.06	2.79	2.88	3.28	1.36
Ce	ppm	11.44	5.40	7.62	0.19	10.86	10.21	9.93	4.98
Nd	ppm	6.70	4.83	4.38	0.11	6.44	6.26	5.26	4.55
Sm	ppm	1.66	1.79	1.02	0.04	1.34	1.52	1.05	1.93
Pb	ppm	1.60	4.57	18.91	0.06	0.95	0.84	1.60	0.33
Th	ppm	b-d	b-d	b-d	b-d	b-d	b-d	b-d	b-d
U	ppm	b-d	b-d	b-d	b-d	b-d	b-d	b-d	b-d

Sample		AM7a	AM7a	AM7a	AM7a	AM7a	AM7a	AM7a	AM7a
Inclusion		Ph1 In1	Ph1 In3	Ph1 In4	Ph2 In1	Ph3 In1	Ph3 In2	Ph4 In1	Ph4 In2
Na_2O	%	1.19	0.24	0.51	1.83	0.12	0.86	2.55	4.36
MgO	%	28.46	41.57	37.58	31.03	46.31	40.50	21.11	35.33
Al_2O_3	%	5.25	0.88	2.03	4.40	0.39	2.79	10.56	0.42
SiO_2	%	48.00	38.00	40.00	48.00	39.00	41.00	48.00	48.00
P_2O_5	%	0.47	0.08	0.15	0.20	0.06	0.10	0.39	0.07
K_2O	%	0.27	0.04	0.10	0.32	0.19	0.06	0.28	0.15
CaO	%	5.29	1.19	1.99	3.39	0.61	2.55	8.01	1.70
TiO_2	%	0.93	0.17	0.33	0.79	0.06	0.38	1.39	0.03
MnO	%	0.44	0.25	0.24	0.14	0.18	0.08	0.19	0.16
Fe_2O_3	%	9.70	17.59	17.07	9.91	13.27	11.68	7.52	9.78
Forsterite	%	80.70	80.70	80.70	88.41	86.77	88.01	86.26	86.61
Cr	ppm	402.61	480.86	232.42	57.60	214.86	241.75	162.08	227.75
Co	ppm	492.00	197.55	180.82	79.85	144.29	46.21	199.60	145.24
Ni	ppm	3741.60	2103.58	1956.19	518.03	1658.69	791.54	4450.14	1854.43
Cu	ppm	670.68	78.56	215.99	10.76	56.89	151.11	1970.02	131.69
Zn	ppm	348.05	136.49	135.49	69.09	122.64	43.83	176.96	88.31
Rb	ppm	5.34	0.88	1.86	4.61	0.04	1.08	5.09	5.67
Sr	ppm	251.37	30.86	83.21	73.49	5.06	51.35	341.00	12.70
Y	ppm	11.65	2.18	4.90	7.43	1.06	4.74	17.57	1.14
Zr	ppm	74.33	11.52	27.47	41.18	3.08	24.40	115.16	17.25
Nb	ppm	2.59	0.57	0.89	2.42	0.02	0.78	4.13	0.58
Cs	ppm	0.50	0.00	0.01	0.02	b-d	b-d	0.57	b-d
Ba	ppm	121.34	16.49	51.87	67.94	0.16	18.17	124.64	13.35
La	ppm	4.82	0.79	1.92	2.89	0.20	1.26	5.43	0.94
Ce	ppm	15.69	2.52	5.66	11.21	0.85	3.95	17.48	2.18
Nd	ppm	9.46	1.62	3.97	5.95	1.01	3.60	14.23	0.80
Sm	ppm	3.00	0.60	1.17	2.40	0.28	1.51	3.82	0.16
Pb	ppm	0.47	0.17	0.29	1.02	0.05	0.10	4.79	7.62
Th	ppm	0.28	0.05	0.05	0.18	b-d	0.09	0.69	0.46
U	ppm	0.05	0.01	0.02	0.07	b-d	0.03	0.07	0.20

Appendix 5, results of LA-ICP-MS analysis of olivine-hosted melt inclusions. (b-d below detection).

Sample		AM7a	AM7a	AM7a	AM7a	AM7a	AM7b	AM7b	AM7b
Inclusion		Ph5 In1	Ph5 In2	Ph6 In1	Ph7 In1	Ph8 In1	Ph3 In1	Ph4 In1	Ph5 In1
Na_2O	%	0.11	4.51	0.22	0.91	0.34	0.03	0.01	1.46
MgO	%	44.60	30.75	44.13	34.76	42.19	45.69	45.39	35.18
Al_2O_3	%	0.27	1.57	0.73	4.65	0.55	0.81	1.27	4.95
SiO_2	%	39.00	48.00	40.00	41.00	42.00	40.00	39.00	44.00
P_2O_5	%	0.12	0.14	0.11	0.19	0.13	0.04	0.04	0.06
K_2O	%	0.01	0.22	0.03	0.11	0.03	0.00	0.00	0.13
CaO	%	0.37	3.11	0.77	3.57	1.21	0.28	0.25	3.07
TiO_2	%	0.04	0.25	0.10	0.58	0.13	0.02	0.03	0.40
MnO	%	0.19	0.29	0.19	0.18	0.21	0.20	0.19	0.14
Fe_2O_3	%	15.28	11.16	13.72	14.06	13.21	12.92	13.82	10.61
Forsterite	%	83.11	83.86	85.43	84.98	84.96	86.48	85.77	85.55
Cr	ppm	177.72	270.47	180.31	153.88	340.37	2572.62	3419.67	44.87
Co	ppm	151.61	227.01	167.32	136.88	184.75	187.58	186.26	120.50
Ni	ppm	1488.07	1844.60	1833.78	1539.59	2215.44	2493.57	2131.91	1482.37
Cu	ppm	43.74	19.67	11.33	585.94	16.64	3.74	3.11	19.86
Zn	ppm	139.51	178.58	126.19	119.23	123.18	94.79	114.69	75.12
Rb	ppm	0.29	5.85	0.71	2.53	0.58	0.01	b-d	2.49
Sr	ppm	12.37	54.86	26.05	150.98	15.49	0.26	0.57	144.46
Y	ppm	0.57	5.28	1.44	9.51	1.89	0.09	0.22	5.21
Zr	ppm	3.91	37.14	9.21	47.96	10.09	0.11	0.31	27.79
Nb	ppm	0.16	0.96	0.34	1.66	0.33	b-d	0.03	1.06
Cs	ppm	0.06	b-d	0.04	0.01	0.41	b-d	b-d	b-d
Ba	ppm	7.84	41.85	17.00	66.07	6.03	0.15	0.77	45.45
La	ppm	0.29	2.46	0.34	2.72	0.67	0.00	0.02	1.48
Ce	ppm	0.79	5.32	2.01	8.28	1.60	0.01	0.06	4.92
Nd	ppm	0.46	4.58	1.07	5.63	1.37	0.00	0.08	3.68
Sm	ppm	0.06	1.72	0.80	1.83	0.80	0.01	b-d	1.05
Pb	ppm	0.16	59.04	0.07	1.18	0.09	b-d	b-d	b-d
Th	ppm	0.01	0.85	0.08	0.29	b-d	b-d	0.01	0.36
U	ppm	0.00	0.08	b-d	0.03	b-d	b-d	b-d	0.08

Sample		AM7b	AM7b	AM7b	AM7b	AM7b	AM7b	AM7b
Inclusion		Ph6 In1	Ph6 In2	Ph6 In3	Ph7 In1	Ph7 In2	Ph7 In3	Ph10 In1
Na_2O	%	1.55	3.42	4.36	3.47	1.18	0.60	0.02
MgO	%	28.26	15.18	1.91	13.38	33.70	34.87	44.13
Al_2O_3	%	7.14	16.07	19.34	12.35	5.64	5.72	0.21
SiO_2	%	45.00	45.00	46.00	48.00	42.00	39.00	38.57
P_2O_5	%	0.12	0.28	0.12	0.07	0.12	0.06	0.04
K_2O	%	0.19	0.39	0.45	0.38	0.20	0.06	0.00
CaO	%	6.31	11.80	14.34	8.98	4.58	5.39	0.28
TiO_2	%	1.27	2.15	2.67	1.85	0.62	0.82	0.01
MnO	%	0.14	0.05	0.11	0.18	0.17	0.19	0.24
Fe_2O_3	%	10.02	5.66	10.71	11.34	11.78	13.29	16.49
Forsterite	%	86.05	86.22	86.13	84.92	86.37	85.13	81.29
Cr	ppm	11.13	1967.81	4003.14	1476.06	2783.50	2420.81	304.80
Co	ppm	127.27	13.81	108.77	72.96	131.22	153.80	202.49
Ni	ppm	1779.83	1544.60	492.87	1144.89	1578.05	2773.62	1929.39
Cu	ppm	297.99	659.54	1073.48	218.61	151.04	408.43	7.13
Zn	ppm	33.55	76.37	149.39	87.43	98.40	179.64	102.43
Rb	ppm	3.69	4.51	2.93	5.01	3.14	0.59	0.11
Sr	ppm	209.50	419.00	452.54	434.58	130.86	50.26	0.33
Y	ppm	9.91	27.36	18.48	20.81	9.94	9.59	0.13
Zr	ppm	66.75	136.79	154.64	143.05	50.10	42.28	0.21
Nb	ppm	4.13	6.19	9.59	4.53	1.54	1.59	b-d
Cs	ppm	b-d	b-d	b-d	b-d	b-d	b-d	b-d
Ba	ppm	73.61	133.72	155.80	131.62	87.71	16.48	0.21
La	ppm	3.49	7.44	7.26	7.85	3.50	2.06	0.01
Ce	ppm	13.19	22.04	28.21	17.94	9.88	6.44	0.05
Nd	ppm	9.02	18.77	22.83	16.81	6.91	5.06	b-d
Sm	ppm	2.14	6.60	7.45	4.67	2.08	2.71	b-d
Pb	ppm	b-d	b-d	b-d	b-d	b-d	b-d	b-d
Th	ppm	0.77	1.63	5.68	0.52	0.95	0.02	0.26
U	ppm	0.06	0.23	0.41	0.18	0.29	0.09	b-d

Appendix 5, results of LA-ICP-MS analysis of olivine-hosted melt inclusions. (b-d below detection).

Appendix 6
Field Locations and maps for MPG samples

Sample	Grid Reference	Sample	Grid Reference
BHI1	NM440852	BM14	NM081144
BHI2	NM441842	BM15	NM081156
BHI3	NM421832	BR4	NM288404
BHI16	NM302473	BR5	NM271562
BHI17	NM267466	BR6	NM328615
BHI18	NM298391	BR9	NM319643
BHI19	NM307331	BR11	NM321641
BHI20	NM263342	BR12	NM306663
BHI26	NM245161	BR13	NM309674
BHI27	NM234135	BR14	NM313701
BHI28A	NM219118	BR15	NM310803
BHI28B	NM220090	BR16	NM296825
BHI29	NM189283	BR17	NM312861
BHI30	NM135940	BB19	NM452123
AM7	NM862490	BB20	NM464220
AM7B	NM865506	BB21	NM565129
AM10A	NM960472	BB22	NM473222
AM10B	NM962474	BB23	NM547269
AM10C	NM964476	MR0	NM640449
BM2	NM874784	MR8	NM424305
BM5	NM926817	MR9	NM395289
BM6	NM958898	MR10	NM383296
BM6A	NM958898	MR11	NM340266
BM7	NM973900	MR12	NM331237
BM8	NM974902	MR12A	NM207233
BM12	NM023988	MR13	NM112193
BM12B	NM023988		

Fig. A6.1. Table of sample names and field locations

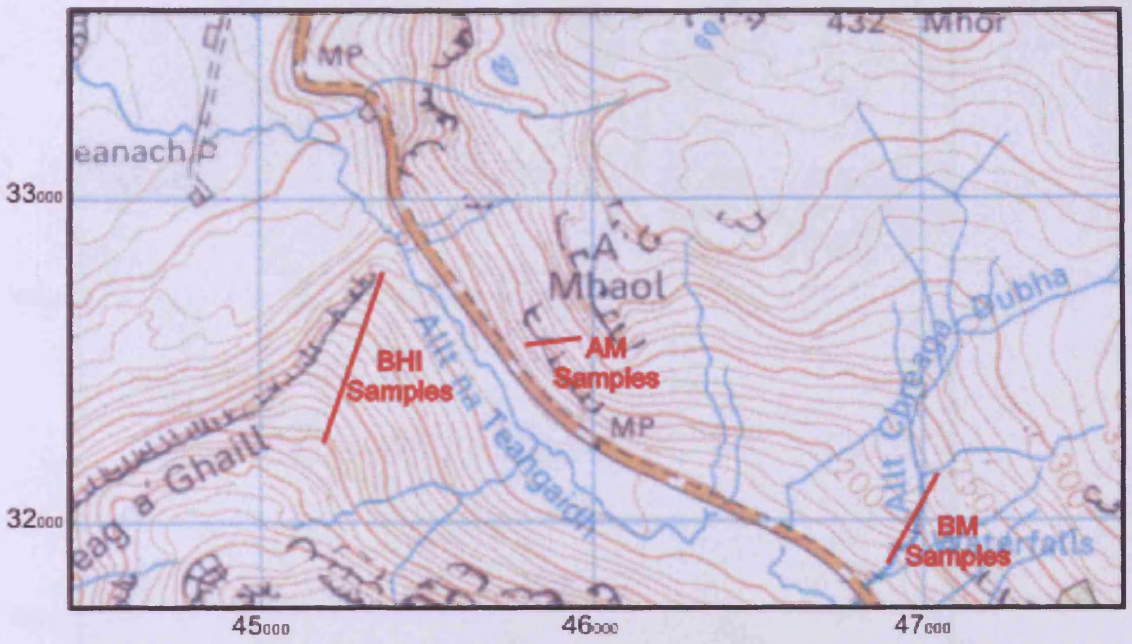

Fig. A6.2. Map showing locations where BHI, AM and BM samples were collected.

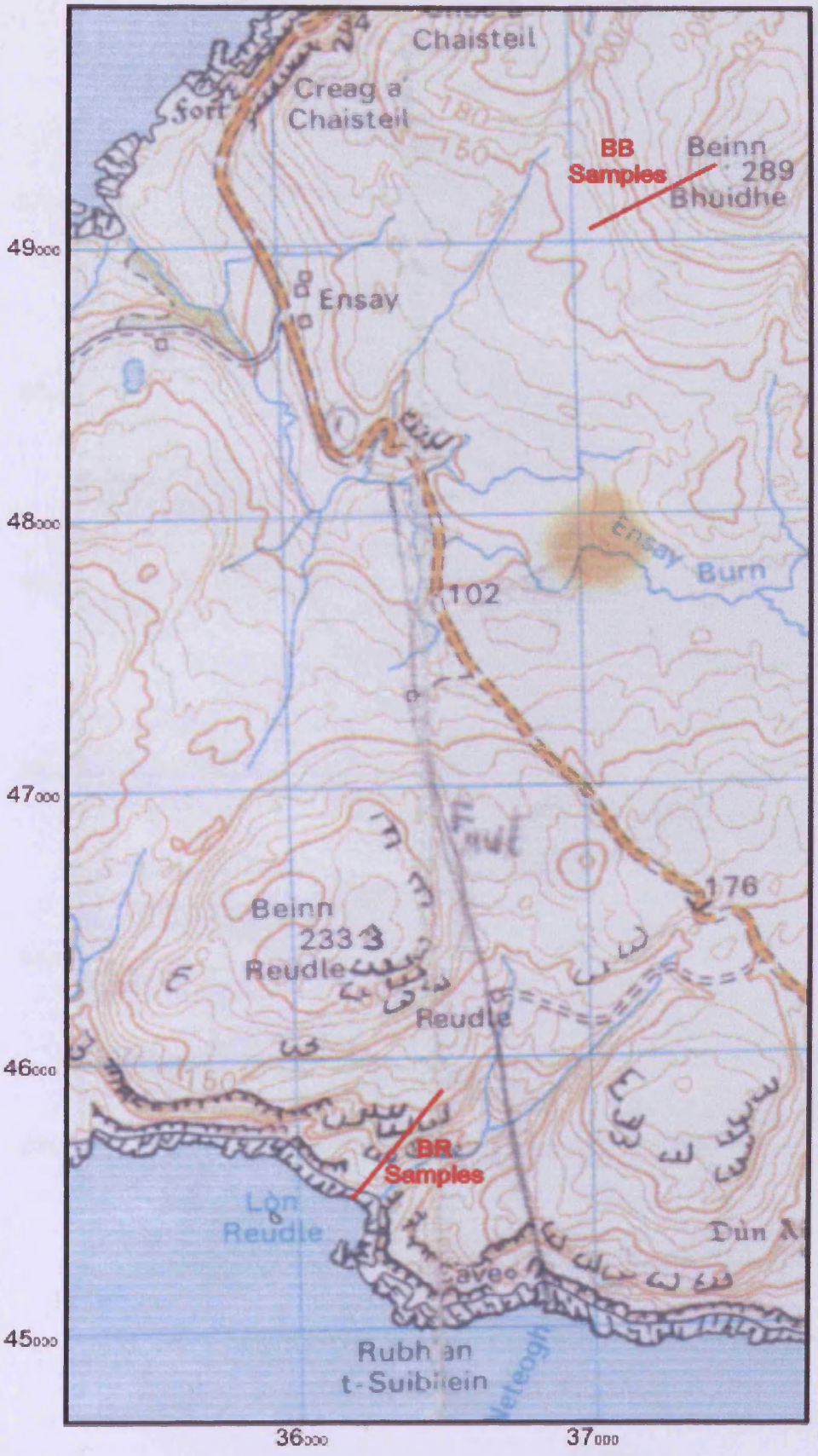

Fig. A6.3. Map showing the locations where BR and BB samples were collected.

Fig. A6.4. Map showing location where MR samples were collected.